



TECHNISCHE
UNIVERSITÄT
WIEN
Vienna University of Technology

DISSERTATION

Satellite Observations with VLBI

ausgeführt zum Zwecke der Erlangung des akademischen Grades eines Doktors der technischen
Wissenschaften unter der Leitung von

Prof. Dr. Johannes Böhm

E120-4

Department für Geodäsie und Geoinformation

Höhere Geodäsie

eingereicht an der Technischen Universität Wien
Fakultät für Mathematik und Geoinformation

von

Andreas Hellerschmied

Hasnerstraße 27/39

1160 Wien

Wien, September 2018

Acknowledgments

Five years ago – still being a student in the Master’s program – Johannes Böhm asked me to join his VLBI group at TU Wien and I happily accepted his offer. This turned out to be a defining decision, not only for my academic career, but also for my personal development. After finishing my Master’s degree, Johannes offered me a job as university assistant and guided me through my PhD studies which I am proud to conclude with this thesis. I am very grateful for Johannes’ continuous support throughout my years at TU Wien, for his competent guidance and – at the same time – for giving me an enormous degree of freedom at work. I hope that I will also have such great superiors at my future jobs. Thank you Johannes!

I want to express my sincere gratitude to the McCallums, Jamie and Lucia. Without their collaboration, support and effort it would not have been feasible to accomplish this work. Not only once did they sacrificed their leisure time and worked night shifts at the antenna control room in order to carry out VLBI experiments and to collect the data that I needed for my studies. They warmly welcomed me on my visit at Hobart and provided an exciting study environment. I appreciate Lucia’s positive attitude – without her extra portion of motivation this thesis would probably not have been realized. I want to thank Jamie for not getting tired of answering hundreds of my questions. Without his support I would have been lost from time to time.

Thanks to all my colleagues, office-mates and friends at the higher geodesy group at TU Wien for the friendly and relaxed working atmosphere and for many inspiring conversations. Especially, I want to thank David Mayer, my long-term study and office buddy – for occasionally providing distraction during long office days.

My life partner and friend Cathrine deserves my heartfelt gratitude. Thanks for your love, patients, encouragement, and support – and also for cheering me up whenever I was frustrated with my work. I love you. Finally, I want to thank my parents and family for their perpetual support throughout my life. Without them I would not be where and who I am now. Thank you!

Andreas Hellerschmied, September 2018

Abstract

The application of the Very Long Baseline Interferometry (VLBI) technique for observations of artificial Earth-orbiting satellites instead of extra-galactic radio sources has been vividly discussed in the geodetic community for several years. Promising applications – among others – can be found in the field of inter-technique frame ties. In this respect, the fundamental idea is to establish a co-location in space by combining the sensors of different space-geodetic techniques on a common satellite platform orbiting the Earth. Observations of this satellite can then be used to connect the technique-specific coordinate frame solutions. This approach is particularly relevant for the realization of the International Terrestrial Reference Frame (ITRF), which is a combination product of long-term time series of observations with VLBI, Satellite Laser Ranging (SLR), Global Navigation Satellite Systems (GNSS), and Doppler Orbitography and Radiopositioning Integrated by Satellite (DORIS). Additionally, the ITRF combination fundamentally relies on so-called local ties – terrestrially measured vectors between the reference points of geodetic instruments at co-location sites. Connecting the individual techniques via a co-location in space (i.e. by establishing so-called space ties), complementary to using local ties, provides promising possibilities to reveal technique-specific biases, and to investigate discrepancies between local tie vectors and space geodetic coordinate solutions which are widely present on the cm level. Additionally, a co-location in space promotes the rigorous integration of all space-geodetic techniques, which was identified as one of the main goals of the Global Geodetic Observing System (GGOS) of the International Association of Geodesy (IAG). From the perspective of VLBI, satellite observations would allow to connect the purely geometric coordinate frame realized by VLBI observations of extremely remote radio sources, with the dynamic coordinate frames of the geodetic satellite techniques (GNSS, SLR, and DORIS) which are subject to the Earth's gravity field.

Although space ties between the satellite techniques have already been shown, the space tie with VLBI has not been realized so far, and could only be studied by simulations. One of the main reasons for this deficiency is, that actual observation data is widely missing. Observations of satellites with geodetic VLBI systems are non-standard, and the required observation and analysis processes were not in place in order to collect real observation data. Encountering this issue, a goal of this work was to establish – for the first time – a closed process chain which enables to obtain group delays based on observations of satellites with VLBI. This process chain includes all required processes from scheduling, over observations, correlation and post-correlation processing, to the final analysis of the delays. To stay as close as possible to data acquisition and process-

ing scheme which is operationally used for geodetic VLBI sessions, standard software tools were adopted for satellite observations: The Vienna VLBI and Satellite Software (VieVS) was used for scheduling and data analysis, the software DiFX for correlation, and the Haystack Observatory Postprocessing System (HOPS) for the fringe fitting.

The second goal of this work was to apply the established process chain to perform actual observation experiments, in order to validate and test all processing steps, and to refine and adapt them whenever necessary. Hence, in 2015 and 2016 a series of VLBI sessions with observations of GNSS satellites (GPS and GLONASS) was carried out mainly on the Australian baseline Hobart-Ceduna. End of 2016 the network was extended by the antenna at Warkworth (New Zealand). All antennas were equipped with L-band receivers suitable to record the GNSS L1 and L2 signals, and with modern backends. The final experiments in this series lasted for up to 6 h and yielded results in terms of observed minus computed (O-C) residuals on the level of a few ns. In November 2016 the Chinese APOD-A nano satellite was tracked over a few days whenever visible by the Australian AuScope VLBI array. This small cube satellite was a particularly interesting observation target, as it can be considered as a first realization of a co-location satellite enabling GNSS, SLR, and VLBI on a common platform in a low Earth orbit (LEO). APOD was equipped with a dedicated VLBI beacon emitting narrow-bandwidth tones in the S- and X-band which could be observed with standard receiver equipment used for geodetic application. Although APOD was challenging to track due to the low orbit height of about 450 km, all observations were successfully correlated, and yielded O-C residuals below 10 ns. All experiments are described in detail within this thesis.

Although the results of the conducted satellite observation experiments did not reach an accuracy level which would allow for studying actual frame ties with VLBI, the work is still valuable due to the gained hands-on observation experience. Furthermore, the newly developed procedures and programs now enable to perform more observations in a semi-manual manner, similar to standard observations of natural radio sources – enabling further research and development in the field of VLBI satellite observations.

Contents

1	Introduction	1
1.1	Scientific Opportunities	5
1.2	Objectives and Outline of this Work	7
2	Very Long Baseline Interferometry for Geodesy and Astrometry	11
2.1	Basic principle	12
2.2	Data Acquisition Scheme	13
2.3	The next-generation VLBI system	18
3	Satellite Observations with VLBI	21
3.1	Previous Work and Applications	21
3.1.1	Simulation Studies	24
3.1.2	Frame Ties Between SLR, GNSS, and DORIS	24
3.2	VLBI Observations of GNSS Satellites	25
3.2.1	Previous Observation Experiments	27
3.3	Observation Aspects	28
3.3.1	Framework Conditions for Satellite Observations	28
3.3.2	Technical Observation Restrictions	30
3.4	Satellite Tracking	34
3.4.1	Stepwise Tracking	35
3.4.2	Continuous Tracking	37
3.4.2.1	ACU Tracking Capabilities	39
3.4.2.2	Satellite Tracking with the Field System	40
4	Process chain for VLBI satellite observations	43
4.1	Overview	44
4.2	The Vienna VLBI and Satellite Software	44
4.2.1	Features for VLBI Satellite Observations	48
4.2.1.1	VSO Observation Files	48
4.2.1.2	Scheduling of Satellite Observations	49
4.2.1.3	Near-field Delay Modeling	49

4.2.1.4	Parameter Estimation	53
4.3	Scheduling Satellite Observations with VieVS	54
4.3.1	Conditions for a Valid Scan	55
4.3.2	Orbit Predictions	56
4.3.3	Scheduling Workflow	59
4.3.4	Scheduling Modes	61
4.3.5	Output Files	64
4.3.6	Challenges	65
4.4	Observations	65
4.5	Correlation	66
4.5.1	DiFX Workflow	67
4.5.2	Correlator Input Model for Satellites	70
4.6	Post-correlation Processing	72
4.7	Analysis	74
5	VLBI Observations of GNSS Satellites	75
5.1	Aims and Outline	75
5.2	Overview of Experiments	76
5.3	Scheduling and Experiment Design	77
5.3.1	Experiment Design	78
5.4	Observations	82
5.4.1	Antenna Specifications	82
5.4.2	Observation Mode	85
5.4.3	Tracking and Signal Acquisition	85
5.5	Correlation	88
5.5.1	Correlation Results	90
5.6	Post-Processing and Generation of Total Delays	96
5.6.1	Polarization Issue	97
5.7	Data Analysis	101
5.7.1	Residual Delays	101
5.7.2	Discussion	104
5.8	Outlook	106
6	Observing the APOD Satellite with the AuScope VLBI Array	109
6.1	The APOD-A nano Satellite	111
6.1.1	Orbit Determination	112
6.2	The AuScope Geodetic VLBI Array	113
6.2.1	Satellite Tracking with AuScope	114
6.3	Scheduling and Experiment Design	114
6.3.1	Observation Mode	116

6.4 Observations	117
6.5 Correlation	118
6.6 Post-Correlation Processing	123
6.7 Data Analysis	125
6.7.1 Residuals Delays	126
6.7.2 Parameter Estimation – A Simple Test Case	128
6.8 Discussion and Outlook	129
7 Discussion and Outlook	133
A Scheduled VLBI Experiments With Satellite Observations	141
B Schedule Summaries of Satellite Observation Experiments	145
B.1 GNSS observations	145
B.2 APOD observations	152
C AZEL tracking files for AuScope VLBI antennas	157
Acronyms	159
List of Figures	163
List of Tables	165
List of Listings	167
Bibliography	169

Chapter 1

Introduction

The goals of GGOS The Global Geodetic Observing System (GGOS) has been established as a flagship component by the International Association of Geodesy (IAG) in 2003. A major goal of GGOS is to provide a high-quality and consistent Terrestrial Reference Frame (TRF) in order to meet the requirements of science and society which are facing increasing challenges on a changing planet. The TRF is the fundamental basis of global change monitoring, and enables to measure minute changes in the system Earth in a long-term and consistent way. Considering this important role, and the potential to directly affect crucial eco-political decisions, the quality of the TRF has wide-ranging and global implications on the future economical, environmental, and societal development on our planet. Emphasizing these aspects, the importance of a highly accurate and stable reference frame has been recognized by the A/RES/69/266 United Nations Resolution. To detect even the smallest changes in the system Earth, GGOS aims at the realization of a reference frame with an accuracy of 1 mm in position and a stability of 0.1 mm/year on a global scale (Plag & Pearlman, 2009). These stringent requirements were identified by the scientific community, as any bias or drift in the TRF propagates directly into the geophysical interpretation depending on the reference frame. Hence, for accurate monitoring and precise predictions, the accuracy and stability of the reference frame should be at least one order of magnitude better than the geophysical effects to be monitored. Probably the most prominent example is the global sea level rise which needs a precise reference to be determined on a temporal and spatial scale. Although the sea level rise is numerically small with a global mean of about 3.2 mm/year (IPCC, 2013), its precise determination is the main basis for crucial political decisions – effecting the lives of millions of people worldwide in areas at risk of flooding.

The International Terrestrial Reference Frame The ambitious goals of GGOS concerning the reference frame accuracy and stability can only be achieved by a rigorous combination and integration of the different ground- and space-geodetic techniques. Today, the most accurate realization of a global TRF aiming at this goal is the latest International Terrestrial Reference Frame (ITRF2014; Altamimi *et al.*, 2016). The ITRF2014 is an improved release compared to preceding realizations (e.g. Altamimi *et al.*, 2011). In addition to station positions at reference epochs and

corresponding linear velocities, it provides an enhanced modeling of non-linear station motions, including seasonal signals in station positions and parametric models for sites subject to post-seismic deformation. The ITRF2014 is a combination product based on the reprocessed solutions of the four space-geodetic techniques: Very Long Baseline Interferometry (VLBI), Satellite Laser Ranging (SLR), Global Navigation Satellite Systems (GNSS), and Doppler Orbitography and Radiopositioning Integrated by Satellite (DORIS). It is using the full observation history of these techniques up to the end of 2014. Additionally, the ITRF combination fundamentally depends on terrestrial local tie measurements conducted at co-location sites where two or more techniques are operated. Local ties are differential vectors connecting the reference points of two instruments measured by precise terrestrial surveying (directions, distances and leveling) or by the GPS technique (Altamimi *et al.*, 2016).

Different studies that evaluated the consistency among the contributing techniques revealed that the technique ties are still problematic. Counting the number of ITRF2014 co-locations between VLBI, SLR, and DORIS, only eleven VLBI-SLR, twelve VLBI-DORIS, and eleven SLR-DORIS local ties exist (Altamimi *et al.*, 2016). As the number of SLR-DORIS-VLBI ties is too small to provide a reliable link, GNSS occupies an important position by connecting the other three techniques with 212 additional tie vectors. Hence, GNSS is fundamental in the ITRF combination by connecting the other three techniques, since almost all VLBI, SLR, and DORIS stations are co-located with a GNSS antenna. However, not only the small number of direct links between SLR, VLBI, and DORIS can be considered as problematic, also the poor global distribution of critical co-location sites is not satisfying. The fact that the three other techniques are mainly connected indirectly via co-located GNSS antennas is also problematic as it exacerbates the identification of technique-specific biases (Krügel & Angermann, 2005). Furthermore, the ITRF2014 combination showed (or re-confirmed), that there are significant discrepancies between space geodesy solutions and terrestrial local ties in the combination: more than 50% of the SLR and VLBI ties to GNSS show residuals larger than 5 mm and about 30% exhibit residuals larger than 10 mm (Altamimi *et al.*, 2016). These differences between the local ties derived from terrestrial surveys on the one hand and coordinate differences derived from observations of space-geodetic techniques on the other hand are well known, and were already revealed in previous TRF combinations e.g. in the ITRF2008 (Altamimi *et al.*, 2011), or the DTRF2008 (Seitz *et al.*, 2012). Although Altamimi *et al.* (2016) state that these tie discrepancies are most likely related to systematic errors in the techniques rather than to the poor determination of the local ties themselves, the actual reasons could not be clearly revealed so far. An alternative and independent approach for linking the space-geodetic techniques is needed in order to investigate these issues more deeply.

Co-location in space A promising concept is to co-locate the techniques not only on the ground, but also on platforms in space, in order to establish frame ties independently. Hence, Earth orbiting satellites equipped with the necessary instrumentation enabling to observe them with VLBI, GNSS, SLR, and DORIS could be used as an independent link between the techniques, complementing the local ties established at co-location sites on the ground. This concept was

proposed e.g. by Rothacher *et al.* (2009) for the implementation in the GGOS framework as an important key-component for technique-integration. The significance and opportunity of this concept was also highlighted by the fact that already two dedicated co-location satellites missions – GRASP (Nerem & Draper, 2011) and E-GRASP/Eratosthenes (Biancale *et al.*, 2017) – have been proposed to the leading space agencies NASA and ESA, respectively. Although the significance of both missions was recognized and acknowledged, both were rejected eventually.

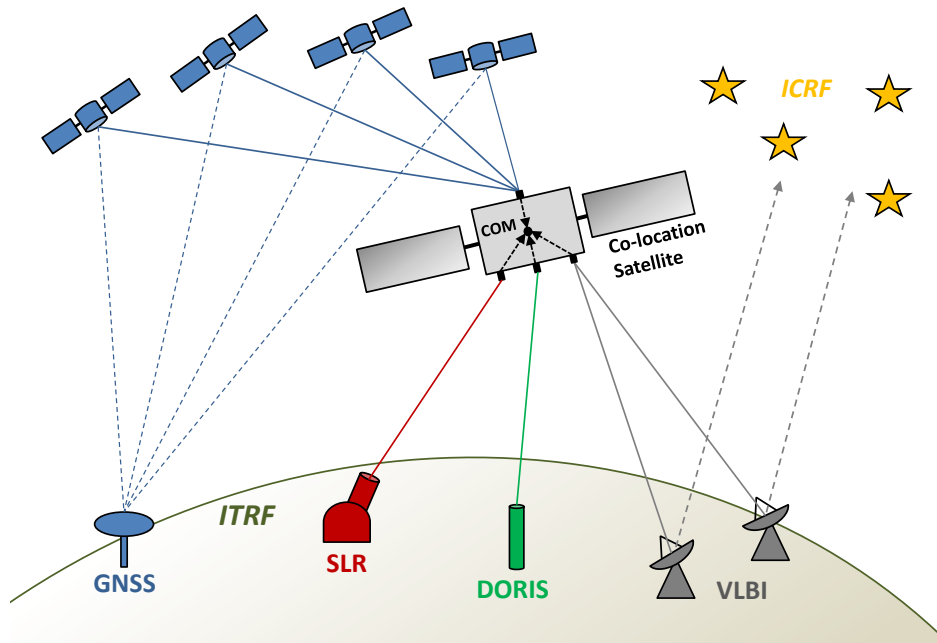


Figure 1.1: Concept of co-location in space. The co-location satellite is equipped with instruments that enable observations by SLR, DORIS, VLBI, and GNSS. The locations of the technique-specific antennas onboard the satellite are precisely calibrated w.r.t. the center of mass (COM) of the platform in order to connect the coordinate frames of the different techniques.

The basic principle of the co-location of space-geodetic techniques in space following the concept of GRASP and E-GRASP/Eratosthenes is outlined in Fig. 1.1. The co-location satellite is equipped with a VLBI signal transmitter, an SLR retro-reflector, and receivers for GNSS and DORIS, which enable tracking by these techniques. Assuming a precise calibration of the relative positions of the different sensors w.r.t. the center of mass (COM) of the satellite, such a configuration enables to combine the coordinate frames of the different techniques, realizing so-called "space ties" (in accordance with the term "local tie" used for terrestrial tie vectors). The combination can happen either on the satellite itself, by comparing satellite positions estimated through observations of the various techniques, or by a precise determination of the positions of the tracking antennas on Earth the in the satellite's system (Plank, 2014). Hence, a co-location satellite following the GRASP concept would represent a calibrated common reference point orbiting the Earth and connecting all observing ground stations to one another – fully complementary to the co-location on the ground.

Besides the capability to identify and correct the remaining major discrepancies and systematic

effects of the contributing space-geodetic techniques, space ties have the potential to realize frame ties with unprecedented accuracy achieved through virtually continuous measurements of the tie vectors in space (Anderson *et al.*, 2018). The fraction of observations involved in linking the techniques would drastically increase, as all ground stations on Earth that observe the co-location satellite would directly participate in the determination of the technique ties. The combination of long time series of observations containing tie measurements, and the fact that more ground stations contribute to frame ties – not only those with co-located ground instrumentation – should drastically improve the accuracy and stability of the ITRF, and should enable the study of technique related biases and systematic errors (Anderson *et al.*, 2018).

From the perspective of VLBI There have already been successful attempts to combine the three satellite techniques GNSS, SLR, and DORIS via co-location in space as outlined in Sec. 3.1.2. However, space ties with VLBI have not been realized so far and could solely be studied in simulations (see Sec. 3.1.1). Different studies, e.g. by Plank *et al.* (2014 and 2016) and by Anderson *et al.* (2018), point out the great potential of VLBI satellite observations for establishing frame ties with the satellite techniques. Furthermore, simulated VLBI observations of satellites were used to investigate various critical aspects for future co-location satellite missions, such as suitable orbits, the distribution of ground stations, scheduling strategies, and the feasibility of different types of observables obtainable through VLBI antennas.

However, the actual link between the satellite techniques (GNSS, SLR, and DORIS) and VLBI has not been established so far. The essential problem in this respect is the absence of real satellite observations with VLBI radio telescopes. While GNSS, SLR, and DORIS are operationally applied for observations of Earth satellites, geodetic VLBI is intrinsically different with its roots being settled in astronomy. Present applications of VLBI satellite tracking can mainly be found in the field of planetary sciences, with VLBI being used for the navigation and positioning of spacecrafts (for example: Duev *et al.* 2012, Hanada *et al.* 2010, Lebreton *et al.* 2005, Lanyi *et al.* 2005). The requirements on observation schemes and data processing essentially differ between VLBI observations being carried out for the purpose of interplanetary navigation and for establishing frame ties on an Earth orbiting satellite. Hence, observation and processing routines established for planetary science cannot simply be adopted for the needs of geodesy.

Although the promising prospects of VLBI satellite observations attracted attention in the geodetic community in recent years, actual observation experiments were rare, and the end-to-end realization of VLBI satellite observations was an unsolved long-term issue. Starting in 2009, several groups within the VLBI community reported on effort to observe GNSS satellites in the L-band. Initial experiments were carried out to investigate basic signal chain characteristics and tracking capabilities of antennas, involving radio observatories in Germany, Sweden, and Italy (see Sec. 3.2.1). Although several basic experiments showed the feasibility of tracking satellites and recording their signal, actual observables in terms of baseline delays – as common in geodetic VLBI – were not derived.

Major problems arose due to receiver equipment of legacy geodetic VLBI antennas being re-

stricted to observations in the S- and X-band, not covering the L-band frequency domain. Furthermore, the post-correlation processing software packages which are routinely used in the geodetic VLBI to derive the actual observables have not been tested and adopted for the application on satellite observations. Other major problems were caused by inappropriate scheduling software, the missing support of satellites as observation targets in all kind of interchange files and, finally, missing capabilities of analysis software to process the observables. Summing this up, it can be said that the complete VLBI process chain – from observation planning, over signal acquisition and post-correlation processing, to data analysis and the derivation of geodetic results – was not ready for observations of satellites.

Nevertheless, real VLBI satellite tracking experiments are considered as extremely valuable, as they provide plenty of hands-on experience complementing the (theoretical) information derived from simulation studies only. This is needed to generate a holistic view covering all aspects of VLBI satellite observations. Only actual experiments are capable to reveal unknown deficiencies on the data acquisition level, such as tracking issues, and enable to adopt existing VLBI infrastructure components – hardware as well as software – according to the specific requirements of satellite observations, and to test them. Hence, today’s experiments – although they may not yet deliver results accurate enough to be used for geodetic products – provide a great test bed for future missions with potentially high impact on geodesy and Earth sciences.

1.1 Scientific Opportunities

The co-location of space-geodetic techniques on a platform in space addresses a wide spectrum of science cases and research topics. A small selection of selected examples is given below.

Unification of reference frames and Earth rotation Terrestrial and celestial reference frames, and the Earth orientation parameters (EOP) that describe the transformation between both frames, are fundamental for any kind of positioning on the Earth and in space, and provide valuable information about complex dynamics and interactions within the system Earth.

Besides contributing to the TRF realization, VLBI is the only technique that is able to determine the International Celestial Reference Frame (ICRF2; Ma *et al.*, 2009), which is based on well-defined positions of extragalactic radio sources (mostly quasars) measured in the radio frequency domain. Furthermore, VLBI is the most suitable technique for observing the full set of EOP. Practically, the determination of celestial pole offsets and the Earth’s rotation angle (expressed as Universal Time UT1) solely relies on the VLBI technique. Additionally to VLBI, the satellite techniques GNSS, SLR, and DORIS contribute to realization of the International Terrestrial Reference System (ITRS), and participate in the determination of EOPs, such as pole coordinates and the length-of-day parameter (LOD). These satellite techniques rely on measurements between tracking stations on the Earth’s surface and satellites, whose orbits are subject to various gravitational and non-gravitational forces. Whereas the reference frames of GNSS, SLR, and DORIS are realized dynamically by satellite orbits, the VLBI frame is realized kinematically by observations of

remote radio sources. Hence, the reference frames of VLBI and the satellite techniques are of a completely different nature. So far, the only physical link between the (kinematic) VLBI frame and the (dynamic) frames of SLR, GNSS, and DORIS are the local ties at co-location sites on the ground, which reveal significant discrepancies w.r.t. the terrestrial frames of the individual techniques, as described above. A co-location on a satellite would connect all technique frames in space and would provide a direct link between the dynamic satellite frames and the kinematic frame of VLBI. For example, it would enable to determine the (dynamic) satellite orbit directly in the ICRF.

Commonly, the ICRF and the ITRF are determined independently of one another, which leads to inconsistencies that map into the EOP that connect both frames. Targeting this issue, the Resolution No. 3 (2011)¹ of the International Union of Geodesy and Geophysics (IUGG) urges that the highest consistency between the ICRF, the ITRF, and the EOP is a primary goal in all upcoming realizations of the ICRS. Although this resolution has not yet been implemented, research in this direction has been initiated (e.g. Seitz *et al.*, 2014) and this topic is being addressed by the ICRF3 Working Group² of the International Astronomical Union (IAU). The common and consistent determination of the the celestial and the terrestrial frame, and of EOPs would strongly benefit from the integration of VLBI and the satellite techniques (SLR, GNSS, and DORIS) via a co-location in space.

Temporal variations of the EOPs contain subtle information on mass transport in the system Earth, which can be roughly divided into the solid Earth, the external fluid layers, and the outer and inner core. Accurately determined EOPs are the basis for various studies that investigate different aspects of this complex system, such as coupling mechanisms at the core boundaries by Dehant *et al.* (2017), or the mechanisms of angular momentum exchange between the solid Earth and the atmosphere-ocean system (link to climate change; Dickey *et al.*, 2011). Given that a co-location in space is expected to improve the consistent determination of EOP, TRF, and CRF, such studies will benefit.

Sea level rise The global sea level rise is one of the main concerns related to climate change. Estimates of the sea level rise have been derived from time series of tide gauges measurements obtained over a time span of more than a century. Since tide gauges yield measurements relative to the land which they are attached to, their observations are vulnerable to geophysical processes that cause a vertical land movement, such as post-glacial isostatic uplift. In order to precisely determine the sea level (and its changes) in a global scale, the measurements are performed w.r.t. the ITRF. The connection to the ITRF is usually established by co-located GNSS stations. Therefore, the ability to measure minute changes of the sea level is limited by the stability of the ITRF, which is one of the main error sources in the determination of the global sea level rise (Blewitt *et al.*, 2010).

¹https://iag.dgfi.tum.de/fileadmin/IAG-docs/IUGG_Resolutions_2011.pdf

²https://www.iau.org/science/scientific_bodies/working_groups/

Since the launch of the TOPEX/Poseidon mission¹ in 1992 the sea level has been routinely observed from space using satellite radar altimetry. The obtained data provide global and regional measurements of sea level variations over several decades. Also the satellite altimetry poses stringent requirements on the stability and accuracy of the ITRF. On the one hand, tide gauges co-located with GNSS antennas tied to the ITRF are needed to detect drifts and to calibrate the altimetry measurements. On the other hand, any uncertainties in the ITRF positions and velocities of the tracking stations (usually SLR, GNSS, and DORIS), which are used to determine the orbit of the altimetry satellite, increase the error budget of the derived sea level measurements.

To enable long-term sea level studies, sea level measurements and the level of the land which tide gauges are attached to, have to be determined with an accuracy that corresponds to a small fraction of the sea level signals of 1 to 3 mm/year (according to IPCC, 2013, the global mean sea level rise is 3.2 mm/year). Hence, the ITRF that is used as geometric reference for such measurements has to be established with an commensurate level of uncertainty. This circumstance is also reflected by the GGOS goal aiming at a reference frame stability of 0.1 mm/year (Plag & Pearlman, 2009). This goal can only be reached by improving the current TRF solutions through a better integration and combination of the underlying space-geodetic techniques – which is the main goal of a co-location in space.

The examples given above just reflect a small fraction of scientific applications where a co-location in space would potentially have a high impact on. More science cases for which a co-location in space (and the resulting improvements in the reference frame accuracy and stability) would play an important role are, for example, the determination of ice mass loss, geodynamical investigations of post-glacial rebound, the assessment of natural hazards, or the enhancement of Earth observation products by an improved precise orbit determination for Earth observation satellites. For more detailed information on scientific applications of a technique co-locations in space the author refers to publications on the GRASP and E-GRASP/Eratosthenes missions, e.g. Biancale *et al.* (2017), Nerem & Draper (2011), and Bar-Sever *et al.* (2009).

1.2 Objectives and Outline of this Work

As pointed out in the introduction, the unavailability of dedicated process schemes for carrying out end-to-end experiments, and the resulting lack of observation data, are major shortcomings in the field of VLBI satellite observations. With this background, the main objectives and key-tasks for the work presented in this thesis can be defined as follows:

Establish a complete end-to-end process chain for VLBI satellite observations. The starting point of this work was to prepare all required components for a process chain that covers: observation planning – related to VLBI it is referred to as scheduling –, signal acquisition

¹<https://sealevel.jpl.nasa.gov/missions/topex/>

including antenna and recorder control, correlation and post-correlation processing of the raw observation data in order to derive actual delay observables, and – finally – the geodetic analysis. The goal was to use and adopt as many standard processes as possible, in order to stay close to the standard process chain operationally applied for the observation of extra-galactic sources, such as quasars. The established process chain is described in Chap. 4.

Carry out experiments to gather hands-on experience. Only actual observation experiments are suitable to test the practical applicability of all processes. A main investigation goal was to test the suitability of existing antenna infrastructure for satellite observations with a special focus on tracking capabilities and the signal chains. Furthermore, actual observation (raw) data is required to test and adopt correlation and fringe fitting software for the application on satellite signals. Fortunately, we had the opportunity to use the VLBI antennas infrastructure controlled by the University of Tasmania (UTAS, Australia), consisting of the AuScope VLBI array (Lovell *et al.*, 2013) plus the (astronomical) antennas at the observatories in Ceduna (South Australia) and Hobart (Tasmania) for extensive tests. In 2015 and 2016, GNSS satellites (GPS and GLONASS), as well as the Chinese satellite APOD-A (Sun *et al.*, 2018) – which can be considered as a first realization of a co-location low Earth orbit (LEO) satellite combining SLR, VLBI, and GNSS – were observed in series of experiments. These sessions are discussed in detail in Chap. 5 (GNSS observations) and in Chap. 6 (observations of APOD-A), presenting a full description of the applied data acquisition schemes, and discussions of the results. Although this work focuses on the experiments carried out in cooperation with our colleagues from UTAS, it should be noted, that much more test sessions were realized between 2014 and 2016, mainly in cooperation with European researchers and radio observatories in Italy (Medicina and Sardinia), in Sweden (Onsala), and in Germany (Wettzell). A full list of sessions is shown in Appdx. A.

While experiment-specific characteristics and circumstances are discussed in the corresponding Chapters, the final Chapter (7) is used to review the accumulated experiences in a broader and more general context, to discuss future perspectives, and to provide an outlook on future research tasks.

To complete the scope of this work, the fundamentals for understanding all discussed aspects of VLBI satellite observations, are presented in two additional Chapters: Chap. 2 gives an introduction to the geodetic VLBI technique in general. Rather than introducing the theoretical foundation of radio interferometry in every detail – which is available in other literature anyway – this Chapter focuses on data acquisition schemes operationally applied in the geodetic VLBI. This can be considered as the origin for the development of the process chain for satellite observations presented in Chap. 4, as we tried to adopt as many standard processes as possible. Chap. 3 tries to impart a solid basis of fundamental knowledge by discussing various important and general aspects related to VLBI satellite observations. Starting with a review of previous work in this field and a detailed view on the scientific opportunities of this new observation approach,

more practical aspects, such as satellite tracking schemes, are introduced.

Chapter 2

Very Long Baseline Interferometry for Geodesy and Astrometry

The modern Very Long Baseline Interferometry (VLBI) has its origins in the astronomical application of two-element radio interferometers with cable connected antennas, which were used to study distant radio sources. With the advent of high speed tape recorders and ultra-stable atomic time and frequency standards in the late 1960's, it was possible to construct phase-coherent interferometers, without physical (cable) connection between the individual elements. This enabled to place the antennas arbitrarily far apart and, hence, led to a drastic increase of the attainable resolution. The great potentials for geodetic applications were recognized soon, and the first experiments aimed at achieving geodetic accuracy on a baseline of several hundred kilometers were carried out in the late 1960's (e.g. Hinteregger *et al.*, 1972)¹.

Since the 1970's the technique rapidly evolved, and is today, beyond numerous applications in astronomy, a well established space-geodetic technique, and plays an indispensable role in astrometry. VLBI is the only technique able to determine and maintain the International Celestial Reference Frame (ICRF) which is currently realized by positions of extra-galactic radio sources (Ma *et al.*, 2009). Furthermore, VLBI contributes to the realization of the International Terrestrial Reference Frame (ITRF) with precise station positions, and essentially contributes to the determination of the ITRF scale (see e.g. Altamimi *et al.*, 2016). VLBI is the only technique able to monitor the full set of Earth Orientation Parameters (EOP) at regular intervals. In particular, the Earth rotation angle ($dUT1 = UT1 - UTC$) and nutation parameters are uniquely provided by VLBI. Beyond all that, VLBI allows to access valuable information on interactions within the system Earth and enables to derive numerous geophysical parameters by analyzing the long history of VLBI observations.

The VLBI is a truly international effort, as it requires globally distributed observatories to collaborate in order to derive various products. World-wide VLBI observations are organized an

¹Readers interested in the history of VLBI may be referred to Kellermann & Moran (2001) or Campbell (2000) and the references therein.

coordinated by the International VLBI Service for Geodesy and Astrometry (IVS)¹, which was established in 1999 as an official service of the International Association of Geodesy (IAG)² and of the International Astronomical Union (IAU)³. Goals of the IVS are to support operational as well as research and development activities in all aspects of the geodetic and astrometric VLBI technique, to provide VLBI products to the user community, and to integrate VLBI into the Global Geodetic Observing System (GGOS; Plag & Pearlman, 2009). Official IVS products are the realization of the Celestial Reference System (CRS) via positions of extra-galactic radio sources, positions of network stations which contribute to the realization of the Terrestrial Reference System (TRS), and the full set of EOPs. Currently, The IVS station network comprises more than 30 radio observatories world-wide⁴.

2.1 Basic principle

The VLBI technique requires at least two remote antennas simultaneously observing the signal of a distant radio source. The received signals are precisely time-tagged and recorded at both stations, and then cross-correlated to derive the difference in arrival times at the stations, i.e. the time delay τ – the main observable relevant for geodetic applications.

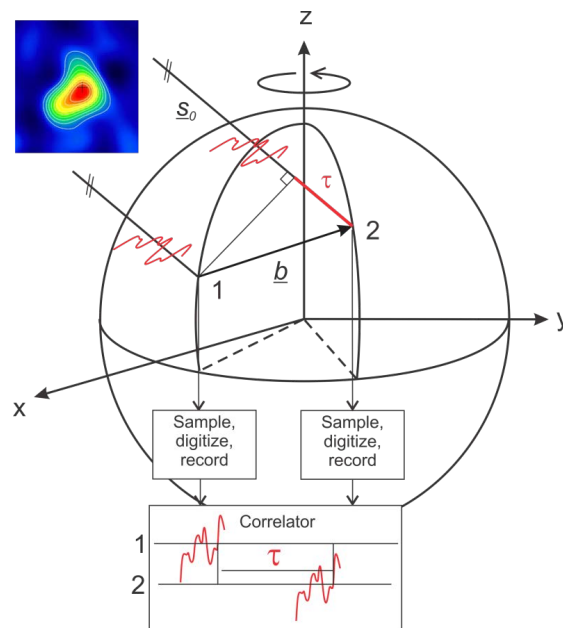


Figure 2.1: Geometric principle of VLBI (from Schuh & Böhm, 2013). The time delay τ on the baseline \vec{b} can be measured by cross-correlating the signals of a distant radio source recorded at two stations.

¹<https://ivscc.gsfc.nasa.gov/>

²<http://www.iag-aig.org/>

³<https://www.iau.org/>

⁴All IVS network stations are listed at <https://ivscc.gsfc.nasa.gov/about/org/components/ns-list.html>.

The underlying geometric principle of VLBI as outlined in Fig. 2.1 is rather simple and straight forward: In conventional geodetic VLBI, extra-galactic radio sources¹ are observed. Due to the huge source distances, incoming wavefronts can be assumed to be plane. Hence, the source directions \vec{s}_0 can be assumed to be parallel for all ground-based stations. Considering this so-called *plane wave approximation*, the relation between the delay τ and the baseline vector \vec{b} can be described by resolving a rectangular triangle according to Equ. 2.1. The delay τ between the reception times at station one (t_1) and station two (t_2) is calculated as the negative scalar product of \vec{b} and \vec{s}_0 scaled by the speed of light c (Campbell, 2000).

$$\tau = -\frac{\vec{b} \cdot \vec{s}_0}{c} = t_2 - t_1 \quad (2.1)$$

In geodetic VLBI sessions, usually lasting for 24 h, globally distributed radio antennas observe a large number of radio sources distributed over the celestial sphere. The signals are recorded in several channels (typically 16 channels with 8 MHz bandwidth each) allocated over wide frequency ranges in the S- (~ 2.3 GHz) and X-band (~ 8.4 GHz). The signals are digitized, precisely time-tagged using the time standard of the station's atomic clock, recorded on hard discs and sent to correlation facilities where the delay τ for each baseline observation is derived by cross-correlating the corresponding data streams. More details on the data acquisition procedures are presented in the following Section (2.2).

Based on these delays τ the length of the baseline \vec{b} (and hence station positions), the direction to the source \vec{s}_0 , all parameters describing the transformation between the celestial coordinate frame of the sources and the terrestrial frame of the stations (EOP), and numerous parameters of phenomena influencing the propagation of the microwave radiation on its way from the source to the receiver, can be derived by applying appropriate models and estimation schemes.

2.2 Data Acquisition Scheme

This Section describes the data acquisition processes operationally applied for geodetic VLBI sessions as organized routinely by the IVS.

Scheduling The initial step of each VLBI session is the observation planning, commonly referred to as scheduling. A VLBI observation schedule defines which antennas observe a specific source simultaneously at a particular time, i.e., which antennas form a scan. A proper schedule is important for the feasibility and the performance of a session, because it defines the exact timing of each antenna within a globally distributed network.

Depending of the goals of a session, e.g. determination of EOP, or the measurement of source

¹In general active galactic nuclei (AGN) are observed. A specific type of AGN, so-called quasars, are commonly observed in geodetic VLBI.

positions in an astrometric session, suitable sources have to be selected, and the chronological order of observations has to be defined. The required observation time in order to reach the target signal-to-noise ratio (SNR), i.e. the so-called on-source time, has to be determined individually for each scan and antenna. On the one hand, the on-source time depends on the sensitivity of observation network, and therefore on parameters such as the antenna's source equivalent flux densities (SEFD; quantifying the antenna sensitivity), the sizes of the antennas, or the observation mode (digitization and recorded bandwidth). On the other hand, it is affected by source parameters, such as the flux density at the observed frequency band. The comprehensive complexity of the scheduling task becomes obvious when considering the large number of restrictive parameters (e.g. antenna slew rates, horizon masks, cable wrap limits, scan duration thresholds, etc.) which have to be taken into account properly in order to enable successful observations, and to derive geodetic products of high quality.

Due to their complexity VLBI schedules are usually not created manually – they are generated automatically by dedicated scheduling software. To enable an automatic selection of the subset and sequence of observed sources, these scheduling programs apply suitable optimization approaches, e.g. optimizing for an even distribution of sources over topocentric view directions to facilitate the estimation of accurate troposphere parameters in the data analysis¹.

Currently, the following software packages are used for VLBI scheduling: The program SKED (Gipson, 2012), which is developed and maintained at the NASA Goddard Space Flight Center (GSFC), is widely used to schedule geodetic VLBI sessions, e.g. all operational 24 h sessions of the IVS (R1 and R4 sessions). SCHED (Walker, 2014) is another software developed at the National Radio Astronomy Observatory (NRAO) and mainly used for astronomical and astrometric observations. For a detailed description of scheduling astrometric sessions with SCHED and geodetic sessions with SKED, respectively, the author refers to Petrov *et al.* (2009). In 2012 a VLBI scheduling module was added to the Vienna VLBI and Satellite Software (VieVS; Böhm *et al.*, 2018) named VIE_SCHED (Sun *et al.*, 2014). VIE_SCHED is a fully operational scheduling program, as described in Sec. 4.2.

The compiled observation plans are then written to dedicated schedule files, comprising all information required to carry out a complete VLBI experiment. These "global" schedule files define the complete observation time plan, as well as all setup parameters for the equipment at all participating stations, e.g. all setup parameters for the recorders, defining the observed frequency bands, the sampling, or data formats. Schedule files are usually written in two predefined file formats: SKD (Gipson, 2010) and VEX (VLBI EXperiment; Whitney *et al.*, 2002). SKD is the native format of the program SKED², whereas VEX is the more up-to-date format. Prior to VLBI sessions the properly prepared global schedule has to be sent to all participating observatories.

¹Such approaches optimize the sky coverage at individual stations, see Petrov *et al.* (2009) or Sun *et al.* (2014).

²Although the VEX format is supported by SKED since 1997 (Gipson, 2010).

Observations At the stations the information in the global schedule file are used to run VLBI sessions in an automatic manner using the VLBI Field System (FS; Himwich *et al.*, 2003)¹. The FS is a suite of programs, maintained at the GSFC, providing the coordinating control of VLBI observation and data acquisition. It runs on a Linux platform at each VLBI antenna and enables control of all tasks needed for VLBI operation from a central point, e.g. handling the recorder equipment, receiver calibrations, antenna motion control, collection of metrological data, etc. The FS operator interface is based around the concept of user-typed commands in the Standard Notation for Astronomical Procedures (snap; Himwich & Vandenberg, 2001) format. These snap commands are used to set or monitor the state of the hardware and various system features. Sequences of snap commands, along with time control commands required to synchronize operations at different stations, written to local control files – named snap files (*.snp*) – enable almost automatic VLBI operations with a minimum of manual interaction.

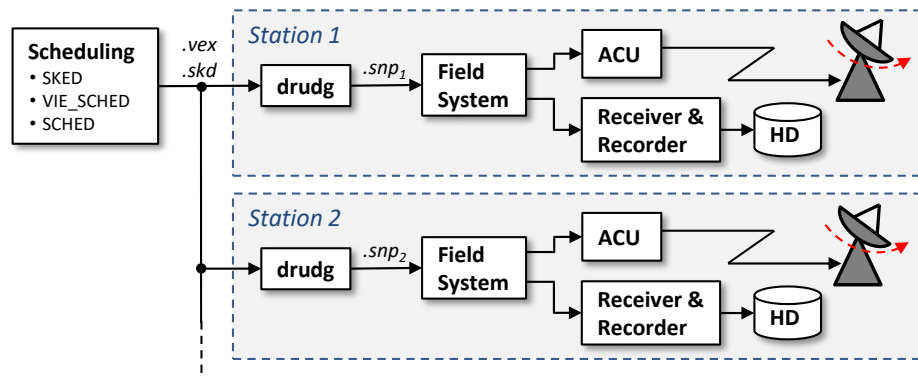


Figure 2.2: VLBI scheduling and observation workflow. The global schedule file (*.vex* or *.skd* formatted) is created by dedicated VLBI scheduling software and distributed to all stations. At the stations the program *drudg* is used to extract all relevant information and to write local control files (*.snp_i*) for the Field System (FS). The FS controls both, the antenna motion through the antenna control unit (ACU), and the receiver and recorder equipment. The recorded data is stored on hard discs (HD) before it is transferred to the correlation facility.

As illustrated in Fig. 2.2, the program *drudg*, which is part of each FS distribution, is used to extract locally relevant information from the global schedule file (*.vex* or *.skd*) and writes the station-dependent snap files (*.snp_i*). These snap files are then loaded by the FS which executes all contained snap commands according to their time-tags. Basically, the FS controls the major components of the VLBI system: (1) it controls the antenna motion via an interface to the antenna control unit (ACU), and (2) it controls the station’s receiver and recorder components.

The ACU basically controls the antenna’s hardware functions and is usually provided as proprietary solution by the antenna manufacturer. It usually consists of a control computer with remote control interfaces and a programmable logic control unit (PLC) that actuates the antenna’s hardware components (e.g. the axis drives).

The radio signals of the observed source are collected by the antennas main reflector and

¹The complete documentation of the FS is available at [fpt://gemini.gsfc.nasa.gov/pub/fsdocs/](http://gemini.gsfc.nasa.gov/pub/fsdocs/).

focused into the antenna feed. There, the radio signals are converted to cable-bound electrical signals and amplified by a low noise amplifier (LNA) close to the feed in order to minimize the influence of thermal noise of the following components in the receiver chain. After a down-conversion of the radio signals from the S- and X-bands to the so-called intermediate frequency bands (IF) at several 100 MHz, the IF bands are again down-converted to extract several baseband channels with a bandwidth of a few MHz each, allocated across the IF frequency span¹. The band-limited signals in each baseband channel are then sampled and digitized, usually applying 1 or 2 bit quantification (Sovers *et al.*, 1998). The digital bit-streams are then formatted into data frames with precise time-tags obtained from the station’s ultra-stable atomic clock, and written to a data storage device based on hard discs. The data is recorded either on so-called eight-packs (removable storage devices of the Mark5 System with a capacity of typically 8 TB), which are then physically shipped to the correlator, or to temporary storage devices. Nowadays, fast internet connections and suitable transfer protocols (e.g. jive5ab²) often enable to transfer the data electronically to the correlator – realizing the so-called e-transfer of VLBI raw data. Of course, e-transfer is the desired way to transfer data in future, as it shortens the total turnaround time tremendously.

Most modern VLBI stations use components of the Mark5 VLBI system³ developed at the MIT Haystack Observatory (US), or of the Japanese K5 system⁴ developed by the National Institute of Information and Communications Technology (NICT), to build their receivers. For system details the interested reader is referred to the reference documents.

Correlation In the correlation step, the recorded data at all participating stations are combined pairwise in order to determine the difference in arrival times τ by comparing the recorded bit streams (see Fig. 2.1). This is done in dedicated correlation facilities, either by using special-purpose signal processing hardware, or (more flexible) correlation software installed on high performance computer clusters. The basic principle is described vividly by Sovers *et al.* (1998): the two bit streams, representing the recorded antenna voltages $V_1(t)$ and $V_2(t)$ as function of time t , are shifted in time relatively to each other until the cross-correlation function R in Eq. 2.2 is maximized.

$$R(\tau) = \frac{1}{T} \int_0^T V_1(t) \cdot V_2^*(t - \tau) dt \quad (2.2)$$

T represents the averaging time interval, the asterisk means that $V_2(t)$ is complex conjugated,

¹In the standard GEOSX mode used for the IVS R1 and R4 sessions in total 16 baseband channels with 8 MHz bandwidth are recorded. Six are down-converted from the S-band and ten from the X-band. This scheme of observing signals in comparably narrow bands allocated across wide frequency spans in the S- and X-band enable the application of bandwidth synthesis (Rogers, 1970).

²<http://www.jive.nl/~verkout/evlbi/jive5ab-documentation-1.9.pdf>

³<https://www.haystack.mit.edu/tech/vlbi/mark5/>

⁴<http://www2.nict.go.jp/sts/stmg/K5/index-e.html>

and τ is the difference in arrival times. This process is discussed in detail e.g. by Thomas (1987). For the practical evaluation of the cross-correlation, an a priori delay model with sufficient accuracy is required – a so-called correlator input model. It allows to limit the search window for the maximum of $R(\tau)$. Suitable models are also necessary to compensate for the Doppler shift induced by Earth rotation which causes an oscillation of several kHz of VLBI observables at the X-band.

In recent years the rather inflexible hardware correlators have been gradually replaced by software correlators, i.e. dedicated correlation software installed on high performance computation clusters. One example is the correlation software DiFX (Deller *et al.*, 2007), which is widely used nowadays for VLBI. For example, DiFX has been used since 2010 to correlate all IVS sessions at the correlation center at the Max-Planck-Institut für Radioastronomie (MPIfR)¹ in Bonn, Germany.

Post-correlation processing The correlation process is carried out in parallel for all recorded baseband channels (typically at 14 frequencies ω_i in the S- and X-band). Each channel produces average amplitudes and phases in an interval of 1 or 2 sec at epochs the t_i . These phase and amplitude samples, $\phi(\omega_i, t_i)$ and $p(\omega_i, t_i)$, are stored for later analysis with post-correlation software as described e.g. by Lowe (1992).

The main purpose of the post-correlation processing is to prepare the correlation results for the final processing by estimation software, which includes the establishment of reference epochs t_0 and reference frequencies ω_0 for the observables, or the application of a phase calibration using discrete tones that were injected soon after signal detection in the antenna feeds (e.g. Rogers, 1975). However, the main task is to fit the phase ϕ_0 , the group delay τ_{gd} , and the phase delay rate $\dot{\tau}_{pd}$ to the set of phase samples $\phi(\omega_i, t_i)$ determined through correlation for each frequency channel ω_i and epoch t_i . These phase-derived observables are determined (for the phase ϕ and the circular frequency ω) in a bilinear least-squares adjustment to the measured phase samples $\phi(\omega, t)$ using Eq. 2.3 (Sovers *et al.*, 1998).

$$\phi(\omega, t) = \phi_0(\omega_0, t_0) + \frac{\partial \phi}{\partial \omega}(\omega - \omega_0) + \frac{\partial \phi}{\partial t}(t - t_0) \quad (2.3)$$

The phase delay τ_{pd} , the group delay τ_{gd} and the phase delay rate $\dot{\tau}_{pd}$ are defined as:

$$\tau_{pd} = \frac{\phi_0}{\omega_0}, \quad \tau_{gd} = \frac{\partial \phi}{\partial \omega}, \quad \dot{\tau}_{pd} = \frac{1}{\omega} \frac{\partial \phi}{\partial t} . \quad (2.4)$$

Consequently, the interferometer is capable to derive four different data types: amplitudes, phase delays, group delays and phase delay rates. The group delay rate cannot be measured

¹<https://www.mpifr-bonn.mpg.de/>

accurately enough to be used for geodetic applications, and amplitudes are mostly used in astronomy for imaging or for source structure studies. Currently, the prime geodetic observable is the group delay τ_{gd} , which can be derived virtually without ambiguities from wide-band observations¹. Although phase delays would yield unparalleled accuracies, they are still problematic. With ambiguities being the major issue, they have only been shown on short baselines (e.g. Herring, 1992).

The determination of these phase-derived observables is commonly referred to as *fringe fitting*. The main software suite used for geodetic VLBI is the Haystack Observatory Postprocessing System (HOPS)². It is designed to manipulate data generated by a MkIII, MkIV, or DiFX VLBI correlator, and provides utilities for data editing and problem diagnosis, along with the popular fringe fitting program *fourfit*. Other fringe fitting programs, complementary to *fourfit*, are the program FRING, which is part of the Astronomical Image Processing System (AIPS)³, or PIMA (Petrov *et al.*, 2011).

2.3 The next-generation VLBI system

Since 2005 the IVS has been working on a next-generation VLBI system by reviewing all current hardware and software components, and operational procedures. The ambitious goals of this initiative, formerly known as *VLBI2010* (Niell *et al.*, 2006), were to enable an accuracy of 1 mm in positions (from 24 h sessions) and 0.1 mm/year in velocity on a global scale, to carry out continuous measurements to obtain uninterrupted time series of station positions and EOPs, and a short turnaround time to get initial geodetic results within 24 h after observations.

In comprehensive simulation studies (e.g. Pany *et al.*, 2011) a vast decrease of the source-switching interval was found to be a key-aspect for reducing the influence of the dominant error source in VLBI – the troposphere. To reduce the total amount of time spent to observe a single source, (1) the on-source time, i.e. the observation time required to reach the target SNR, has to be reduced, and (2) the slew times between consecutive observations have to be minimized. To enable fast source switching, the design aspects for VLBI2010 Petrachenko *et al.* (2009) recommend to build smaller antennas (~12 m diameter) with fast slew rates of e.g. 12°/sec in azimuth. To compensate for the sensitivity loss due to the smaller dishes, and to further reduce the on-source time, a new approach has been developed in which several widely space frequency bands are observed to derive a so-called broadband delay. Petrachenko *et al.* (2009) recommend a four band system and the usage of broadband antenna feeds to span a frequency range from about 2 to 14 GHz.

In recent years many key components of VLBI2010, such as new antennas following the suggested specifications, have been realized under the name *VLBI Global Observing System (VGOS)*. Since 2012, a series of broadband test observations were conducted successfully, involving the

¹Or from observations in several narrow bandwidth channels spread over a wide frequency range.

²<https://www.haystack.mit.edu/tech/vlbi/hops.html>

³<http://www.aips.nrao.edu/index.shtml>

new VGOS-type antennas at GSFC (USA), Westford (USA), Wettzell (Germany), and Yebes (Spain) (e.g. Niell *et al.*, 2016). Six new VGOS antennas also participated in the IVS CONT17¹ campaign, demonstrating the promising development of the new VGOS system.

The new VGOS antennas also provide new possibilities for VLBI satellite observations. The rather small and fast slewing antennas are in general much more suitable for satellite tracking than the mostly large and slow pre-VGOS antennas. Furthermore, the small dishes (~12 m) facilitate a proper tracking due to the larger beam-width (see Sec. 3.4). New broadband feeds and receiver systems enable to observe artificial satellite signals in a larger frequency range, not being restricted any more to the S- and X-band.

¹<https://ivscc.gsfc.nasa.gov/program/cont17/>

Chapter 3

Satellite Observations with VLBI

3.1 Previous Work and Applications

The idea of observing artificial satellites with radio interferometry techniques is not a novelty. Soon after the VLBI technique was established in the early 1970's, applications for the precise determination of satellite orbital elements were investigated and tested. Taking advantage of the extraordinary accuracy in angular resolution of the recently developed VLBI technique, differences in arrival times (geometric time delays) and the relative Doppler frequency shift (fringe rate) were investigated to be used for the determination of synchronous orbits (e.g. Rosenbaum, 1972; Ramasastry *et al.*, 1972; Ramasastry & Rosenbaum, 1972; Preston *et al.*, 1972; Kawase & Tanaka, 1979). Back then, the overall achievable accuracy was limited by different issues, such as insufficient modeling of corrections for the propagation medium (Preston *et al.*, 1972), or by problems with the observation configuration (e.g. Kawase & Tanaka, 1979). Hence, VLBI was outperformed by other orbit determination techniques and did not reach the operational level.

Since then, the circumstances vastly changed: the VLBI established an important role in different fields, such as astronomy, astrometry and geodesy, and is a widely used technique nowadays. Throughout the last decades large-scale and globally distributed ground station networks were built, and a huge progress in error modeling, data processing and analysis was made, also opening new perspectives on the application of VLBI for the observation of artificial signal sources.

Space missions Radio-interferometric techniques have a long history in tracking of spacecrafts in interplanetary and deep space missions. VLBI was identified to be useful supplementing other tracking techniques which provide accurate positioning data in the line-of-sight direction, but lack in accuracy perpendicular to it, such as classical range and Doppler (range rate) measurements. The extreme high angular resolution of VLBI enables to constrain orbital errors in the transverse direction, perpendicular to the line-of-sight, while range and range rate measurements are able to constrain in the line-of-sight direction.

Starting with the pioneering work of the NASA Deep Space Network (DSN; Border, 2009), which started to employ VLBI tracking with observations of the Voyager probes (Brunn *et al.*,

1978 and Christensen *et al.*, 1980), VLBI measurement techniques play a fundamental role in numerous space missions nowadays¹. Among numerous applications, recent examples are Δ VLBI observations of the Mars Explorer Rover B (MER-B) by the Very Long Baseline Array (VLBA) and the DSN (Lanyi *et al.*, 2005), VLBI observations of the Huygens probe during its descent and landing on the surface of the Saturn moon Titan (Lebreton *et al.*, 2005), and tracking of the ESA spacecrafts Mars Express (during the Phobos fly-by) and Venus Express (e.g. Molera Calvés *et al.*, 2010 and Cao *et al.*, 2010). VLBA observations of Mars orbiting satellites (Park *et al.*, 2015) and of the Cassini spacecraft orbiting Saturn (Jones *et al.*, 2011) provide angular positions of the center of mass of both planets with respect to ICRF. Duev *et al.* (2012) successfully tested their concept called PRIDE (Planetary Radio Interferometry and Doppler Experiment), providing ultra-precise estimates of spacecraft state vectors based on a combination of the VLBI phase referencing technique and radial Doppler measurements, with observations of ESA's Venus Express mission. Furthermore, PRIDE was successfully applied for observations of the Mars Express spacecraft Duev *et al.* (2016), and it was chosen as tracking technique for ESA's JUICE (JUpiter ICy moons Explorer) mission which should be launched in 2022 (Dirkx *et al.*, 2017).

Lunar missions Besides the application in interplanetary space missions, VLBI also demonstrated its potential in the close vicinity of Earth, during a number of lunar missions in the last decade. The Japanese lunar mission SELENE (SELenological and ENgineering Explorer, 2007 to 2009; Kato *et al.*, 2008) employed highly precise differential VLBI observations to improve the orbit determination of lunar orbiters, as described by Hanada *et al.* (2010), Goossens *et al.* (2011b), and Goossens *et al.* (2011a). Also the Chinese lunar exploration programs Chang'E-1 (2007-2009), Chang'E-2 (launched 2010), and Chang'E-3 (launched 2013) made use of the VLBI technique to improve the orbit determination of moon orbiters (e.g. Yan *et al.*, 2010), and – in the latter one – to determine the position of a lander on the Moon's surface. Klotek *et al.* (2018), Haas *et al.* (2016), and Tang *et al.* (2016) reported on observations of the lunar lander Chang'E-3 in twelve so-called OCEL (Observing of the Chang-E-3 Lander) sessions observed by global IVS network stations between 2014 and 2016. By joint observations of the lander and nearby quasars a so-called delay calibration approach was realized (see e.g. Haas *et al.*, 2016). In preparation of these lunar exploration missions Chinese and Japanese scientists also tracked Earth satellites to test their newly developed infrastructure (e.g. Hanada *et al.*, 2008 and Huang *et al.*, 2006).

Earth satellites In recent years the idea of using VLBI for the precise orbit determination (POD) of geostationary satellites was revived, e.g., for the geostationary satellites of the Chinese GNSS constellation COMPASS/BeiDou (e.g. Huang *et al.*, 2011).

Regarding possible applications in geodesy, Preston *et al.* (1972) already pointed out to utilize VLBI observations of Earth orbiting satellite for the estimation of baseline vectors, enabling the

¹An overview of various radiometric tracking techniques is provided, e.g., by Thornton & Border (2003). Different radio interferometric techniques are described and compared by Lanyi *et al.* (2007).

determination of station positions with respect to the Earth's center of mass, and providing the otherwise purely geometric VLBI technique sensitivity to the Earth's gravitation field. Besides of these goals still being relevant, and the omnipresent task to enable orbit determination, the main driving force in geodesy nowadays is the improvement of reference frames, as outlined in the introduction (Chap. 1). In particular, the main goal is to establish inter-technique ties between space-geodetic techniques via a co-location of instrumentation on a common satellite platform in the Earth orbit, i.e. to establish so-called "space ties" analogous to local ties on the ground. In this respect, recent research and development in geodesy mainly considers two possible scenarios for satellite observations with VLBI:

Observation of GNSS satellites: With the development of new GNSS, such as the European Galileo constellation, there will soon be more than 100 GNSS satellites in orbit. Considering GNSS satellites as potential observation targets for VLBI offers great possibilities, especially for establishing frame ties between VLBI and GNSS – and potentially also with SLR¹. In current tests GNSS L-band signals are directly observed by VLBI radio antennas, although it is conceivable to install dedicated VLBI signal beacons on future satellites. This approach is discussed in detail in Sec. 3.2.

Observations of a dedicated co-location satellite: A rigorous combination of SLR, GNSS, VLBI, and DORIS – all techniques contributing to the ITRF – could be achieved by placing the required instrumentation on a common platform in space. The clear advantage of a dedicated co-location satellite is that all mission parameters, such as orbit characteristics, the payload, etc., could be specifically designed for this purpose – yielding highly accurate frame ties. This concept was implemented in two major mission proposals so far: the Geodetic Reference Antenna in Space (GRASP, NASA; Nerem & Draper, 2011) and E-GRASP/Eratosthenes (ESA; Biancale *et al.*, 2017). Unfortunately, both missions were rejected. Currently (August 2018), there is no satellite in space combining all four space-geodetic techniques. Although not being designated for this task, some satellites, e.g. the Earth observation satellite Jason-2, can be observed by GNSS, DORIS, and SLR, opening possibilities for first proof-of-concept studies based on real data (see Sec. 3.1.2 for more details). So far, the only possibility to study VLBI observations of a co-location satellite prototype was provided by the Chinese APOD mission (Sun *et al.*, 2018). Actual test observations of APOD with VLBI are introduced and discussed in Chap. 6.

At the end of this short review it should be mentioned that the major space agencies, such as NASA, ESA, and CNSA (Chinese National Space Administration), have long-term experience in utilizing VLBI (or related technologies) for observations of artificial modulated signals of spacecrafts. Several examples are given above, in which Differential One-way Ranging (DOR; e.g.

¹All operational Galileo, BeiDou, and GLONASS satellites, as well as two GPS satellites of Block-IIA, are equipped with laser retroreflector arrays (e.g. Sośnica *et al.*, 2015). Furthermore, it is planned to equip all GPS Block III satellites with SLR capabilities (Thomas & Merkovitz, 2014).

Thornton & Border, 2003), Δ -DOR, and phase referencing observations were used to determine highly precise angular measurements in order to enhance the orbit determination of space probes. These applications predominantly observe frequency bands with very narrow bandwidth using a high-resolution digitization with up to 8 bit. In contrast, the observation experiments discussed in this work (see Chap. 5 and 6) make use of VLBI equipment mainly designed for geodesy and astrometry (e.g. antennas of the IVS ground station network), which is set up almost exclusively for the observation of very weak natural radio sources in wide frequency bands and by applying a digitization with 1 or 2 bit resolution only. Furthermore, most VLBI tracking systems for space applications are designed for the needs of specific missions in terms of signals characteristics, signal acquisition, and analysis methods, etc., limiting the field of application. Fundamental differences also result from purely geometric aspects, i.e. by the much shorter source distance in the case of Earth satellites (see also Sec. 3.3.1): the demands on antenna tracking and pointing schemes dramatically increase in the Earth's near-field, common visibility of the target is limited to short baselines, some assumptions for the a priori delay model may change (e.g. modeling in the BCRS vs. in the GCRS), and the application of phase referencing using natural radio sources as calibrators is vastly limited due to varying view angles from different terrestrial sites. Hence, tracking systems for space application cannot be adopted off-handedly for the observation of Earth satellites with geodetic VLBI antennas.

3.1.1 Simulation Studies

Although space ties with VLBI have not been realized so far, a number of extensive simulation studies were conducted over the last years in order to investigate various aspects of VLBI satellite observations.

Plank *et al.* (2014) and Plank (2014) investigated general aspects such as suitable satellite orbits and ground station networks, finding that station position estimates at the level of a few millimeters in weekly solutions are feasible based on VLBI satellite observations only. Initial scheduling strategies for VLBI observations of GNSS satellites were simulated and investigated by Plank *et al.* (2016). This study leads to the conclusion that combined observations of quasars and GNSS satellites allow to determine frame ties in terms of relative Earth rotation parameters (ERP) and scale at the level of 30 to 50 μ as. This corresponds to an alignment of the two reference systems on the level of 1 to 2 mm at the Earth's surface.

Anderson *et al.* (2018) conducted extensive simulations of VLBI observations of the proposed European Geodetic Reference Antenna in Space (E-GRASP/Eratosthenes; Biancale *et al.*, 2017) to investigate the conceptual capabilities of different VLBI observation modes – including time of flight measurements (TOF) and Differential-VLBI (D-VLBI) – for realizing frame ties.

3.1.2 Frame Ties Between SLR, GNSS, and DORIS

There have already been successful attempts to combine the three satellite techniques GNSS, SLR, and DORIS via co-location in space. Selected examples are given hereinafter.

Thaller *et al.* (2011) demonstrated the feasibility to combine GNSS and SLR by utilizing two new-generation GPS and four GLONASS satellites which are equipped with SLR retro-reflectors as co-location platforms in space.

Zoulida *et al.* (2016) studied the combined analysis of GNSS, SLR, and DORIS on-board the Jason-2 satellite with the goal to investigate the integration of a LEO multi-technique satellite as space tie in the ITRF combination.

Bruni *et al.* (2018) assessed possible contributions of the space tie between GNSS and SLR on-board GPS and GLONASS satellites to the realization of the terrestrial reference frame. This paper concludes, that such space ties realized by the co-location on-board of GNSS satellites, at present, cannot replace terrestrial ties in the ITRF computation.

3.2 VLBI Observations of GNSS Satellites

Motivation and applications Within the VLBI community the idea of observing GNSS satellites was first discussed for the purpose of phase center mapping. Therefore, the joint IVS/IGS/ILRS working group on GPS phase center mapping (Corey, 2001) was established in the year 2000. The goal was to investigate VLBI observations of GPS L-band signals for measuring the mean phase center location of the full, 12-element phased array on each satellite, and to determine the relative signal phase of the 12 individual radiating elements in each array. The key questions were, what accuracy of both types of measurement would yield, and how the technical challenges of observing GPS satellites with VLBI antennas, including correlation and data analysis, could be solved. Unfortunately, this working group concluded, that at all probability VLBI measurements will not be accurate enough (Schmid & Rothacher, 2003) – at least not with the technical means of the early 2000's.

Hase (1999) proposed to adopt this approach to determine the phase centers of GPS antenna arrays directly in the ICRF by relative measurements to quasars in the close vicinity. In general, VLBI observations of GNSS satellites would allow to determine satellite positions directly in the ICRF, hence, connecting the geometric reference frame of VLBI with the dynamic reference frame of the satellite constellation. Furthermore, Dickey (2010) pointed out that this would enable the VLBI technique to directly access the center of mass of the Earth and to establish the position of the Earth's center directly in the ICRF. Summarizing that, VLBI observations of GNSS satellites would allow to connect the dynamic reference frame of GNSS – which is determined by the satellite orbits being subject to the Earth's gravity field – with the purely geometric reference frame of VLBI.

Simulation studies (e.g. Plank *et al.*, 2014 and 2016; see Sec. 3.1.1) indicated, that reasonable results in terms of VLBI station position repeatabilities can be achieved based on observations of GNSS satellites.

New opportunities with Galileo In view of the advent of new GNSS constellations, such as the European Galileo system, the approach of observing GNSS signals with VLBI became again a hot

topic in the VLBI community. Recently, it was proposed to equip the next-generation Galileo II satellites, which are currently in the definition phase and should be deployed in 2025, with dedicated VLBI transmitters (e.g. Hellerschmied *et al.*, 2017a). Contrary to the modulated L-band GNSS signals, the VLBI beacons mounted on the satellites should imitate the signal of a quasar, thus, making it suitable for observations with the standard receiver chains used in geodetic VLBI systems. Such a VLBI beacon could be realized relatively simply by a broadband and low power transmitter, emitting white noise in a broad frequency range, for instance between 3 to 14 GHz, and with a power density of about 1 Jy at the ground. Future VGOS antennas will be equipped with broadband feeds, e.g. the Quad-ridged Flared Horn (QRFH) designed by Caltech (Akgi-ray *et al.*, 2013), capable to receive these signals. In principle this would allow for an excellent ionosphere calibration (due to the wide frequency range), yielding VLBI observations with approximately 5 ps delay precision after 1 sec integration time according to Petrachenko (2016).

From the perspective of VLBI, observations of a dedicated broadband noise signal would be much easier to handle than observations of the GNSS L-band signals. Standard geodetic VLBI antennas are not designed to receive signals in the L-band frequency domain (see Sec. 2.2). Even VGOS broadband receivers will not cover such low frequencies (see Sec. 2.3). Potential problems also arise from the vastly different power levels of strong GNSS signals and the faint signals of natural sources, especially if both types of sources should be observed alternately within a single session, as proposed by simulation studies (see Sec. 3.1.1). Furthermore, a small point-like signal source would be preferable to mitigate phase center issues as present with GNSS antenna arrays. Summarizing that, the whole processing and analysis scheme for geodetic VLBI observations could be much easier adopted to artificial signals similar to those of quasars, than to GNSS signals with vastly different characteristics in terms of modulation, signal level, bandwidth and frequency domain.

Beyond doubt, 24 Galileo satellites at about 24,000 km altitude (or satellites of other GNSS constellations) – each with SLR, VLBI, and GNSS capability – would provide unparalleled opportunities. Beyond the benefits mentioned above, this would provide excellent ability to improve inter-technique ties between GNSS, VLBI, and SLR. Three or more VLBI beacons installed on the edges of the platform would even allow to precisely determine the orientation of the satellite (Petrachenko, 2016).

Technical observation aspects Concerning observation-related aspects Plank (2014) assessed limitations for GNSS satellites related to the geometry of the antenna network. Due to their relatively high orbit of about 20,000 km, mutual visibility exists even on long inter-continental baselines. For instance, a satellite at 20,000 km altitude can still be observed at local elevation angles of up to 30° on baselines as long as 10,000 km. Furthermore, the change rates of topocentric view angles (azimuth and elevation) are reasonably low for GNSS satellites, with values lower than 0.5°/sec at an elevation of 85°. This enables observations even with slow antennas and without highly precise satellite tracking features.

Political aspects However, even neglecting the pure technical aspects, setting up international observing sessions on a regular basis, e.g. by the IVS, might still be challenging: would the VLBI community be prepared to sacrifice parts of its accuracy by spending valuable antenna time to observations of satellites? This is certainly a controversial point. Finding an optimal ratio between scans to satellites and to quasars in global VLBI sessions will be challenging.

3.2.1 Previous Observation Experiments

In recent years different groups reported on successful attempts to observe GNSS satellites with VLBI. A brief overview is given hereinafter.

In 2009 and 2010 initial experiments were carried out using the European antennas in Medicina (Italy), Noto (Italy), and Onsala (Sweden). Several GLONASS satellites were observed in three sessions on 21 January, 2009 (Tornatore *et al.*, 2010b), on 28 June, 2010 (Tornatore *et al.*, 2010a), and on 16 August, 2010 (Tornatore *et al.*, 2014). All antennas were equipped with L-band receivers and used the standard VLBI receiver chain to record GLONASS L1 signals. Due to the limited frequency ranges of the receivers only GLONASS L1 signals (carriers at about 1600 MHz) could be recorded. GPS L1 and L2 signals were out of the reachable band. The satellites were tracked by applying a stepwise tracking with a 20 sec repositioning interval. While the data recorded in the first experiment on 21 January, 2009, could not be correlated due to wrong recorder settings at the stations, fringes were found for GLONASS observations in the following two sessions.

In 2013 and 2014 several experiments were carried out by using the antennas at Wettzell (Germany) and Onsala (Sweden), as described by Haas *et al.* (2014), Hellerschmied *et al.* (2014), and Haas *et al.* (2015). Again, only GLONASS L1 signals were observed due to limited receiver capabilities. The main goal of these experiments was to test newly implemented L-band capabilities of the S-band receiver chain of the 20 m antenna at Wettzell (see Kodet *et al.*, 2013). Fringes were found for all GLONASS scans.

In parallel to the Australian GNSS–VLBI experiments in 2015 and 2016, which are described in detail in Chap. 5, several experiments were organized for European stations too. These sessions included VLBI antennas in Italy (Medicina and Sardinia), Germany (Wettzell), and Sweden (Onsala). A complete list including brief descriptions of the experiments can be found in Appdx. A. Unfortunately, only a small subset of these sessions was actually correlated, and for non of them delay observables were obtained. Hence, a geodetic data analysis was not carried out.

Haas *et al.* (2017) reported on first VLBI observations of GNSS signals on an intercontinental baseline between Onsala (Sweden) and Hartebeesthoek (South Africa). These sessions were part of an European Space Agency (ESA) pilot project within ESA’s Alcantara program, with the goal to investigate synergies between VLBI and GNSS.

3.3 Observation Aspects

In this Section important observation aspects are discussed which are specific for VLBI satellite observations and do not apply to conventional observations of extra-galactic radio sources. In the first part (Sec. 3.3.1), differences in the framework conditions between both observation approaches are outlined, followed by a discussion of the resulting observation restrictions in the second part (Sec. 3.3.2).

3.3.1 Framework Conditions for Satellite Observations

In the conventional geodetic VLBI, extra-galactic radio sources (mostly quasars) are routinely observed in order to derive various target parameters, as outlined in Chap. 2. Due to the virtually infinite distance between the observer and the radio source, incoming wavefronts can be assumed to be plane (*plane wave approximation*), and their proper motion can usually be neglected. Hence, such sources can be treated as invariant points on the celestial sphere with static source positions. The source coordinates are usually defined in terms of right ascension (Ra) and declination (De). Accurate positions can be found in source catalogs, such as the latest realization of the International Celestial Reference Frame (ICRF2, Ma *et al.*, 2009). When observing extra-galactic sources with VLBI antennas, the continuous change in the topocentric view directions due to the Earth rotation (about $15^\circ/\text{h}$) has to be considered and adjusted. Otherwise, a source would quickly move out of the narrow antenna's field of view. This correction is usually calculated and applied automatically by the antenna control systems.

In case of satellite observations the situation becomes more complex. Considering that satellites move rather fast (dependent on the orbit height), the complexity of scheduling and observation increases, as the sources are no longer stationary targets. In general the timing gets more critical, because the source positions, and thus, the view directions of the observing antennas, change quickly in time. For this reason satellites have to be tracked actively during data acquisition. Different options for tracking schemes are introduced in Sec. 3.4. The applied tracking procedures already have to be considered in the scheduling, e.g. to include and prepare the required tracking data.

Contrary to standard VLBI, source distances cannot be assumed to be infinite, which results in a different observation geometry, as illustrated in Fig. 3.1. When observing extra-galactic radio sources, the view direction vectors \vec{k} are parallel for two distant stations. Typically, satellites orbit the Earth in heights between about 180 km (lowest possible orbits) and about 36,000 km (geostationary orbit). Due to the relatively short ranges between satellites and VLBI antennas, the view direction vectors, represented by \vec{k}_1 and \vec{k}_2 , cannot be assumed to be parallel. Hence, a so-called *cross-eyed observation configuration* has to be applied, where the satellite's source coordinates, defined in a geocentric celestial system (by Ra and De), differ between sites.

In general, VLBI observations are restricted to satellites which actively emit radio signals that can be observed by the available station equipment, i.e. by the antenna feeds and the receiver

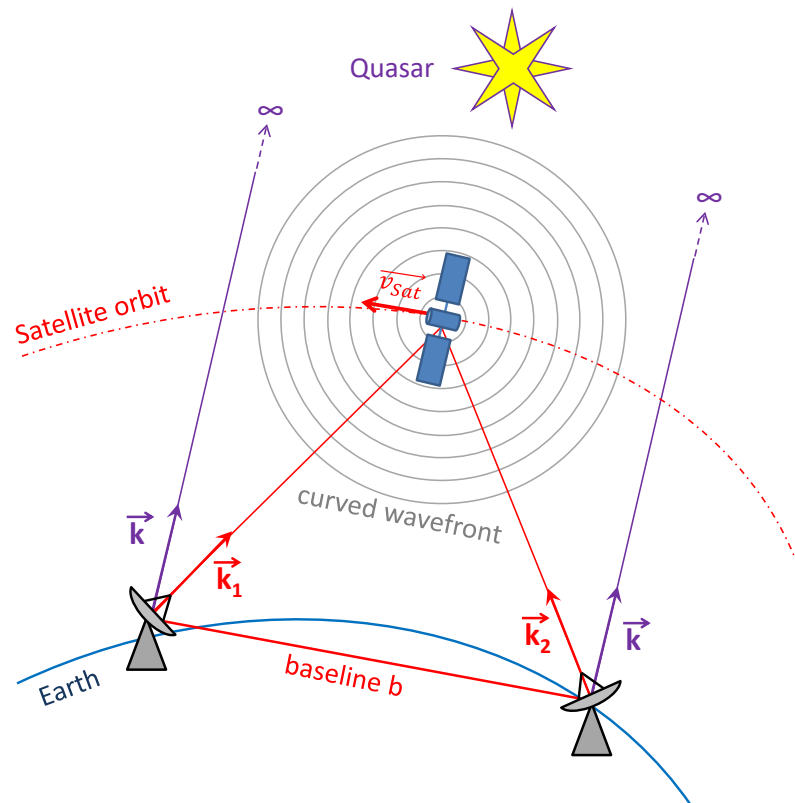


Figure 3.1: Observation geometry for satellites. Due to the finite source distance the plane wave approximation is not valid for satellites and, therefore, topocentric antenna view directions differ between sites ($\vec{k}_1 \neq \vec{k}_2$). For observations of quasars (or other types of AGN) which are considered to be at infinite distance, the view directions \vec{k} are assumed to be parallel.

electronics. Satellite signals differ from natural signals, e.g. of quasars, in terms of bandwidth, frequency, and flux density. Quasars emit radio waves in a broad frequency range in the microwave domain (ideally showing rather flat spectra) and are operationally observed in the S- and X-band in current geodetic VLBI sessions. Typically, the observed signals are noise-like and faint, with flux densities from several tens of mJy to a couple of Jy. Contrary to quasars, satellites usually broadcast modulated signals, in band-limited frequency channels, and the power level experienced on the Earth's surface is much higher. For successful VLBI observations it is a prerequisite to account for these specific signal characteristics during data acquisition. VLBI receiver systems have to be prepared and adopted accordingly, e.g. with L-band receivers for the observation of GNSS signals, and possibly by additional attenuation modules to prevent receiver saturation. The specific characteristics of satellite signals already have to be considered on the scheduling level, in particular for the generation of the schedule files: the recording parameters, such as the channel frequencies, the bandwidths, and the sampling scheme, have to be precisely adjusted to the characteristics of the observed signals.

3.3.2 Technical Observation Restrictions

The major technical observation restrictions arise from the requirement of common visibility of the target from at least two sites, and from the limited capabilities of (large) VLBI antennas to precisely track the comparatively fast moving satellites during data acquisition. Both aspects are addressed below.

Common visibility One fundamental principle of VLBI is that the target has to be simultaneously observed from at least two antennas forming a common baseline. Per definition common visibility exists, if the satellite is visible above the cut-off elevations (commonly 5°), or above the elevation mask at both stations. Common visibility, and the maximum elevation at which a satellite is observable on a baseline, depends (1) on the baseline length, and (2) on the orbit height. Plank (2014) investigated the impact of both parameters on the maximal common elevation angle at which a satellite can be observed using simple geometric relations, see Fig. 3.2. According to this, a GNSS satellite (about 20,000 km orbit height) is observable at a common elevation of maximum 43° on a 8,000 km long baseline. For more details the reader is referred to Plank (2014).

Antenna slew rates Currently, the slew rates of most legacy VLBI antennas¹ in the IVS network² are within a range of about $0.4^\circ/\text{sec}$ to $3^\circ/\text{sec}$. Antennas built according to the VGOS specifications (Petrachenko *et al.*, 2009) are in general more compact, with main-reflector diameters of about 12 m, and very fast, with slew rates of up to $12^\circ/\text{sec}$ (see Sec. 2.3). For example, the

¹Antennas built in the pre-VGOS era are herein referred to as "legacy antennas".

²<https://ivscc.gsfc.nasa.gov/about/org/components/ns-list.html>

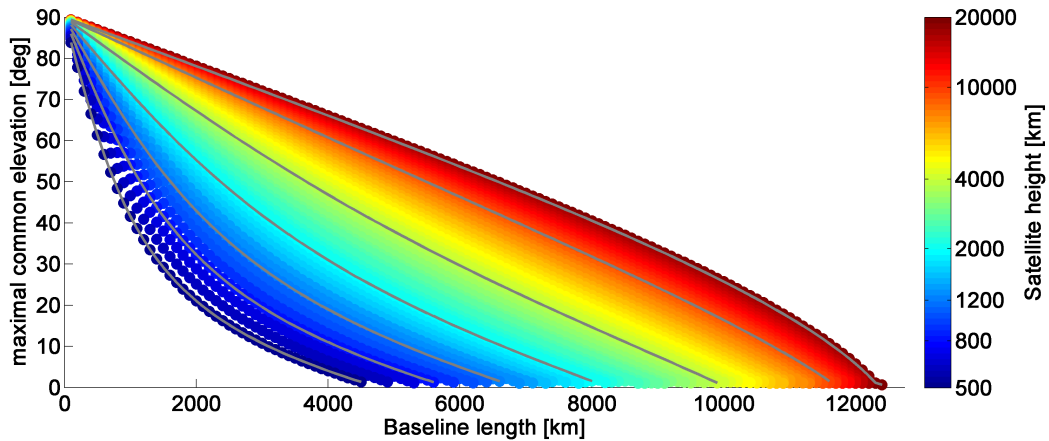


Figure 3.2: Maximum common elevation angle as a function of baseline length and satellite orbit height. The gray lines indicate various orbit heights as indicated next to the colorbar. Adopted from Plank (2014).

VGOS twin telescopes at Wettzell (Germany) have slew rates of $9^\circ/\text{sec}$ in elevation and $12^\circ/\text{sec}$ in azimuth.

When observing extra-galactic radio sources, the pointing directions of the antennas have to be adjusted to the Earth rotation during the on-source time. This correction amounts to $0.25^\circ/\text{min}$, and is automatically applied by the antenna controller. In case of satellite observations much higher slew rates are required to track the moving targets while their signals are recorded. The predominant parameter for the speed of a satellite is the orbit height, meaning that satellites in low orbits move faster than satellites in high orbits. The required tracking speeds, i.e. slew rates of the antenna axes, are not only dependent on the orbit height, but also on the local elevation angle at which the target is observed. In general, the topocentric view angles change slowly at low elevations, and show higher change rates the closer the target comes to the zenith. Plank (2014) investigated the slew rate requirements of azimuth-elevation mount type antennas (AzEl mount) for various satellites and found increasing demands, especially on the Az slew speed at high elevations. Taking the LAGEOS satellite as an example (orbit height of about 6,000 km), slew speeds higher than $0.5^\circ/\text{sec}$ are needed above 80° elevation. For GNSS satellites (about 20,000 km altitude) the situation is more relaxed with maximum slew rates lower than $0.5^\circ/\text{sec}$ up to 89° elevation. Plank (2014) concluded that the slew speed requirements for many satellites, in particular in LEO orbits, exceed the capabilities of most legacy VLBI antennas. For more details the author refers to Plank (2014).

When investigating the slew rate requirements for satellite observations the different antenna mount types have to be considered. While most IVS antennas are constructed with an azimuth-elevation mount, also other mount types are used. Each mount type shows certain pointing directions, so-called *keyholes*, at which coordinate singularities occur, i.e. the coordinate of one axis is undefined for a particular antenna position (e.g. the Az is undefined for an El of 90° in case of AzEl mounted antennas). Although the antennas may be able to point at particular keyhole positions, it is not possible to continuously track through this position. For example, the

Az angle would have to change instantaneously by 180° (requiring an infinite Az slew speed) when tracking a target directly through the zenith with an AzEl antenna. Brief characterizations of the different mount types used for IVS antennas, with respect to tracking satellites, are given below. More details on antenna mount types can be found e.g. in Salzberg (1967).

Azimuth-elevation mount (AzEl): The moving elevation axes rotates about the fixed vertical axis (azimuth axis). The Az motion typically covers a range larger than 360° , e.g. $\pm 270^\circ$ relative to either North or South, and the El range is between 0° and 90° . To enable a coverage of more than 360° in Az the position of the cable wrap, i.e. the bunch of cables connecting the receiver electronics in the moving elevation chamber and the non-moving facilities fixed to the ground, has to be tracked to consider ambiguities. Maximum Az rates occur close to the zenith, with a keyhole in zenith direction. Hence, tracking a satellite through the zenith is not possible.

Equatorial mount (HaDec): The antenna positioner consists of a fixed axis (equatorial axis) pointing to the direction of the celestial pole, and a moving axis at right angles, the declination axis. The covering is dependent on the site's latitude. In general, the equatorial motion range (hour angle) is less than $\pm 180^\circ$, and less than $\pm 90^\circ$ in declination. The only keyhole is in direction of the celestial pole. Hence, a satellite cannot be tracked through this direction.

X-Y mount (XYNS and XYEW): Two perpendicular axes, X and Y, are mounted at right angles with a vertical separation due to design constraints. The fixed axis is either aligned with the North-South direction (XYNS mount) or the East-West direction (XYEW mount). This mount type was mainly designed for satellite tracking, as it has full tracking capability through the zenith. Two keyholes occur in the horizontal plane (in the North and South, or the East and West, respectively, according to the alignment of the fixed axis) where tracking is prevented.

AzEl and XYEW antennas were used for the observations of GNSS satellites (about 20,000 km orbit height, see Chap. 5), and AzEl antennas only for tracking the Chinese APOD-A nano satellite (about 450 km orbit height, see Chap. 6). For AzEl antennas, the largest slew rates occur during direct overflights crossing the local zenith. This situation is illustrated exemplarily for a notional antenna at sea level observing APOD (Fig. 3.4), and a GNSS satellite (Fig. 3.3). Both figures depict the resulting Az and El rates as a function of the El angle. For a GPS satellite (or GNSS in general) the situation is quite relaxed with El rates lower than $0.01^\circ/\text{sec}$. The Az rate rises rapidly very close to the zenith ($\text{El} > 89.5^\circ$) towards infinite – this behavior illustrates the keyhole in zenith direction. When observing APOD the slew rates are much higher, roughly by a factor of 100 compared to the GPS case. The El rate rises slightly with increasing El and reaches values of up to $1^\circ/\text{sec}$. Similarly to the GPS satellite the Az rate stays very low and then rises rapidly close to the zenith, reaching $0.1^\circ/\text{sec}$ at an El of 85.5° .

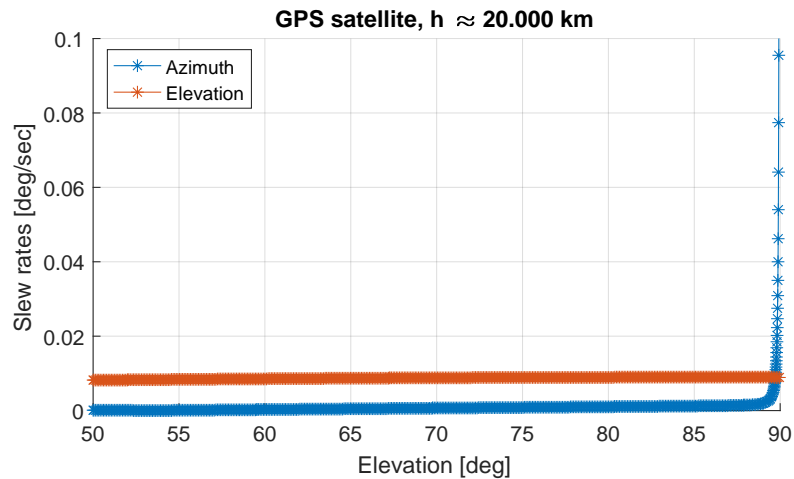


Figure 3.3: Slew rates of a notional VLBI antenna at sea level when tracking a GPS during a direct overpass through the local zenith.

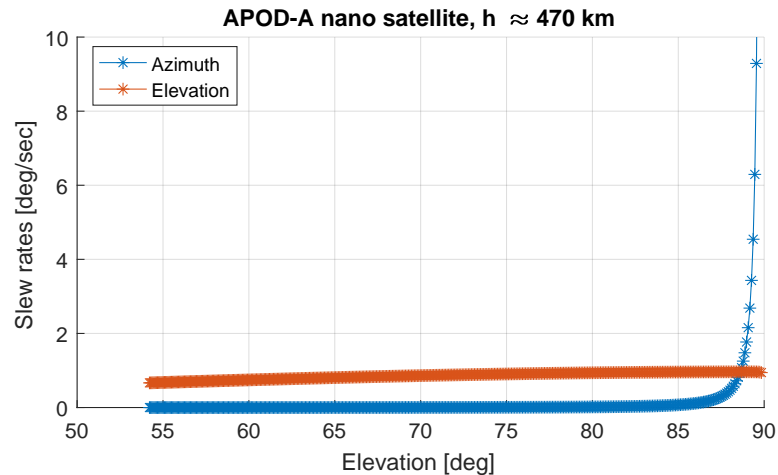


Figure 3.4: Slew rates of a notional VLBI antenna at sea level when tracking the APOD-A nano satellite (LEO orbit) during a direct overpass through the local zenith.

Based on these Figures (and only considering the slew rates) we can conclude, that tracking a GNSS satellite is rather uncritical, also for slow legacy antennas. Contrary, tracking a LEO satellite, such as APOD, impose much higher demands on the antenna agility, and even surpass the capabilities of many slower VLBI antennas.

Cable wrap AzEl antennas usually have a cable wrap which allows to turn more than 360° about the Az axis. Fig. 3.5 illustrates the cable wrap of the antenna WETTZ13S as an example. Only in the neutral segment (*N*) Az pointing directions are unambiguous. The cable wrap impose hard limitations on the Az movement which have to be considered in the scheduling. This is particularly important when observing a source close to a limit (in the *CW* or *CCW* segment). If the target crosses a limit, the antenna has to turn 360° to continue the scan, which may consume a fair amount of time. This is less critical when observing extragalactic sources, as the targets only

move with $0.25^\circ/\text{min}$ along the celestial plane. However, cable wrap limits are highly critical when observing (fast) satellites over longer orbit arcs, because the cable wrap limits may quickly be reached while data is recorded. Hence, the scheduler has to take care that a satellite track starts in the correct cable wrap segment (see Sec. 4.3.1).

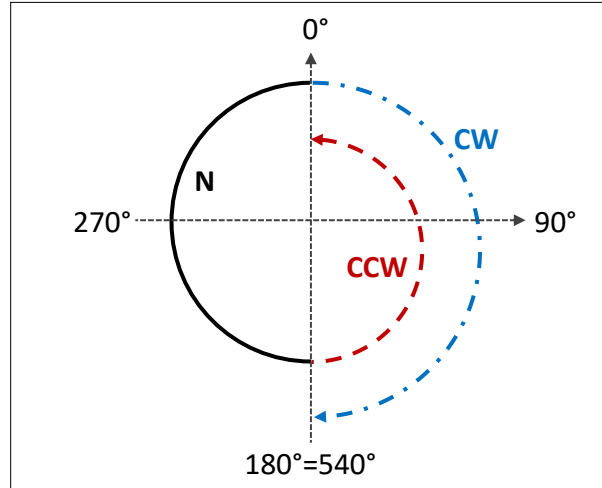


Figure 3.5: Cable wrap of the antenna WETTZ13S (Wetzell, Germany). The limits of the cable wrap are 0° and 540° , enabling the antenna to turn in total 540° about the azimuth within these limits. The cable wrap is divided into three segments: (1) the counter clock-wise segment (CCW, 0° to 180°), (2) the neutral segment (N, 180° to 360°), and (3) clock-wise segment (CW, 360° to 540°). For azimuth values between 0° and 180° the cable wrap position is ambiguous (CW or CCW).

3.4 Satellite Tracking

To enable a flawless signal acquisition, a moving satellite has to be kept within the field of view of the observing antennas while data is recorded. Ideally, the observed object is centered within the antenna beam throughout observations, i.e. the main lobe of the antenna’s radiation pattern is pointing accurately towards the target. In general, the width of the main lobe depends on the antenna diameter D and on the wavelength of the observed radio signal λ , and is commonly characterized by the half power beam width (HPBW). The HPBW is defined as the angular separation at which the magnitude of the radiation pattern decreases by 50% (or by -3 dB) from the peak of the main beam, and it can be approximated by

$$HPBW \approx \frac{\lambda}{D}. \quad (3.1)$$

Taking the 26 m antenna (HOBART26, Ho) and the 12 m antenna (HOBART12, Hb) at the Mount Pleasant observatory in Hobart (Tasmania) as example, Equ. 3.1 yields a HPBW of $4.72'$ and $10.23'$, respectively, for observations in the X-band ($\lambda \approx 3.57$ cm). The narrower the beam (i.e. the smaller the HPBW) the more difficult it is to keep a satellite accurately within the field of

view, and the higher the accuracy demands on the applied tracking scheme are. Hence, for satellite observations antennas with rather small diameters are preferred. The decrease in sensitivity is usually irrelevant for Earth satellites, because a strong enough signal level is easy to maintain.

To enable automated satellite observations with VLBI, analogous to the standard observation procedure for geodetic sessions described in Sec. 2.2, suitable orbit data for the observed satellites have to be either added directly, or provided along with the global schedule file (e.g. VEX formatted file). Furthermore, the source type (satellite or quasar) has to be declared for each scan, e.g. by using a dedicated flag. Then, the Field System (FS) program `drudg` (see Sec. 2.2) has to extract all site relevant information from the global schedule file, to write dedicated FS commands (so-called snap commands) for satellite tracking to the local station control files (snap and procedure files, see Sec. 2.2). The purpose of these satellite snap commands is to point the antenna towards the satellite at the right times, i.e. to enable tracking.

However, automated tracking and observation of satellites is currently restricted by the limited support of satellite targets in various process components: The currently used standard formats for schedule files (VEX and `skd`) do not allow to declare whether a satellite or a quasars is observed in a scan, and do not provide suitable options to include (or refer to external) satellite orbit data, e.g. in terms of TLE datasets or simple Az-El tables. The proposed VEX2.0 format¹ would improve this situation, as it would enable to include orbit data (e.g. TLE) directly in the schedule, and to define the source type properly. The next component in the standard process chain, the program `drudg`, does not support moving satellites as observation targets either, and is not able to write dedicated FS commands for satellite tracking to the according local control files. Standardized interfaces between the FS and antenna control systems, which would be required to enable satellite tracking modes provided by the antenna controllers, are also undefined. In general, there is no standardized way in the geodetic VLBI community for how to treat satellite tracking in the observation process, i.e. in all processes from the schedule file to the antenna motion control.

Nevertheless, different approaches and possibilities for the implementation of satellite tracking with VLBI antennas are discussed in the following sections.

3.4.1 Stepwise Tracking

When applying the stepwise tracking approach the antenna is repositioned – virtually stepwise – in a defined time interval (reposition interval $\Delta t_{reposit}$) in order to keep the moving satellite within the antenna’s field of view during data acquisition. As illustrated in Fig. 3.6 the antenna is pointed to the direction of the satellite, usually defined by topocentric celestial coordinates, at a time t_i . The subsequent position is commanded at $t_{i+1} = t_i + \Delta t_{reposit}$. The reposition interval $\Delta t_{reposit}$ has to be chosen so that the satellite stays within the antenna beam while tracking. For tracking GNSS satellites with an orbit height of about 20,000 km, only requiring a very slow

¹For more information the author refers to <https://safe.nrao.edu/wiki/bin/view/VLBA/Vex2>.

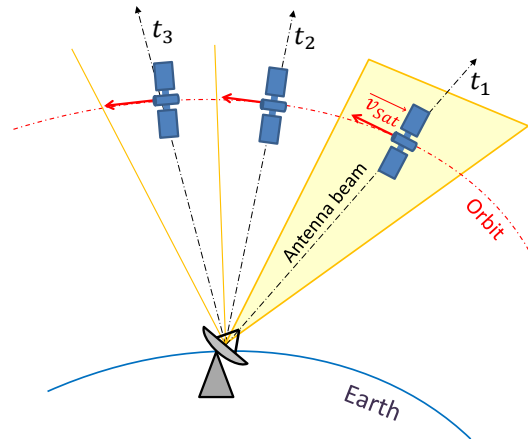


Figure 3.6: Stepwise satellite tracking approach. The antenna is repositioned in short time intervals ($\Delta t_{reposit} = t_i - t_{i-1}$) of e.g. 10 sec in order to keep the moving satellite within the antenna beam while its signal is recorded.

antenna motion (see Fig. 3.3), values for $\Delta t_{reposit}$ of about 10 sec are common (widely used for the GNSS observations listed in Table A.1 and discussed in Chap. 5). Depending on the reposition interval, the acceleration of the antenna positioner, and the inertia antenna structure, the tracking motion is more or less smooth, as the antenna already accelerates to the next position, before stopping at the previous one. However, it is recommended to test the applicability of stepwise tracking for each VLBI antenna before applying it for longer sessions to prevent the antenna from taking damage from the unusual motion sequence.

The great advantage of this satellite tracking approach is, that it is viable based on the currently used schedule file formats (VEX 1.5b1 and skd) and the standard processes used for conventional VLBI observations by the IVS, i.e. via the NASA Field System and standard tracking modes for extra-galactic sources (see Sec. 2.2). That is the case, because a satellite track is basically treated like a series of sources with static coordinates in the celestial frame.

To incorporate this stepwise tracking in the standard schedule files, the satellite orbit is fragmented and approximated by discrete positions at particular epochs (t_1, t_2 , etc., see Fig. 3.6). For each epoch the satellite position is defined as a distinct source, equal to the definition of a natural and stationary radio source. To implement the cross-eyed observation configuration, which is introduced in Sec. 3.3.1, the source positions have to be defined in a *topocentric* equatorial coordinate system (e.g. see Vallado, 2013, Chap. 3.3.2), in terms of topocentric right ascension α_t and declination δ_t . As the topocentric source coordinates differ between stations per definition, and because the current VEX format does not allow to define site dependent source coordinates, separate *station dependent VEX files* are required rather than a single global VEX file for a single experiment.

However, the reposition interval $\Delta t_{reposit}$ has to be selected carefully. If $\Delta t_{reposit}$ is too small,

the vast number of new positioning commands¹ block, or at least delay the execution, of other commands on the stack. Hence, the positioning commands are not executed in time and the tracking fails. We experienced that behavior for example during tracking tests of the APOD-A nano satellite with the antenna ONSALA60 located at the Onsala Space Observatory, Sweden. In the Experiments 263a, 263b, and 263c (see Tab. A.1) it was tested to track this fast moving LEO satellite by applying a stepwise tracking with a 1 sec reposition interval implemented in the VEX files. This approach failed, because the individual positioning commands took too much time (more than 1 sec) to be processed by the Field System (although various system checks were deactivated). Thus, the Field System and the antenna control system were simply overcharged.

To circumvent such overcharging issues, the Field System may be bypassed by commanding the source positions directly to the antenna control unit (ACU). The particular implementation depends on the ACU features and its communication interface. Taking again the issue at station ONSALA60, which is described above, as an example, the solution was to bypass the Field System: The ACU of this antenna is able to directly read tables with time-tagged position commands, provided in terms of standard snap-formatted source commands. This feature allowed to bypass the Field System by making use of such a table and, hence, enabled maintain a fast position update rate (Δt_{repos}) of 1 sec.

The drawback of stepwise satellite tracking is, that the source is not steadily centered within the antenna beam. As the satellite moves continuously while the observing antenna is repositioned only sequentially, the target steadily moves in and out of the center of the antenna's main lobe. Such a time-variable mis-pointing can cause amplitude variations in the acquired signals, and possibly other effects, e.g. systematic phase variations. Depending on the source distance (i.e. the orbit height), the resulting speed of the satellite, the antenna's beam-width (i.e. diameter), and the reposition interval, the effects are more or less pronounced. Hence, potential effects on the derived observables have to be evaluated for individual application cases.

Fig. 3.7 depicts the accumulated power of the L-band signals of the GPS satellite PRN 27 observed in Session 328a (November 23, 2016) with the 30 m VLBI antenna at Warkworth, New Zealand (WARK30M). Stepwise satellite tracking was tested with a reposition interval of 9 sec. The monitored power clearly reflects the chosen reposition interval, with a significant and systematic amplitude variation with a period of exactly 9 sec. The author has to note, that this is an extreme example and that the amplitude variations depicted here are exceptionally pronounced compared to what was experienced throughout a large number of other observations.

3.4.2 Continuous Tracking

To circumvent drawbacks of the stepwise tracking approach, such as amplitude variations due to slight periodic changes of the off-axis view angle (see Fig. 3.7), more sophisticated tracking schemes are needed. A tracking approach is referred to as *continuous*, if the antenna slews

¹For commanding a VLBI antenna to a desired source position through the Field System usually the the snap command `source=<source name>, <Ra>, <Dec>, <catalog reference epoch>` is used.

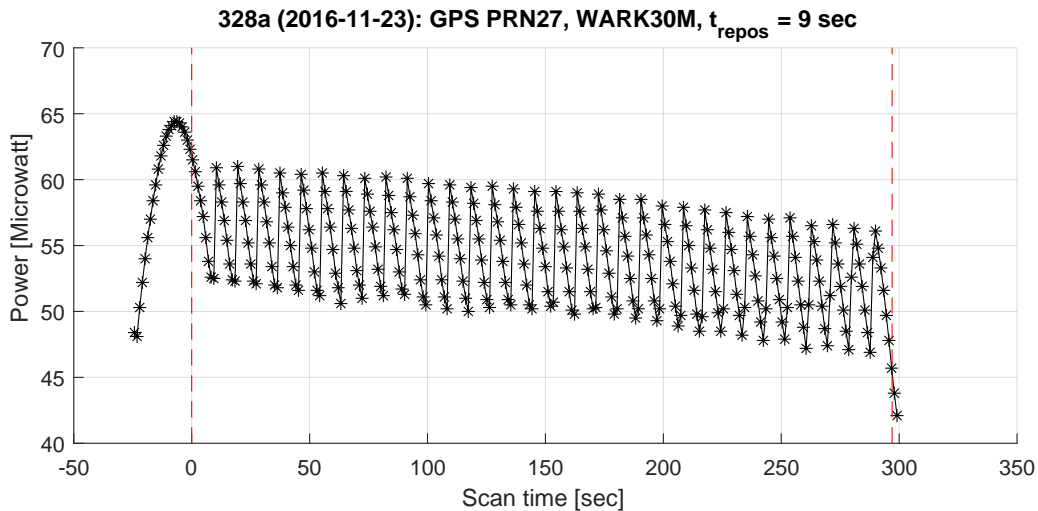


Figure 3.7: Signal power monitored at station WARK30M (Warkworth, New Zealand) while tracking the GPS satellite PRN 27 in Session 328a, observed on November 23, 2016. The *dashed red lines* mark the start and end of the 297 sec long track. The antenna reposition interval of 9 sec yields a clear and systematic variation in signal power with a period of exactly 9 sec. The steady rise in signal power, beginning about 25 seconds before the actual scan start, illustrates the satellite when initially entering the antenna’s main lobe and then moving through the beam. In this case the antenna was pointed towards the satellite’s position at scan start (scan time = 0 sec) about 60 sec prior to the start of the scan.

smoothly and constantly in order to keep the satellite target centered within the antenna’s field of view while tracking. This can be achieved – in an ideal case – by precisely adopting the antenna’s slew speed (and acceleration) on the satellite motion, without alternating acceleration and deceleration of the antenna axes.

Two principle approaches to realize continuous tracking have been applied so far: (1) The antenna control unit (ACU) provides a dedicated tracking mode suitable to follow satellites smoothly, or (2), if the first option is unavailable, satellite tracking features can be implemented in the NASA Field System (FS). Both options are discussed in the following Sections, 3.4.2.1 and 3.4.2.2.

Satellite orbit predictions For both options satellite orbit predictions are required at the stations, which are then used by the FS, or by the ACU, respectively, to calculate the antenna pointing angles. For such applications, Two-Lines Elements (TLE, see Sec. 4.3.2) are widely used, which basically provide sets of mean Keplerian orbit elements. TLE datasets are publicly available for thousands of space objects¹. Orbit predictions are also provided in other formats, such as the Consolidated Prediction Format² (CPF) used for tracking satellites by SLR telescopes, and the standard SP3 format³ which is used e.g. by the IGS to provide predictions of GNSS satellite orbits in their ultra-rapid solutions.

¹TLE datasets are available e.g. at <https://celestrak.com/>.

²https://ilrs.cdis.eosdis.nasa.gov/data_and_products/formats/cpf.html

³<ftp://igs.org/pub/data/format/sp3c.txt>

Process automatization In contrast to the stepwise tracking described in Sec. 3.4.1, all currently available continuous tracking schemes require orbit data (e.g. TLE) which is not supported by the current standard schedule file formats¹. Furthermore, the FS program *drudg*, which is used to translate a (VEX or *skd*) schedule file to locally executable *snap* commands, does not support dedicated *snap* commands for satellite tracking by now. Due to these limitations, completely automatized observations, as common in conventional VLBI sessions, are currently not viable and, meanwhile, workarounds have to be used.

3.4.2.1 ACU Tracking Capabilities

The availability of satellite tracking features depends on the functional range of the specific ACU of an antenna. There is no standard approach and, hence, implementations are usually proprietary software solutions.

To get an idea how the implementation of a dedicated ACU satellite tracking mode may look like, the realization at the Geodetic Observatory Wettzell (GOW, Germany) shall be used as example. All three VLBI antennas at the GOW are equipped with similar antenna controllers by the manufacturer Vertex Antennentechnik GmbH. Besides different modes to track celestial objects, this ACU provides a mode for tracking satellites based on TLE datasets – the so-called two-line track mode. This two-line track mode is embedded in the FS by programming the required communication interface in the station-specific code part of the FS according to the interface specifications of the ACU. To enable satellite tracking via the FS, a dedicated *snap* command is used to specify the satellite to be tracked and the file that contains the according TLE dataset. When executing this *snap* command, the corresponding TLE dataset is loaded by the ACU, which then switches to the two-line track mode and starts to track the satellite. Internally, the ACU calculates a stack of antenna positions in terms of azimuth and elevation angles in an interval of 0.2 sec using the TLE data and suitable models for coordinate transformation. To enable a smooth antenna motion, the ACU applies a cubic spline interpolation on the sampling points in the stack, and calculates the actual target velocity using the path gradient of the spline. The antenna's slew speeds are then adopted accordingly. For more details on the implementation and the satellite tracking workflow the author refers to Hellerschmied *et al.* (2014). This mode was successfully tested for observations of GLONASS satellites (Sessions G140116a, G140116b, G140121a, and G140121b, see Tab. A.1) and for tracking the APOD-A nano satellite in the Sessions 207b, 263b, and 263c (see Tab. A.1). The tracking was smooth and it enabled to keep the fast moving APOD satellite (LEO orbit, see Sec. 6.1) accurately centered within the antenna's field of view – even at high elevation angles. This allowed capturing its signal in the S- and X-band without showing any obvious amplitude variations.

It should be highlighted that the integration of ACU functions in the FS is station specific. The implementation depends on the range of functions and the interface specifications of the ACU.

¹VEX2.0 (<https://safe.nrao.edu/wiki/bin/view/VLBA/Vex2>), which is currently in the definition phase, will in future enable to add TLE datasets directly to the global schedule file.

3.4.2.2 Satellite Tracking with the Field System

If an antenna's ACU does not provide features for satellite tracking, e.g. by using TLE data, dedicated tracking software can be integrated in the FS. The tracking software uses the provided orbit data to calculate antenna pointing angles on the FS computer, and then forward the pointing data to the ACU to steer the antenna positioner.

Currently, the following tracking software solutions are available: (1) Moya Espinosa & Haas (2007) programmed a satellite tracking module for the FS called SATTRACK, and (2) starting with version 9.11.2 the NASA FS itself is able to process TLE orbit data and provides new snap commands specifically for satellite tracking (Himwich & Gipson, 2012).

Both solutions are quite similar in design and application. They use TLE data for orbit propagation and can be controlled via dedicated snap commands in the FS. Prior to a satellite track, the most recent TLE data has to be downloaded and stored in a dedicated folder on the FS computer. After execution of the snap command for satellite tracking, the tracking software loads the TLE data and calculates a narrow sequence (interval of 1 sec per default) of satellite positions by applying the SGP4 orbit propagation models (Hoots & Roehrich, 1980). The satellite positions are then converted to a stack of azimuth-elevation angles. This ephemeris stack is available in the shared memory of the FS and can be used by the antenna control interface of the FS (function *antcn.c*) to guide the antenna. Also here, SATTRACK or the FS features, respectively, only provide the framework for the satellite tracking by computing a stack of tracking points. The actual implementation is again station dependent, and has to be realized according to the interface specifications and requirements of the ACU.

However, satellite tracking based on these FS add-ons is not truly continuous. The tracking still has a sequential character, comparable to the stepwise tracking, since it is based on discrete tracking points, without an interpolation of the slew rates between them. The difference to stepwise tracking described in Sec. 3.4.1 is, that the time series of tracking points is calculated directly on the FS computer, rather than being defined in the VEX file. With all tracking points defined in the VEX file in terms of individual sources, individual "source" snap commands have to be executed per tracking point. When using e.g. the SATTRACK module, only a single snap command needs to be executed to start the internal calculation of the pointing data and the tracking. In general, the latter option allows higher position update rates compared to stepwise tracking via a VEX file.

The attainable tracking quality strongly depends on the antenna specifications, the antenna equipment, and its capability to process positioning commands at a high rate. While Earth observation satellites in LEO orbits were successfully tracked in the X-band using the SATTRACK module at the 20 m VLBI antenna at Onsala, Sweden (Moya Espinosa & Haas, 2007), the TLE tracking features of the FS failed to track the APOD satellite with the 12 m AuScope antennas at Kathrine and Yarragadee (for more information on the AuScope antennas see Sec. 6.2). When trying to track APOD in Sessions 200a (see Tab. A.1) by using the TLE tracking mode of the FS with a position update rate of 2 sec, all scheduled commands were either blocked, or executed

with a delay. Hence, the antenna did not track properly, and the recorder did not start. After changing the position update rate to 5 sec in Session 202 (see Tab. A.1), all commands were executed as scheduled. However, then the update rate was too low to properly track APOD, resulting in huge amplitude variations and partial signal losses.

Chapter 4

Process chain for VLBI satellite observations

Since 2014 our VLBI group at Technische Universität Wien (Vienna) contributed to numerous VLBI experiments in which satellites (mainly GNSS) were tracked as main observation target. Usually, our task was the observation planning, and the preparation and provision of all control files that were required to actually observe these sessions. A list of experiments for which we created the observation schedules by using the satellite scheduling features of our in-house VLBI software VieVS (see Sec. 4.3) is shown in Appdx. A.

Although the first experiments in 2014 showed that our scheduling capabilities were in place, and that satellite tracking and recording of raw baseband data worked, further capabilities to actually derive group delays – as common in the geodetic VLBI – were still missing. Only a fraction of the observed experiments were actually correlated (e.g. as shown by Tornatore *et al.*, 2014 or Haas *et al.*, 2014), and for non of them proper observables were obtained, which could then serve as input for a geodetic data analysis.

Facing these deficiencies, we started to enhance our capabilities – beyond scheduling and acquisition of the raw data – and began to develop and adopt a complete set of (software) tools that enable to derive delay observables in a geodetic style, and to analyze them. In a fruitful collaboration with the University of Tasmania (UTAS, Australia) we developed for the first time an end-to-end process chain for satellite observations with VLBI antennas which aims at deriving group delay observables as common in geodetic VLBI. UTAS was the perfect match as project partner, as it owns and controls several radio observatories in Tasmania and on the Australian mainland. Another major asset was the comprehensive experience of the UTAS staff members, especially those at the Mt Pleasant observatory (Hobart, Tasmania), namely Jamie McCallum, Lucia McCallum, and Jim Lovell, in handling the observatory hardware, in VLBI observation techniques, in correlation and post-correlation processing of VLBI raw data, and in analyzing astronomical as well as geodetic and astrometric VLBI sessions. Hence, this collaboration allowed us approaching all aspects of VLBI satellite observations, and enabled to flexibly test new developments in real observations experiments.

The established processes were initially tested in the frame of VLBI observations of GNSS satellites in 2015 and 2016 on the Australian baseline Hobart-Ceduna. These experiments are described in detail in Chap. 5. Later in 2016, the process chain was adopted for observations of the Chinese APOD-A nano satellite with the AuScope geodetic VLBI array (see Chap. 6). While a general introduction to the applied process chain is outlined in this Chapter, experiment specific adaptations and details are discussed in the according chapters.

The observation and analysis schemes described on the following pages can be considered as guideline and reference for future experiments. They pave the way for future research and development in the field of VLBI satellite observations, as they tremendously simplify the implementation of further experiments.

4.1 Overview

The process chain introduced on the following pages comprises all components necessary to derive geodetic-style group delay observables from direct observations of satellites with VLBI radio telescopes. The general rule was to apply and adopt as many standard processes as possible to stay close to the standard data acquisition scheme for geodetic VLBI sessions which is introduced in Sec. 2.1.

Fig. 4.1 shows an overview of the process workflow. The Vienna VLBI and Satellite Software (VieVS; Böhm *et al.*, 2018) plays a central part, as it is used in the very beginning for scheduling of the observations, as well as for the final analysis of the obtained group delays. A general introduction to VieVS is given in Sec. 4.2, with the focus on data analysis features specifically for satellite observations in Sec. 4.2.1. The scheduling of VLBI satellite observations using VieVS is discussed in Sec. 4.3. After sending the schedules to the participating VLBI stations, the observations are carried out. Details on satellite observations in terms of antenna and receiver control schemes are discussed in Sec. 4.4. The recorded raw baseband data is then correlated using the software DiFX (Deller *et al.*, 2007), which is widely used in geodetic VLBI. The required correlator input model, providing a priori near-field delays for the satellite observations, are calculated in VieVS and written to the DiFX control files (see Sec. 4.5.2). After correlation the Haystack Observatory Postprocessing System (HOPS)¹, with its main component being the fringe fitting program fourfit, is used to derive the observables in terms of group delays (Sec. 4.6). In the end, the group delays are exported to VieVS where the observation results are analyzed and used to estimate various parameters in a least-squares adjustment (see Sec. 4.7).

4.2 The Vienna VLBI and Satellite Software

The Vienna VLBI and Satellite Software (VieVS; Böhm *et al.*, 2012 and Böhm *et al.*, 2018) is a state-of-the-art software package capable to handle different aspects of the VLBI applications

¹<https://www.haystack.mit.edu/tech/vlbi/hops.html>

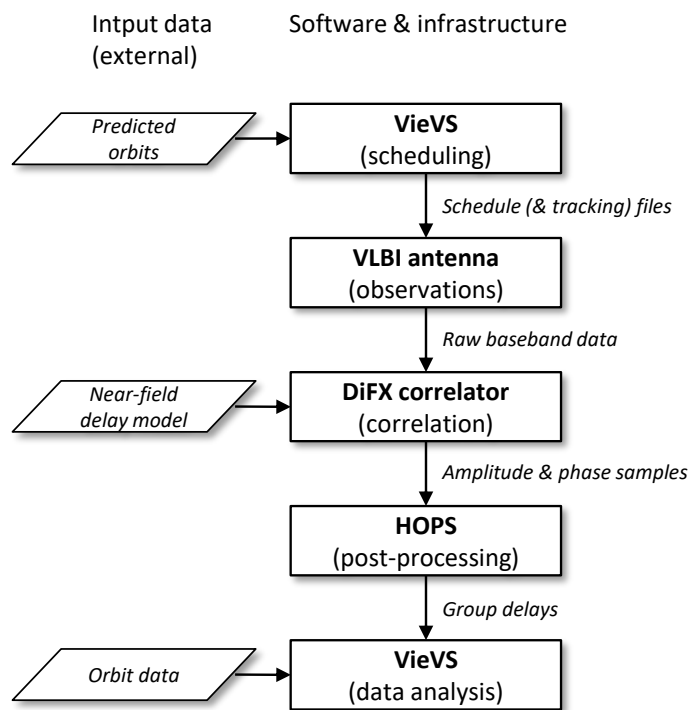


Figure 4.1: Simplified process workflow for VLBI satellite observations illustrating important external input data (*rhomboid boxes, left*), the used software and infrastructure (*rectangular boxes, right*), and the essential interchange data (*italic text*).

for geodesy and astrometry, such as scheduling, simulations, and analysis. It is developed and maintained at the Department of Geodesy and Geoinformation (GEO) at the Technische Universität Wien (TU Wien) since 2008, and also incorporates contributions from many international colleagues. VieVS is written in MATLAB, which is a commercial programming environment and not free of costs. However, it is rather easy to code with MATLAB, and it provides extensive libraries of predefined functions. Hence, it tremendously simplifies modifications of the code, and eases the implementation of new program features. This makes VieVS highly suitable for a wide range of research tasks, such as testing new models, and developing new strategies for VLBI data analysis and scheduling.

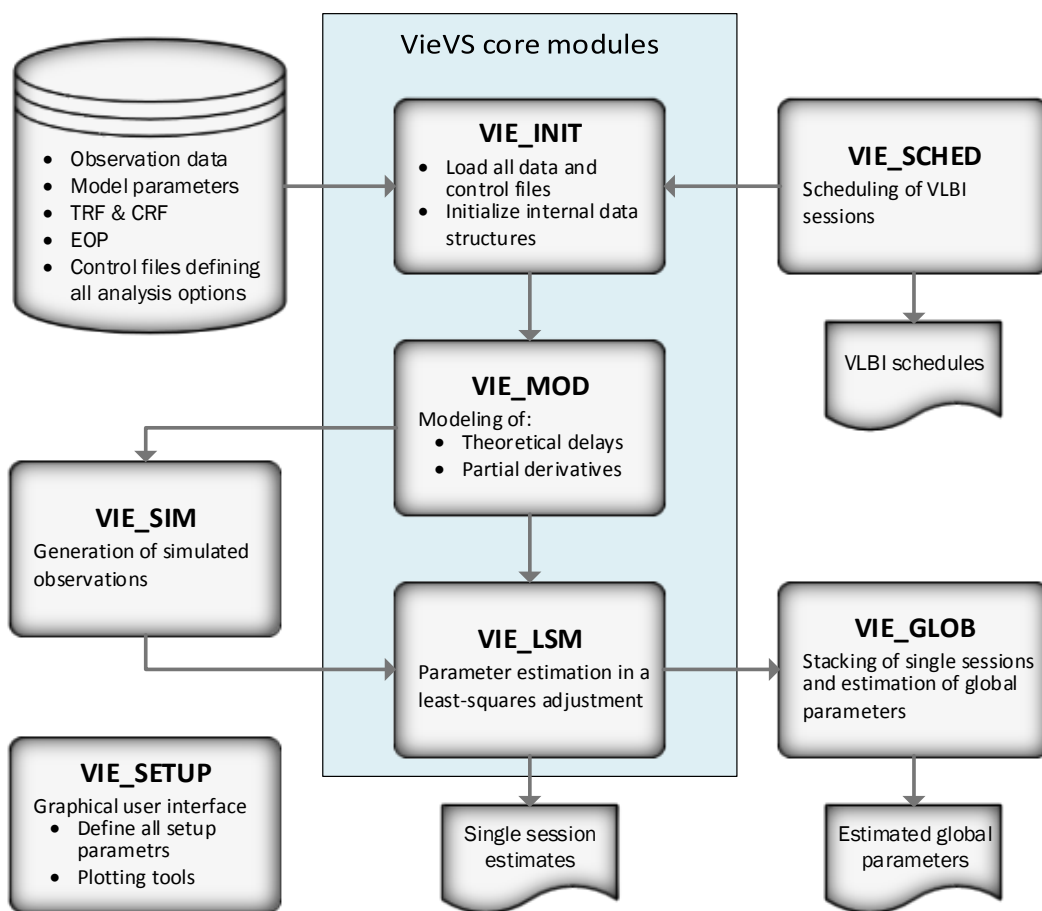


Figure 4.2: Modules structure of VieVS 3.0.

VieVS is organized in several modules in order to maintain a clear structure, see Fig. 4.2. For single session analysis the following three *core modules* are required:

VIE_INIT reads in all data and control files required for the processing. The most important input data are the actual observation files (supported file formats are NGS cards, vgosDB, and VSO, see Sec. 4.2.1.1), various parameters for modeling atmospheric delays (mapping functions, gradients, etc.) and geophysical station displacement effects, station and source

positions in a specific TRF and CRF, and a priori EOP time series. Along with the data files, various control files are loaded to define the desired processing settings, such as selection of the applied models, and handling of various analysis problems (outliers, etc.). VIE_INIT stores all the input data in MATLAB data structures that are then loaded and updated by the other VieVS modules.

VIE_MOD basically models a theoretical delay value for each observation in the input data by applying the user-defined models. All models are implemented according to the IERS conventions (Petit & Luzum, 2010) and their electronic updates. As a key component the so-called consensus model (IERS conventions, Chap. 11) should be mentioned here, which is used per default to calculate a priori delays for astronomical radio sources (located in the far-field). Furthermore, VIE_MOD calculates the partial derivatives for all target estimates required for the least-squares adjustment in VIE_LSM.

VIE_LSM carries out a least-squares adjustment based on the differences between the observed and the computed delays (O-C) in a VLBI session to estimate the selected target parameters. A standard Gauss-Markov model is applied as described e.g. by Chipman (2011). In general, all estimates are parametrized in terms of piece-wise linear offsets (PWLO), see Teke (2011) for more details. The default estimates for geodetic 24 h sessions (e.g. IVS R1 and R4 sessions) are station and source positions (one offset per session), EOPs (hourly PWLO), ZWD (PWLO in a 30 min interval), tropospheric gradients (PWLO every 4 h) and one clock model per station (quadratic polynomial plus PWLO every 30 min).

In addition to the core modules, VieVS provides the following *extension modules*:

VIE_SETUP represents the graphical user interface of VieVS. It is used to define all setup parameters, and provides convenient session analysis and plotting features, which can be used for an ad-hoc interpretation of the processing results.

VIE_SCHED is a VLBI scheduling software for geodetic and astrometric purposes. Initially, programmed to investigate suitable scheduling strategies for the VLBI2010 initiative through simulations (Sun, 2013 and Sun *et al.*, 2014), it evolved to a fully operational and state-of-the-art scheduling package. In recent years it was used, for instance, to schedule the AUSTRAL VLBI sessions (Plank *et al.*, 2017b). Lately, it was updated enabling an enhanced integration with the the simulation features in VieVS, enabling comprehensive investigations e.g. towards optimized scheduling parameters (Schartner *et al.*, 2017). The program implements a fully automatic selection of astronomical observation targets based on different optimization strategies and scheduling modes, such as the station-based, and the star scheduling mode (McCallum *et al.*, 2017). The generated observation plans can be written to schedules files (VEX and skd formatted) that allow to control real sessions, and to observation files (e.g. NGS formatted) filled with artificial observables for simulations.

VIE_SIM generates simulated delay observables by taking into account the three main stochastic error sources: wet troposphere delays, station clocks, and measurement noise. These error contributions are simulated based on random numbers enabling Monte Carlo simulations (multiple simulations of the same session). The simulated observations can then be analyzed in **VIE_LSM** enabling a statistical interpretation of the derived results, e.g. by investigating the scatter of the estimates. For more details on the simulation scheme the reader is referred to Pany *et al.* (2011).

VIE_GLOB is a tool for the estimation of so-called global parameters, i.e. of parameter that stay stable over longer timescales. **VIE_GLOB** basically stacks the normal equation matrices of a number of individual sessions, e.g. of the whole VLBI observation history, to estimate precise parameters based on a large number of sessions observed over a long time span. Common applications are the estimation of terrestrial and celestial reference frames as described by Krásná *et al.* (2014) and (Mayer *et al.*, 2017, CRF determination).

More information about VieVS is provided on the webpage <http://vievswiki.geo.tuwien.ac.at>. The current user manual in combination with the lecture material of our yearly workshops provide a solid reference.

4.2.1 Features for VLBI Satellite Observations

In preparation for this work, VieVS was updated with several feature to support VLBI observations of satellites in addition to standard observations of natural radio sources, such as quasars. The major implementations are described below. Beyond that, all plotting and session analysis feature in **VIE_SETUP**, as well as all error handling features, for example to remove outliers and to handle clock breaks, were updated to support satellite observations. Most features for VLBI satellite observations are already incorporated in VieVS since release version 3.0¹, or will be added to upcoming releases.

4.2.1.1 VSO Observation Files

VieVS initially supported two types of observation file formats: (1) NGS cards², and (2) vgosDB databases (see Bolotin *et al.*, 2017, and references therein). NGS cards are basically text files providing the most impotent quantities for each observation. In VieVS the following values are read in: delay reference epoch, observed baseline delay (ambiguities corrected) and delay rate plus formal errors, meteorological in situ measurements (pressure, temperature, humidity), cable calibration corrections, and ionosphere delay correction plus formal error. In the vgosDB format the VLBI data for one session is stored in various (binary) netCDF files, organized in a predefined tree-like folder structure. Each netCDF file represents an atomic piece of data,

¹See <http://vievswiki.geo.tuwien.ac.at>.

²The NGS format definition can be found at https://lacerta.gsfc.nasa.gov/mk5/help/dbngs_format.txt.

such as observed values with their formal errors, or source coordinates. This format provides the possibility to keep alternative models, e.g. for tropospheric delays, in the same session data tree.

Unfortunately, both file formats do not support satellites as observation targets, i.e. there is no possibility (e.g. a flag) to define whether a satellite or a quasar was observed in a specific scan. Therefore, a new observation file format was defined for VieVS, named *VieVS Observation format (VSO)*¹. VSO files are text files in which every line represents one (baseline) observation. All provided quantities are organized in column mode, see Tab. 4.1. Unavailable parameters, such as missing in situ measurements of pressure and temperature, are indicated by the error code -999 in the according column and will be modeled or ignored in VieVS. VSO files can be loaded by VIE_INIT and be used fully equivalent to NGS cards in VieVS, with the additional option to define whether a satellite or a quasar was observed by setting the flag in column 10 accordingly. For specific purposes, sub-types of the VSO format are defined (indicated in VSO file header). Important ones are the *VSO type 4* (only containing the observation plan in columns 1 to 10; no measurements), *VSO type 1*, only containing the observation plan (columns 1 to 10) plus modeled delays (column 11), and *VSO type 6* containing all information/columns listed in Tab. 4.1, i.e. observed delays plus all listed corrections and meteorologic measurements.

4.2.1.2 Scheduling of Satellite Observations

One key-component for realizing satellite observations with VLBI is a suitable scheduling program. Hence, VieVS was updated with dedicated scheduling features that enable to schedule observations of satellites along with observations of quasars in a common session (Hellerschmied *et al.*, 2017b). These features are introduced in detail in Sec. 4.3.

4.2.1.3 Near-field Delay Modeling

The purpose of VLBI delay models is to determine theoretical delays based on the known geometric constellation of an observation (positions of source and observer at the observation epoch), and by applying various corrections to take into account signal propagation effects, e.g. caused by the neutral atmosphere and the ionosphere, and due to relativistic effects. In VieVS theoretic delays are modeled in the module VIE_MOD by applying the consensus model (IERS conventions, Petit & Luzum, 2010), and are mainly used to reduce the observations for the least-squares adjustment. This analytical consensus model is designed for extra-galactic radio sources and is based on the plane-wave approximation by ignoring the effect of the source's distance (Eubanks, 1991). For Earth-based VLBI observations of extra-galactic sources it yields a precision of 1 ps.

However, the consensus model is inaccurate for sources at finite distances, and the error is not tolerable for sources within our Solar System. For source distances less than 200 kpc (kilo

¹The VSO file format is defined at http://viewswiki.geo.tuwien.ac.at/doku.php?id=public:views_manual:data. A similar format was already used for the simulation studies by Plank *et al.* (2014).

Table 4.1: Parameters provided in the VSO observation file format (column mode).

Column	Parameter	Unit/format
1 to 6	reference epoch	date and time
7	name of station 1	8 char. string
8	name of station 2	8 char. string
9	source name	char. string
10	observation type flag	"s" or "q"
11	delay	nsec
12	delay formal error	nsec
13	ionosphere delay	nsec
14	ionosphere delay formal error	nsec
15	cable correction station 1	nsec
16	cable correction station 2	nsec
17	temperature station 1	°C
18	pressure station 1	mbar
19	relative humidity station 1	%
20	temperature station 2	°C
21	pressure station 2	mbar
22	relative humidity station 2	%

parsec) the inaccuracy due to the effect of the curved wavefront ("near-field effect") exceeds 1 ps for a 12,000 km long baseline on Earth (Sekido & Fukushima, 2006). Hence, dedicated models – hereinafter referred to as "near-field delay models" – are required that consider effects caused by the finite distance of the source. Various authors describe different approaches to model such near-field delays. Selected examples are given below.

Sekido & Fukushima (2006) describe an analytical model that can be considered as an expansion of the consensus model. Therein, the effect of the curved wavefront is represented by introducing a pseudo source vector, yielding a modeling precision better than 1 ps for all radio sources above 100 km altitude from the Earth's surface. The model is evaluated in the barycentric celestial reference system (BCRS) and the delays are expressed in the TT frame (Terrestrial Time), thus, making it fully compatible with the consensus model.

Moyer (2003) presents a delay modeling approach suitable for VLBI observations of spacecraft. It is based on a numerical solution of the light-time equation for the two ray paths between the signal source (spacecraft, satellite) to two observers (VLBI antennas creating a baseline). It accounts for the effects of both special and general relativity.

Duev *et al.* (2012) describe a similar formalism based on an iterative solution of the light-time equation in the BCRS (basically an application of the approach by Moyer, 2003). The iteration

steps are required for a precise determination of the signal transmission time at the spacecraft by solving the light-time equation for the down-leg. For more details the author refers to the cited paper.

Klioner (1991) describes a consistent relativistic VLBI delay model suitable for extra-galactic sources, as well as for sources at "finite" distances that are located within our solar system or even in close vicinity to Earth. The model delivers theoretical delays which are accurate on the level of 1 ps.

Near-field delay model in VieVS According to Petit & Luzum (2010), Sec. 10.3, Earth satellites are recommended to be analyzed in the GCRS rather than in the BCRS. Hence, the models mentioned above that evaluate delays in the BCRS are suitable for interplanetary spacecraft rather than for Earth satellites. Assuming that both observers and the signal source are situated in the neighborhood of the Earth enables to describe all ray propagation processes solely in the GCRS by applying the formalism described by Klioner (1991, Sec. 6). This model is valid for any source within a distance of 10^6 km from Earth and, therefore, highly suitable for VLBI satellite observations. Hence, this model was implemented in the module VIE_MOD in VieVS as described below.

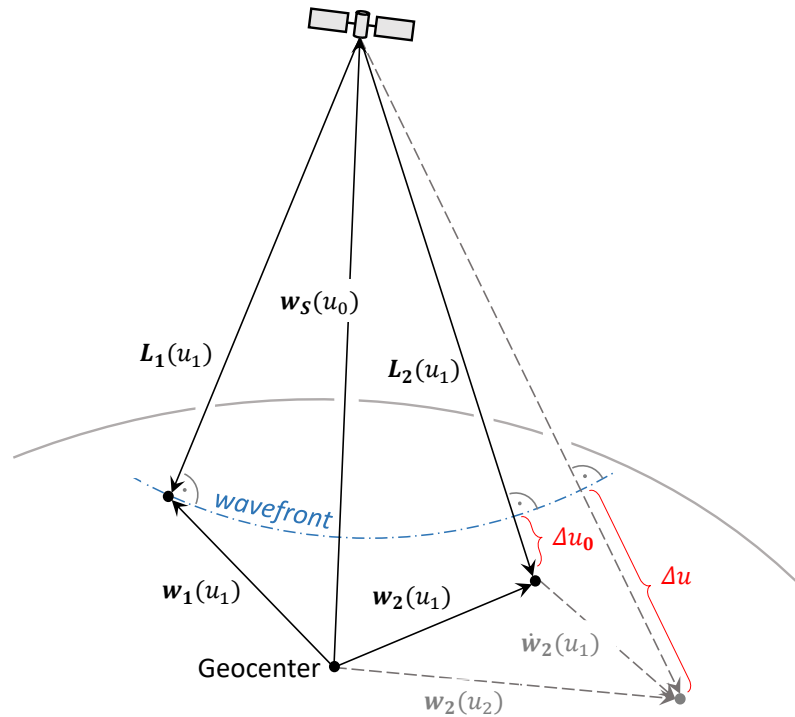


Figure 4.3: Delay model geometry according to Klioner (1991)

The geometric constellation for the model by Klioner (1991) is illustrated in Fig. 4.3. All time values u refer to the GCRS coordinate time (TCG) and all vectors \vec{w} represent CGRS spatial coordinates. The GCRS coordinate time delay Δu is calculated as the difference of the signal reception times u_2 and u_1 at station 1 and 2, respectively.

$$\Delta u = u_2 - u_1 = \Delta u_0 \left(1 - c^{-1} \frac{\vec{L}_2}{L_2} \cdot \dot{\vec{w}}_2(u_1)\right) + \Delta u_{gr} \quad (4.1)$$

The second term in Equ. 4.1 takes into account the retarded baseline effect (e.g. Thompson *et al.*, 2017) which is described by a linear movement of station 2 with the velocity $\dot{\vec{w}}_2(u_1)$ for the time span of Δu_0 . This effect may amount to 33 ns. Δu_0 represents the pure geometric delay derived from the distances between the satellite at the signal emission time u_0 ($\vec{w}_s(u_0)$) and the station i at the epoch u_1 ($\vec{w}_i(u_1)$).

$$\Delta u_0 = \frac{L_2 - L_1}{c} \quad \text{with} \quad L_i = \|\vec{L}_i\| \quad \text{and} \quad \vec{L}_i = \vec{w}_s(u_0) - \vec{w}_i(u_1) \quad (4.2)$$

The last term in Equ. 4.1 (Δu_{gr}) models relativistic effects caused by the Earth. The absolute value of this correction may amount up to 21 ps.

$$\Delta u_{gr} = \frac{2GM_E}{c^3} \ln \frac{(w_2 + w_s + \|\vec{w}_2 - \vec{w}_s\|)(w_1 + w_s - \|\vec{w}_1 - \vec{w}_s\|)}{(w_2 + w_s - \|\vec{w}_2 - \vec{w}_s\|)(w_1 + w_s + \|\vec{w}_1 - \vec{w}_s\|)} \quad (4.3)$$

$$\text{with} \quad \vec{w}_s = \vec{w}_s(u_0) \quad \text{and} \quad \vec{w}_i = \vec{w}_i(u_i)$$

The time of signal emission at the satellite u_0 is calculated iteratively by solving Equ. 4.4.

$$u_{0_{i+1}} = u_1 - c^{-1} \|\vec{w}_s(u_{0_i}) - \vec{w}_1(u_1)\| + c^{-2} (\vec{w}_s(u_{0_i}) - \vec{w}_1(u_1)) \dot{\vec{w}}_s(u_{0_i}) \quad (4.4)$$

In the first iteration u_{0_i} is set equal to u_1 . u_1 is defined in the VSO observation file as delay reference epoch, and is used as start value for u_{0_i} . For all upcoming iteration steps u_{0_i} is set to the result $u_{0_{i+1}}$ of the previous iteration. The iteration is stopped as soon as $\|u_{0_{i+1}} - u_{0_i}\|$ is smaller than a defined threshold, e.g. 1 ps. Equ. 4.1 and 4.3 are then evaluated using the final value for u_0 and $\vec{w}_s(u_0)$, respectively.

All above quantities scale to the GCRS and Δu is evaluated in the TCG frame. To evaluate the observed delay $\Delta \tau$ (proper time of the observer) Equ. 4.5 is used. τ_i denotes the reception time at station i .

$$\Delta \tau = \tau_2 - \tau_1 = \Delta u_0 \left(1 - c^{-1} \frac{\vec{L}_2}{L_2} \cdot \dot{\vec{w}}_2(u_1)\right) + \Delta u_{gr} - \frac{1}{c^2} \left\{ \frac{\dot{w}_2^2(u_1)}{2} + U_E(u_1, \vec{w}_2(u_1)) \right\} \Delta u_0 \quad (4.5)$$

The coefficient of Δu_0 in the last term of Equ. 4.5, with U_E being the gravitational potential of the Earth, is practically constant for Earth-based observers with a value of $-6.969290 \cdot 10^{-10}$. This

values corresponds to the constant L_G defined in IERS conventions (Petit & Luzum, 2010, Chap. 1.2) to scale between the Terrestrial Time (TT) and the Geocentric Coordinate Time (TCG), see Equ. 4.6.

$$\frac{dT T}{dT C G} = 1 - L_G \quad \text{with} \quad L_G = 6.969290134 \cdot 10^{-10} \quad (4.6)$$

Satellite orbit data in VieVS Satellite positions and velocities are required to evaluate the near-field delay model described above (\vec{w}_s and $\dot{\vec{w}}_s$, respectively). VieVS supports two file formats for orbit data: (1) the standard SP3 format¹, which is widely used for GNSS satellites, and (2) simple ASCII tables with time-tagged satellite positions and velocities in the terrestrial frame². Both formats contain orbit sampling points at reference epochs. To calculate accurate satellite positions and velocities between these sampling points, e.g. for the evaluation of Equ. 4.4, a 9th-order Lagrange interpolation is applied. Numerical differentiation of the positions is used to derive velocities in case they are not provided in the loaded orbit files.

4.2.1.4 Parameter Estimation

VIE_LSM, the estimation module in VieVS, fully supports the estimation of all geodetic standard parameters based on delays derived from satellite observations, analogous to observations of quasars. The observed minus computed residuals (O-C), required as input for the least squares adjustment, are calculated by subtracting the modeled near-field delay (see Sec. 4.2.1.3) from the according observed delay loaded from the VSO file.

Estimation of satellite positions As additional feature, the estimation of satellite positions was added. They are estimated in terms of piece-wise linear offsets (PWLO) w.r.t. the a priori orbit data in the satellite coordinate system (radial, along-track, cross-track). The partial derivatives are derived by differentiating the observation equation (Equ. 4.1) w.r.t. the GCRS satellite positions and by applying a subsequent rotation into the satellite coordinate system. Due to the fact that the term for the gravitation effects Δu_{gr} is comparatively small with absolute values less than 21 ps according to Klioner (1991), it was neglected for the derivation of the partial derivatives. Furthermore, the scaling between TCG and TT was neglected due to its rather small influence. Using the mathematical notation introduced in Sec. 4.2.1.3, the simplified observation equation can be written as

$$\Delta u = u_2 - u_1 = \Delta u_0 \left(1 - c^{-1} \frac{\vec{L}_2}{L_2} \cdot \dot{\vec{w}}_2(u_1) \right). \quad (4.7)$$

¹The SP3 format is described in <ftp://igs.org/pub/data/format/sp3c.txt>.

²See http://viewswiki.geo.tuwien.ac.at/doku.php?id=public:views_manual:data.

By differentiating Eq. 4.7 w.r.t. the GCRS satellite position \vec{w}_s , we get the expression for the partial derivatives in the GCRS shown in Eq. 4.8.

$$\frac{\partial \Delta u}{\partial \vec{w}_s} = \frac{1}{c} \left[\frac{\vec{L}_2}{L_2} - \frac{\vec{L}_1}{L_1} \right] - \frac{1}{c^2} \left[\dot{\vec{w}}_2 - \frac{\vec{L}_1}{L_1} \frac{1}{L_2} (\vec{L}_2 \cdot \dot{\vec{w}}_2) + L_1 \frac{\vec{L}_2}{L_2^3} (\vec{L}_2 \cdot \dot{\vec{w}}_2) - \frac{L_1}{L_2} \dot{\vec{w}}_2 \right] \quad (4.8)$$

Kinematic orbit modeling The estimation of three dimensional satellite positions (or offsets) as implemented in VieVS is referred to as kinematic orbit modeling approach. A kinematic modeling is a purely geometric approach without using any information on satellite dynamics, e.g. gravity field, or atmospheric drag (see e.g. Švehla & Rothacher, 2005). In VieVS the kinematic orbit is represented by three kinematic coordinates per epoch that are estimated in a least-squares adjustment based on VLBI delay observables. Compared to a dynamic orbit model, which is in principle based on the numerical integration of the equation of motion, a much denser network of globally distributed observatories covering the complete orbit arc would be required to derive reasonable estimates. However, for specific scenarios, e.g. to get first satellite position estimates in the commissioning phase of a new satellite, a kinematic orbit model might be suitable.

4.3 Scheduling Satellite Observations with VieVS

With the standard VLBI scheduling programs, such as SKED (Gipson, 2012) or SCHED (Walker, 2014), not being prepared to support satellites as observation targets routinely, preparing such schedules was quite labor and time intensive due the large amount of manual interactions required to prepare the observation plans and interchange files for controlling such experiments. In order to close this gap, VieVS was updated with a comprehensive suite of features to schedule VLBI satellite observations and to issue all required control and interchange files to control real experiments in a semi-automatic manner – similar to standard observations of quasars. The new features – hereinafter referred to as *VieVS satellite scheduling program* (Hellerschmied *et al.*, 2017b) – were implemented as add-on to the existing geodetic scheduling module of VieVS, VIE_SCHED (see Sec. 4.2). The integration in VIE_SCHED allows to seamlessly combining standard scheduling features for quasars, such as a geodetic-style scheduling with optimization of the sky coverage at stations, with the new features for scheduling satellite observations.

The VieVS satellite scheduling program comprises the following main features¹:

- Seamless combination of observations of satellites and quasars in a common VLBI schedule.
- Convenient user interface consisting of an updated VIE_SCHED GUI to define the initial session parameters, and an interactive text- and graphic-based scheduler interface to compile actual observation plans for satellite experiments.

¹The complete program reference manual is available at: http://viewswiki.geo.tuwien.ac.at/doku.php?id=public:views_manual:satellite_scheduling:satellite_scheduling.

- Manual ("scan by scan") and automatic scheduling modes are provided for assembling observation plans.
- Integrated satellite orbit determination based on NORAD Two-Line Elements (TLE).
- Features to easily maintain and update a local TLE orbit file database.
- Generation of statistics, plots, and schedule summaries.
- Creation of VEX-formatted schedule files that enable to control real VLBI satellite observations.

The program provides fully operational and tested scheduling features for VLBI satellite observations. Besides the actual creation of VLBI schedules, it also allows to easily check the available observation times for selected satellites prior to scheduling a session. This is useful to find suitable session times in the first place, in order to apply for observation time at the observatories.

4.3.1 Conditions for a Valid Scan

A major task of the scheduling program is to determine whether a satellite is observable for particular times with the defined observation configuration. In case of satellite observations, this task is more complex than for extra-galactic sources due to the framework conditions for near-field targets outlined in Sec. 3.3.1, and the resulting technical observation restrictions (see Sec. 3.3.2). In short, observations of satellites are highly dynamic and, hence, additional checks are required in order to ensure that the antennas are able to track the target properly. When observing natural sources with quasi static positions in the celestial sphere it is usually sufficient to check certain scan conditions, such the minimum Sun distance threshold, only once per scan. In case of satellite observations all scan conditions have to be rigorously checked throughout the whole scan duration, as the outcome of these checks may change within seconds due to the comparably large velocity of the observation target. In VieVS the following scan conditions are taken into account:

Common visibility: Common visibility of the target from at least one baseline is the fundamental condition for a valid scan. For visibility checks, the globally defined cut-off elevation, as well as horizon masks of antennas (if available in a catalog file) are considered.

Antenna slew rate limits: In order to ensure that the antennas are able to follow the satellite while data is recorded, the slew rate limits of both antenna axes must not be exceeded. As discussed in Sec. 3.3.2, the slew rates – mainly of large legacy antennas – may not be sufficient to track certain satellites. The slew rate requirements depend on various factors, such the orbit altitude, the local elevation angle at which the observations are carried out, and the antenna mount type.

Sun distance: To avoid signal corruption, or – in the worst case – even damage of the receiver hardware due to the strong radiation emitted by the sun, a minimum angular separation between the Sun and the observation target has to be kept.

Cable wrap: The cable wrap position of AzEl antennas (see Sec. 3.3.2) has to be tracked properly, in order to check whether an antenna reaches the cable wrap limits while slewing, and to enable the determination of slew times between consecutive scans. This is particularly important when observing satellites over longer tracks, as azimuth angles at the antennas may vastly change¹. Furthermore, it is important to start a satellite track in the correct cable wrap segment, enabling the antenna to steadily slew to the scan end position without reaching any motion limits.

4.3.2 Orbit Predictions

Predicted satellite orbits are required at two stages in the scheduling and observation scheme: (1) for the observation planning, which is carried out up to weeks before the actual session is observed, and (2) to calculate antenna pointing data for tracking the satellite during the session. The accuracy requirements on the orbits used for scheduling are not that critical, because they are mainly used to determine the scan times, and to check the scan conditions (a scan is not completely lost, if the observations starts 1 sec before the satellite is actually visible). The orbit data used for tracking, on the other hand, have to be accurate enough to allow a proper tracking, i.e. to keep the satellite accurately within the antenna’s field of view during observations.

Basically, orbit predictions are provided by various institutions, in different data and file types, and for different satellite constellations. Well known resources for orbit predictions are SP3 files (Standard Product 3), e.g. provided by the International GNSS Service (IGS; Dow *et al.*, 2009) for GPS satellites, CPF files (Consolidated Prediction Format; Rinklefs, 2006) provided by the International Laser Ranging Service (ILRS; Gurtner *et al.*, 2005), and Two-Line Elements (TLE) provided by the North American Aerospace Defense Command (NORAD).

The IGS provides different GNSS orbit products in terms of SP3 files². However, only the ultra-rapid solutions for GPS satellites that are released four times a day contain predicted orbits, and only for a couple of hours into the future. This tremendously limits their applicability for the observation planning, which is usually done days or weeks prior to session start.

The ILRS provides orbit predictions in terms of CPF files, which are routinely used for satellite tracking with the SLR telescopes. Each CPF file contains several days worth of orbit data for a specific satellite, usually with predictions for four days after the release date. This permits the integration of satellite positions well past the epoch of the last file entry, and enables the use

¹For example, the APOD-A nano satellite (LEO) crosses the local sky at a station in under 10 min, yielding a change in azimuth angle of up to 180° in that time. The local pointing angles for observations of extra-galactic sources do not change more than 15° per hour due to Earth rotation.

²The SP3c format is described at <ftp://igs.org/pub/data/format/sp3c.txt>. IGS products are available at <http://www.igs.org/products>.

for observation scheduling (with limited accuracy requirements) up to several months into the future. Nevertheless, CPF data is only available for satellites that are part of the current ILRS observation program¹, strongly limiting the selection of potential observation targets for VLBI.

Propagation of Two-Line Elements in VieVS Due to the limitations in terms of data availability and prediction periods of other orbit data types, TLE data are used for orbit predictions in VieVS. Contrary to SP3 and CPF files, which basically contain time sequences of discrete satellite positions (and velocities) in Cartesian coordinates, enabling numerical orbit integrations, TLE data consist of mean Keplerian orbital element sets plus additional parameters for modeling certain perturbing forces². TLE datasets generated by NORAD can directly be used to calculate satellite position and velocity vectors by applying designated analytical orbit models – so-called Simplified General Perturbation Models (SGP) – without time-consuming numerical integrations. Additionally to the primary attractive force due to gravitation of an idealized spherical Earth, non-gravitational perturbation forces (e.g. atmospheric drag) and gravitational forces (e.g. due to the equator bulge and the non-uniform density distribution of the Earth, and the attraction of Sun and Moon) are considered at modeling the motion of a satellite. To get accurate results it is absolutely necessary to use an SGP model that is compatible with the orbit model used to generate the TLE data, i.e. to use the SGP model that was applied to fit the TLE model parameters to the observations. Hoots & Roehrich (1980) define and describe the application of five slightly different SGP models. Further details are discussed by Vallado *et al.* (2006) and Vallado (2013).

In VieVS the SGP4 and the SDP4 models are implemented which are both compatible with NORAD TLE data (Hoots & Roehrich, 1980). SGP4 is the "near Earth" model for satellites with a round-trip time of less than 225 min (corresponding to an orbit altitude of about 6,000 km), whereas SDP4 is the "deep space" model used for all other objects. Both models differ in terms of the modeled perturbation influences that change with the orbit height.

When propagating TLE data the coordinate system of the results has to be considered properly. According to Vallado *et al.* (2006) the commonly accepted output coordinate system is an Earth Centered Inertial (ECI) system, which axes are aligned to the true equator and a mean equinox (TEME), realizing a system that is commonly referred to as ECI TEME. Vallado (2013) provides a detailed definition, along with the required transformation to obtain coordinates in the GCRS with reference epoch J2000.0. After applying the transformation into the geocentric J2000.0 system, the satellite coordinates and velocities are used by the VieVS satellite scheduling program to determine target visibilities, to calculate antennas pointing data, to check the scan conditions described in Sec. 4.3.1, etc.

Public NORAD TLEs are derived from radar and optical observations of the US Space Surveillance Network (SSN), with the major advantage, that daily updated datasets are available at no

¹The current ILRS missions are listed at https://ilrs.cddis.eosdis.nasa.gov/missions/satellite_missions/current_missions/index.html.

²The TLE format is described at https://spaceflight.nasa.gov/realdata/sightings/SSapplications/Post/JavaSSOP/SSOP_Help/tle_def.html.

charge for thousands of space objects via web services¹. This provides a great flexibility in the selection of observation targets, as TLE data is available for virtually all Earth satellites.

In general it is difficult, if not impossible, to make a qualified statement on the accuracy of TLE-derived satellite positions, as the provider (in general NORAD) does not provide any statistical information on that. The feasibility to track GNSS satellites based on TLE was shown in numerous experiments (basically all GNSS observations in Tab. A.1 were observed with stepwise tracking based on TLE data). However, it is questionable, if the TLE accuracy is sufficient for more challenging tracking tasks, e.g. when tracking satellites in an extremely low orbit at high elevations. However, this always depends also on the tracking scheme, and the local implementations at the stations.

An alternative to standard TLE data derived from SSN observation data are so-called *supplement TLEs*². They have the standard TLE format, but are derived from other orbit predictions directly provided by the satellite operators, e.g. from the GPS almanac data or from the GLONASS rapid ephemeris solutions. Supplement TLE data are also derived from the latest CPF data provided by the ILRS. Hence, ILRS predictions can indirectly be used for orbit predictions in VieVS by using supplement TLEs. Presumably, supplement TLE data are more accurate and trustworthy than standard TLEs, as the data available from satellite owners/operators can be assumed to be more accurate than the uncooperative tracking data available from the SSN. Furthermore, information on the accuracy of the SGP model fit for each satellite is provided for each set of TLE data, indicating the number of required iterations and the final calculated RMS of the residuals.

In any case, the accuracy of TLE propagation degrade with the time since the data was issued, i.e. the TLE data that was issued right before the session delivers the most accurate results. Depending on the time between the generation of an observation schedule and the actual observations, it is recommended to update the schedules based on the most current TLEs shortly before a session. When updating the scan times in a schedule that was generated a few weeks ago based on the satellite visibility information derived from most recent TLE data, the scan start and end times may slightly change – usually a few seconds at most. Hence, updating the scan times based on the most recent ephemeris is not critical in most cases. The situation is different, if the antenna tracking data is based on TLE data, as the highest accuracy possible is desirable for this task in order to achieve an accurate pointing. Therefore, it is recommended to always save a generated schedule in the VieVS internal data structures, download the most recent TLEs, reload the schedule in VieVS shortly before the session starts (e.g. on the day before), recalculate the antenna pointing data (basically topocentric RaDec positions that are written to the VEX file enabling stepwise satellite tracking, see Sec. 3.4.1), and rewrite the station dependent VEX files which will be used to control the antenna motions. All required functions to follow these steps are available via the user interface of the VieVS satellite scheduling program.

¹Resources for NORAD TLE data are e.g. <https://www.celestrak.com/> and <https://www.space-track.org/>.

²Supplement TLEs are available at <http://www.celestrak.com/NORAD/elements/supplemental/>.

4.3.3 Scheduling Workflow

The basic scheduling setup has to be defined in the GUI of VIE_SCHED before program start. The user has to define the VLBI station network, select a TLE orbit file and a subset of satellites whose orbits are defined in there, set date and time for the session, and some general scheduling parameters, such as a global value for the cut-off elevation and the minimum Sun distance for observations. The most recent TLE data can be obtained easily from web services by using the integrated functions to maintain and update a local TLE library that is used for all orbit prediction tasks.

On program start, the required input data are loaded: Station coordinates are taken per default from the standard TRF files of VieVS (e.g. providing ITRF2014 coordinates). SKED catalog files (Vandenberg, 1997) provide all required VLBI antenna properties (e.g. slew rates, mount types, cable wrap limits, horizon masks, SEFD values, reflector diameters, etc.), information on the available receiver equipment at the stations, and also positions and flux values of natural radio sources. The observation setups for satellite observations (e.g. defining the observed frequencies, channel bandwidths, and the sampling) are loaded from VieVS-specific catalog files, which have to be set up properly prior to scheduling. All these information are either required for the scheduling task itself (e.g. to determine visibilities and scan lengths), or to define all setup parameters for the station equipment that are written to the VEX formatted scheduling files.

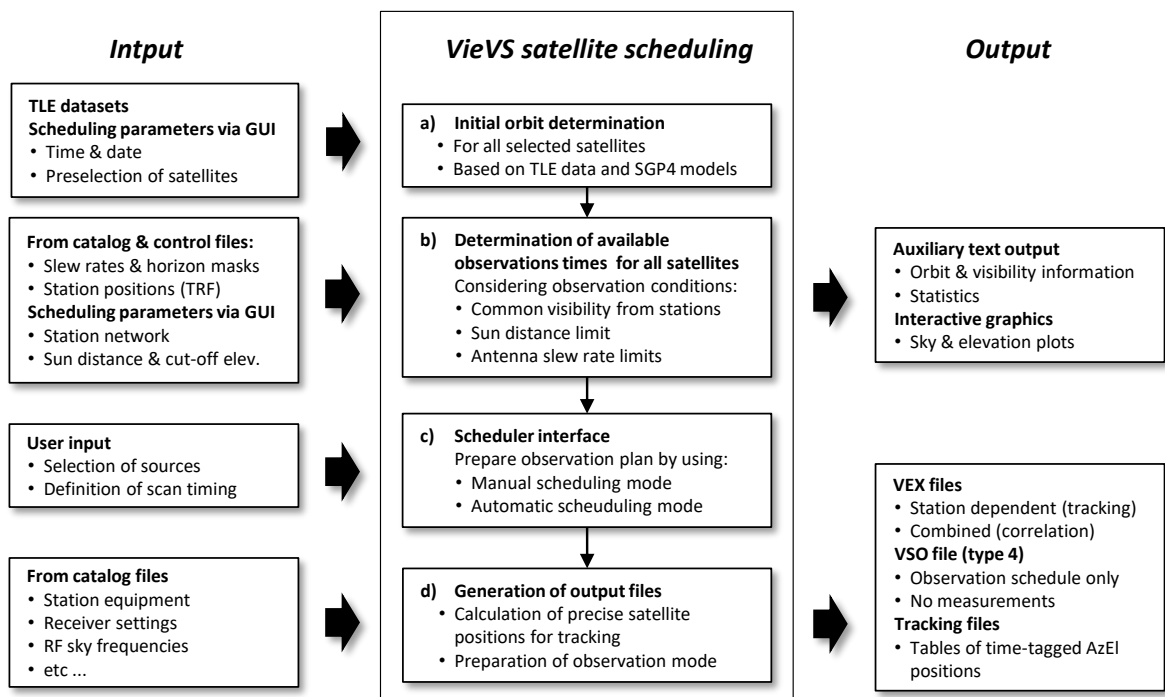


Figure 4.4: Workflow of the VieVS satellite scheduling program. The input data and user-specified input parameters are depicted on the left side. The actual processing steps are shown in the middle, and the program output on the right side.

The scheduling workflow is illustrated in Fig. 4.4. The left column shows all input data and

the user-defined input parameters. The processing steps are drawn in the middle, with their corresponding output is shown in the right column.

- a) Initial orbit determination:** In the initial processing step a dense time series of positions and velocities are calculated for all satellites that were selected in the GUI before, and for the whole session duration. The time-series interval is settable in the GUI. The orbit propagation is performed by using the allocated TLE data and the according analytical models (SGP, see Sec. 4.3.2). These position and velocity time series are internally stored and used as basis for all subsequent computations.
- b) Determination of available observations times for all satellites:** In the next step, the available observation times for all satellites are calculated, considering the conditions for valid satellite observations described in Sec. 4.3.1. Satellite visibilities are calculated for individual stations, and the common visibility from all stations (or a subset of stations) is evaluated. This information is then presented to the user in terms of auxiliary output in the form of descriptive text (in the MATLAB command window) and interactive graphics. Among other details, the text based output contains general information on satellite overpasses (e.g. events of highest local elevation), times series of topocentric antenna pointing angles plus rates (optional), and the exact timing of the available observation time windows. Examples for the auxiliary graphics are shown in Fig. 4.6 (sky plot) and in Fig 4.5 (elevation plot). The *elevation plot* illustrates the topocentric satellite elevations as a function of time for each station. This information is particularly valuable, as the fundamental condition whether a satellite is observable, depends on it being located above the defined cut-off elevation or the station's horizon mask, respectively. Beyond that, violations of the scan conditions, and the resulting valid observation times, are indicated. The bottommost subplot indicates the common visibility of the selected station network. The azimuthal directions and cable wrap positions are additionally indicated in corresponding *sky plots*.
- c) Scheduler interface:** The actual observation plan can be assembled via the text-based scheduler interface (in the MATLAB command window), and by applying the different scheduling modes (see Sec. 4.3.4) accessible from there. Besides the scheduling features this interface provides many convenient options, for example to load and save schedules, to change scans in existing schedules, to change the basic scheduling settings (e.g. remove or add stations of the current network), or to print statistics, and create plots. The elevation plot and the sky plots (examples in Fig. 4.5 and 4.6, respectively) have an interactive character. Hence, antenna pointing angles and cable wrap positions are indicated and updated, positions of satellites and natural sources are shown for the current scan time, and observation targets can be selected via mouse click on the corresponding icons in the sky plots.
- d) Generation of output files:** After the user finished assembling the desired observation plan by applying the functions in the scheduler interface, schedule files can be generated. Basically, schedule files are written in the current VEX format, comprising all information that

is needed to actually run a session, i.e. along with the observation timing and source positions, all setup parameters for the equipment of the participating antennas have to be defined. All receiver setup parameters are taken from (the initially loaded) catalog files, according to the selected observation mode. Basically, two types of VEX files can be written: (1) station dependent VEX files enabling a stepwise satellite tracking based on topocentric RaDec positions (see Sec. 3.4.1), and (2) combined VEX files required for the correlation with DiFX (see Sec. 4.5). Additionally to VEX files, the program is also able to write the observation plan to type 4 VSO files (see Sec. 4.2.1.1), which just contain the basic observation timing at all stations, required to generate the correlator input model for satellite observations, as outlined in Sec. 4.5.2. If satellites should be tracked by using dedicated tracking modes of the antennas (see Sec. 3.4.2), additional tracking files are required that describe the orbits of the observed satellites in some way. VieVS provides features to issue tracking files containing time-tagged satellite positions in specific formats, e.g. as used for tracking the APOD-A satellite described in Chap. 6. More details on the available output files are discussed in Sec. 4.3.5.

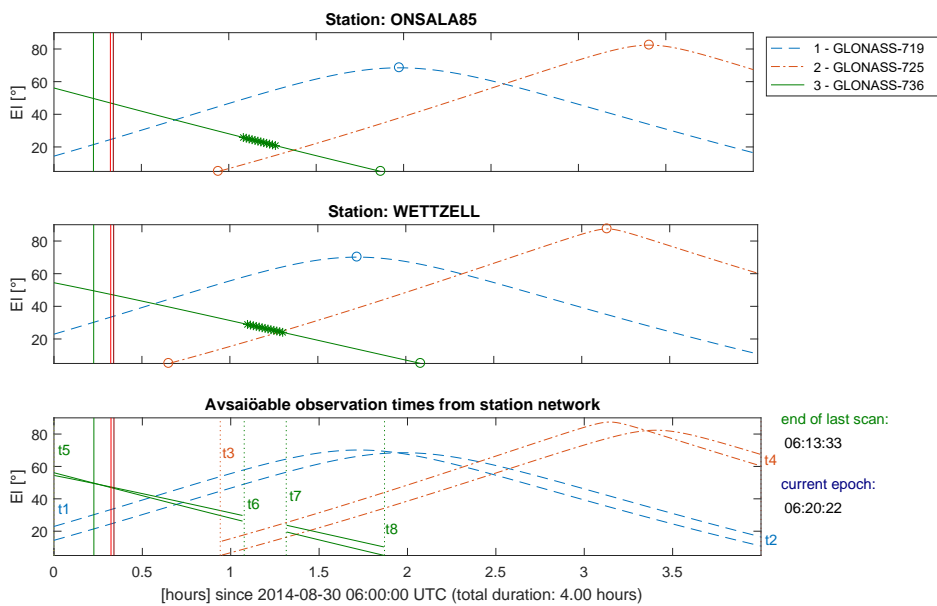


Figure 4.5: Elevation plot for station Wetzzell and Onsala85, showing the tracks of three GLONASS satellites from 6:00 to 10:00 UTC on 30 August, 2014. The *two upper plots* depict the local satellite elevation at both stations versus time. The cut-off elevation is 5° . The *highlighted section* of the track of GLONASS-736 tags a violation of the min. Sun distance condition that is set to 4° . The *bottommost subplot* summarizes the available observation times for all satellites (*vertical dotted lines and time tags t_i*) with common visibility from both stations. The end time of the last scan and the current scheduling time are indicated by *vertical solid lines* and in text form in *green and dark blue*, respectively.

4.3.4 Scheduling Modes

The VieVS satellite scheduling program provides different scheduling modes allowing the user to assemble observation plans with mixed observations of quasars and satellites. On program

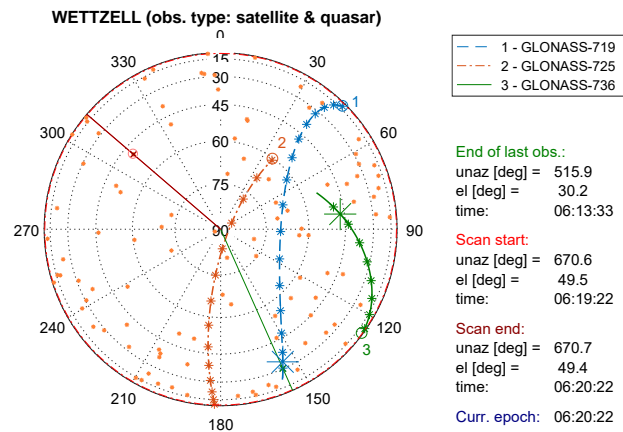


Figure 4.6: Sky plot for station Wetzell depicting the observation constellation described in the caption of Fig. 4.5. For the current scheduling epoch (06:20:22 UTC) positions of the satellites on their tracks (*large asterisks*), and positions of quasars (*orange dots*) are indicated. The antenna pointing positions (*unaz* depicts the cable wrap azimuth) are indicated for the end time of the last scan, and the start and end time of the currently added scan (of a quasar) by *text* and *pointers* in the sky plot, respectively.

start, a subset of sources, natural ones and satellites, are selected in the GUI as described above (Sec. 4.3.3). These sources are then considered when assembling the actual observation plan using the scheduling modes described hereinafter.

Manual scheduling mode When using the manual scheduling mode the schedule is assembled manually by selecting each observed source scan by scan. This mode is suitable for short test sessions, as the user maintains full control on source selection and the observation timing. In general, the program provides the following functions in order to arrange scans:

- Combination of quasar and satellite scans in a common schedule with the possibility to define different observation modes for different source types via catalog file entries.
- Automatic calculation of slew times between consecutive scans, considering the cable wrap of AzEl antennas. This allows for an automatic calculation of scan start times, based on the antenna positions at the end of the previous scan and the location of the new observation target.
- Automatic calculation of on-source time for natural sources, based on the target SNR, observation mode (number of channels, bandwidth, and bit resolution), antenna SEFD, and source flux (the mathematical implementation is described by Sun, 2013). For satellite scans the on-source time still has to be defined manually, because suitable information on the signal power level is missing anyway in most cases, which, in combination with the varying characteristics of modulated signals, prevents the application of currently applied approaches to calculate scan durations automatically.
- Definition of antenna sub-networks, i.e. exclude antennas from scans or predefined different station networks for quasar and satellite observations.

Based on these features, the user just has to select the sources that should be observed. Scan start and end times are determined automatically¹. There are different options to select a source, e.g. by entering the name of a related source tag, or by selecting a source with the mouse cursor in one of the sky plots. Interactive plots (sky plots and elevation plot) support the user in the source selection by depicting the current observation constellation.

Automatic scheduling mode Prompted by the aim to observe longer sessions of a few hours duration an automatic scheduling mode for combined observations of quasars and satellites was implemented, because a manual source selection would be too time intensive. The source selection is based on the station-based scheduling approach, as described by Sun (2013), optimizing for sky-coverage and, additionally, for a minimum time spent on slewing. The optimization can be applied equally for satellites and for quasars. Sub-netting options are also available. Following the simulations of Plank *et al.* (2016), investigating scheduling strategies for GNSS satellites, the combination of scans of satellites and quasars is implemented in terms of blocks with alternating source type, i.e. the user can define alternating blocks in a defined duration for a preselected list of satellites and quasars, respectively. This allows for example to schedule a sequence of 10 min blocks with quasar observations followed by 50 min blocks with observations of GNSS satellites, as applied for Sessions 126b, 131a, and 132a (see Sec. 5.3).

Combination of modes Both scheduling modes described above, manual and automatic, can be combined while setting up the schedule for a session, e.g. by using the automatic scheduling for 2 h, then manually add two scans to particular sources, and then switch back to the automatic mode. In addition, the program allows to add blocks of quasar scans that are scheduled with the standard geodetic and automatic source selection features of VIE_SCHED (station-based approach including all available scheduling options, see Sun *et al.*, 2014). This allows for example to first schedule a block of observations of strong quasars with sky coverage optimization (e.g. required for ZWD and clock estimation) with a total duration of 30 min, then add a few satellite tracks for the next 20 min using the manual scheduling mode, and in the end of the session add again a 1 h block of geodetic-style quasar scans. Such an observation sequence was implemented in the Sessions a332 observed in November 2016 with the AuScope VLBI array (see Sec. 6.3). This Session was basically set up as a concatenation of blocks with quasar observations optimizing for sky coverage, and in between scans of the APOD satellite whenever it was visible by at least two antennas. The result was a classical geodetic VLBI schedule, intersected by a couple of scans of APOD throughout the 24 h session duration.

¹Although all timing parameters may also be set manually.

4.3.5 Output Files

VieVS allows writing different output files enabling to run actual experiments, and to correlate and process the recorded data. The following files are supported:

Station dependent VEX files are used as station control files for VLBI satellite observations when satellites are tracked by applying a step-wise tracking approach (see Sec. 3.4.1). In addition to the receiver setup parameters, they directly contain the satellite ephemeris in terms of discrete topocentric RaDec positions, whereby each tracking point is defined as individual (astronomical) source. To take into account, that the topocentric source (satellite) coordinates differ between sites (see Sec. 3.3.1), individual "station dependent" VEX files are required for each antenna location, only containing station specific parameters¹. Before writing these files an intermediate step is required to calculate precise topocentric RaDec positions for all observed satellites. The calculations are based on the loaded TLE orbit data, accurate TRF station positions, and a complete implementation of the transformation between the celestial frame (of radio sources) and the terrestrial frame (of stations) according to the IERS conventions (Petit & Luzum, 2010). Precise EOP data provided by the IERS are used per default, as common in VieVS. For the implementation of stepwise tracking, the reposition interval is settable. The default value for tracking of GNSS satellites is 10 sec.

Combined VEX file are basically a merger of all station dependent VEX files in an experiment, comprising information on the observation modes of all antennas. Such VEX files are needed as input for the correlation of the recorded data with DiFX (see Sec. 4.5). The source positions of satellite targets are just dummy values (per default the topocentric RaDec values of the first antenna in the station list are used), as they are not needed for the correlation.

VSO files (type 4) contain the basic observation timing at all stations, i.e. a simple table of all baseline observations (see Sec. 4.2.1.1). They are required to generate the correlator input model for satellite observations as outlined in Sec. 4.5.2.

Tracking files depict text files containing a series of time-tagged satellite (or also quasar) positions that can be loaded directly by the antenna control unit (ACU) in order to track the target(s)². VieVS allows to accurately determine satellite tracking points in terms of azimuth and elevation positions based on TLE ephemeris data, or on tables of time-tagged TRF satellite positions³. Based on these tracking points it is possible to generate tracking files for the scheduled satellite observations. To issue tracking files in the required format,

¹As described in Sec. 2.2, VEX files used for standard VLBI sessions are usually not station dependent and contain a complete description of all observations at all participating stations, i.e. only one VEX file is required per session. Satellite observations are an exception, as the current VEX format provides no options to define site dependent source coordinates in terms of topocentric RaDec.

²Please note that the availability and accessibility of such tracking features are dependent on the antenna controllers used at the stations.

³See http://vievswiki.geo.tuwien.ac.at/doku.php?id=public:views_manual:data.

e.g. readable by the ACUs of the AuScope VLBI antennas (see Sec. 6.2.1), the file parser in VieVS has to be adopted accordingly.

4.3.6 Challenges

Considering the experience gained by scheduling numerous sessions over the last years with the VieVS satellite scheduling program (a list is shown in Tab. A.1), correctly defining all station setup parameters needed for writing proper VEX files, was identified as the main challenge. While even complex schedules with several hours of mixed observations of quasars and satellites could be created within a few hours, collecting the necessary information on the stations' equipment and capabilities was much more time consuming in most cases.

For standard geodetic VLBI observations in the S- and X-band (see Sec. 2.2) all required station setup parameters for the operationally applied observation modes (e.g. "GEOSX" for IVS R1 and R4 sessions) are defined in the SKED catalogs (Vandenberg, 1997) and can be taken from there. These modes are well proven and tested. However, satellites are not operationally observed and suitable modes are not defined in the according catalogs per default – they still have to be defined prior to scheduling. In addition, other information, such as source fluxes in the L-band, are not available in the SKED catalogs, and have to be prepared and added before scheduling. When scheduling satellite observations, in many cases the user has to deal with different receiver systems and antennas (e.g. with L-band systems for observations of GNSS satellites) than typically used in geodetic VLBI. Hence, it is extremely important to contact the observatory staff prior to the actual observation planning in order to collect all required information. It is advisable to involve the observatory staff already at this early stage of session planning to clarify their technical and personnel possibilities. It is also recommended to consult the staff at the correlator prior to observations, to ask whether the data that will be recorded by using the selected observation mode can be correlated properly, or if parameters required for the correlation are missing in the interchange files. It has proven as good practice to create VEX files (with dummy observations) just for testing the desired observation mode prior to the actual scheduling, and to send them to the participating observatories and correlation facilities. Then, the observatory and correlator staff have the possibility to cross-check the files, and to report and adopt any shortcomings before the actual observation schedules are created.

Summarizing that, a close cooperation and a good communication with the involved observatories and correlators are key factors to successfully carry out such non-standard VLBI experiments.

4.4 Observations

The observation scheme for satellites, outlined in Fig. 4.7, is very similar to the standard VLBI observation procedure described in Sec. 2.2 and Fig. 2.2, respectively. The main difference is, that for satellite observations, station dependent VEX files (vex_i , see Sec. 4.3.5) are used to

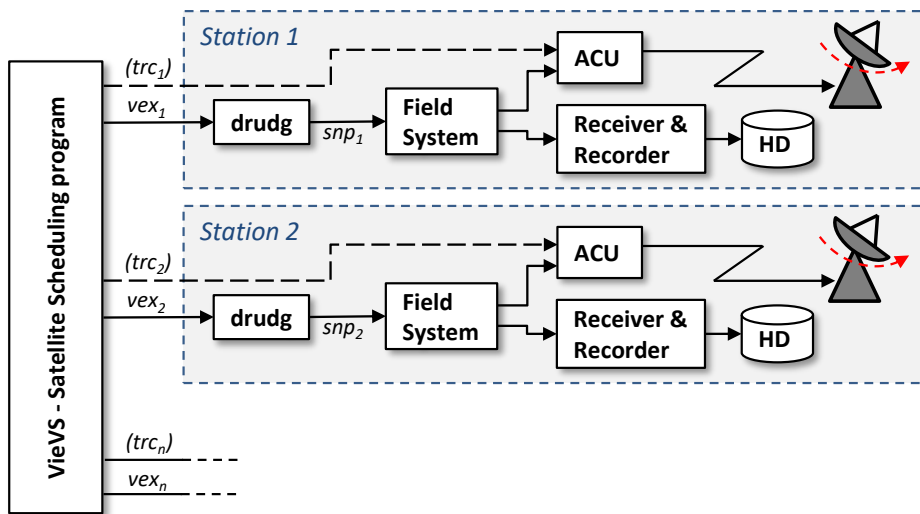


Figure 4.7: Observation scheme for satellites. Station dependent VEX files (vex_i) and optionally tracking files (trc_i) are prepared by the VieVS satellite scheduling program for each station i . The receiver and recorder equipment are controlled by using the standard procedures of the Field System based on the VEX schedules. The antenna motion is either controlled via the Field System and the VEX files enabling stepwise satellite tracking, or directly by dedicated ACU tracking modes and the loaded tracking files.

control the receiver and recorder equipment on the one hand, and to enabling stepwise satellite tracking on the other hand. The VEX files are processed with `drudg` at each station i to generate snap files (snp_i) containing the complete schedule of commands required to control the station equipment by using the Field System, i.e. the antenna motion via the ACU and the receiver and recorder.

Along with the VEX files, the VieVS satellite scheduling program optionally allows to write tracking files (trc_i), containing time-tagged AzEl positions as described in Sec. 4.3.5. On the condition that the ACU provides a dedicated tracking mode that is able to process such data, these files can be used to control the antenna motion in order to conduct satellite tracking directly by the ACU. It is not possible to give a general statement on how to enter or control such tracking modes, as this depends on the ACU capabilities and on the local implementations at the stations. Dependent on the local procedures it may be required to modify the snap file by adding specific commands for a satellite tracking mode controlled by the Field System (e.g. as described by Hellerschmied *et al.*, 2014), or to manually switch the tracking modes and load the tracking data directly at the ACU as described in Sec. 6.4 for satellite observations with the AuScope VLBI array.

4.5 Correlation

The distributed FX software correlator (DiFX; Deller *et al.*, 2011) was adopted for the correlation of VLBI observations of satellites. DiFX was initially developed for usage with the Australian Long Baseline Array (LBA) and is publicly available since 2007 (Deller *et al.*, 2007). Today, it is widely used to substitute outdated VLBI hardware correlators. DiFX depicts an FX-style correla-

tor (see e.g. Thompson *et al.*, 2017, and Romney, 1999) implemented in software and intended to run in multiprocessor computing environments, such as clusters of commodity machines of variable size, or specially designed high-performance computation clusters. The program runs on Linux and Mac OS X machines and the code written in C++ is accelerated by heavily using vector arithmetic libraries (in particular the Intel Performance Primitive library¹). The distribution across multiple computation nodes is enabled by using implementations of the Message Passing Interface (MPI). The correlation algorithm is very well suited to be implemented in parallel computing architectures due to its highly parallel nature. For more details on the software architecture the reader is referred to Deller *et al.* (2007) and Deller *et al.* (2011).

The application of DiFX for near-field VLBI observations of satellites is outlined in the next Section (4.5.1). In general, the only difference to classical applications², i.e. the correlation of astronomical sources situated in the far-field, is the correlator input model (IM). The IM contains geometric delay models to initially align the data streams of all telescopes before the actual correlation is started. Hence, for near-field observations, a suitable delay model has to be generated, as discussed in Sec. 4.5.2. Provided that the IM is set up accordingly, the correlator does not differentiate between near- and far-field observations.

4.5.1 DiFX Workflow

DiFX is a suite of software, consisting of the main correlator program (*mpifxcorr*), different auxiliary programs required to set up all input files for the correlation, and a huge variety for utilities for validation, monitoring, etc., to facilitate easy operations³. The correlation workflow for satellite observations using the DiFX core programs, in connection with VieVS being used for creating the near-field IM, is described in the next paragraphs according to Fig. 4.8.

Set up the DiFX control files The first step is to create the control files for (1) the main correlation program *mpifxcorr* (*.input*), and (2) for the program *calcif2* (*.calc*) that handles the creation of the correlator input model files (*.im*). More details on the IM are discussed in Sec. 4.5.2. Both files are created with the auxiliary program *vex2difx*, so that not further manual editing is necessary. *vex2difx* takes a combined VEX file (*.vex_{comb}*) that is written by the VieVS satellite scheduler (see Sec. 4.3.5) and the main DiFX configuration file (*.v2d*), and generates one or more pairs of *.input* and *.calc* files (usually one per scan).

The *.vex_{comb}* file contains a complete description of the experiment *as observed*, i.e. the schedule of scans, antenna and source properties, and the applied observation mode. Certain information that is not available prior to an experiment (e.g. EOP data or antenna clock offsets⁴) need

¹<https://software.intel.com/en-us/intel-ipp>

²How to run a standard correlation is outlined at https://www.atnf.csiro.au/vlbi/dokuwiki/doku.php/difx/difx_run.

³All DiFX programs and utilities are listed at <https://www.atnf.csiro.au/vlbi/dokuwiki/doku.php/difx/utils> and an up-to-date online documentation is available at <https://www.atnf.csiro.au/vlbi/dokuwiki/doku.php/difx/start>.

⁴DiFX allows to define clock models for each antenna w.r.t. a reference antenna in terms of offset and rate. Initial

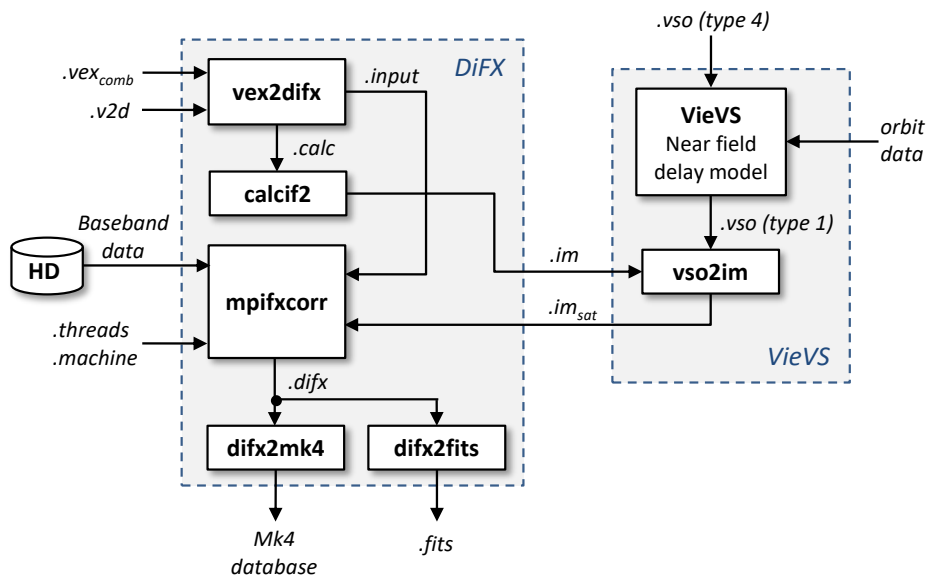


Figure 4.8: Correlation of satellite observations with DiFX.

to be provided to *vex2difx* some way. This can be either done by adding it to the *.vex_comb*, or the associated *.v2d* file¹. Hence, the *.v2d* files allow to add missing information, or even to override information in VEX files.

The *.v2d* file is the main configuration file for the correlation. It basically consists of a number of global parameters that affect the way that correlation jobs are created, and several sections that can be used to customize the correlation on a per-source, per-mode, or per-scan basis. Besides other settings, the location of baseband data on the file system is defined, the default global correlation setup (spectral resolution of the produced visibilities, integration time, etc.) can be changed, the selection of a sub-set of frequency bands or specific scans to correlate is available, or the application of a sub-channel frequency selection (referred to as "zoom mode", and applied for the APOD observations as described in Sec. 6.5) can be specified in the *.v2d* file.

Generate the correlator input model (IM) In order to cross-correlate data from a number of different antennas, the changing delays between those antennas have to be calculated, and used to align the recorded data streams at a predetermined point in space throughout the experiment (Deller *et al.*, 2007). This predetermined point in space is per definition the Geocenter. Therefore, the delays on virtual baselines connecting the antennas with the Geocenter are needed (here-

estimates of the station clock offsets are usually obtained by comparing the station clocks with GPS time. The standard procedure is to first correlate a few scans of strong calibrator sources distributed over the sessions time with the initial clock model, and then derive improved clock models based on the initial correlation results. Improved clock parameters (offset, rate) are usually determined through fringe fitting in AIPS or with HOPS, so that the residual delays become zero at the reference antenna. This is a standard procedure and shall not be further discussed here.

¹The EOP data can be added to \$EOP block in the VEX file, or to the EOP block in the *.v2d* file; antenna clock offsets to the \$CLOCK block in the VEX, or to the ANTENNA block in the *.v2d* file. However, it is good practice to add such additional information to the *.v2d* file and to leave the VEX file unchanged ("as observed").

inafter referred to as *geocentric delays*). Together with the clock model defined for each antenna in the *.v2d* file the data streams are then aligned during the correlator run time.

DiFX uses an installation of the program CALC¹, which is developed by the Goddard Space Flight Center (GSFC) and enables to calculate the required delays based on a priori EOP data, antenna and source coordinates, and analytical models to determine the effects of various geophysical influences. CALC is contained in the program *CalcServer* (part of DiFX) which is called via Remote Procedure Call (RPC) on request, enabling a flexible client/server architecture.

In DiFX the user does not interact directly with CALC or *CalcServer*, respectively. Instead, the program *calcif2* loads the *.calc* file created by *vex2difx* that contains all information to evaluate the delay model in CALC, i.e. information on antenna locations, source locations, scan timing (start times, durations, etc.), and EOP. *calcif2* connects via RPC to an instance of *CalcServer* to obtain modeled delays samples, converts them to delay polynomials (per default of degree 5 and in an interval of 120 sec), and writes the polynomial coefficients to the issued delay model file (*.im*). These delay polynomials can be easily evaluated for all required time epochs in the correlation process.

The *.im* files created that way contain models of geocentric delays for all observing antennas valid for sources in the far-field, e.g. for quasars, etc. – sources that are routinely observed with VLBI. To align the data streams of near-field observations, e.g. of Earth satellites, these delay models are not suitable due to the differences in the observation geometry as described in Sec. 3.3.1. Hence, dedicated near-field delay models have to be added to the *.im* files. Basically, there is more than one way to do that. For this work we replace the delay polynomial coefficients in the original *.im* files that were initially created with *calcif2* by using the standard delay model in CALC, with near-field delay models calculated in VieVS. This yields input model files suitable for satellite observations (*.im_{sat}*). The applied procedure is described in detail below in Sec. 4.5.2.

Run the correlator The correlation program *mpifxcorr* is started in an MPI environment (by using the MPI command *mpirun*) to enable the distribution of the processing workload over multiple CPUs. Additionally to the correlation input file (*.input*), which contains a complete definition of the correlation job, and the input model file (*.im_{sat}*), two more control files are needed that describe the computer infrastructure: the *.machines* and the *.threads* file.

The *.machines* file is used by *mpirun* to determine which machines will run *mpifxcorr*. It is a simple text file containing a list of computers (nodes) on which to spawn the software correlator process. The *.threads* file specifies how many threads to start by *mpifxcorr* on each processing node. Both files are typically created by the DiFX utility program *genmachines*.

The calculated visibilities are exported in a DiFX native format to directories with the extension *.difx*.

¹See https://vlbi.gsfc.nasa.gov/software_calc_solve.htm. The current version of DiFX (2.4.1) uses an installation of CALC9.

Convert output format To further use and process the binary DiFX output visibilities (*.difx*) they need to be converted from the DiFX native format to other standard formats. DiFX provides two auxiliary programs to do so: *difx2mk4* to create *Mk4 databases*, and *difx2fits* to create FITS-formatted output files (*.fits*).

FITS is a versatile format readable by a number of program packages used to analyze radio interferometry data, e.g. the Astronomical Image Processing System (AIPS)¹ of the National Radio Astronomy Observatory (NRAO). The binary FITS format is widely supported due to publicly available libraries and, for instance, can directly be loaded in MATLAB, which provides convenient options for inspecting the visibility data.

For geodetic observations usually the specialized post-correlation processing software package HOPS² is used which is closely tied to the visibility data format produced by the Mark4 hardware correlator (Whitney *et al.*, 2004). The binary Mk4 databases³ created by *difx2mk4* can be directly loaded by HOPS.

4.5.2 Correlator Input Model for Satellites

To generate correlator input model files suitable for satellite observations (*.im_{sat}* in Fig. 4.8), the delay polynomial coefficients in the original *.im* files generated with *calcif2* are replaced. This procedure requires three steps: (1) calculation of a dense time series of geocentric near-field delays for all satellite observations in the session, (2) fitting polynomials to the modeled delays, and (3) replacing the original delay polynomial coefficients in the *.im* files with those derived from the near-field delays.

In the first step, the VSO type 4 file created by the VieVS satellite scheduling program (see Sec. 4.3.5) is loaded in VieVS by the module VIE_INIT. When creating this VSO file in VIE_SCHED, all scheduled observations are subdivided into a dense time series of dummy observations (per default in a 1 sec interval) and the baselines between stations are rearranged in order to yield baselines between the Geocenter and both stations⁴. When loading this VSO file in VieVS, the near-field delay model in VIE_MOD (see Sec. 4.2.1.3) is evaluated for these geocentric baselines and for all dummy observation epochs, yielding a dense time series of geocentric near-field delays covering all observation times. The modeled delays are then automatically added to the input VSO file, yielding the VSO type 1 file (observation schedule plus delays, see Sec. 4.2.1.1).

In the next step, the program *vso2im* (part of VieVS) loads the VSO type 1 file containing the modeled geocentric delays and the original *.im* file(s), and fits polynomials according to the specifications (polynomial degree and timing) in the *.im* files to the delay time series. Fig. 4.9 depicts the residuals between the delay sampling points and the evaluated polynomial representation of the same delays for Scan 168 in Session a332 (observation of the APOD satellite, see

¹<http://www.aips.nrao.edu/index.shtml>

²<https://www.haystack.mit.edu/tech/vlbi/hops.html>

³The Mark4 format is defined at https://www.haystack.mit.edu/tech/vlbi/hops/mk4_files.txt.

⁴For example, a 60 sec satellite track on the baseline between the stations A and B is divided into 60 dummy observations with a duration of 1 sec each on the baselines Geocenter-A and Geocenter-B, respectively.

Tab. A.1). For this scan, the input model consists of four polynomials valid for 30 sec each (vertical black lines indicate the polynomial durations). In most cases the residuals are on the level of 1 ps which is by far accurate enough to yield satisfying correlation results (assuming that the underlying delay sampling points are accurate enough).

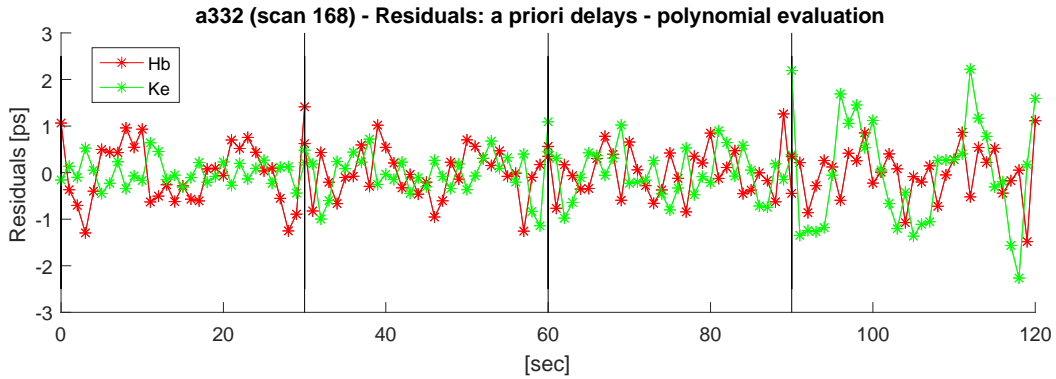


Figure 4.9: Residuals between the delay sampling points (modeled in VieVS) and the evaluated polynomial representation for Scan 168 in Session a332 (scan of the APOD-A nano satellite). The vertical black lines indicate the boundaries of the concatenated 5th-degree polynomials, each one valid for 30 sec.

In the last step, *vso2im* replaces the polynomial coefficients of the original *.im* files and writes corresponding files for satellite observations (*.im_{sat}*).

DiFX native support for modelling near-field delays Starting with DiFX version 2.5.1 an implementation of CALC 11 is available in DiFX through a program called *difxcalc* (Gordon *et al.*, 2016). In future, CalcServer (enabling CALC 9) should be phased out in favor of *difxcalc*. *Difxcalc* should improve the support of near-field observation in DiFX, as it is able to directly model near-field observation by applying different model options, namely the models by Sekido & Fukushima (2006), by Duev *et al.* (2012), and the satellite ranging model described in the IERS conventions (Petit & Luzum, 2010). The implementation of spacecraft positions is enabled via the SPICE toolkit¹ and by linking a SPICE ephemeris file in the *.v2d* file. Alternatively, spacecraft state vectors can manually be added to a dedicated SPACECRAFT section in the *.calc* file inserted to *difxcalc*².

A preliminary version of *difxcalc* (personally provided by D. Gordon from NVI, Inc.) was tested to correlate observations of the APOD-A nano satellites, which are introduced in Chap. 6. All three model options in *difxcalc* were tested in actual correlations and the results were compared with correlation results based on *.im_{sat}* files generated with VieVS (the same orbit data was used). By using the Sekido & Fukushima (2006) model in *difxcalc* we were not able to obtain fringes for most tracks. We got fringes by applying the Duev *et al.* (2012) model and the ranging model. However, the residual delay rates were much larger than those we found when

¹<https://naif.jpl.nasa.gov/naif/toolkit.html>

²More information on the correlation of near-field targets using *difxcalc* is available at <https://www.atnf.csiro.au/vlbi/dokuwiki/doku.php/difx/spacecraft>.

applying the input model by VieVS, indicating a worse consistency between these models and the observations. Therefore, and because difxcalc was still not fully supported by calc2if at that time (it could only be used as a stand-alone tool divorced from calcif2, not enabling all needed setup options), we stuck to the VieVS-generated *.im_{sat}* for correlating all experiments described in Chap. 5 and 6.

4.6 Post-correlation Processing

The main purpose of the post-correlation processing, as introduced in Sec. 2.2, is the determination of the actual observables, i.e. of (multi-band or single-band) group delays based on the visibilities (amplitude and phase samples) computed in the DiFX correlator. This is handled in the so-called fringe fitting process. The reason why fringe fitting is a necessary steps is, that the correlation is done using a specific model that incorporates information about source and station coordinates, time epochs, the frequency sequence, station clock parameters, EOP data, etc. Many of those model parameters contain significant errors that will result in non-zero residual delays and phases, varying in time. The task of fringe fitting is, to minimize those residual signals as far as possible by estimating corrections to the intermediate quantities of group delay and delay rate derived from the correlator input model. The estimated corrections are then recombined with the delay and delay rate of the input model in order to get total observables. The derived total values are relatively insensitive to modeling errors, i.e. slightly inaccurate assumptions in the input model are largely absorbed by the fringe fitting (Capallo, 2017).

The post-correlation processing is handled by the Haystack Observatory Postprocessing System (HOPS). Additionally to the fringe fitting program *fourfit*, which is standard in geodetic VLBI, HOPS provides a whole suite of software for editing, inspecting, and displaying data. *fourfit* carries out a two-stage fringe search to determine multi-band delay, single-band delay, and delay rate. In the first step, a search over a large 3-dimensional grid is carried out to find the single-band delay, multi-band delay, and delay rate values for which the coherent sum of all complex visibility points in the correlator output over time and frequency is maximized. In the second step, the previously determined value triple is refined by a 3-dimensions interpolation in the same volume, until the maximum of the correlation amplitude is found. For more details on the processing algorithms implemented by *fourfit* the author refers to Capallo (2017).

Post-correlation processing workflow The post-processing workflow is illustrated in Fig. 4.10. The basis for fringe fitting with HOPS/*fourfit* is an Mk4 database created by DiFX (*difx2mk4*). It consists of a root file (basically a flavor of VEX, describing how the information in the Mk4 data files originated), one or multiple correlator files (referred to as "type-1 files", containing the correlation lag data records for various modes), and one station file per antenna ("type-3 file") containing station specific information, such as model coefficients and phase calibration data.

fourfit loads the Mk4 database, and determines single-band, multi-band delays, and delay rates (including statistical data in terms of formal errors) by applying the grid search approach

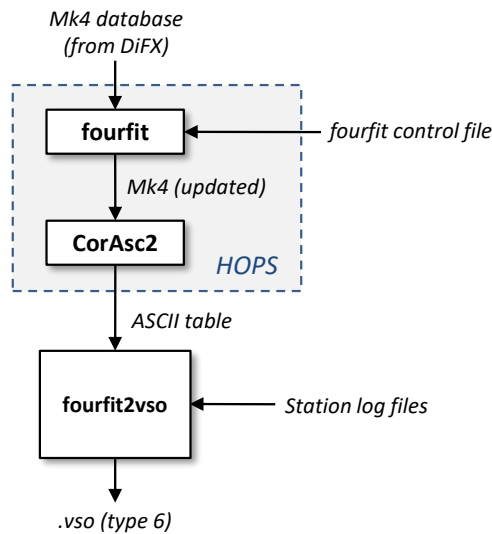


Figure 4.10: Post-correlation processing workflow. The HOPS programs *fourfit* and *CorAsc2* are used to fringe fit the correlator visibilities, and to write the derived group delays to an *ASCII table*. *fourfit2vso* converts the observables to the VieVS-readable VSO format and inserts meteorological measurements from the *station log files*.

described above according to the processing settings defined in the *fourfit control file*. The parameters in the control file allow, for example, to set the search window for multi-band and single-band delays, to manually select frequency bands for the multi-band delay computation, or to carry out fringe fitting only for a fraction of the total scan time. Hence, the latter option is very useful for satellites observations, as it enables to chop up long satellite tracks into a series of short scans, e.g. with a duration of 1 sec each. The strong satellite signals enable to use very short accumulation times in order to reach the target SNR. However, only scan durations equal to integer seconds are supported by *fourfit*. Therefore, other fringe fitting programs, such as the FRING task in AIPS, have to be used to calculate observables in sub-second intervals (an example is shown in Fig. 5.11). *fourfit* updates the initial Mk4 database by adding one or more binary fringe files (referred to as "type-2 files") containing records with the fringe fitting results. One type-2 file is generated per frequency band, baseline, and delay evaluation time (per default one per scan).

In the next step, the HOPS utility program *CorAsc2* is called via a Linux shell script to extract the data records needed for the further analysis and processing, and to export them to an *ASCII table*. The records of interest contain – among other useful information – the fringe reference time, SNR, reference frequency, and total values of the estimated delay and delay rate plus formal errors for each evaluated observation.

In the final step, the *ASCII table* containing the estimated observables is loaded along with the *station log files*¹ by the program *fourfit2vso*, which is coded in MATLAB. It extracts the required

¹Field System logs, containing a list of all executed snap commands in a session, along with status information of various station components, meteorological measurements, warnings, and error messages.

information, i.e. total delays plus formal errors and delay reference epochs from the ASCII table, meteorological measurements (pressure, temperature, and humidity) and cable calibrations from the station logs, interpolates the meteorologic data for the observation epochs, and writes the data to VSO type 6 files (see Sec. 4.2.1.1). Per default, one VSO file is created separately for each observed frequency band, e.g. individually for the results of S- and X-band observations.

The program also allows correcting for dispersive propagation effects of the ionosphere on the observed microwave signals based on observations in two frequency bands. First order effects are accounted for by calculating the ionosphere free linear combination according to Equ. 4.9 (Alizadeh *et al.*, 2013). The ionosphere free delays τ_{if} are determined as linear combination of the observed group delays in two bands (e.g. S and X), τ_{g1} and τ_{g2} , respectively. The factors c_1 and c_2 are functions of the effective frequencies of the observed baseband channels, f_{g1} and f_{g2} .

$$\begin{aligned}\tau_{if} &= c_1 \cdot \tau_{g1} - c_2 \cdot \tau_{g2} && \text{with} \\ c_1 &= \frac{f_{g1}^2}{f_{g1}^2 - f_{g2}^2} \\ c_2 &= \frac{f_{g2}^2}{f_{g1}^2 - f_{g2}^2}\end{aligned}\tag{4.9}$$

4.7 Analysis

The delay observables derived in the fringe fitting can be inserted in terms of VSO files to VieVS for data inspection and analysis. VieVS is introduced in Sec. 4.2 with a focus on specific features for satellite observations in Sec. 4.2.1. In general, satellite observations can be used analogously to observations of quasars for the calculation of delay residuals (O-C) in VIE_MOD, and the estimation of all geodetic standard parameters in VIE_LSM, such as station coordinates and EOP. All standard modeling options in VIE_MOD are available for both, quasar and satellite targets.

Examples for the analysis of satellite observation data in VieVS are presented in Sec. 5.7 and Sec. 6.7, for observations of GNSS satellites and the APOD-A nano satellite, respectively.

Chapter 5

VLBI Observations of GNSS Satellites

In this Chapter a series of VLBI observations of GNSS satellites is discussed that was conducted in a common effort by Technische Universität Wien (TU Wien, Austria) and the University of Tasmania (UTAS, Australia). All experiments were observed in the years 2015 and 2016, basically, by applying the observation and data processing schemes described in Chap. 4 – including all steps from scheduling to analysis.

Most experiments were carried out on a single baseline between the radio observatories at Ceduna and Hobart, which are both located in Australia. The observatory in Warkworth (New Zealand) joined final experiments in December 2016. The approach was to directly observe the modulated GNSS L-band signals by tracking the satellites with the VLBI antennas and recording the signals with the standard VLBI signal chains. In the subsequent processing, the digitized GNSS signals were treated like the noise emitted by natural sources – neglecting any modulations of the artificial signals. The goal was to compute group delays by cross-correlating the recorded baseband data, as common in geodetic VLBI. By applying this observation approach, the VLBI GNSS observations yielded results in terms of O-C residuals is on the level of a few ns.

5.1 Aims and Outline

A general discussion of VLBI observations of GNSS satellites – regarding scientific motivations, potential applications, and observation aspects – is presented in Sec. 3.2. The specific goal of the experiments described hereinafter was to establish and streamline all processes required to observe (GNSS) satellites with VLBI, including the experiment planning, tracking and observation schemes, correlation and post-correlation processing, and the final analysis of the derived group delay observables. Eventually, the accumulated experience resulted in the process chain described in Chap. 4. Another goal was to investigate the interaction between the unusual signals and the default VLBI station hardware, which is only possible in actual observation experiments.

After giving a brief overview of the observed sessions in Sec. 5.2, the experiment design and scheduling, including the first-time application of the automatic satellite scheduling features in VieVS, are discussed (Sec. 5.3). Our experience on using various standard VLBI hardware

and different recorder backends in connection with GNSS satellite signals are discussed in Sec. 5.4. The correlation using DiFX (Deller *et al.*, 2011) with a dedicated input model for near-field observations and the post-correlation processing are described in Sec. 5.5. The final analysis of the data in VieVS in a way common in geodetic VLBI is discussed in Sec. 5.7.

5.2 Overview of Experiments

Table 5.1: List of VLBI experiments with observations of GNSS satellites involving the antennas HOBART26 (Ho), CEDUNA (Cd), and WARK30M (Wa).

Exp. code	Stations	Date	Time (UT)	Targets	Comments
179a	Ho, Cd	June 2015		GPS, GLO, Q	Initial tracking tests
	Ho, Cd	28.06.15	18-20	GPS, GLO, Q	13 different satellites, changed sky frequency for each target
236a	Ho, Cd	24.08.15	12-16	GPS, Q	4 satellites repeatedly
238a	Ho, Cd	26.08.15	12-16	GPS, GLO, Q	5 satellites repeatedly
126b	Ho, Cd	05.05.16	17-23	GPS, Q	5 satellites repeatedly, DBBC in Ho
131a	Ho, Cd	10.05.16	17-23	GPS, Q	5 satellites repeatedly, DBBC + Mark4 at Ho
132a	Ho, Cd	11.05.16	17-23	GPS, Q	5 satellites repeatedly, Not observed due to high winds
328a	Wa	23.11.16		GPS	Initial tracking tests
g336	Ho, Cd, Wa	01.12.16	03-06	GPS, Q	4 satellites repeatedly

The experiments described in this Chapter were observed in the years 2015 and 2016, as listed in Tab. 5.1. Most observations were performed on a single baseline with two antennas owned by UTAS: the 26 m telescope at the Mt Pleasant observatory in Hobart (HOBART26, Tasmania) and the 30 m antenna in Ceduna (CEDUNA, South Australia; McCulloch *et al.*, 2005). The baseline indicated in Fig. 5.1 has a length of about 1700 km. Both antennas are equipped with L-band receivers and state-of-the-art receiver systems, as described in detail in Sec. 5.4.1. Initial (station by station) tracking tests were carried out in June 2015 to test the antennas' abilities to reliably track satellites in a stepwise fashion (see Sec. 3.4.1), to check the L-band receiver chains, and to ensure that the receivers are not saturated by the strong GNSS L-band signals. The first VLBI experiment with the experiment code 179a was observed on June 28, 2015. Within this 2 h session 13 different GPS and GLONASS satellites, along with quasars, were tracked. After 179a was successfully correlated, two further sessions (referred to as 236a and 238a, 4 h duration

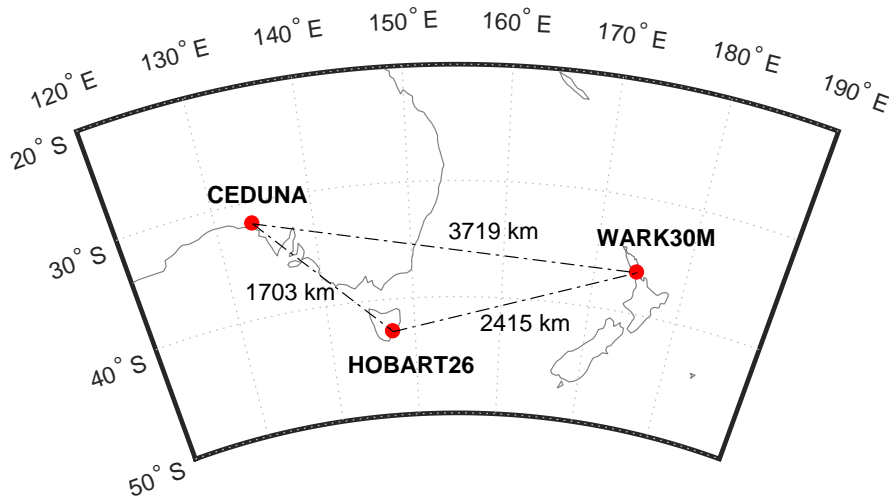


Figure 5.1: GNSS observations were performed with the antennas at Ceduna (CEDUNA), Hobart (HOBART26), and Warkworth (WARK30M).

each) were conducted in August 2015, using a changed observation mode and scheduling strategy (see Sec. 5.3 for more details). The results of these first experiments in 2015 are described by Hellerschmied *et al.* (2016). A final set of single baseline experiments with an extended duration of 6 h was scheduled for May 2016. Unfortunately, only the first two, 126b and 131a, could be observed. Experiment 132a was discontinued due to high winds. These sessions are described in detail by Plank *et al.* (2017a). The 30 m antenna in Warkworth (WARK30M; Petrov *et al.*, 2015), New Zealand (see Fig. 5.1), joined the station network in late 2016 enabling the first three station VLBI observations of GNSS satellites. After an initial single-station tracking test a final experiment including all three antennas was observed on December 1, 2016.

For the sake of brevity, the discussions in this Chapter mainly focus on the experiments observed in 2016, i.e. on Sessions 126b, 131a, and g336. The previous experiments are discussed by Hellerschmied *et al.* (2016).

5.3 Scheduling and Experiment Design

All experiments were scheduled with the VieVS satellite scheduling program introduced in Sec. 4.3. In the scheduling three types of output files were generated, as described in Sec. 4.3.5: (1) station dependent VEX files enabling stepwise satellite tracking, (2) a combined VEX file comprising the observation modes of all antennas needed for the correlation in DiFX, and (3) a VSO type 4 file describing the observation timing. The latter one is required for the computation of the near-field correlator input model (IM). For the orbit predictions (see Sec. 4.3.2) GPS and

GLONASS supplement TLE data¹ were used. These datasets were derived from the latest GPS almanac ephemerides and from the latest GLONASS rapid satellite ephemerides², respectively. In general, the initial scheduling was done one to three weeks before the sessions were observed to determine the scan times and target sequence. A final scheduling iteration was carried out the day before an experiment in order to recalculate the satellite tracking data (topocentric right ascension and declination) for the station dependent VEX files based on the most recent TLE data.

Scheduling summaries for all sessions listed in Tab. 5.1 are provided in App. B.1. They indicate the sequence of observation targets and the timing of the experiments.

5.3.1 Experiment Design

In the course of the experiment series listed in Tab. 5.1 various observation settings were applied and tested. The development of the experiment design is outlined in the following paragraphs.

Calibration sources Initial tests showed that it is helpful to observe at least a few scans of quasars along with satellites, evenly distributed over the session time, e.g. at session start and end, and once per hour in between. These scans can then be used to establish an accurate station clock model for the correlation (written to the DiFX control files and applied for both, satellite and quasar scans) by applying standard VLBI processing with DiFX and HOPS as common in geodetic VLBI (see Sec. 2.2 and 4.5.1 for more details). It is a good practice to select strong quasars with a high flux density of several Jy as *calibration sources*, as they most likely yield a high SNR and, hence, clear and strong fringe detections. In VieVS the SKED catalogs are used to get information on the sources' flux densities that are required for the determination of the on-source time needed to reach the specified target SNR. However, the SKED catalogs only provide fluxes for the S- and X-band. L-band fluxes are not included. Assuming a rather flat spectrum, S-band fluxes were used as rough estimate for the L-band. Of course, the preferable option would be to extend SKED's flux catalog with values for the L-band, which are publically available via dedicated online databases³. Practically, strong sources were selected with a flux density of at least 2 Jy in L-band and a flat spectrum in the microwave domain. The lower limit for the on-source times was manually set to 60 sec which is by far enough to yield a sufficiently high SNR. In most sessions the source 1921-293 was selected as calibrator, as it is widely visible in the Southern hemisphere and the spectral energy distribution (SED) indicates an extremely high flux density of about 10 Jy in L-band⁴.

First VLBI experiment: 179a In this initial 2 h VLBI experiment on the baseline Hobart-Ceduna ten different GNSS satellites were observed (six GPS and four GLONASS) in 13 scans of satellites.

¹Downloaded from <http://www.celestrak.com/NORAD/elements/supplemental/>.

²<ftp://ftp.glonass-iac.ru/MCC/PRODUCTS/>

³E.g. from the NASA/IPAC Extragalactic Database at <http://ned.ipac.caltech.edu/>.

⁴See [http://ned.ipac.caltech.edu/cgi-bin/datasearch?objname=\[HB89\]%201921-293](http://ned.ipac.caltech.edu/cgi-bin/datasearch?objname=[HB89]%201921-293).

A strong calibrator source (1921-293) was observed on session start, in the middle, and in the end (see schedule summary in List. B.1).

The experiment was scheduled by using the manual mode of the satellite scheduling program in VieVS (see Sec. 4.3.4), so that satellites are observed in tracks with 5 min duration each. While the antennas were repositioned every 10 sec in order to implement a stepwise tracking (see Sec. 3.4.1), the GNSS L-band signals were recorded continuously throughout the tracks. These 5 min tracks allow to derive multiple delay observables per track, commonly in an interval of 10 sec (see Sec. 5.6).

Digital baseband converters (DBBC) were used to down-convert and record the satellite signals at the stations (see Sec. 5.4.1). The DBBCs use the integrated automatic gain control (AGC) to adjust the internal signal gain to the power level of the received signals. As the observed GNSS satellite signals are several magnitudes stronger than the rather radio-silent cosmic background, the AGC system needs some time (in general several sec, depending on the signal strength) to properly adjust when initially steering the antenna from the empty sky to a radio-loud satellite. To take this AGC behavior into account the antennas were pointed at the nominal start positions of each satellite track about 1 min prior to the actual start of the recording. Hence, the satellite slowly entered the antenna beam, which gave the AGC enough time to smoothly adjust to the satellite's power level before the recording started. This additional AGC calibration phase prior to the actual track is shown in Fig. 3.7 that illustrates the received power level at station WARK30M in Experiment 328a. The received power slowly raised when the GPS satellite PRN 27 entered the beam, reaching the maximum amplitude after about 30 sec.

The observation mode was set up to record eight channels with 16 MHz bandwidth each by applying a 2 bit sampling: four channels where we only expected to get signals from quasars (lower band-edge sky frequencies at 1302.0 MHz, 1362.0 Hz, 1412.0 MHz, and 1482.0 MHz), and two channels dedicated to record the GNSS L1 and L2 signals. For GPS, where every satellite uses the same frequencies¹, these channels were centered at 1227.6 MHz and 1127.7 MHz (L2), and 1574.4 MHz and 1574.5 MHz (L1). In case of GLONASS the channel frequencies varied, depending on the corresponding sky frequency of the observed satellite², with the second channel offset by 0.1 MHz w.r.t. the first channel. The frequency offset of 0.1 MHz was added as a precaution due to expected problems with the Mark4 rack at Hobart.

4 h experiments in August 2015: 236a and 238a After investigating the data obtained in Experiment 179a, it turned out that re-observing the same satellites periodically within a session is useful due to several reasons: it helps to assess the quality of the a priori delay model, which in turn facilitates the interpretation of the residual delays in the analysis. Furthermore, periodical re-observations also help to reveal systematic features in the acquired data, e.g. whether observed delay offsets between channels are related to specific satellites. Therefore, all experiments after

¹The GPS L1 and L2 carrier frequencies are located at 1574.42 MHz and 1227.60 MHz, respectively.

²The GLONASS signal plan is available at http://www.navipedia.net/index.php/GLONASS_Signal_Plan.

179a aimed at observing a limited number of satellites (about five) several times within a session. Fig. 5.2 illustrates the satellite scans in Experiment 236a, in which four GPS satellites were repeatedly tracked for 5 min.

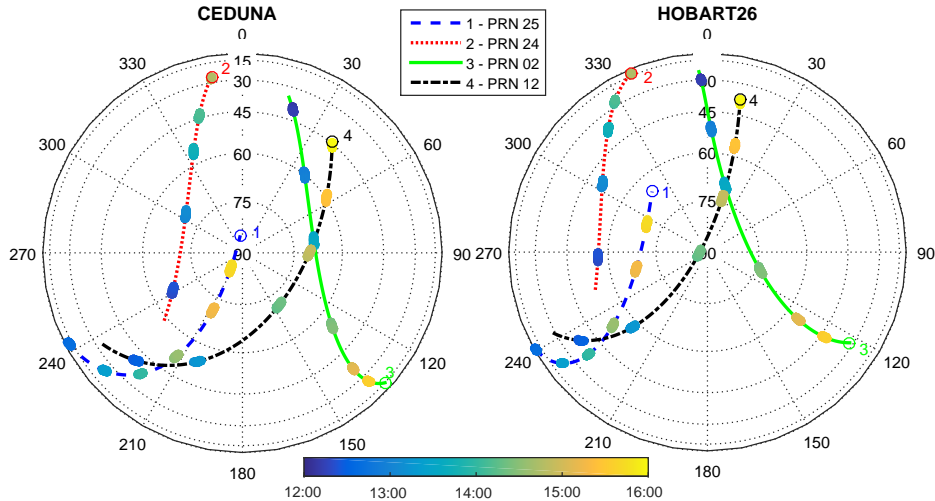


Figure 5.2: Sky plots for both stations in Experiment 236a observed on August 24, 2015 from 12:00 to 16:00 UTC (Hellerschmied *et al.*, 2016). The observation time is color-coded.

Studying the results of Experiment 179a we found significant delay offsets between the recorded channels that were different depending on the observed satellite. Furthermore, the Mark4 rack in Hobart showed frequency-dependent instrumental delays that could not be distinguished from geodetic signals without a proper calibration across the whole frequency band. In order to distinguish between instrumental, satellite-specific, and modeling effects, we used a fixed frequency setup for all subsequent experiments. This helped to identify the changes of the frequency selection in the backend (different sky frequencies were set for individual GPS and GLONASS satellites) as reason for the observed – seemingly satellite-dependent – channel offsets.

In the first 4 h experiment (236a) only GPS satellites were observed, while in the second one (238a) a mixture of GPS and GLONASS satellites was scheduled (see List. B.2 and B.3). To acquire the L1 and L2 signals of both, GPS and GLONASS satellites, 16 MHz wide channel centered at four sky frequencies were recorded: 1575.0 MHz and 1227.0 MHz for GPS, and 1602.0 MHz and 1246.0 MHz for GLONASS. Each of the four frequency bands was recorded twice, in two orthogonal linear polarizations (X and Y), in order to be able to reconstruct the circular polarized signals emitted by the satellites. Hence, in total eight baseband channels were recorded. The variation of the GLONASS L1 and L2 carrier frequencies is ± 4 MHz, so the signals are still in regions with flat bandpass response within the 16 MHz channels.

6 h experiments in May 2016: 126b, 131a, and 132a A final set of single baseline experiments with a duration of 6 h each was observed in May 2016. For the first time, the newly implemented automatic scheduling mode for combined observations of satellites and quasars was used (see Sec. 4.3.4 for a detailed description). The source list of all experiments consisted of five GPS

satellites (PRN 5, 2, 19, 24, and 12) and a selection of five to ten quasars with a high flux density of at least 2 Jy in the L-band domain. The scheduling strategy aimed at observing alternating blocks with quasar scans (for about 10 min) and with scans of the selected GPS satellites (about 50 min). The on-source times for quasars were set manually to 60 sec and the satellites were observed in terms of 5 min tracks. Schedule summaries are presented in the Listings B.4, B.5, and B.6 for the Sessions 126b, 131a, and 132a, respectively. The schedule of Session 126b is illustrated in Fig 5.3 showing sky plots for both stations.

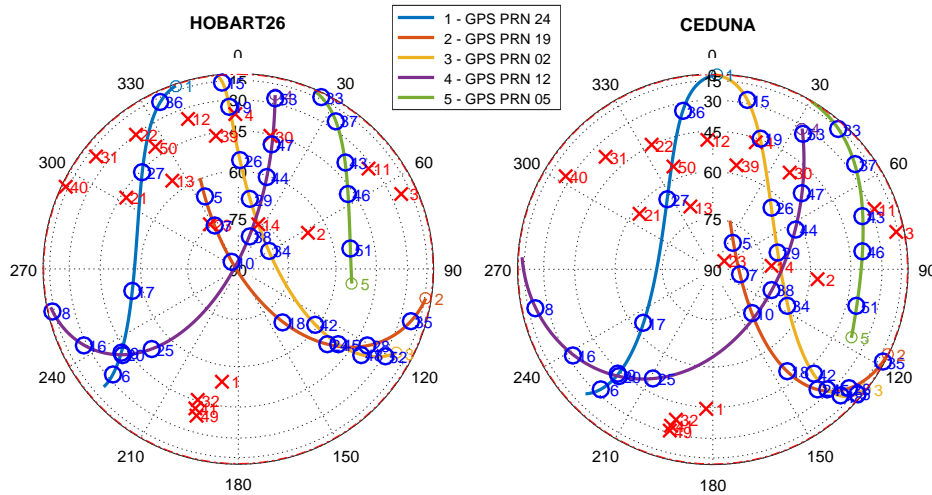


Figure 5.3: Sky plots for both stations in Experiment 126b observed on May 10, 2016 from 17:00 to 23:00 UTC. Red crosses and blue circles indicate scans to quasars and satellites, respectively. The scans numbers (53 in total) are indicated next to the markers.

The Sessions 131a and 132a were scheduled for the same time on two consecutive days. By using the same scheduling parameters in ViEVS and the same selection of sources, it was easily possible to reproduce the 131a schedule for the next day with the automatic scheduling mode. Hence, the 132a schedule contained the same source sequence as Session 131a. Such a constellation provides interesting possibilities to investigate the stability of our process scheme by comparing the observation results of the two sessions. Unfortunately, 132a could not be observed due to strong winds in Hobart.

At Hobart, where the data was recorded per default with a Mark4 rack and a Mark5A recorder (see Sec. 5.4.1), the observations in Sessions 126b and 131 were additionally recorded with the DBBC and Mark5B+ receiver system. The parallel recording allowed to compare the redundant data.

Although the GLONASS observations in the previous experiment were correlated successfully, we opted to only observe GPS satellites in this set of 6 h sessions. The fact that the L-band ranging signals are emitted at the same frequencies in case of GPS simplifies the interpretation of the observation results, as potential influences of changes in the carrier frequencies can be precluded. Due to the reasons outlined above, again a common observation mode with fixed sky frequencies was used for all observed sources. The applied observation mode is described in Sec.

5.4.2.

First 3 station experiment in December 2016: g336 On December 1, 2016, the first three station experiment was observed by the antennas at Hobart (HOBART26), at Ceduna (CEDUNA), and at Warkworth (WARK30M). In total four GPS satellites (PRN 2, 6, 19, and 24) were observed repeatedly in terms of 5 min tracks over the session duration of 3 h – similar to previous experiments. Additionally 1921-293 was observed for 10 min at session start and end, and at the transits (highest local elevation angle) at stations. Observations of the quasar at transits (largest change rates in the polarization) potentially enable a polarization calibration of the acquired data. To maintain full control on the observation timing, i.e. to schedule observations of the calibration source at transit times, the manual scheduling mode in VieVS was used. The station sky plots are shown in Fig. 5.4 and the scheduling summary is depicted in List. B.7.

The same observation mode (fixed sky frequencies) as used in the 6 h experiments observed in May 2016 was applied (see Sec. 5.4.2).

Another goal of this session was to test whether the AGC of the DBBC receiver systems caused periodic amplitude variations which were found when investigating the data of Sessions 126b and 131a (see Sec. 5.5.1). Therefore, the AGC units were manually deactivated at Ceduna and Hobart after the initial gain calibration prior to the start of each individual satellite track. This approach yielded constant gains over each 5 min track. At Warkworth the DBBC's AGC unit remained active in the default mode, so that the data recorded there could be used as reference.

5.4 Observations

5.4.1 Antenna Specifications

All described observations of GNSS L-band signals were carried out by the three antennas at Ceduna (CEDUNA, Cd), Hobart (HOBART26, Ho), and Warkworth (WARK30M, Wa). Their geographical locations are indicated in Fig. 5.1. Relevant specifications of the used antenna hardware and backends at all three sites are listed in Tab. 5.2.

The 30 m antennas in Ceduna and Warkworth were both initially built and used as satellite communication antennas, and were then converted to radio telescopes mainly used for radio astronomy, see McCulloch *et al.* (2005) and Woodburn *et al.* (2015), respectively. Both antennas have an azimuth-elevation mount. Hence, they are not able to track satellites through the local zenith due to the zenith-keyhole (see Sec. 3.3.2). HOBART26 is a XY-mount type antenna and has a main reflector with 26 m diameter. Due to the XY-mount HOBART26 is more suitable for satellite tracking, as the keyholes are located in the horizontal plane (see Sec. 3.3.2). Therefore, HOBART26 has full overhead tracking capabilities.

All three antennas are rather slow with maximum slew rates of $40^\circ/\text{min}$ (Ho, Cd) and $18^\circ/\text{min}$ (Wa) in both axes. However, due to the low slew rate requirements for tracking GNSS satellites, as discussed in Sec. 3.3.2, the antennas are still suitable for this study. The extremely slow

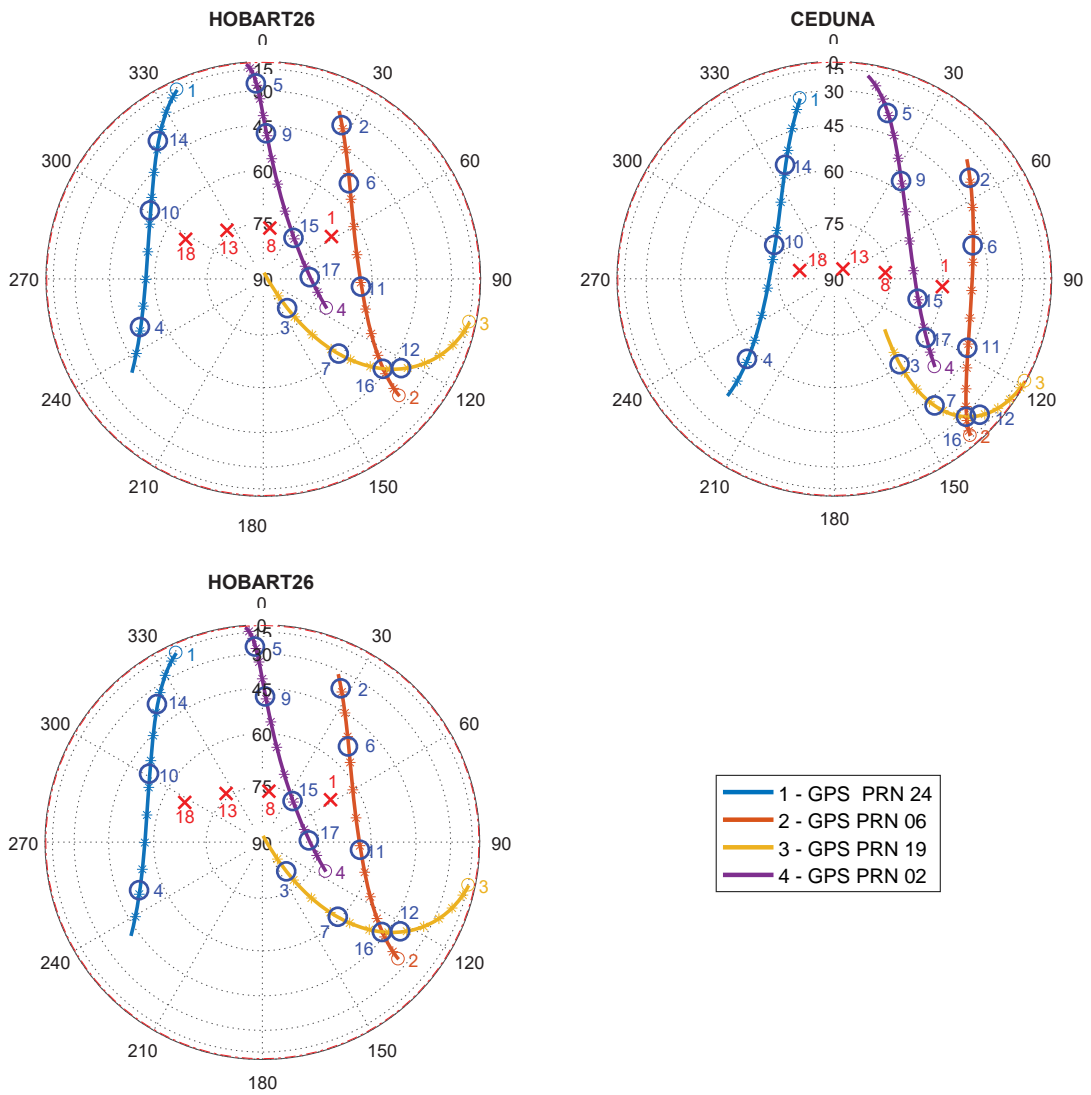


Figure 5.4: Sky plots for all three stations in Experiment g336 observed on December 1, 2016 from 3:30 to 6:30 UTC. Red crosses and blue circles indicate scans to the calibration source (1921-293) and GPS satellites, respectively. The scans numbers (18 in total) are indicated next to the markers.

Table 5.2: Station specifications for observations of L-band GNSS signals.

	Hobart	Ceduna	Warkworth
Station code	HOBART26	CEDUNA	WARK30M
2 letter code	Ho	Cd	Wa
<i>Antenna specifications</i>			
Diameter	26 m	30 m	30 m
Mount type	XY	AZEL	AZEL
Axis 1 slew rate	40°/min	40°/min	18°/min
Axis 2 slew rate	40°/min	40°/min	18°/min
<i>L-band receiver specifications</i>			
Nominal operating range	1.2 - 1.7 GHz	1.2 - 1.7 GHz	1.1 to 1.7 GHz
SEFD	450 Jy	1200 - 1600 Jy	14000 Jy
Polarization	linear (XY)	linear (XY)	linear (XY)
Sampler	DBBC-2, Mark4	DBBC-2	DBBC-2
DBBX control software	v104	v104	v105_1
Recorder	Mark5A, Mark5B+	Mark5C	Mark5B+
baseband data format	Mark4, Mark5B	Mark5B	Mark5B

accelerations can be considered as benefit regarding the stepwise satellite tracking approach (see Sec. 3.4.1) which was applied throughout all experiments. The low acceleration in combination with the large inertia of the antenna structures lead to a largely continuous antenna motion when applying a reposition interval of about 10 sec.

At Ceduna and Hobart the nominal operating ranges of the L-band receivers are between 1.2 and 1.7 GHz, and the sensitivities represented in terms of SEFD are about 450 Jy at Hobart and between 1200 and 1600 Jy at Ceduna. The receivers are tuned to perform best at ~ 1.4 GHz, near the 1420 MHz Hydrogen line. For astronomical purposes, where sensitivity is a limiting factor, the usable range is from ~ 1.4 GHz to 1.7 GHz¹, because the SEFD is about twice as high at 1.4 GHz than at 1.2 GHz. However, for the discussed satellite observations the receivers allow to observe down to 1.2 GHz as the SEFD is not a limitation given the strong signals. At Warkworth the nominal receiver range is between 1.1 GHz and 1.7 GHz with an SEFD of about 14000 Jy. Due to the strong satellite signals, the preset antenna sensitivities yield high SNR even with integration times as short as 1 sec (see Sec. 5.5.1).

The telescope backends at Hobart and Ceduna are equipped with quadrature hybrids that can be used to generate circular polarized signals. Unfortunately, when using the quadrature hybrids, the calibration is only valid for a narrow frequency range of about 30 MHz. This makes accurate calibration across the complete GNSS frequency range impossible, and would poten-

¹As noted at <http://auscope.phys.utas.edu.au/observatories.html>.

tially introduce frequency- and time-dependent elliptical polarization into correlation. To avoid that, we opted to bypass the quadrature hybrid and to directly record the two orthogonal linear polarizations – referred to as X and Y – with all antennas throughout all experiments.

5.4.2 Observation Mode

As outlined in Sec. 5.3.1, the experiment design and, hence, the observation mode – i.e. the selection of received, down-converted, sampled, and recorded frequency bands – changed throughout this experiment series. Throughout all sessions, eight baseband channels with a bandwidth of 16 MHz were recorded using a 2 bit sampling. Using the Mark4 rack and the Markt5A recorder (only at Hobart) the raw baseband data was recorded in the Mark4 native format. When using a DBBC in combination with a Mark5B/C recorder Mark5B-formatted raw data was recorded.

Due to the polarization characteristics of the used L-band receiver systems at Hobart and Ceduna, two linear and orthogonal polarizations were recorded. In principle, this should enable to reconstruct the circular polarized GNSS signals. However, the combination of the two linear polarizations turned out to be more problematic than initially estimated, see Sec. 5.6.

Investigations of the correlation results of Session 179a showed that changing the channel frequencies during an experiment caused significant delay offsets, especially when using the Mark4 rack at Hobart. Therefore, an observation mode with a static frequency setup was used for all following experiments. Due to the reasons described in Sec. 5.3.1 we opted to only observe GPS satellites in the last set of experiments in 2016 (126b, 131a, and g336). As shown in Tab. 5.3, eight 16 MHz channels were recorded, set on four different sky frequencies. Each frequency is recorded twice, in X and Y polarization, respectively. Channels 1 and 5 were centered on the GPS L2 carrier (1227 MHz), and channels 4 and 8 on the GPS L1 carrier (1575 MHz). Additionally, four channels at two frequencies in between (1376 and 1410 MHz) were recorded in order to achieve a better frequency coverage for the estimation of multi-band delays based on quasar observations. Hence, signals of quasars are expected in all eight channels, whereas GPS signals only in channels 1, 4, 5, and 8.

5.4.3 Tracking and Signal Acquisition

Tracking Throughout the observations (usually 5 min tracks) the satellites were tracked by applying a stepwise tracking approach, as outlined in Sec. 3.4.1. Therefore, station dependent VEX files were created with the VieVS satellite scheduling program containing satellite positions in terms of topocentric right ascension and declination in an interval of usually 10 sec, i.e. the antenna reposition interval was 10 sec. Only in Experiment g336 the reposition interval was set to 9 sec in order to clearly identify the cause for periodic variations in the received signal power as shown in Fig. 3.7. The amplitude variations could clearly be traced back to the stepwise antenna repositioning, because the periods of the amplitude variations exactly reflect the reposition

Table 5.3: Observation mode used for experiments 126b, 131a, and g336.

Channel num.	Label	Sky frequency ^a	Polarization	Bandwidth	Signal
1	L2 _x	1219 MHz	X	16 MHz	L2 GPS
2	Q1 _x	1376 MHz	X	16 MHz	Quasar
3	Q2 _x	1410 MHz	X	16 MHz	Quasar
4	L1 _x	1567 MHz	X	16 MHz	L1 GPS
5	L2 _y	1219 MHz	Y	16 MHz	L2 GPS
6	Q1 _y	1376 MHz	Y	16 MHz	Quasar
7	Q2 _y	1410 MHz	Y	16 MHz	Quasar
8	L1 _y	1567 MHz	Y	16 MHz	L1 GPS

^a Lower band edge frequency.

intervals of 9 sec and 10 sec, respectively. The effect of the periodic antenna repositioning on the amplitudes and the delay observables is further discussed in Sec. 5.5.1.

As an additional measure to ensure the timely execution of all snap commands in the local station control files (*snp_i* files loaded and processed by the Field System, see Sec. 4.4) the preob procedures¹ were turned off. When applying a stepwise tracking, individual scans are defined in the *snp* files for every single tracking point, i.e. in an interval of just 9 or 10 sec. With the preob procedures turned on, there would probably not be enough time to carry out all system checks and the antenna positioning commands in time, causing delays in the tracking, or at least a series of error messages by the Field System.

Apart from minor amplitude variations, the stepwise tracking worked well and was applicable for all three antennas. The tracking accuracy could also be confirmed by comparing the scheduled antenna positions with the actual antenna positions taken from antenna log files. The agreement was good with maximum deviations of about 0.1° (about a fifth of the beam-width in the L-band) in most scans.

In two tracks during the Experiments 126b and 131a that were observed at high local elevations CEDUNA could not keep up with the required motion speed in azimuth and lost the signal. Furthermore, CEDUNA was occasionally a bit late on source, although the delayed scan starts did not cause a significant loss of data. The reason for these minor tracking issues at CEDUNA can be attributed to slightly wrong slew rates in the catalog files used for scheduling and the neglect of the very low acceleration. Therefore, the slew times were estimated too optimistically at some occasions. This situation could be improved by a proper re-estimation of the actual antenna slew rates and accelerations, and by properly modeling the acceleration phase in the scheduling². Apart from these minor tracking issues at CEDUNA, there are several larger gaps in the data of

¹The pre-observation procedures – referred to as *preob* – include various system checks that are carried out prior to every scan in the observation schedule. This includes, for example, measurement of the system noise temperature t_{sys} . The preob time, which commonly has a duration of 10 sec, has to be taken into account in the scheduling.

²In the most up-to-date version of VieVS (version 3.1) the modeling of antenna accelerations is already included.

the Sessions 126b and 131a due to intermediate problems with CEDUNA's antenna drives and due to strong winds at both sites.

Observed signals Signals of natural radio sources, such as quasars, are usually so faint that they are covered by the thermal noise of the receivers and only become visible after accumulating the signal in the correlation process. Compared with these natural radio signals, artificial GNSS L-band signals are vastly stronger and can be directly visualized in real-time during the observations by using a customary spectrum analyzer attached to one of the intermediate frequency (IF) channels. Fig. 5.5 shows the L1 signal emitted by a GPS satellite during Experiment 179a, captured with a spectrum analyzer in the IF domain. The option to visualize the satellite signals in real-time was widely used for real-time checks during the observations, e.g. to check whether the antenna was pointing at the desired target in time. It was clearly visible when a satellite entered and left the antenna beam when switching between sources: the signal slowly gained strength during the 1 min pre-observation time (for calibrating the AGC in the DBBC, see Sec. 5.3.1), and then faded again. A spectrum analyzer was also used to initially check for signs of saturation of the receiver electronics, in particular of the low-noise amplifier (LNA) in the front end.



Figure 5.5: GPS L1 signal spectra observed in the Experiment 179a and visualized with a spectrum analyzer connected to an intermediate frequency (IF) channel in Hobart. The depicted IF spectra is down-converted from the RF domain using a local oscillator frequency of 1100 MHz.

In order to deal with the strong GPS L-band signals fixed attenuator settings were applied in the Mark4 rack at Hobart, which were confirmed to be valid in initial tracking tests. When using a DBBC (default at Ceduna and Warkworth) the implemented AGC was confirmed to be capable to adjust the signal gain properly during the scheduled calibration time (about one minute before the recording started, see 5.3.1).

The full GPS L1 and L2 signals with their main peaks (carrier tone) and side lobes were successfully acquired. Fig. 5.6 shows the auto-correlation spectra of three different GPS satellites recorded in Experiment 126b: PRN 12, 2, and 19. While PRN 2 and 19 belong to block IIR, PRN 12 is newer block IIR-M satellite. The L1 spectra are rather consistent for all three satellites and show a dominant peak at the frequency of 1575.42 MHz indicating the carrier peak of the

C/A code. The surrounding broadband signals depict the P(Y)-code (block IIR and block IIR-M) and the M-code (starting with block IIR-M). The L2 spectra show noticeable differences. While PRN 12 shows a strong peak, the other two only show the broadband signal. As reason for these differences the satellites' block types could be identified (e.g. Hegarty, 2017): The L2 signals of PRN 2 and 9 (block IIR) only consist of the P(Y)-code, while PRN 12 (block IIR-M) additionally transmits in the L2C-code and M-code. For comparison, the GPS L1 and L2 signal spectra of block IIR and IIR-M satellites are illustrated in Fig. 5.7.

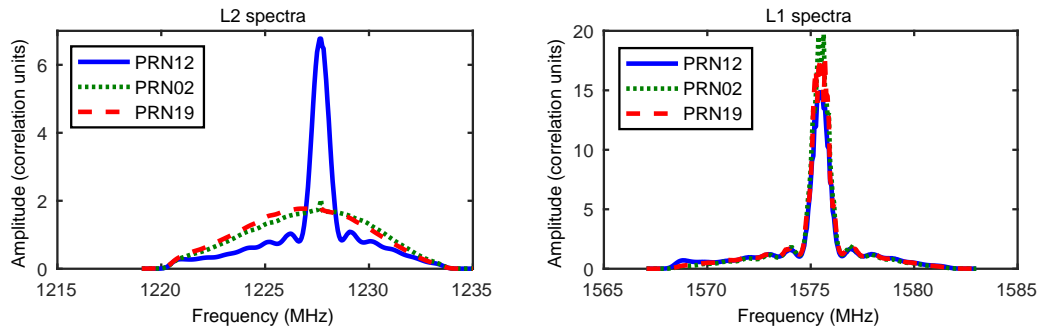


Figure 5.6: Auto-correlation spectra of three GPS satellites observed in Experiment 126b in L2 (left) and L1 (right). The amplitudes were normalized based on template spectra of quasar sources (Plank *et al.*, 2017a).

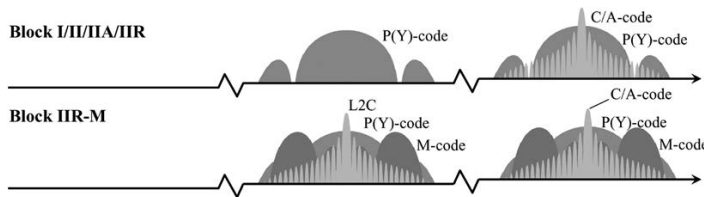


Figure 5.7: GPS L1 and L2 signal history (modified from Hegarty, 2017, p. 207).

For each 6 h experiment (126b and 131a) about 1 TB of baseband data was recorded per station. The recorded data was then sent to Hobart for the correlation and post-correlation processing that is described in the following sections.

5.5 Correlation

The recorded data was correlated by applying the correlation scheme for VLBI satellite observations described in Sec. 4.5. In short, the DiFX correlation software (Deller *et al.*, 2011) was used to process the baseband data recorded at the stations and to generate complex visibilities. Observations of quasars that were observed along with the GNSS satellites in all sessions were used for initial fringe fitting to establish accurate correlator clock models.

Suitable correlator input models (IM), providing modeled geocentric delays for the near-field observations, were created with VieVS (see Sec. 4.5.2). The delay modeling in VieVS was based

on highly accurate IGS final orbits, provided in terms of SP3 files. Geocentric delays were modeled in VieVS in an interval of 10 sec and written to a VSO (type 1) file. Then, 5th-order polynomials valid over 120 sec were fitted onto these data points using the function *vso2im* as described in Sec. 4.5.2. Fig. 5.8 depicts the residuals of the polynomial fit for Experiment g336, i.e. the differences between the delay sample points and the fitted 5th-order delay polynomial. In general, the residuals are on the sub-ps level, indicating an accurate fit.

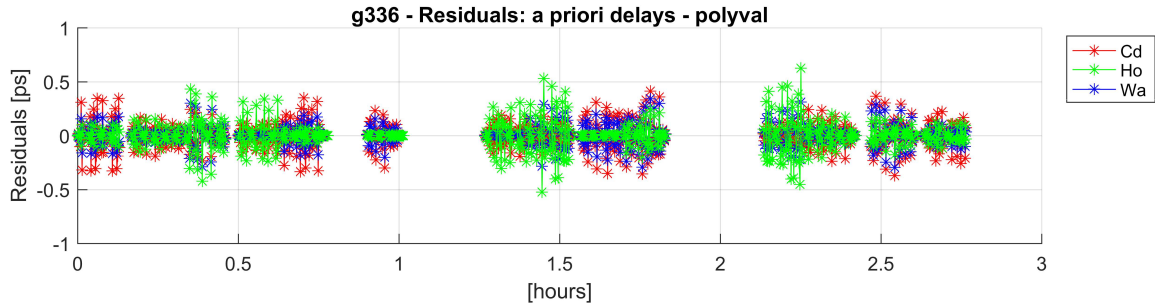


Figure 5.8: Residuals between the delay sampling points (modeled in VieVS) and the evaluated polynomial representation (5th-order polynomials valid over 120 sec) for Experiment g336.

Initial correlation tests were performed with DiFX version 2.4.1. The production correlations that produced all results discussed in this work were performed with the trunk version of DiFX from June 2016 (v7326). Primarily, the correlations were carried out on a small computation cluster (32 bit system) at the Mt Pleasant observatory in Hobart. For validation purposes, a subset of the observations was re-correlated in Vienna on the Vienna Scientific Cluster 3 (VSC3¹) where the same DiFX version was installed on a 64 bit system. Cross-checks showed that the correlation results were consistent.

Initial correlation tests were performed with a high spectra resolution of 7.8125 kHz and an integration time of 0.25 sec, enabling to deal with large residual delays and high delay rates. These investigations showed that the accuracy of the IM was sufficient to use a coarser spectral resolution. Hence, all subsequent (production) correlations were performed with bandwidths of 62.5 kHz (yielding 256 spectral channels per 16 MHz baseband channel) and a with integration times of 0.1 sec. The high temporal resolution enabled to investigate short timescale variations in the correlation results.

The GNSS signals were recorded in two orthogonal linear polarizations: X and Y. Correlation of the recorded baseband data yields in total four correlation products for auto- and cross-correlations, respectively: XX, XY, YX, and YY. Issues related to the linear polarized data are discussed in Sec. 5.6.1.

In general, the GNSS signals are staggeringly strong in the visibility data – typically, with correlation amplitudes of almost 100% for the L1-band, and above 50% for the L2-band. In comparison, strong quasars might yield correlation amplitudes of a few percent only. The baseband

¹<http://vsc.ac.at/systems/vsc-3/>

channels capturing the L2 signals with a lower band edge of 1219 MHz (see Tab. 5.3) are located near the lower frequency limit of the L-band receivers (about 1.2 GHz at Hobart and Ceduna) where the sensitivity is significantly lower compared to higher frequencies. Therefore, the correlation amplitudes of the L2 GNSS signals are less pronounced. The impacts on the fringe fitting is discussed in Sec. 5.6.

The visibilities computed in DiFX are then written to two output formats: (1) to fits files, required to investigate the correlation results in AIPS (see Sec. 5.5.1), and (2) to Mk4 databases used for the (production) post-correlation processing in HOPS/fourfit which is discussed in Sec. 5.6.

5.5.1 Correlation Results

Initial fringe fitting was performed with the FRING task in AIPS¹. In general, AIPS is a more flexible tool and provides more options to investigate the correlated data than the Haystack Post-processing System (HOPS²), which is the standard software package for post-correlation processing in geodetic VLBI. For example, it is not possible in fourfit (the fringe fitting program of HOPS) to define non-integer integration times³, i.e. the minimum integration time is 1 sec. For studying short timescale variations in the data the FRING task in AIPS was used, because it allows for setting sub-second integration times.

Typical cross-spectra Typical cross-correlation spectra for both GPS satellites and quasars are shown in Fig. 5.9 and 5.10 for the L1- and the L2-band, respectively. Basically, the extreme ends of the bandpass do not contain any signal (see *top panels*) and, therefore, do not contribute strongly towards the delay estimation. The GPS satellite, as well as the quasar, show continuous phases against frequency (*middle panels*), including the spread spectrum peak in the GPS L1 signal. The residual phases (*lower panels*) show some structure towards the outer edges of the bandpass. Nevertheless, there is a good agreement between the residual phases of both source types, which suggests that the large differences in the signal strength do not introduce any obvious systematics. A bandpass calibration has not been applied as it is not part of the processing in HOPS/fourfit (although it would be feasible in AIPS). The absence of any non-linearity in the response makes bandpass calibration a viable option for such observations.

Short timescale variations To investigate short timescale variations fringe fitting with a short integration time of 0.1 sec was performed with the FRING task in AIPS using the entire 16 MHz baseband channels. The result of the fringe fitting are residual delays with respect to the a priori delay model defined in the correlator input model (IM). In order to avoid confusion with the

¹<http://www.aips.nrao.edu/index.shtml>

²<https://www.haystack.mit.edu/tech/vlbi/hops.html>

³Referring to fringe fitting the term *integration time* denotes the period for which the delays and delay rates are fitted (usually the complete scan/on-source time in case of standard observations of quasars). This must not be confused with *integration time* with reference to correlation, where actually the accumulation period it meant.

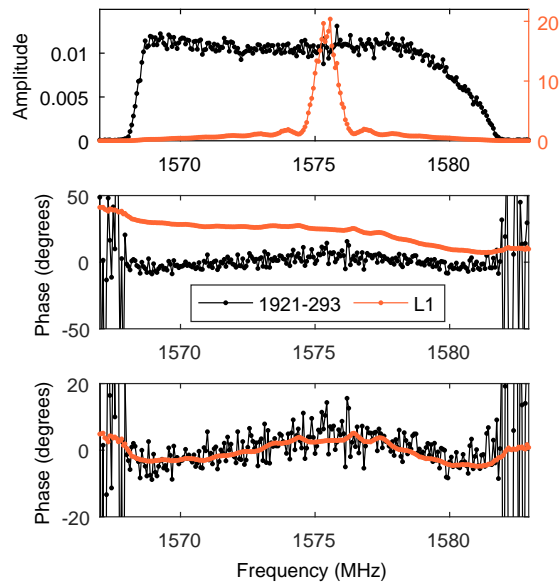


Figure 5.9: Typical GPS L1 cross-correlation spectrum recorded in Experiment 126b, averaged over one scan (10 sec for the GPS satellite and 60 sec for the quasar source). The amplitudes of the GPS source (*orange*, scale on the right) and the quasar (*black*, scale on the left) are shown in the *top panel*. The raw phase before fringe fitting (per scan), and the residual phase after the delay calibration are depicted in the *middle* and *bottom panel*, respectively. Although the residual bandpass phase shows some structure, mostly towards the band edges, there is a good overall agreement between the bandpass response of the satellite and the quasar (Plank *et al.*, 2017a).

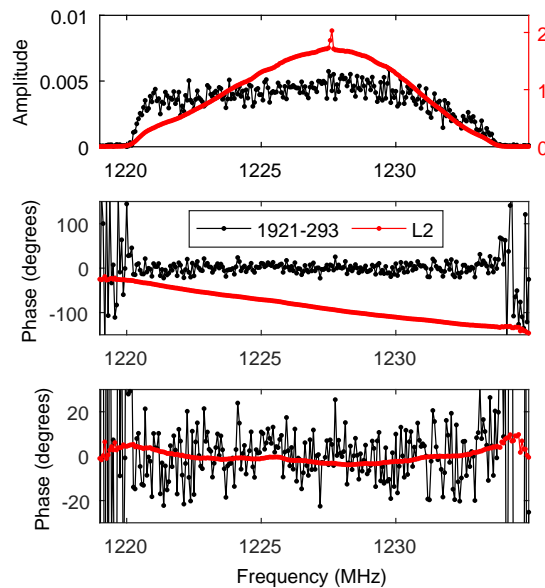


Figure 5.10: Same as Fig. 5.9 for the GPS L2-band (Plank *et al.*, 2017a).

(observed minus computed) residual delays discussed in Sec. 5.7, the residual delays of the fringe fitting are referred to as *fringe delays* hereinafter. The investigations revealed a number of rapid variations in the correlation amplitudes, as well as in the delays.

A prominent feature of the visibilities is a significant amplitude variation with a period of 2 sec. This can be seen in the auto-correlation, as well as in the cross-correlation spectra, as illustrated in Fig. 5.11 for Experiment 126b. The amplitudes show a clear bifurcation between two levels with transitions on integer-second boundaries. These variations are linked to the AGC systems within the DBBC that adjust the attenuation and sampling thresholds on a 1 sec timescale. The gain control system struggles to maintain an optimum sampling level and, hence, alternates periodically between two different gain levels. An initial indication, that these variations are linked to the gain control in the DBBC was the fact, that data recorded at Hobart using the analogue Mark4 rack with fixed attenuators (see Sec. 5.3.1) did not show this behavior.

In further consequence, the gain variations lead to variations in the fringe SNR (as illustrated in Fig. 5.11, *bottom panel*) and in the estimated single-band delays. The varying gain affects the relative amplitudes of different parts of the frequency spectrum, and emphasizes or de-emphasizes the central band of the recorded signals. The resulting "delay noise" can reach peak-to-peak amplitudes of up to 1 ns and is in general more pronounced in the L1-band where the central peak of the GPS signal is stronger. The influence of these gain variations on satellites of different GPS block types emitting different combinations of navigation signals (yielding more or less pronounced central transmission peaks as illustrated in Fig. 5.6 and 5.7) needs to be further investigated.

One possible option to mitigate the spurious delay variations linked to the DBBC's gain control system is to disable the AGC loops prior to start of the recordings. This was tested in Experiment g336 as previously outlined in Sec. 5.3.1. Before the recordings started at each satellite track, the AGC was manually deactivated at the stations HOBART26 and CEDUNA. For validation purposes the AGC remained active at WARK30M. The effect of this procedure is clearly visible in the auto-correlation spectra shown in Fig. 5.12 and 5.13 for WARK30M and HOBART26, respectively. While the gain, and therefore the signal amplitude, changes between different levels in an integer-second interval at WARK30M, they stay rather constant over time at HOBART26. Although the situation is improved by disabling the AGC, real variations in the power level will still cause gain errors and, hence, a non-optimal sampling. The amplitudes of these errors are expected to be on the same level as errors caused by the stepwise tracking scheme.

Another option to deal with the DBBC gain variations is to fringe fit only the peak channels of the signal spectrum. When doing so, relative amplitude differences between the peak channels and channel at the band edges should not play any role. However, initial tests did not yield satisfying results. Increasing the dynamic range of the receiver by sampling the data with an improved quantification, e.g. by using an 8 bit resolution instead of only 2 bit, should also reduce the compression effects from the strong transmitter tones. Unfortunately, this could not be tested, because the DBBCs at the stations were not prepared for such sampling modes at the time the

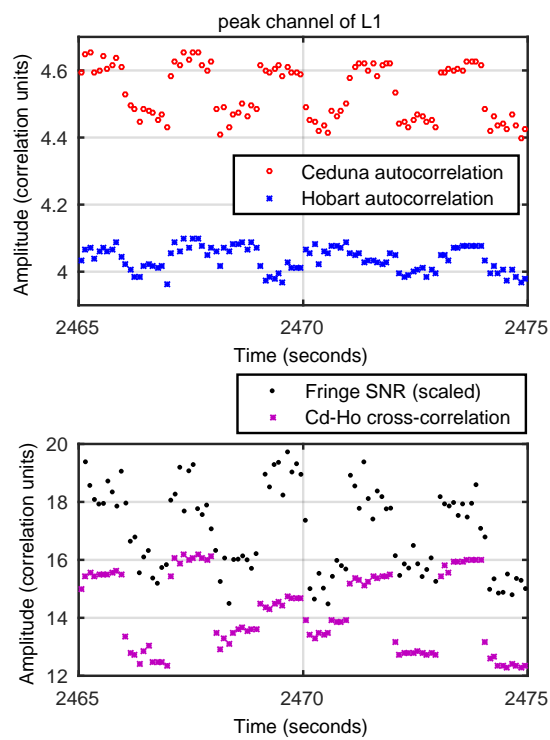


Figure 5.11: Gain variations of GPS L1 in Session 126b as visible in the auto-correlation (*top*) and the cross-correlation (*bottom*). The correlation amplitudes vary with a period of 2 sec, causing variations in the fringe SNR with the same period (Plank *et al.*, 2017a).

experiments were conducted.

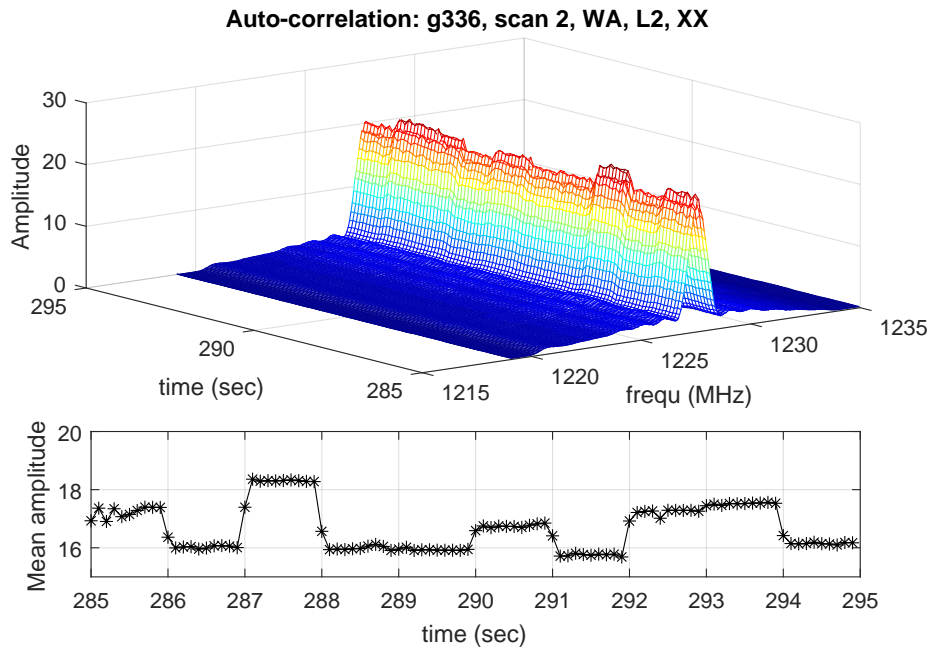


Figure 5.12: Auto-correlation amplitude of the L2 signal of GPS PRN 06 recorded at station WARK30M in Experiment g336. The *top panel* shows the auto-correlation amplitude of the full 16 MHz channel ($L2_x$) for the last 10 sec of scan 2, while the average of the peak-channels (center frequency ± 0.5 MHz) is depicted in the *bottom panel*. Amplitudes are represented in correlation units. The depicted auto-spectrum was computed with DiFX by applying the processes described in Sec. 4.5.1, exported to fits files, and plotted with MATLAB.

High temporal resolution also reveals the effect of the applied stepwise tracking (see Sec. 3.4.1). Both, the correlation amplitudes as well as the measured fringe delays show clear periodic variations with periods equal to the antenna reposition interval of 9 sec (in g336) and 10 sec (in all other sessions). Due to the relatively small angular offset between consecutive tracking points the amplitude variations are generally rather small amounting about 1% of the total amplitude. The resulting peak-to-peak variations in the measured high time resolution delays are significant with values typically between 40 and 400 ps. The amplitudes vary from track to track, and are in general less pronounced at low elevation angles. Presumably, also the accuracy of the TLE orbit data used to calculate the tracking points plays a role in this respect. Some of the largest variations experienced throughout all sessions are shown in Fig. 5.14 with a clearly visible period of 10 sec. Applying an integration time in the fringe fitting equal to (or longer than) the antenna reposition interval, we assume that the short timescale tracking effects largely cancel out. Tests confirmed, that fringe delays computed with an integration time of 10 sec neither show these spurious tracking signals, nor any obvious artifacts. Hence, 10 sec (9 sec for g336) integration times were used for the fringe fitting production runs described in Sec. 5.6.

However, given that the rapid fringe delay variations are linked to the antenna reposition

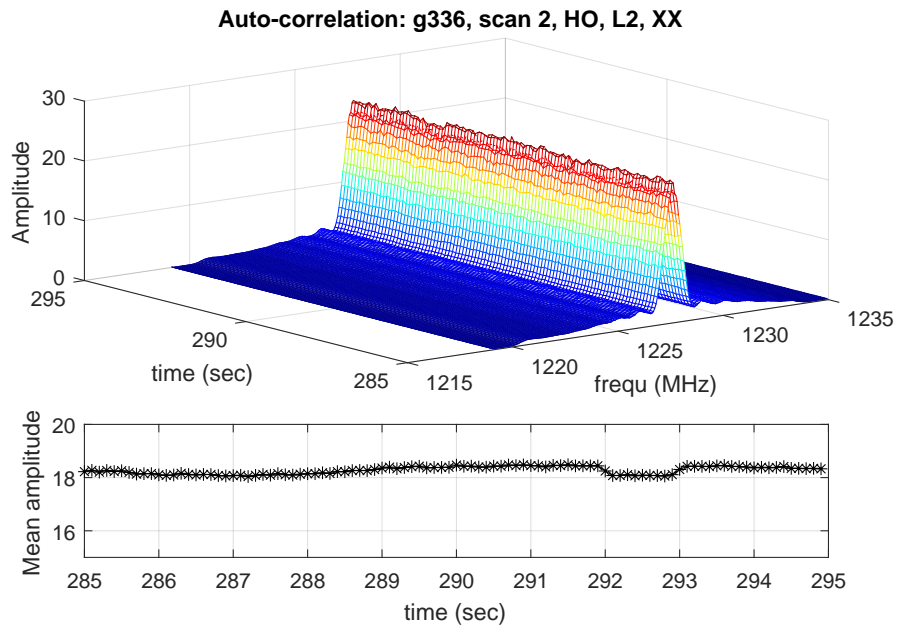


Figure 5.13: Same as Fig. 5.12 for station HOBART26.

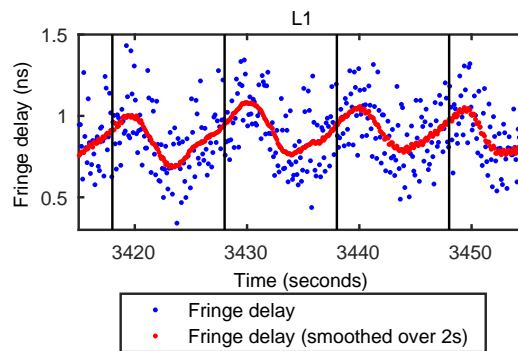


Figure 5.14: Fringe delays of the GPS L1 signal recorded in Experiment 126b. The data points with a high temporal resolution of 0.1 sec (*blue*), and a running mean using a 2 sec boxcar window (*red*) are shown. The antenna reposition times are indicated by *black vertical lines*. Variations with a period of 10 sec, equal to the antenna reposition interval, are clearly visible (Plank *et al.*, 2017a).

intervals of the stepwise tracking, a continuous tracking scheme (see Sec. 3.4.2) would be preferable in the future.

5.6 Post-Processing and Generation of Total Delays

While AIPS was used to initially investigate the visibilities computed with DiFX, HOPS was applied for the production post-correlation processing in order to derive the actual geodetic observables, i.e. group delays on baselines between stations of the Earth's surface at specific reference epochs. The advantage of the fourfit – the fringe fitting program of HOPS – compared to FRING/AIPS is, that it allows for computing total (baseline) delays¹ in the geodetic sense, namely, referenced to the signal reception at the first station at integer second time. This epoch is commonly referred to as *fringe reference time*. All applied post-correlation processing steps are described in Sec. 4.6. The derived geodetic observables are finally written to VSO files (type 6) which can directly be loaded in VieVS for further investigations and the data analysis described in Sec. 5.7.

While the quasar observations were used to establish a clock model for the correlation and for system checks, the single-band delay precision based on the L-band observations is generally poor. In Experiments 131a and 126b quasars were only detected in the two satellite bands (channels $L1_x$, $L1_y$, $L2_x$, and $L2_y$), whereas there are no detections in the two intermediate bands. Presumably, the non-detections were caused by a configuration error in the recording backend. In g336 the quasar was detected in all recorded channels. The (single-band) fringe delays derived from the L1- and L2-band data in g336 are depicted in Fig. 5.15 (*top panel*). The quasar observations are well aligned with the delays obtained from satellite observations within individual bands and polarization products. However, due to the non-detections in the previous sessions the initial idea to calculate multi-band delays based on the quasar scans was no longer pursued.

The GPS satellite signals were detected in all four allocated L1- and L2-bands: $L1_x$, $L1_y$, $L2_x$, and $L2_y$ (see Tab. 5.3). The integration time for the fringe fitting in fourfit was set to 9 sec for g336 and to 10 sec for all other sessions, i.e. equal to the antenna reposition interval of the stepwise tracking. Single-band delays were calculated based on the correlated satellite observations, resulting in four delay solutions per band (L1 and L2) corresponding to the different polarization products. As shown in Fig. 5.15 (*top panel*) for Experiment g336, this configuration yields in total eight single-band delay solutions every 9 sec for all satellite tracks. The fringe delays of all bands and polarizations are in a range of about ± 30 ns. The scatter within single bands is in general much smaller with about 10 ns in L1 and less than 20 ns in L2. The fringe fitting in fourfit yields extremely high SNR values (referred to as *fringe SNR* hereinafter) as shown in the *bottom panel* in Fig. 5.15. In the L1-band the SNR is quite stable and consistent over the whole experiment at about 15,000. The SNR in L2 is weaker and considerably more variable with

¹Total delays are computed as the sum of the a priori modeled delays and the residual delays (fringe delays) calculated through fringe fitting.

values between 4,000 and 10,000. For comparison, the observed quasar (1921-293) yields SNR values between 20 and 200 in L1 and between 5 and 60 in L2. As a result, the delay precision within the 5 min tracks is a bit better in L1 than in L2 with an RMS scatter from about 10 ps to a few 100 ps in the worst cases. Besides the higher noise the L2 data generally show more significant problems, such as jumps and rapid variations on the ns level within individual satellite tracks.

One clear reason for the lower SNR in L2 is that the $L2_x$ and $L2_y$ channels are already at the edge of the nominal receiver ranges with considerably lower sensitivity (see Sec. 5.4.1). Furthermore, there are bandpass filters in the radio frequency part of the signal chains at Ceduna and Hobart that might cause a non-linear response for the L2 channels. However, this issue needs to be further investigated before definite conclusions can be made. Due to this issue, a proper combination of the L1 and L2 data cannot be considered as reasonable at the moment.

For similar reasons the observations of GLONASS satellites are not discussed further in this work. Although the L1 and L2 signals of GLONASS satellites could be detected throughout all observations, the results in terms of fringe delays are much noisier and variable compared to observations of GPS satellites. Hence, for the further analysis in Sec. 5.7 only GPS observations are discussed, using the XX polarization product of the L1-band data. The total delays of these observations derived through fourfit were written to VSO-formatted observations files, which are directly readable by VieVS.

5.6.1 Polarization Issue

The signals emitted by the GNSS satellites are circular polarized, while orthogonal linear antenna feeds were used to receive the signal, as described in Sec. 5.4.1. Nominally, recording both polarizations should allow to reconstruct the full signal. However, this turned out to be more challenging than expected. Neither of the used telescopes has well-defined polarization characteristics, or has been calibrated for polarization leakage. Furthermore, the telescopes at Ceduna and Hobart have quite unusual optics: While the L-band system at Ceduna is implemented with a tertiary reflector and a receiver directly mounted on the dish surface, HOBART26 is a XY-mount type antenna with the L-band receiver in the prime focus.

Amplitudes When observing the circular polarized signal of a GNSS satellite all four polarizations – cross-hand (XY and YX) as well as parallel-hand (XX and YY) – have approximately equal amplitudes. This is not the case for observations of quasars, which show clear signs of the relative orientation of the probe with amplitudes swapping between parallel- and cross-hand products during observations.

Offsets and variations By investigating the fringe delays in L1 and L2 derived from the different polarization products as presented in Fig. 5.15 (*top panel*) for Experiment g336 we find significant offsets between the different polarization products. The differences between the various

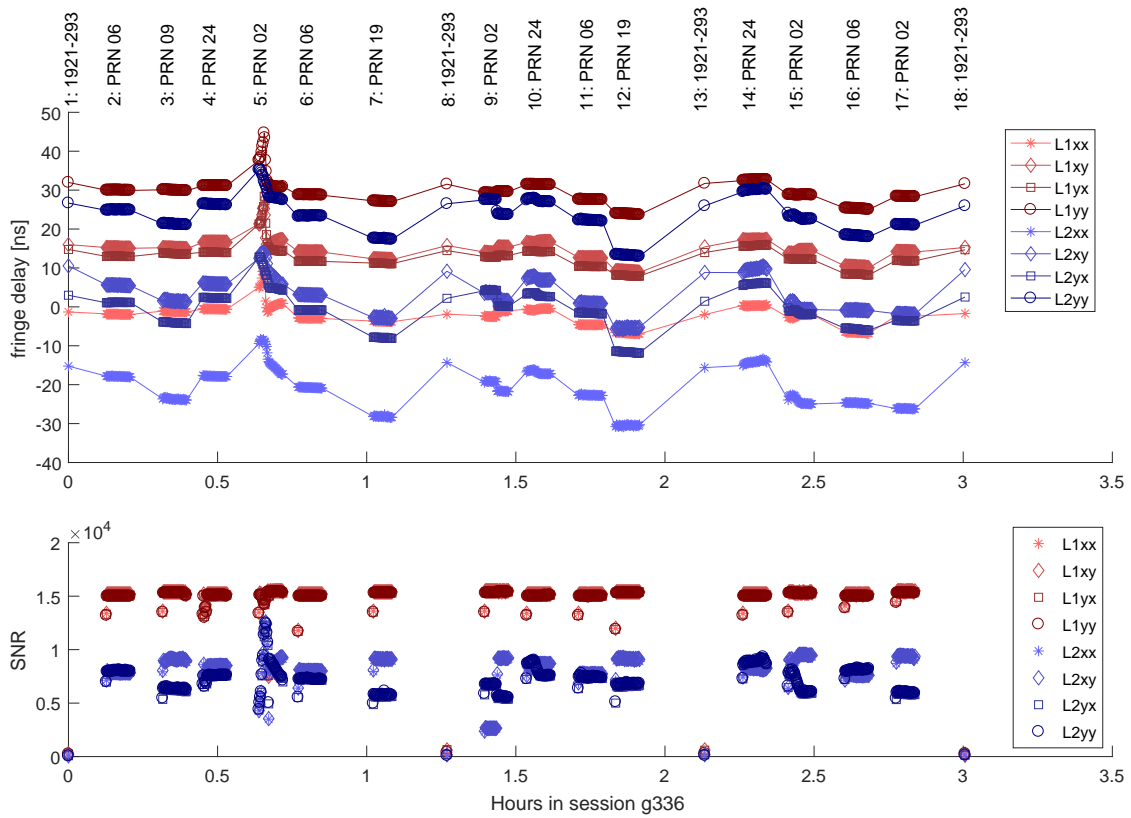


Figure 5.15: Fringe delays and SNR of the baseline HOBART26-CEDUNA in Experiment g336 computed with fourfit. The *upper panel* shows fringe delays for all four polarization products of the L1- and L2-band. Scans numbers and the observed sources are indicated above. The corresponding SNR values are depicted in the *lower panel*.

polarization products in g336 are depicted in Fig. 5.16 for L1 (*top panel*) and L2 (*bottom panel*). In general, the differences show offsets that are quite stable over time with standard deviations of less than 0.8 ns in L1 and less than 1.7 ns in L2. While the offsets between the cross-hand products are rather small (means of 1.8 ns in L1 and 3.7 ns in L2), they amount up to tens of ns in the parallel-hand products (means of 31.5 ns in L1 and 44.6 ns in L2). The largest proportions of these rather stable offsets should correspond to the different path lengths of the X and Y polarized signals in the receiver. On closer inspection we find small variations at the level of 1 to 2 ns between the XX and YY polarized fringe delays on top of the larger constant offsets. These variations are specific for individual satellites as illustrated in Fig. 5.17 that shows the parallel-hand differences in the L-band of Experiment 131a. This is an indication that the unresolved polarization issue causes delay variations related to the changing geometry of the observation constellation.

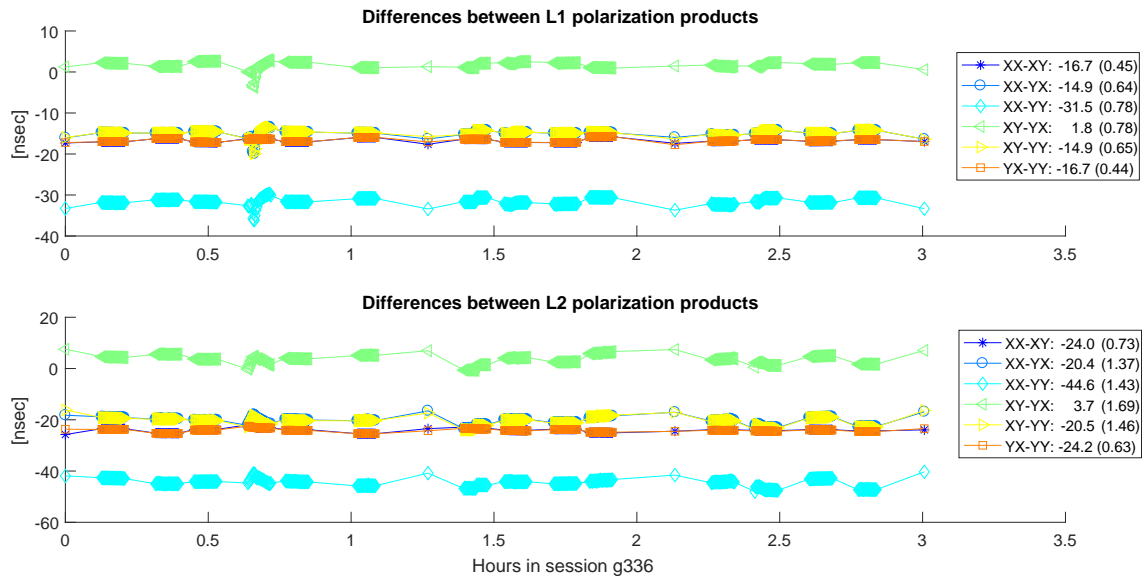


Figure 5.16: Difference between the fringe delays of different polarization products on the baseline HOBART26-CEDUNA in Experiment g336 (as shown in Fig. 5.15) in the L1- (*upper panel*) and L2-band (*lower panel*). The arithmetic mean and the standard deviation (in brackets) of each data-point series are indicated in the legend. The fringe delays of different polarization products show constant offsets in the range between ~ 2 and ~ 32 ns, superimposed by smaller variations on the (sub-)ns level.

Another effect is rapid variations in the fringe delays which occasionally occur in single satellite tracks as illustrated in Fig. 5.18. Presumably, these variations are caused by the linear polarized signals, or gain variations in one of the polarizations, because such signatures are only visible in certain polarization products.

To be able to perform a full polarization calibration of the data, the parallactic angle coverage of the observed quasars has to be optimized. This was not done prior to Session g336 in which long 10 min scans of a strong source (1921-293) were scheduled at the transits at all stations (see Sec. 5.3.1 for more details on the experiment design). This potentially enables a polarization

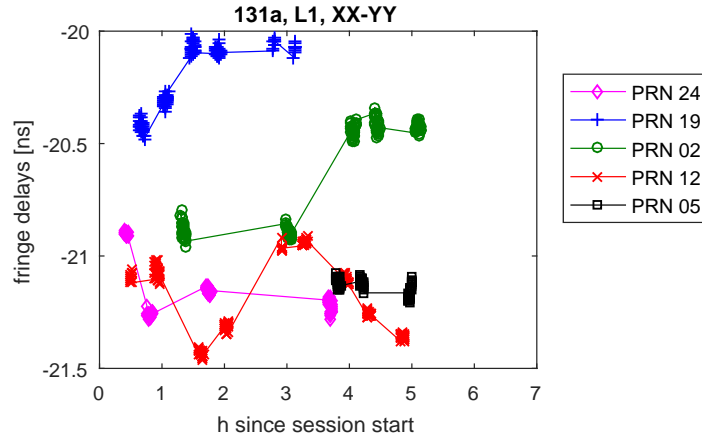


Figure 5.17: Difference between the XX and YY polarization products in the L1-band of Session 131a. The large constant offset of about 20 ns is superimposed by smaller variations specific to each of the observed satellites (Plank *et al.*, 2017a).

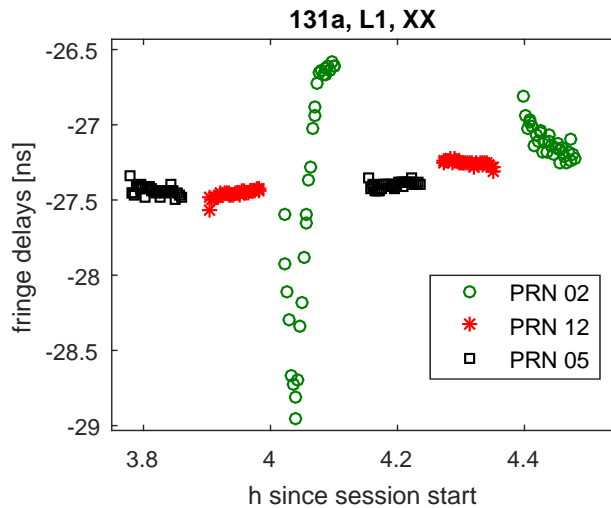


Figure 5.18: Fringe delays in the L1-band of Experiment 131a. Example for the rapid variation of the XX fringe delays in one track of satellite GPS PRN 02 (Plank *et al.*, 2017a).

calibration, but has not been tested yet. Anyway, it is questionable if the calibrations obtained from quasars measurements can directly be applied on the GNSS satellite observations, given the vast changes in the gain.

Due to the polarization issues discussed above it was not possible to combine the different polarizations in order to derive a distinct delay solution for the L1- and L2-bands. Given that the amplitudes of all four polarization products are on the same level, and that the observation results are very similar in YY and XX, we opted to focus on the XX product only in the following data analysis.

5.7 Data Analysis

The analysis scheme for VLBI satellite observations introduced in Sec. 4.7 was applied to study the group delays obtained from the observations of GNSS satellites. These investigations were carried out using the Vienna VLBI and Satellite Software (VieVS) which allows to perform a geodetic data analysis based on observations of natural sources, as well as on satellites, as described in Sec. 4.2. Although the current data are not suitable to estimate parameters in a least squares adjustment (e.g. troposphere parameters or station coordinates) – due to the systematics still present in the data, as described above – all necessary tool were developed in VieVS and could be tested. Furthermore, the data collected on the single baseline between Ceduna and Hobart is not well suited for the estimation of orbit parameters, because these observations only constrain the orbit estimates in the direction orthogonal to the baseline. Hence, parameter estimation based on GNSS satellite observations is not further discussed in this work.

5.7.1 Residual Delays

The quality of the delay measurements, as well as of the delays modeled in VieVS, can be assessed by comparing the observed delays with the corresponding modeled delays, i.e. by investigating the observed minus computed (O-C) delay residuals.

Observations The observations are given in terms of total single-band delays calculated by the post-correlation processing described in Sec. 5.6. Here, only the results of the XX polarization products of the L1-band are discussed. However, the YY product delivers similar results, and we opted to skip the analysis of the L2 data due to the lower SNR (see discussions in Sec. 5.5 and 5.6). It should be noted, that the observations shown here were already reduced by subtracting the clock models (offset and rate per station) previously applied in the correlation step (via *.v2d* files, see Sec. 4.5.1). This was done in order to reduce the largest proportion of instrumental delays and station clock offsets and, hence, to get smaller delay residuals and to facilitate their interpretation. Consequently, the discussed observations do not contain information about the absolute residuals and their shift on the y-axis is arbitrary. However, reducing the initial clock

models has no effect on a subsequent parameter estimation, because station clock models would have to be estimated and reduced anyway.

In standard VLBI processing corrections for the contribution of the ionosphere on the observed delays are derived from observations in two frequency bands, usually in the S- and X-band. With the present GNSS observation data, such corrections are not available and alternative approaches are required. VieVS provides a tool to calculate ionosphere corrections based on global total electron content (TEC) maps that is described by Tierno Ros *et al.* (2011). TEC maps are provided for example by the IGS¹ in the IONosphere Map EXchange format (IONEX²). For this study, the observed total delays were reduced by ionosphere corrections calculated in VieVS based on IGS TEC maps.

Computed delays For the computation of the theoretical (near-field) delays in VieVS IGS final orbits provided in terms of SP3 files were used. In an intermediate step, phase center corrections were applied (e.g. Schmid *et al.*, 2016 and Montenbruck *et al.*, 2015), and the original SP3 files were re-written with corrected satellite positions. This step is required, because the satellite positions in public SP3 files refer to the center of mass of the GNSS satellites, while the reference point for our VLBI measurements is the phase center of the antenna array. The phase center corrections provided in the ANTenna EXchange format (ANTEX³) by the IGS⁴ were applied using the NAvigation Package for Earth Observation Satellites (NAPEOS; Springer, 2009) in the version v3.3.1.

The station positions, earth orientation parameters (EOP), and propagation effects due to the atmosphere were modeled using standard approaches commonly applied in the geodetic VLBI (e.g. Schuh & Böhm, 2013) and, therefore, shall not be discussed here in detail. Standard geophysical models implemented in VieVS were applied to determine accurate station positions for the observation epochs. While the influence of the hydrostatic fraction of the atmosphere was modeled (using the Vienna Mapping Functions; Böhm *et al.*, 2009), no corrections for the wet part and for an azimuthal asymmetry (tropospheric gradients) were applied. The C04 EOP time series⁵ provided by the IERS was used for the transformations between the celestial and the terrestrial reference system.

Single baseline experiments: 126b and 131a The O-C residuals without ionospheric corrections for the Experiments 126b and 131a are shown in Fig. 5.19 (a) and 5.20 (a), respectively. Due to the low quality of the quasar observations (or non-detections) the corresponding residuals are not considered here. For both sessions we find residuals within ~ 8 ns (equivalent to ~ 2.5 m) for all satellites over 6 h session duration. In general, the residuals within individual 5 min scans

¹IONEX files by the IGS are available at <ftp://cddis.gsfc.nasa.gov/gnss/products/ionex/>.

²The IONEX format is described at <ftp://www.igs.org/pub/data/format/ionex1.pdf>.

³The ANTEX format is described at <ftp://igs.org/pub/station/general/antex14.txt>.

⁴ANTEX files are provided by the IGS at <ftp://igs-rf.ign.fr/pub/IGS14/>.

⁵Available at <https://www.iers.org/IERS/EN/DataProducts/EarthOrientationData/eop.html>.

show little variations with an RMS scatter of about 10 to 100 ps and are highly correlated. As discussed previously in Sec. 5.6, some scan show rapid changes in the residuals, which we believe is mainly due to unresolved issues with the unusual polarization, due to problems with the gain, or a combination of both. In the sub-plots (b) the residuals are plotted versus the mean elevation at both stations. This reveals in general larger residuals at lower elevations angles, indicating that this is caused by the propagation medium, i.e. the ionosphere or the troposphere. The corrections for delay contributions of the ionosphere in the L1-band based on IGS TEC maps are plotted in the sub-plots (c). For both sessions, which were observed during the local nighttime, the ionosphere contributions amount up to about 4 ns. When applying the corrections the overall residuals drop to within ~ 4 ns (equivalent to ~ 1.2 m), and the strong inverse correlation between elevation angle and residual size is strongly reduced, as shown in the sub-plots (d) and (e), respectively. Still, the residuals of scans of the same satellite show a kind of orbit signal, indicating shortcomings in the modeling.

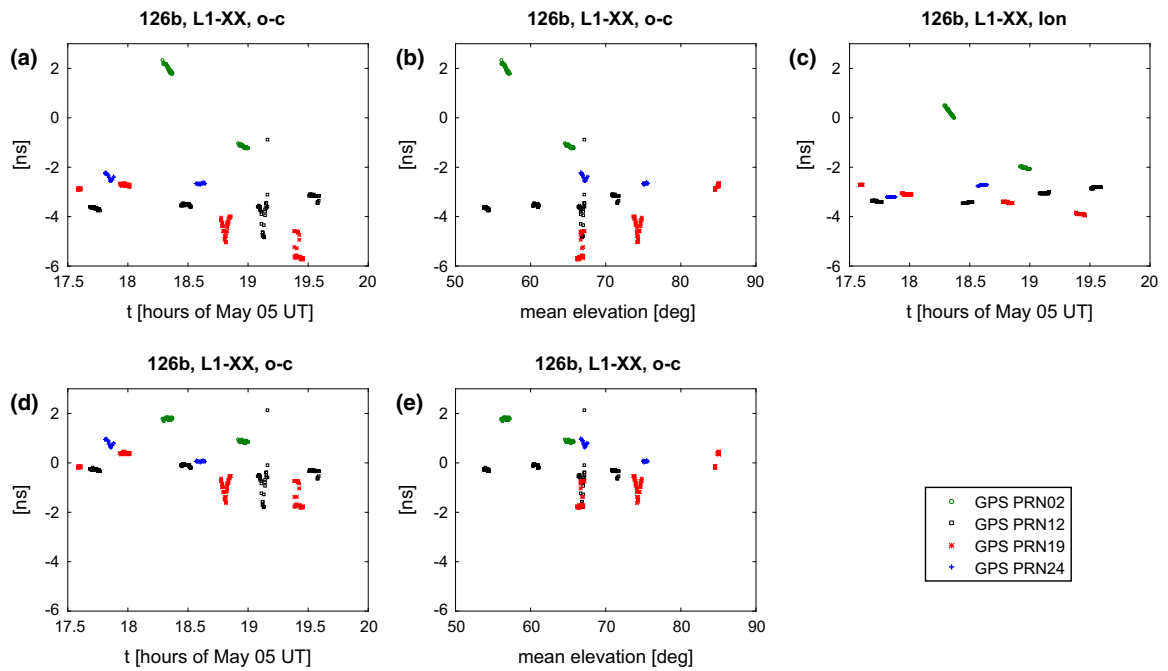


Figure 5.19: Observed minus computed (O-C) residual delays for 126b. The clock model (offset and rate) used for the correlation was removed. The top line shows O-C residuals (a) against time and (b) elevation. The delay corrections due to the ionosphere calculated using IGS TEC maps is shown in plot (c). The bottom line depicts the O-C residuals versus (d) time and (e) elevation after applying the ionosphere corrections (from Plank *et al.*, 2017a).

Experiment g336 The O-C residuals of all three baselines in Experiment g336 are shown in Fig. 5.21. The plotted observations were already corrected for ionospheric effects based on TEC maps, as outlined above. Contrary to previous experiments, also the quasar scans yielded sufficient SNR and single band delays were derived. The according residuals are plotted as *red circles*. While the

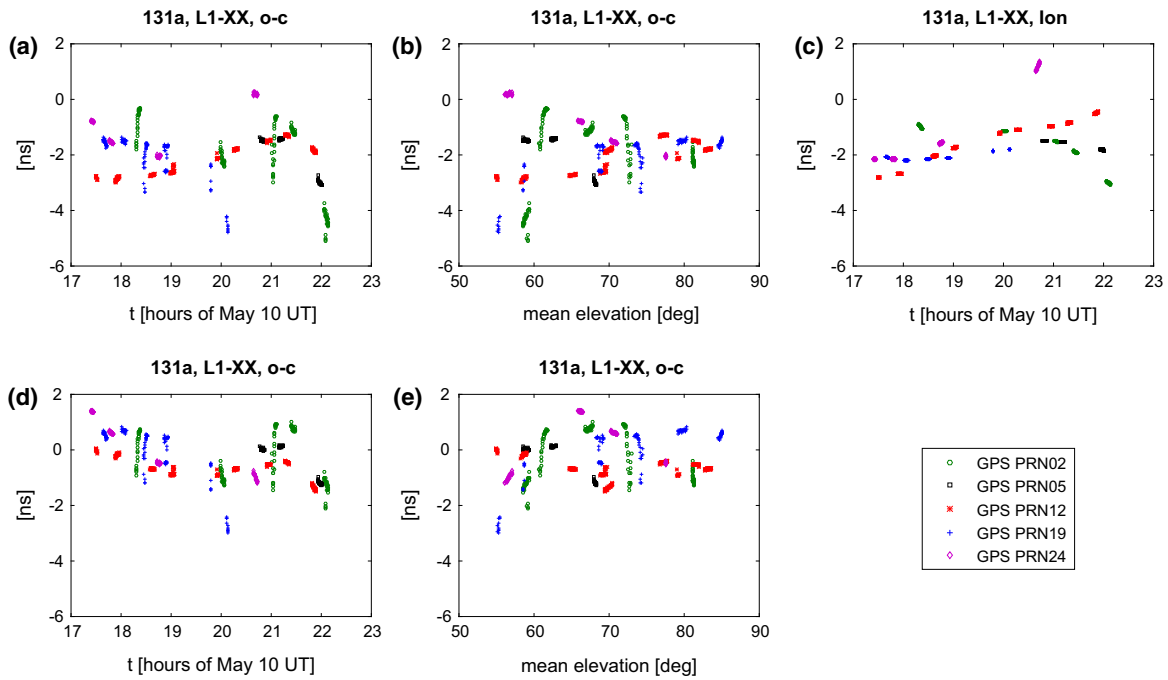


Figure 5.20: Same as Fig. 5.18 for Experiment 131a (from Plank *et al.*, 2017a).

residuals on the baselines Ceduna-Warkworth and Hobart-Warkworth are scattered over a range of about 10 ns, the scatter on baseline Ceduna-Hobart (*top panel*) only amounts about a third with a peak-to-peak range of ~ 3 ns. In general, the residuals of the quasars scans are well aligned within the range of the satellite observation residuals. Similar to previous experiments, the residuals still show a kind of orbit signal related to individual satellites, and some rapid changes especially in the scans of satellite GPS PRN 02 (*G02*) on baselines including Ceduna.

5.7.2 Discussion

Despite the unresolved issue of reconstructing the full transmitted signals based on the linear polarized data records, the achieved results in terms of O-C residuals are meaningful. In the following, different aspects – mainly of the delay modeling – are discussed, with the goal to identify areas with potential for future improvements. Throughout this study the implementation of the near-field delay model in VieVS (described in Sec. 4.2.1.3) was improved, e.g. by refining the light-time iteration, the determination of the satellite position at the time of the signal transmission, and by adding a proper modeling of gravitational delays. However, the total effect of all these refinements on the calculated delays was below 10 ps, which is the estimate of the model accuracy that we are confident to give.

While applying the ionospheric corrections based on TEC maps brings obvious improvements, it also becomes clear, that these corrections do not necessarily cover all effects. For example, the large (and elevation dependent) residuals of PRN 02 in 126b get diminished, but they do not

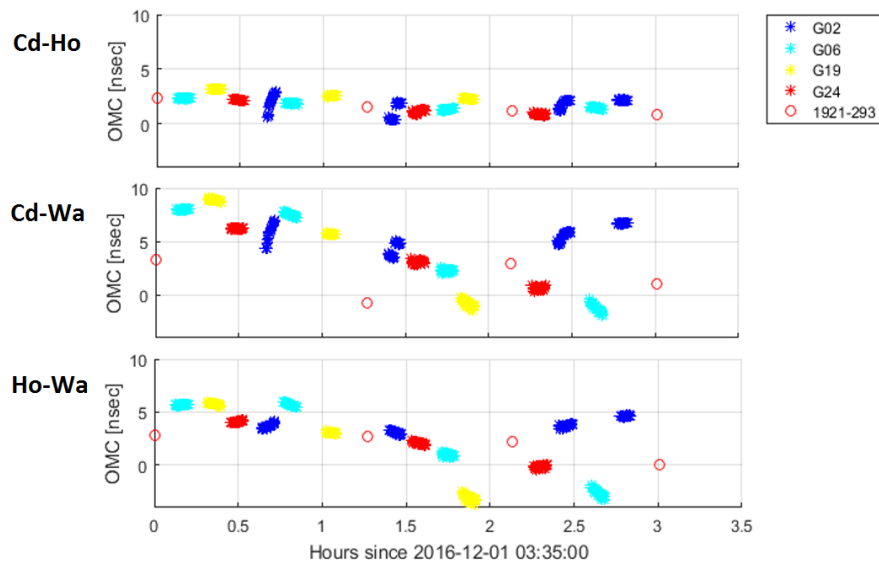


Figure 5.21: Residual delays (observed minus computed) of all three baselines in Experiment g336. The observed delays were calculated by using the XX polarization product of the L1-band.

completely vanish after applying the correction. Applying the ionosphere correction also seem to add an offset to the residuals of PRN 19 in 131a at high elevations. Modeling inaccuracies might be caused by the rather coarse spatial (5° in longitude and 2.5° in latitude) and temporal (2 h) resolution of the global TEC grids provided by the IGS. Further improvement might be achieved by using more sophisticated techniques for the determination of ionospheric delay corrections, such as the method developed by Männel & Rothacher (2016) exactly for the purpose of VLBI satellite observations. In this respect, further investigations might bring fruitful results. Another option, of course, is the derivation of ionosphere corrections based on the simultaneous observations in the L1- and the L2-band, and by applying the mathematical relations indicated in Equ. 4.9. However, a prerequisite for a meaningful combination of the two frequency bands is to solve the still pending polarization issues, enabling to reconstruct the full (circular polarized) signal in the first place.

In the presented data, only corrections for the hydrostatic part of the troposphere were applied. Zenith hydrostatic delays (ZHD) were modeled based on ground pressure values from the empirical Global Pressure and Temperature 3 model (GPT3; Landskron & Böhm, 2018) and the formulations by Saastamoinen (1972). Then, the ZHD was mapped to the actual observation directions by applying the Vienna Mapping Function 1 (VMF1; Böhm *et al.*, 2009). Unfortunately, meteorological in situ measurements were largely unavailable for the discussed experiments. We had to fall back on analytical models for these parameters, although in situ measurements of temperature, pressure, and humidity would allow for modeling the contributions of the troposphere more accurately. In situ measurements of the humidity would also enable to approximate the influence of the wet constitution of the troposphere by applying the model by Askne & Nordius (1987). Troposphere corrections calculated through ray tracing methods, as described e.g. by

Hofmeister & Böhm (2017), would also bear potential for further improvements in this respect.

The satellite positions are given in 15 min intervals in the SP3 files provided by the IGS. For orbit interpolations a 9th-order Lagrange method was applied which yields formal accuracies at the level of 2.5 cm and 3 cm, for GPS and GLONASS respectively, according to the IGS. For Experiment 179a we tried various orbit solutions provided in terms of SP3 files, i.e. final and rapid solutions, and products of different analysis centers. We found differences in the modeled delays of about 2 ps for GPS and up to 15 ps for GLONASS. Although these differences are rather small, the more accurate and consistent final orbits are preferable for the analysis, while the rapid solutions are still by far sufficient for the determination of the correlator input models. According to Schmid *et al.* (2016) the phase center offsets (PCO) of the observed GNSS satellites can be as large as ~ 3 m and would cause a periodic signal in the observed delays. To investigate the influence of the PCO we modeled delays by using orbit data (1) with reference the satellite's center of mass, and (2) with reference to the antenna phase center (i.e. applying a phase center correction). For the Sessions 126 and 131a we found differences between 20 ps and 100 ps (or about 3 cm maximum). Considering that the estimated accuracy of the near-field delay model in VieVS is on the level of 10 ps, it is advisable to apply PCO corrections rather than using the SP3 files directly.

We also assessed the influence of using the IERS final EOP time series rather than the (more accurate) C04 series. Comparisons revealed differences on the level on a few ps at most.

Another potential error source are the terrestrial reference coordinates of station Ceduna, which is usually not used for geodetic experiments. Absolute coordinates were determined by Petrov *et al.* (2009). Concerning station-related model parameters, Vienna Mapping Functions and tidal ocean loading are available, while corrections for atmosphere loading and thermal antenna deformation (Nothnagel, 2009) are still missing. Together with a nominal axis offset of 2 mm, which is currently also neglected in the delay model, the station coordinates are estimated to be accurate on the level of a few cm only.

Investigating the residuals of g336 (shown in Fig. 5.21), it is obvious that the overall residuals are about three times larger on baselines including the station Warkworth. Presumably, the reason for the lower scatter on the Ceduna-Hobart baseline can be found in the deactivation of the automatic gain control system (AGC) of the DBCs at Hobart and Ceduna. As shown previously (in Sec. 5.5.1), this procedure prevents short period amplitude variations in the obtained visibilities, and, apparently, yields more consistent delays.

5.8 Outlook

This Chapter describes a novel realization of VLBI satellite observations, widely adopting standard tools and processing schemes of the geodetic VLBI technique. While there is still room for improvement in all covered areas – from scheduling to analysis – the introduced process chain represents a solid basis for further experiments and technical improvements.

Considering the antennas used for the discussed experiments, certainly the most pressing topic is the combination of the two linear polarized signals in order to reconstruct the full circular polarized GNSS signals. This is needed to derive one single and unambiguous delay solution per band (instead of four, one for each polarization product), and is a prerequisite for the combination of observations in the L1- and L2-band for the sake of ionosphere correction. Therefore, a better calibration of the L-band signal chains is required. Alternatively, other antennas could be used which are equipped with more suitable L-band receivers, enabling to directly receive the circular polarized signals.

Improved sampling of the artificial satellite signals, using a better quantification as common in geodetic VLBI, e.g. 8 bit instead of 2 bit, should mitigate compression effects caused by the overwhelmingly strong signals. A first step towards a proper handling of the strong signals was already made in Experiment g336 by deactivating the gain control of the DBBCs, which – of course – can only be considered as an intermediate solution due to the required manual interactions.

Also the tracking bears room for improvement. Certainly, a continuous satellite tracking is preferable for future experiments, to preclude potential effects of amplitude variations on the derived delays. Therefore, the interfaces between antenna controllers and the Field System have to be updated in order to use existing tracking modes suitable for satellites based on standard antenna control files (e.g. VEX schedules).

In Experiment g336, the antenna network could already be expanded to three antennas. As soon as we have a better understanding of the described technical issues, the logical next step would be to further expand the network size, with the ultimate goal to observe GNSS satellites in a fully global network. Only observations with globally distributed stations are suitable for a proper determination of satellite orbits, and, in further consequence, for establishing the actual link between the reference frames of VLBI and GNSS.

Chapter 6

Observing the APOD Satellite with the AuScope VLBI Array

The Chinese APOD-A nano satellite is a highly interesting observation target for VLBI, because it represents a first realization of a co-location satellite – suitable for practical observation tests – combining the techniques GNSS, SLR, and VLBI on a single platform in a low Earth orbit (LEO). In this Chapter the first (and only) serious attempt to observe this satellite with a VLBI network over multiple passes is introduced and discussed (also see Hellerschmied *et al.*, 2018). The series of experiments was carried out by the AuScope geodetic VLBI array in November 2016, in a common effort of the University of Tasmania (UTAS) and Technische Universität Wien (TU Wien).

The goal of this case study was to track the APOD satellite whenever possible with the AuScope antennas throughout a couple of days and to derive observables in terms of group delays, as common in geodetic VLBI. All observed experiments are listed in Table 6.1. In the subsequent data analysis we found observed minus computed (O-C) residuals on the level of 10 ns for all observed tracks. The observations were also used to test new features in our VLBI data analysis software VieVS for the estimation of satellite orbits, yielding post-fit residuals with a WRMS of about 10 cm.

For this work, the process chain for VLBI satellite observations introduced in Chap. 4 was adopted for the specific requirements of APOD observations whenever needed. An overview of the applied processes is shown in Fig. 6.1. Individual processing steps are discussed in the following sections. After introducing the observation target and the antennas network (Sec. 6.1 and 6.2), the experiment scheduling using VieVS (Sec. 6.3), the observation process with the AuScope antennas (Sec. 6.4), the correlation and post-correlation processing using the software packages DiFX and HOPS (Sec. 6.5 and 6.6), and the data analysis in VieVS (Sec. 6.7) are discussed.

Although delays could be obtained from all observed tracks, the collected observation data are not sufficient – mainly in terms of quantity and geographical distribution – to study the realization of actual frame ties. However, this study is still valuable as it enabled to gain plenty of hands-on experience in the field of VLBI satellite observations, especially regarding tracking procedures for

Label	Stations	Experiment Start [UTC]	Duration [s]	APOD Tracks
316a	Ke, Yg	11 Nov. 2016, 22:15:00	33 min 11 s	1 (211)
317a	Ke, Hb	12 Nov. 2016, 09:34:00	41 min 33 s	1 (27)
317b	Ke, Hb, Yg	12 Nov. 2016, 21:35:00	34 min 49 s	2 (161, 137)
318b	Ke, Hb, Yg	13 Nov. 2016, 10:48:30	25 min 57 s	2 (41, 241)
318c	Ke, Hb	13 Nov. 2016, 21:01:00	25 min 59 s	1 (44)
318d	Ke, Yg	13 Nov. 2016, 22:35:00	22 min 55 s	1 (153)
319a	Ke, Hb, Yg	14 Nov. 2016, 10:00:00	40 min 5 s	2 (74, 201)
a332	Ke, Hb, Yg	27 Nov. 2016, 16:00:00	24 h	4 (86, 256, 29, 189)

Table 6.1: A list of APOD experiments by AuScope in November 2016. Between November 11 and 14, 2016, APOD was tracked whenever possible, yielding Sessions 316a to 319a. Session a332 represents a geodetic 24 h session interrupted by 4 APOD scans. The last column (*APOD tracks*) indicates the number of APOD tracks observed in this session and the duration of each scan in seconds (*in brackets*).

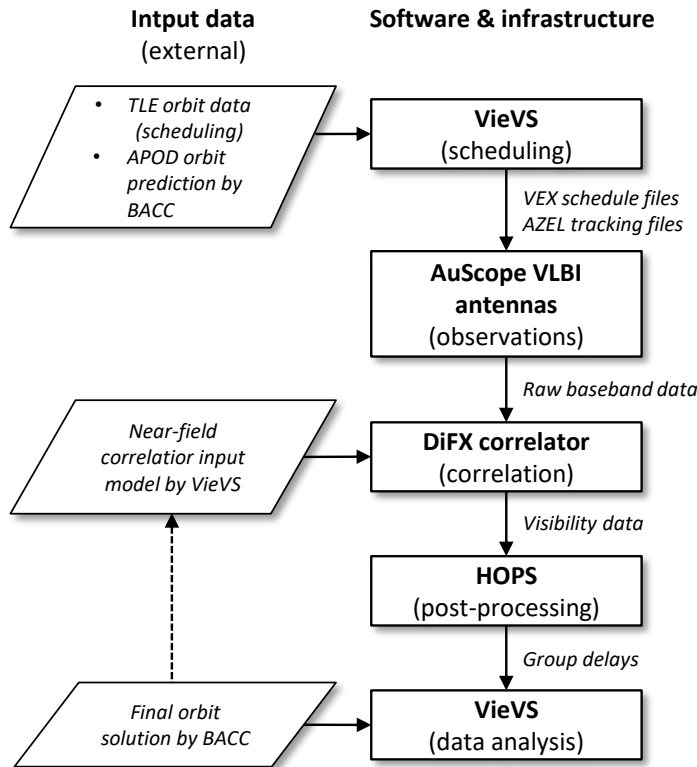


Figure 6.1: Simplified process workflow for VLBI observations of the APOD-A nano satellite with the AuScope geodetic VLBI array (Australia). The diagram indicates the most important external input data (*rhomboid boxes, left*), the used software and infrastructure (*rectangular boxes, right*), and the essential interchange data (*italic text*).

LEO satellites, handling of narrow-bandwidth satellite signals in the correlation and fringe-fitting process, and the application of suitable data analysis schemes.

6.1 The APOD-A nano Satellite

The Atmospheric density detection and Precise Orbit Determination (APOD) mission is operated by the Beijing Aerospace Control Center (BACC, China), and was launched on September 20, 2015. It consists of four cube satellites and is mainly intended to carry out in-situ measurements of the atmospheric density and to derive density parameters through a precisely determined orbit. For more details on the scientific tasks, the satellite’s payload and the Precise Orbit Determination (POD) the author refers to Tang *et al.* (2016) and Sun *et al.* (2018). In this work we discuss VLBI observations of one of these satellites, named APOD-A nano. It was deployed on a near polar orbit with an inclination of about 97° and an initial altitude of about 520 km. At the time of the VLBI observations discussed herein, the orbit altitude of the satellite already descended to about 450 km by maneuvers and the effect of the atmospheric drag. APOD-A nano (hereinafter abbreviated as APOD) has a size of $391 \times 398 \times 398$ mm only, and is equipped (among sensors to measure the atmospheric density) with geodetic payload: a dual-frequency GNSS receiver capable to process GPS and Beidou signals, an SLR retro-reflector, and a VLBI beacon. APOD’s VLBI beacon emits series of narrow-bandwidth tones (literally spikes in the frequency spectra) in the S- and X-band, as listed in Tab. 6.2. The carrier tones (labeled $Carr_S$ and $Carr_X$), centered at $f_{Carr_S} = 2262.01$ MHz and $f_{Carr_X} = 8424.04$ MHz, are symmetrically surrounded by four so-called Differential One-way Ranging (DOR) tones (labeled DOR_{S_i} and DOR_{X_i}) designed according to recommendations of the Consultative Committee for Space Data Systems (CCSDS 401.0-B CCSDS (2009)). The DOR tone frequencies are calculated as $f_{DOR_{1,2}} = f_{Carr} \pm f_{Carr}/440$ and $f_{DOR_{3,4}} = f_{Carr} \pm f_{Carr}/2200$, yielding a frequency span of 38.3 MHz in the X-band and 10.3 MHz in the S-band. The Effective Isotropic Radiated Power (EIRP) of the carrier tones is 4 dBm with the DOR tones being 12 dB weaker.

Label	Band	Center frequency [MHz]
$Carr_S$	S	2262.010
DOR_{S1}	S	2256.869
DOR_{S2}	S	2260.982
DOR_{S3}	S	2263.038
DOR_{S4}	S	2267.151
$Carr_X$	X	8424.040
DOR_{X1}	X	8404.894
DOR_{X2}	X	8420.211
DOR_{X3}	X	8427.869
DOR_{X4}	X	8443.186

Table 6.2: Carrier and DOR tone frequencies as emitted in the S- and X-band by the VLBI beacon of the APOD-A nano satellite.

6.1.1 Orbit Determination

The operational orbit determination is carried out by the BACC solely based on GPS observations. Initially, the POD was performed by analyzing GPS L1 and L2 carrier phase and pseudorange measurements with their proprietary software, yielding an RMS of the residuals below 2 cm and 2 m, respectively (Sun *et al.*, 2018). APOD-A was also observed by SLR, coordinated by the International Laser Ranging Service (ILRS). The SLR measurements were used for an independent validation of the GPS derived orbit, by comparing SLR measurement ranges with ranges derived by GPS POD. In general, comparisons showed a good agreement with three-dimensional position deviations below 10 cm (Sun *et al.*, 2018).

Unfortunately, the on-board GNSS receiver partly failed in January, 2016. Since then, GNSS raw-data records, i.e. pseudorange and carrier phase measurement data, are not accessible via communication down-link by the ground segment any more. Three-dimensional satellite coordinates are still calculated directly by the on-board receiver and transmitted to the tracking stations four times a day. Hence, since January 2016, the orbit determination completely relies on these coordinate data, causing a dramatic drop in the orbit accuracy. For November 2016, the time when our VLBI experiments were observed, the orbit determination residuals are in the range of 10 to 20 m (Sun *et al.*, 2018).

The BACC calculated and provided two sets of orbit solutions for the described VLBI experiments: (1) final orbit solutions, and (2) orbit predictions. Both are solely based on the GPS coordinate data, and are provided in terms of 1 sec time-series of three-dimensional coordinates in the WGS84 system. The final orbit solutions were available with a latency of several weeks, and were used in this study to compute a priori delays using the near-field delay model in VieVS (see Sec. 4.2.1.3), required for the correlation (correlator input model), as well as for the data analysis (computed delays). As previously mentioned, these final orbits show post-fit residuals in the range of 10 to 20 m. Orbit prediction were provided about 12 h before an experiment started, and were used to calculate the tracking data in terms of azimuth and elevation angles required to steer the antennas throughout the observations (see Sec. 6.4). Comparing all predicted and final orbit solutions we used for this study reveals differences of several 100 m (up to 1 km) in along-track, and usually a bit less in cross-track direction. In radial direction, the discrepancies are much lower with values on the level of several m. An example is shown in Fig. 6.2 for the time Experiment 316a (see Tab. 6.1) was observed. Assuming that the final orbits represent the more consistent and accurate solutions, leads to the conclusion that the orbit predictions used for satellite tracking were only accurate on the level of several 100 m. The low accuracy of the predicted and final orbit solutions has wide-ranging consequences on different stages of the study, as discussed in the following sections.

We also investigated the suitability of SLR measurements to improve the present orbit solutions. Unfortunately, APOD was only sparsely observed by SLR at the time the VLBI observations were performed. Hence, SLR data could not reasonably contribute towards a precise orbit determination.

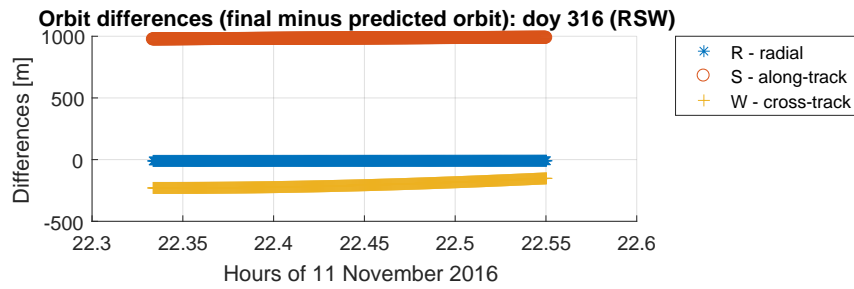


Figure 6.2: Differences between the final and the predicted APOD orbit solution by BACC for Session 316a (November 11, 2016) in the satellite coordinate system (radial, along-track, cross-track).

6.2 The AuScope Geodetic VLBI Array

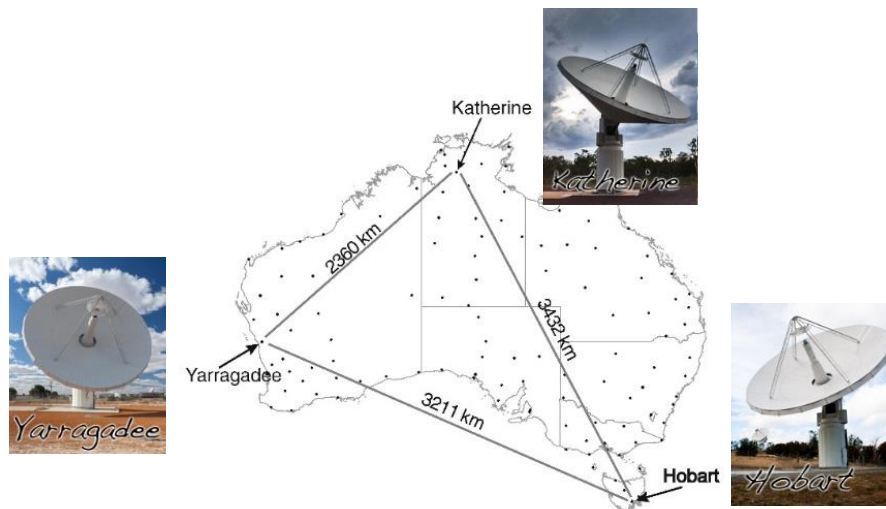


Figure 6.3: AuScope geodetic VLBI array (modified from Lovell *et al.*, 2013).

All discussed observations of the APOD satellite were carried out by the AuScope geodetic VLBI array (Australia), which consists of the three antennas indicated in Fig. 6.3: HOBART12 (Hb), KATH12M (Ke), and YARRA12M (Yg). The resulting intra-continental baselines have lengths between about 2360 and 3432 km.

All three antennas are similar in design. They have small main reflectors with diameters of 12 m and AzEl-mounted antenna positioners (see Sec. 3.3.2) with fast slew rates of up to $5^\circ/\text{sec}$ in azimuth and up to $1.5^\circ/\text{sec}$ in elevation. The receiver systems consisted of antenna feeds designed to acquire signals in the S- and X-band, modern Digital Baseband Converters (DBBC-2) for digitization and formatting, and Mark5B+ recorders. For more technical details the author refers to Lovell *et al.* (2013).

6.2.1 Satellite Tracking with AuScope

Additionally to the standard tracking mode for natural sources such as quasars, the Antenna Control Units (ACUs) of the AuScope antennas provide the so-called *AZEL tracking mode*. In the AZEL mode, the ACUs can directly load text files with time-tagged source positions defined in terms of azimuth and elevation angles. The antenna controllers then interpolate the actual pointing angles between these data points and steer the antenna positioners accordingly. The format of AZEL tracking files compatible with the AuScope ACUs is described in Appdx. C along with a simple example. The tracking files can be created by the VieVS satellite scheduling program as described in Sec. 4.3.5 and 6.3.

In initial tests the applicability of other satellite tracking schemes was tested for APOD observations: the stepwise tracking approach (see Sec. 3.4.1), and the TLE tracking mode implemented in the Field System (see Sec. 3.4.2.2). Both approaches failed when using them to track the APOD satellite, because they are implemented in the Field System that cannot handle the high rate of positioning commands required to track this fast satellite. In contrast, the AZEL tracking mode is directly implemented in the antenna controllers, without any detour via the Field System, i.e. the antenna motion control and the control routines for the recorder systems are decoupled. The shortcoming of the situation that the AZEL tracking mode is not controlled by the Field Systems is, that standard procedures for experiment automation are not available. The tracking modes of the ACUs have to be manually switched between the standard mode for astronomical sources and the AZEL mode. Furthermore, the tracking files have to be manually loaded via the ACU interface at each antenna for all satellite tracks. Hence, time-consuming and error-prone manual interaction is required.

6.3 Scheduling and Experiment Design

Scheduling with VieVS All APOD experiments were scheduled with the VieVS satellite scheduling program as described in Sec. 4.3. It allows for the scheduling of observations of near-field targets along with observations of extra-galactic radio sources, and was used to create all required control files for the stations (VEX-formatted schedules and AZEL tracking files) and for the correlation process (VEX and VSO files). The schedule summaries of all APOD experiments listed in Tab. 6.1 are shown in Appdx. B.2.

Publicly available TLE data¹ were used for the scheduling, i.e. for the determination of the scan times in VieVS. The initial observation planning was performed about one week prior to an experiment. A final scheduling iteration was performed on the day before, as the observation timing may slightly change with updated orbit elements. The tracking file parser in VieVS was updated in order to create AZEL tracking files according to the format specifications outlined in

¹The NORAD ID of the APOD-A nano satellite is 40903. It can be used to download TLE datasets e.g. from <http://www.celestrak.com/>.

Appdx. C. Series of azimuth and elevation tracking points were calculated in 1 sec intervals for each station and satellite track based on the orbit prediction provided by the BACC about 12 h prior to an experiment (see Sec. 6.1.1).

Experiment design The observation geometry was mainly determined by continental-wide baselines (2360 to 3432 km, see Fig. 6.3), and the very low orbit of APOD (about 450 km), which strongly limited common visibility of the target from the AuScope VLBI stations. On average, APOD was visible from individual sites four times a day, for a couple of minutes only. Assuming a cut-off elevation of 5° , the projected fields of view are shown in Fig. 6.4 in terms of red circles. Only in the intersecting areas APOD was simultaneously visible by the corresponding antennas. In general, common visibility was restricted to two of the three stations, to low elevation angles (especially on the baseline Yarragadee–Hobart), and to scan durations of a few minutes at most. Due to these restrictions, it was not possible to observe more than two short single-baseline tracks shortly after another during an overpass, as exemplarily shown for two consecutive APOD tracks (Scans 168 and 169) in Session a332 in Fig. 6.4. APOD, which flew over the Australian continent in South-North direction, could be first observed for 86 sec on the baseline Hb-Yg, and then for another 256 sec on the baseline Yg-Ke. The next occasion for an APOD observation only existed more than 10 h later that day.

Most of the APOD tracks were observed at elevations between 5° and 20° . Only at some rare occasions at higher elevations of up to 37° . The advantage of the low elevation tracks is, that the azimuth and elevation change rates at the observing sites decrease with lower elevations, as discussed in Sec. 3.3.2, whereas the distance between the satellite and the VLBI antennas increase. Consequently, the demands on the tracking accuracy decrease at lower elevations, i.e. it was easier to keep APOD within the antennas' fields of view at low elevations while data was recorded. On the other side, the analysis of low elevation observations only is more challenging, because the influence of the ionosphere, as well as of the neutral atmosphere, increase with decreasing elevation. Furthermore, observations at different elevation angles are required in order to properly decorrelate estimates of station heights, zenith wet delays (ZWD), and station clocks (e.g. Nilsson *et al.*, 2013).

Despite the limitations caused by the observation geometry, APOD observations were scheduled whenever two AuScope antennas had common visibility of the satellite between November 11 and 14, 2016, yielding seven sessions with durations of about 25 to 40 min, as shown in Tab. 6.1 (Experiments 316a to 319a). In all these sessions, on average five quasars¹ were observed prior to one or two single-baseline tracks of APOD. After the satellite track(s), again a block of about five quasar scans followed. The main reasons to include quasar observations in the schedules was to use them for the determination of an initial clock model for the correlation and to

¹For the sake of brevity, only quasars – as the most common type of active galactic nucleus (AGN) observed in the geodetic VLBI – are mentioned. However, probably other types of AGN were observed throughout the described experiments.

check the signal chains.

The Experiment a332 was designed as a geodetic 24 h session including in total four APOD tracks. The session consists of 761 three-station scans (no sub-netting) with observations of strong quasars with a minimum flux density of 0.65 Jy. The session was scheduled in VieVS by applying a station-based scheduling approach, optimizing the sky-coverage at each site in order to decorrelate estimates of station clocks, station heights, and ZWDs (e.g. see Sun *et al.*, 2014). Whenever possible, APOD scans were scheduled in between the quasar scans, yielding four satellite scans within 24 h. The first two APOD tracks in a332 (Scans 168 and 169) are illustrated in Fig. 6.4, and serve as generic example in the following sections. Embedding satellite observations in a geodetic session allows for additional analysis options, e.g. to estimate the ZWD based on quasar observations only, and to apply them in terms of a priori corrections on the APOD observations (for more details see Sec. 6.7).

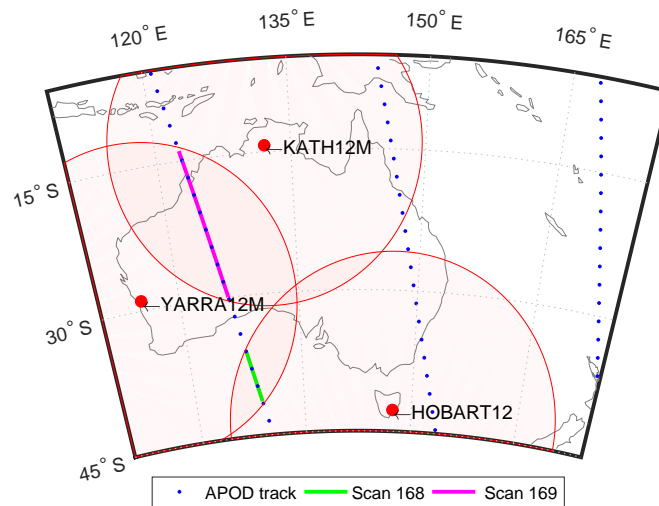


Figure 6.4: Observation geometry for APOD with the AuScope VLBI network. The projected fields of view of all three AuScope antennas are indicated by *red circles* assuming local cut-off elevations of 5° . The ground tracks of APOD in Experiment a332 (observed on November 27, 2016, see Tab. 6.1) are represented by blue dots that indicate successive satellite positions in an interval of 30 sec. Two consecutive APOD Scans, 168 (10:41:04 to 10:42:30 UTC) and 169 (10:44:02 to 10:48:18 UTC) in Experiment a332, are indicated by *green and magenta lines*, respectively.

6.3.1 Observation Mode

The selected observation mode was designed pursuing two goals at the same time: (1) to record the full VLBI signal transmitted by APOD, and (2) to compute reasonable multi-band delays based on the quasar observations. For the latter item, a wide frequency band has to be recorded, whereas for the first one, it is sufficient to cover the APOD tones listed in Tab. 6.2. It was not an option to define and switch between two different frequency modes for quasar and satellite observations, respectively, because changing the recorder settings within a session might cause unknown and unpredictable systematic biases (as we experienced when observing GNSS satellites

in Experiment 179a, see Sec. 5.3.1). Hence, a common observation mode is required fulfilling the requirements of both observation types. The solution was to modify the mode used for the AUSTRAL sessions (Plank *et al.*, 2017b) so that all APOD tones are covered, yielding the channel allocation shown in Fig. 6.5. In total 16 channels with a bandwidth of 16 MHz were recorded, ten in the X- and six in the S-band. The data was sampled with a 2 bit resolution yielding a recording rate of 64 Mbps per channel. Due to strong Radio Frequency Interference (RFI) in the lower S-band at Hobart, a contiguous S-band channel allocation was selected. In the S-band all APOD tones (frequency span of 10.3 MHz) could be recorded in one 16 MHz channel, whereas three 16 MHz channels were required to cover all X-band tones (frequency span of 38.3 MHz). In all other channels, only signals of natural sources were expected.

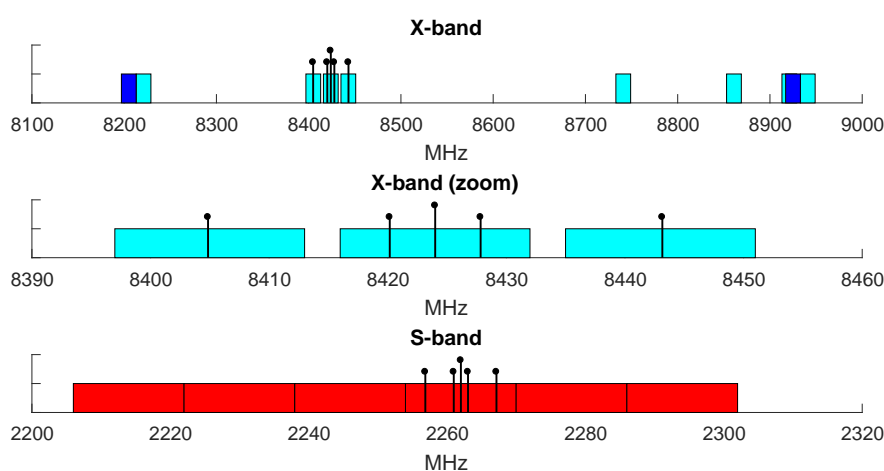


Figure 6.5: Observation mode used for all APOD observations with AuScope in November 2016. The 16 MHz wide channels are depicted by *boxes in blue* (X-band, lower side band), *cyan* (X-band, upper side band), and *red* (S-band, upper side band). The APOD tones are indicated by black lines (carrier tone plus 4 DOR tones in each band).

6.4 Observations

Observation procedure The observations were carried out by following the process scheme introduced in Sec. 4.4, controlled by VEX-formatted schedule files and AZEL tracking files (for the satellite tracks), both generated by the VieVS scheduling program. In case of quasar observations, both, the recorder equipment, as well as the antenna positioners (via the ACUs) were controlled by the information provided in the VEX files through the standard control scheme. During satellite scans, only the recorder systems were controlled by the VEX-schedules, and the antenna motion was guided by the information in the station-specific (AZEL) tracking files. To enable satellite tracking as described in Sec. 6.2.1, the tracking mode of the ACUs had to be manually switched over from the star tracking mode, which is used per default for astronomical sources, to the AZEL tracking mode. Additionally, the AZEL tracking files had to be loaded. To incorporate these manual setup changes at each site about 5 min of idling time was defined in the observation

schedules prior and after APOD tracks. Changing the tracking mode only affected the antenna motion control, while the signal chain was still controlled by the Field System based on the setup parameters defined in the VEX file.

Tracking issues Due to the strong signal power, we were able to assess the received satellite signals live during APOD tracks by a spectrum analyzer (SA) connected to the intermediate frequency (IF) channels at the receiver backends. By live-monitoring the signal on the SA, we experienced that the amplitudes became increasingly unstable with increasing elevation angles, especially in the X-band. While the S-band signals were rather stable throughout all experiments, we even experienced signal loss in the X-band occasionally at elevations above $\sim 30^\circ$. These amplitude variations, caused by an insufficient tracking accuracy, are more pronounced in the X-band due to the narrower beam-width. Antenna beam-widths can be approximated by $BW \approx \lambda/D$, where D is the diameter of the main reflector and λ denotes the wavelength of the observed signal. Hence, the beam-width in the S-band ($\sim 38.1'$) is about four times larger than in the X-band ($\sim 10.2'$), resulting in more relaxed demands on the pointing accuracy in the S-band. Most probably, the tracking issues, which we experienced in terms of amplitude variations in the X-band, were mainly caused by the low accuracy of the APOD orbit predictions used for calculating the tracking data. As discussed in Sec. 6.1.1, the predictions show offsets w.r.t. the final orbit solutions of up to about 1 km. Considering the APOD orbit as of November 2016, Fig. 6.6 illustrates the pointing errors caused by different transverse orbit offsets as a function of the elevation angle. Hence, an offset of 1000 m causes mis-pointing of about $4.2'$ at 30° elevation. With a beam-width of about $10.2'$ in the X-band, pointing errors of a few arc-minutes can already be critical. Furthermore, the internal interpolation of the tracking data in the ACU might also cause pointing inaccuracies. It might not be accurate enough to precisely follow a fast satellite, such as APOD. Assuming that there is already a slight pointing offset caused by the low-quality tracking data, additional inaccuracies due to a non-optimal interpolation of these data in the ACU may sum up to an extent, that together it eventually causes severe pointing problems in the X-band – even at moderate elevation angles.

After the sessions the raw baseband data were shipped to Hobart for correlation and post-correlation processing.

6.5 Correlation

The recorded data was correlated with the DiFX (version 3.5) by applying the processing scheme for near-field observations described in Sec. 4.5.1. All sessions were initially correlated on a small computation cluster at the Mt Pleasant observatory in Hobart. A final correlation iteration – enabling to cross-check the results – was carried of by using the same software installed on the Vienna Scientific Cluster 3 (VSC3)¹ in Vienna, Austria.

¹<http://vsc.ac.at/systems/vsc-3/>

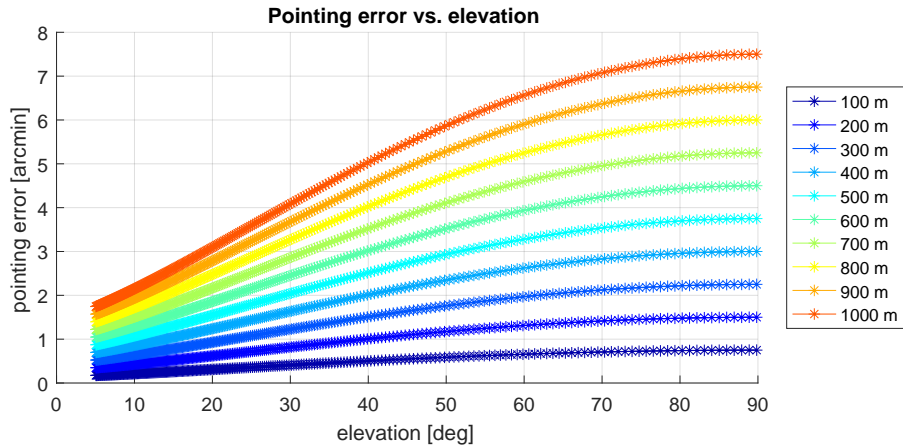


Figure 6.6: Antenna pointing errors caused by different transverse orbit offsets (*color coded*) plotted versus observation elevation. The calculations are valid for the APOD orbit as of November 2016 and a station at sea level.

In the first step, only scans of quasars were correlated in order to establish a priori clock models by applying standard processing with HOPS/fourfit. All recorded (16 MHz) channels were correlated with DiFX by using an integration time of 1 sec and a spectral resolution of 62.5 kHz. While Yarragadee was selected as reference clock, clock models for Hobart and Katherine were determined from strong detections of quasars distributed across the duration of an experiment.

In order to extract the narrow-bandwidth DOR and carrier tones emitted by APOD the zoom-band option in DiFX was used. This enables a sub-channel frequency selection at the correlation stage. 32 kHz wide zoom-bands were centered on all APOD tones in the S- and X-band yielding in total ten zoom-band channels as shown in Tab. 6.3.

Label	Band	Lower Band Edge (MHz)	Bandwidth (kHz)
DOR _{S1}	S	2256.852	32
DOR _{S2}	S	2260.964	32
Carr _S	S	2261.992	32
DOR _{S3}	S	2263.020	32
DOR _{S4}	S	2267.133	32
DOR _{X1}	X	8404.870	32
DOR _{X2}	X	8420.186	32
Carr _X	X	8424.015	32
DOR _{X3}	X	8427.845	32
DOR _{X4}	X	8443.161	32

Table 6.3: Zoom-bands defined in DiFX for the correlation of the APOD observations. The 32 kHz zoom-bands are centered on the DOR and carrier tones in the S- and X-band listed in Table 6.2.

The correlator input models for the APOD scans were calculated in VieVS by applying the processing steps described in Sec. 4.5.2. The near-field delays were modeled by using APOD's final orbit solutions provided by the BACC. The limited accuracy of these orbits (of 10 to 20 m

only, see Sec. 6.1.1) degraded, in turn, the accuracy of the derived delay models.

Detailed investigations showed, that the data collected from APOD and quasar observations, respectively, are consistent. All data were acquired by applying the same observing configuration without any changes in the analog pathway. Zoom-bands as implemented in DiFX do not cause any systematic effects. Hence, there are no intrinsic differences between both data types.

The auto-spectra of Scans 168 and 169 in Session a332 of all zoom-band channels in the S- and X-band are depicted in Fig. 6.7 and 6.8, respectively. While the S-band magnitudes are smooth and stable over time, strong amplitude variations are visible in the X-band data. Most likely, the unstable magnitudes are caused by a slight mis-pointing during satellite tracking. This is clearly indicated by the fact that effects caused by an inaccurate tracking are more pronounced in the X-band, where the beam-width is about four times narrower than in the S-band ($\sim 10.2'$ versus $\sim 38.1'$, see Sec. 6.4). Furthermore, the amplitudes in Scan 169 are even more variable than in Scans 168, reflecting that Scan 169 was observed at higher elevation angles where tracking issues are even more pronounced due to larger change rates of topocentric view directions.

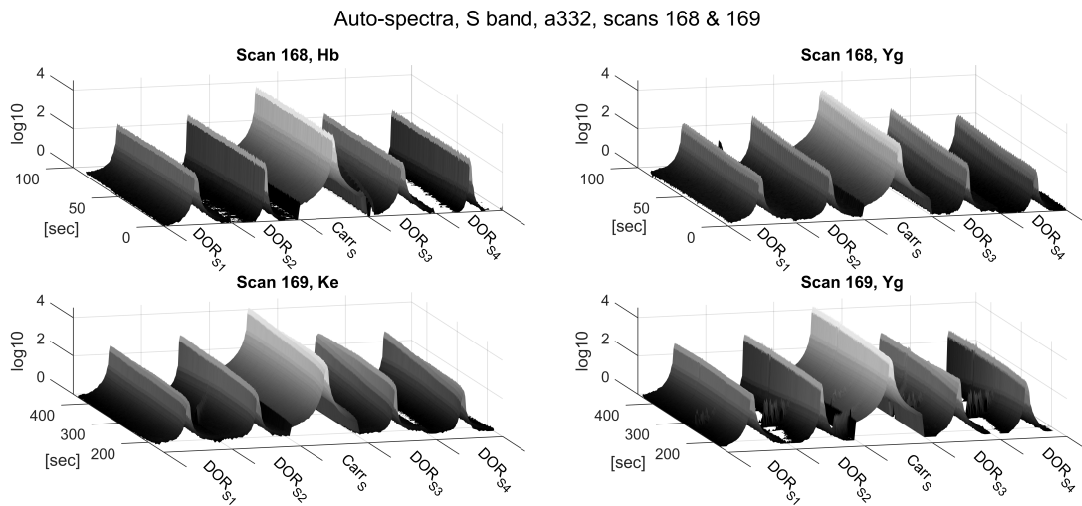


Figure 6.7: Auto-spectra magnitudes of the zoom-band channels in S-band of Scans 168 (upper panels) and 169 (lower panels) of Experiment a332. The (horizontal) frequency axes show all five 32 kHz wide zoom-bands listed in Tab. 6.3 next to one another. The time axes depict seconds since start of Scan 168 (10:41:04 UTC). The depicted auto-spectra were computed with DiFX by applying the processes described in Sec. 4.5.1, exported to fits files, and plotted with MATLAB (from Hellerschmied *et al.*, 2018).

The cross-spectra shown in Fig. 6.9 and 6.10 for the S- and X-band, respectively, reveal similar magnitude patterns. Also here, the S-band magnitudes are more stable over time compared to the X-band. Investigations of the cross-spectra phases, as depicted in Fig. 6.9 to 6.11, lead to the conclusion, that the correlator input model was not accurate enough to stop phase wrapping due to residual delay rates. Due to the (about four times) smaller wavelength, the phases wrap about four times faster in the X-band. Hence, the accumulation time in the correlation process was limited to 0.1 sec, in order not to decorrelate the data.

Finally, the visibility in the native DiFX format was converted to Mk4 databases which are

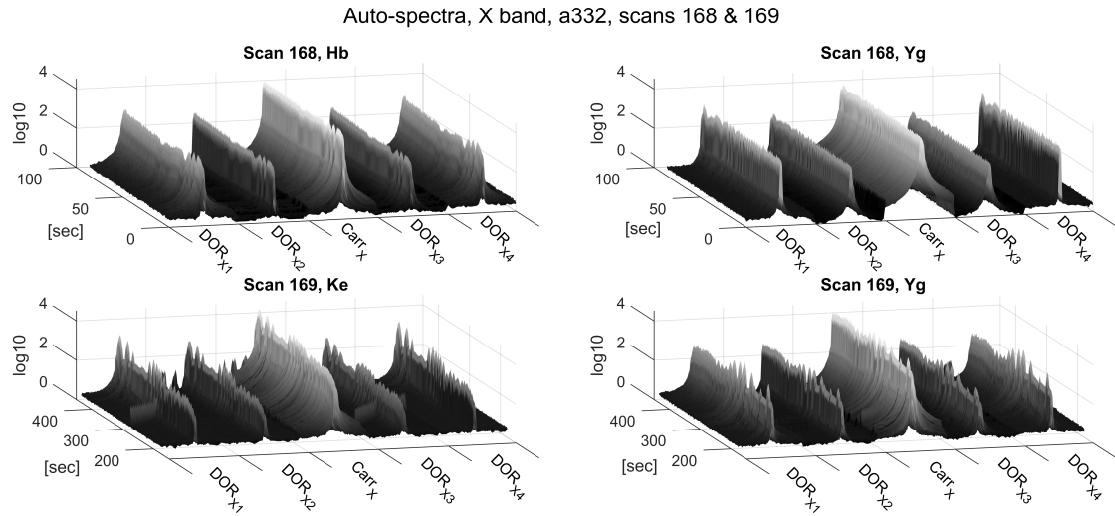


Figure 6.8: Same as Fig. 6.7 for the X-band (from Hellerschmied *et al.*, 2018).

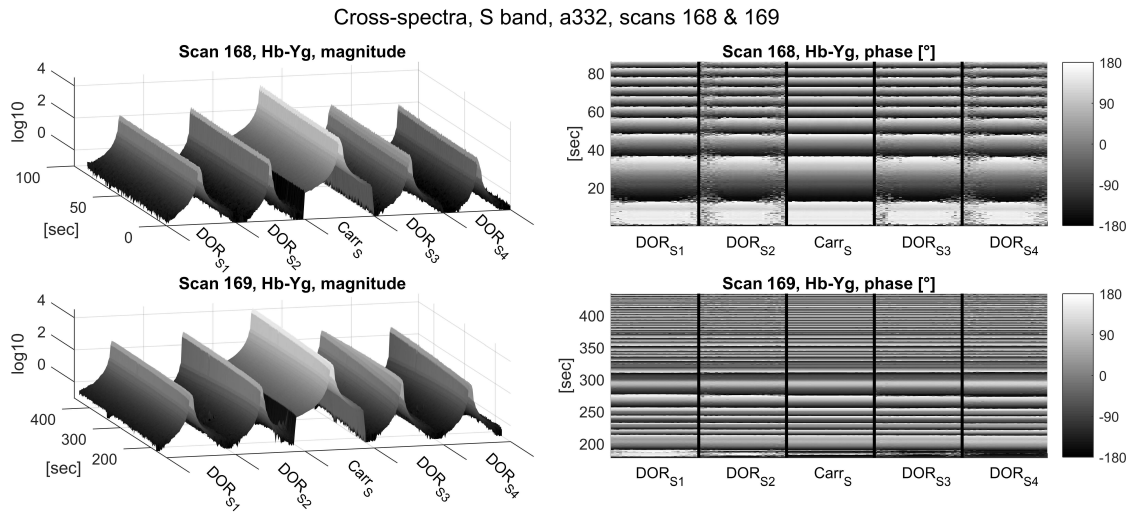


Figure 6.9: Cross-spectra of the zoom-band channels in S-band of Scans 168 (upper panels) and 169 (lower panels) of Experiment a332. Magnitudes are shown in the left and phases in the right column. The (horizontal) frequency axes show all five 32 kHz wide zoom-bands listed in Tab. 6.3 next to one another. The time axes depict seconds since start of Scan 168 (10:41:04 UTC). The depicted cross-spectra were computed with DiFX by applying the processes described in Sec. 4.5.1, exported to fits files, and plotted with MATLAB (from Hellerschmied *et al.*, 2018).

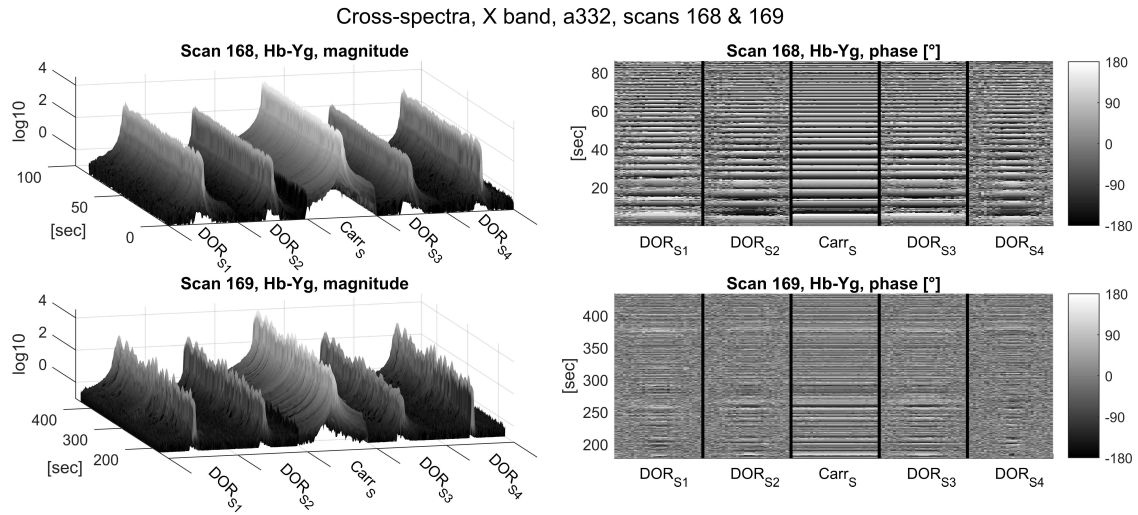


Figure 6.10: Same as Fig. 6.9 for the X-band (from Hellerschmied *et al.*, 2018).

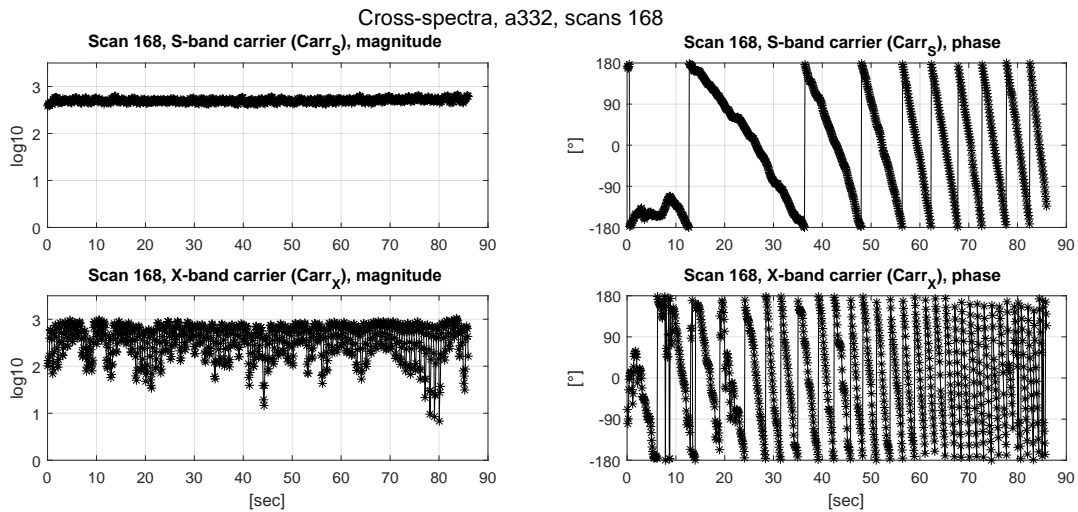


Figure 6.11: Cross-spectra of the APOD carrier tones in the S- (upper panel, $Carr_S$) and X-band (lower panel, $Carr_X$) recorded in Scan 168 in Session a332. The time is indicated in seconds since start of Scan 168 (10:41:04 UTC) (from Hellerschmied *et al.*, 2018).

readable by the HOPS package.

6.6 Post-Correlation Processing

All applied post-correlation processing steps are described in Sec. 4.6, with the most important software component being the fringe fitting program *fourfit* (part of the HOPS package). The fringe fitting of the APOD scans used the visibilities computed for all ten zoom-bands as input. Across the 32 kHz wide zoom-bands the APOD signal is coherent. *Fourfit* was used to fit one multi-band delay for each of the two frequency bands. Due to the residual delay rate, the minimum integration time of 1 sec was used, yielding a 1 sec time-series of delays for each observed APOD track.

On the initial inspection of the computed multi-band delay residuals, large offsets on the order of tens to hundreds of ns between the S- and X-band were found. It was expected, that these offsets were caused by ambiguity issues, i.e. by a combination of a narrow multi-band delay ambiguity spacing and an a priori delay model (used for correlation) not being accurate enough to resolve the ambiguities correctly. The frequency sequence defined by the zoom-bands (see Tab. 6.3) yields a rather narrow ambiguity spacing of 972.8 ns at the S-band and 261.2 ns at the X-band. Manually applying integer multiples of these ambiguities revealed that a constant additional clock offset of $-2.9 \mu\text{s}$ at Hobart and $7.8 \mu\text{s}$ at Katherine removes the large offsets between the two bands¹. It was encouraging to see that the offsets, which are assumed to be related to the orbit modeling or the absolute timing of the observations, stayed approximately the same for all experiments (316a to a332). Another indication of this apparent ambiguity issue is found when applying a manual phase calibration in *fourfit*. A flat residual phase against frequency is obtained, after introducing the additional offsets. This is expected when using zoom-bands that are extracted from the same channel recorded in a common baseband converter, as is the case in the S-band (see Fig. 6.5).

Fringe fitting results for the Scans 168 and 169 in Session a332 are depicted in Fig. 6.12 and 6.13, respectively. While we found clear differences in the correlation magnitudes between the S- and X-band data, the residual multi-band delays and the residual rates are in a good agreement. Throughout all APOD tracks, the time series of both, residual delays and residual delay rates are smooth, as shown in the examples. Small offsets on the ns level between S- and X-band delays reflect the well-known dispersive effect of the ionosphere on microwave signals. In general, the signal-to-noise ratios (SNR) are extremely high, with values typically between 500 and 800 in the S-band. In the X-band the SNR is slightly lower, typically between 200 and 700, and clearly time-variable – reflecting the previously discussed pointing inaccuracies while tracking APOD. The formal delay errors in both bands are typically less than 100 ps.

In order to mitigate first-order effects of the ionosphere, the ionosphere free linear combina-

¹Eventually, refining the a priori delay model (or the underlying orbit data), or manipulating the station clock models, has the same effect. Both approaches relatively shift the recorded bit streams for which (multi-band) delay residuals are estimated.

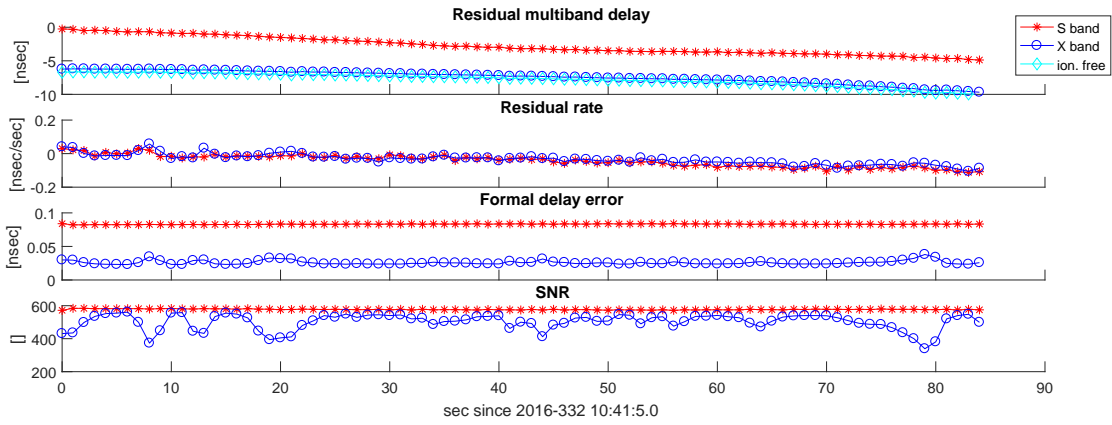


Figure 6.12: Fringe fitting results of Scan 168 in Session a332 computed by fourfit. The time reference indicates seconds since start of this scan (modified from Hellerschmied *et al.*, 2018).

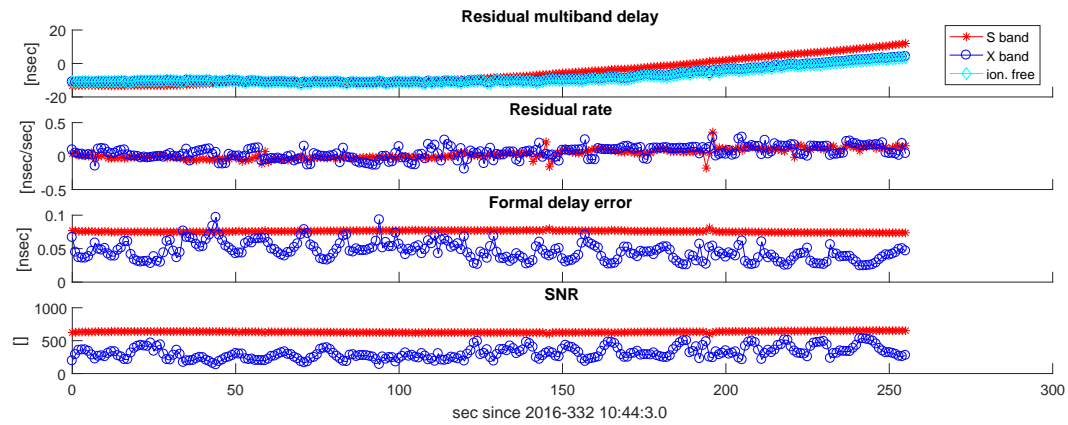


Figure 6.13: Fringe fitting results of Scan 169 in Session a332 computed by fourfit. The time reference indicates seconds since start of this scan (modified from Hellerschmied *et al.*, 2018).

tion of S- and X-band delays was calculated according to Eq. 4.9 (Alizadeh *et al.*, 2013). The ionosphere free delays τ_{if} were computed as linear combination of the observed group delays in the S- and X-bands, τ_{g2} and τ_{g1} , respectively. The multiplicative factors $c1$ and $c2$ are functions of the effective frequencies of the observed S- and X-band channels, $f_{g2} = 2256.85$ MHz and $f_{g1} = 8404.87$ MHz, yielding values of $c1 = 1.0777$ and $c2 = 0.0777$. Hence, the X-band delays get about 14 times larger weights in this linear combination than the S-band delays.

Eventually, the computed multi-band delays (for S- and X-band, and the ionosphere free combination), along with in situ measurements of meteorologic parameters extracted from the station log files, were written to VSO-formatted observation files (VSO type 6, see Tab. 4.1).

6.7 Data Analysis

VieVS 3.0 (see Sec. 4.2) was used to analyze the multi-band delays computed with HOPS/fourfit as described in the previous Section (6.6). In general, VieVS is able to handle both observations types – of artificial satellite signals, as well as of natural extra-galactic radio sources. For this case study, the estimation module in VieVS (VIE_LSM) was upgraded with additional features to estimate satellite position offsets w.r.t. an a priori orbit (see Sec. 4.2.1.4). Per default all parameters are estimated in terms of piece-wise linear offsets (PWLO) by applying a least-squares adjustment on the reduced observations, i.e. on observed minus computed residuals.

The theoretical ("computed") observations are calculated with the near-field delay model outlined in Sec. 4.2.1.3, and by applying standard geophysical modeling in VieVS, as common for geodetic VLBI sessions (e.g. Schuh & Böhm, 2013). The near-field delays are modeled by using the final orbit solutions of APOD as provided by the BACC, see Sec. 6.1.1.

On the observation side, the analysis is based on total delays, which are calculated as the sum of the a priori delays model (used for the correlation) and the residual multi-band delays estimated by the fringe fitting with fourfit. As common in geodetic processing, the observations temporally refer to the signal reception time at station 1 (of a baseline), calculated at integer seconds. Basically, three sets of observation data were calculated in the post-correlation processing (Sec. 6.6), and were available to be loaded by VieVS in terms of VSO files: (1) S-band delays, (2) X-band delays, and (3) the ionosphere free linear combination of observations in both bands. To mitigate influences by the ionosphere, option 3 was used in the data analysis discussed hereinafter, although the quality of the S-band delays – in terms of amplitude stability and SNR, as discussed in Sec. 6.6 – seems to be better.

Multi-band delays were also derived from about 760 scans of quasars observed in Experiment a332 by standard VLBI data processing with DiFX and HOPS/fourfit. The delays were written to an Mk3 database, processed with ν Solve (Bolotin *et al.*, 2014), and exported as a level 4 NGS file. After loading the NGS file in VieVS, a full set of geodetic standard parameters were estimated: station and source coordinates, EOP, ZWD, and station clocks. The WRMS of the post-fit residuals was 38 ps. Fig. 6.14 depicts the ZWD estimates solely based on the scans of quasars in a332.

Then, the ZWD values (estimated from quasar scans) were applied on the APOD observations in a332 to correct for effects caused by the wet fraction of the atmosphere by mapping them to the actual observation directions using the Vienna Mapping Function 1 (VMF1; Böhm *et al.*, 2006).

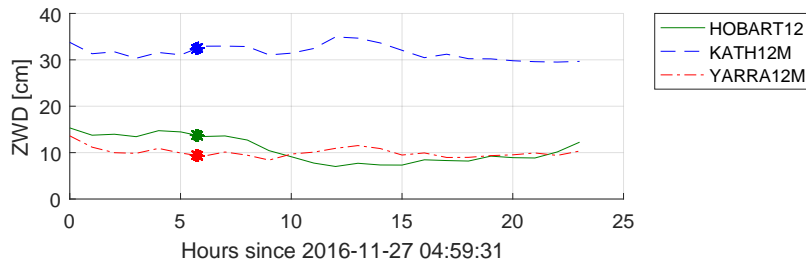


Figure 6.14: Zenith Wet Delay (ZWD) estimates based on the quasars observed in Experiment a332. The observation times of Scans 168 and 169 (APOD observations) are highlighted (modified from Hellerschmied *et al.*, 2018).

6.7.1 Residuals Delays

The O-C residuals enable to assess how well the observed delays match the theoretical delays modeled in VieVS, and to check for remaining systematic features in the data. In order to keep the absolute residuals small, the observations were reduced by the station clock offsets and rates that were previously applied in the correlation step¹. The remaining delay residuals are on the level of about 10 ns for all observed APOD tracks.

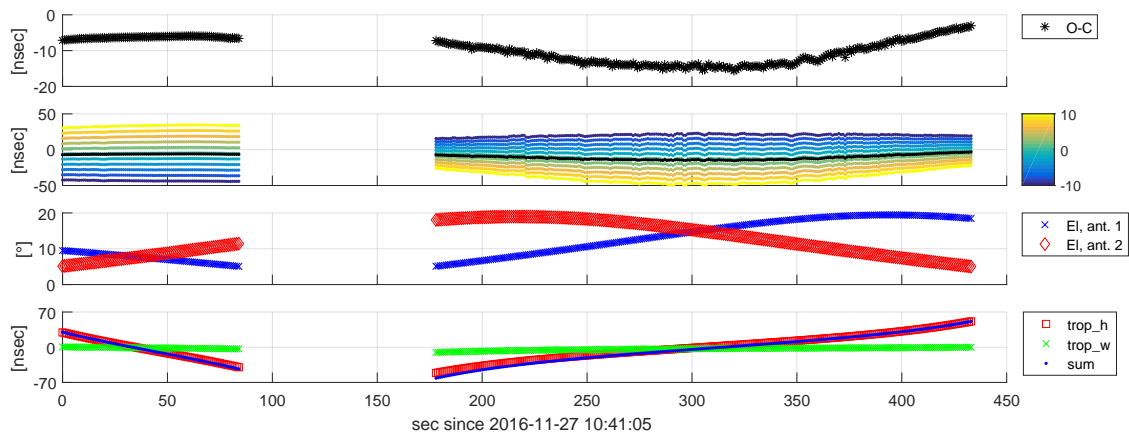


Figure 6.15: Observed minus computed (O-C) delay residuals and modeled delay corrections of Scans 168 and 169 in Session a332. From top to bottom: (1) O-C residuals based on the ionosphere free linear combination, (2) O-C residuals with the APOD orbit being shifted by along-track offsets from -10 to +10 m (*black line* indicates no shift), (3) elevations angles at both stations, and (4) applied corrections for the hydrostatic ($trop_h$) and the wet constituent ($trop_w$) and the sum of both (sum) (from Hellerschmied *et al.*, 2018).

¹Removing the correlation clock model at the observation level has no effect on (geodetic) estimates, because station clocks have to be estimated and reduced anyway.

Fig. 6.15 (*top panel*) depicts the O-C residuals for two consecutive satellite Scans (168 and 169) recorded in Experiment a332. The *bottom panel* shows the major delay corrections applied on the purely geometric near-field delays, targeting the effects of the hydrostatic and wet constituents of the atmosphere. The hydrostatic part (*trop_h*) was computed according to Saastamoinen (1972), by using in situ pressure measurements and the VMF_h mapping function (Böhm *et al.*, 2006). Reductions for the wet part (*trop_w*) were modeled by mapping the ZWDs estimated from quasar observations in a332 (see Fig. 6.14) to the slant directions using the VMF_w mapping function (Böhm *et al.*, 2006). The sum of both constituents is in a range between -61 ns and +51 ns, and reduce the (elevation dependent) effects of the troposphere to a large extent. Compared to the tropospheric influences, other corrections are relatively small and, therefore, not explicitly shown: effects of the antenna axes offsets (max. 44 ps), thermal antenna deformations (max. 1.8 ps; Nothnagel, 2009), and gravitational effects on the near-field delays according to Klioner (1991) (max. ± 24 ps).

Compared to Scan 168, the O-C residuals in Scan 169 are much noisier. Considering the elevation angles at which both scans were observed (Fig. 6.15, *third panel*), we believe that the larger scatter in the second Scan is caused by tracking issues, which are more pronounced at higher elevations.

Investigating the O-C residuals we find systematically curved features throughout all APOD tracks. This characteristic bending signature is strongly pronounced in Scan 169, yielding a variation in the residual delays of about 12 ns during this track. At the first glance, it appears as if this distinct bent shape is caused by some kind of elevation-dependent effect, e.g. caused by the troposphere or the ionosphere. However, detailed investigations led to the conclusion that these systematics are caused by a constant offset in the satellite's along-track position in the orbit data that was used for modeling the theoretical delays. Typically, the largest uncertainties in the orbit determination are present in the along-track direction, especially in the case of LEO satellites due to the predominant effect of the atmospheric drag, which is constantly decelerating the satellite (e.g. Swatschina, 2012 and Bae, 2006). Considering the low quality of the used orbit data (see Sec. 6.1.1), deviations of ± 10 m (or even more) along-track can be expected. For example, if we apply a constant along-track orbit offset of -8 m, the bending signature in the Scans 168 and 169 completely vanishes. The remaining constant offsets between the two scans can be explained by uncorrected stations clocks. This is shown in the *second panel* in Fig. 6.15. The depicted O-C time series were derived from the same observation data, but with different constant along-track orbit offsets (from -10 m to +10 m, color coded) applied when modeling the computed delays.

The presence of these systematic features caused by severe orbit inaccuracies, leads to the conclusion, that it is mandatory to estimate orbit parameters along with other (geodetic) estimates. Otherwise, unmodeled orbit errors would propagate into other estimates, e.g. of ZWD, or station coordinates, etc. – depending on the observation constellation. Accordingly, a simple test case is discussed in the next Section, where the presented O-C values are used for parameter estimation in VieVS.

6.7.2 Parameter Estimation – A Simple Test Case

Based on the O-C residuals discussed in the previous Section, station clock offsets, ZWDs, and orbit offsets were estimated in VieVS. The analysis was confined to these parameters, as it was not sensible to consider further estimates, such as station coordinates and EOP, based on the available observation data. All target estimates were parametrized in terms of piece-wise linear offsets (PWLO; Schuh & Böhm, 2013) with intervals of 30 min, and extremely tight relative constraints of 0.01 mm were applied. This approach basically yields one constant offset per parameter, which is valid for the duration of the whole session. Station Yg was selected as clock reference. Satellite orbits were estimated in terms of PWLO w.r.t. the a priori orbit in the satellite coordinate system (radial, along-track, cross-track). The partial derivatives were derived by differentiating the observation equation by Klioner (1991) w.r.t. the GCRF satellite positions (see Sec. 4.2.1.4) and by applying a subsequent rotation into the satellite coordinate system. Parameters were estimated in a least-squares adjustment based on the delays of the ionosphere free linear combination and by using corresponding formal delay errors for weighting the observables. The formal errors for the ionosphere free linear combination were derived by combining the formal errors of the S- and X-band delays (presented in Fig. 6.12 and 6.13) according to Equ. 4.9.

The post-fit residuals are shown in Fig. 6.16, yielding a WRMS of 9.5 cm. The residuals of Scan 168 show much less scatter than those of Scan 169, which reflects the pattern of the O-C values (Fig. 6.15) and of the multi-band delay residuals (Fig. 6.12 and Fig. 6.13), respectively.

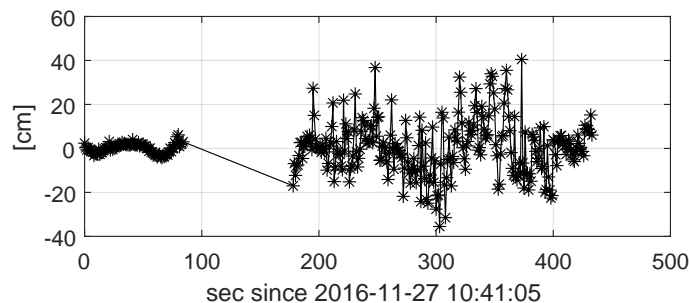


Figure 6.16: Post-fit residuals of Scans 168 and 169 in Session a332 when estimating constant offsets for station clocks, ZWD, and the satellite orbit. The WRMS of the residuals is 9.5 cm.

The estimates along with their formal errors are presented in Table 6.4. The clock estimates are within a realistic range, although their formal errors are quite large with about 2 m. The ZWD at the stations were estimated in addition to the ZWD derived from the quasars observations (see Fig 6.14) which were used to correct the computed delays a priori. The estimates are in the range between 3.4 cm and 14.3 cm. This results in a rather high ZWD at Ke of ~ 46 cm in total. The estimated orbit offsets are within the range of our expectations considering the limited initial accuracy of the used orbit solution. As expected, the along-track offset is by far the largest with -7.8 m. Furthermore, it does satisfy well our expectations of the along-track error being about -8 m, as discussed in Sec. 6.7.1. Estimates of the station clocks and the cross-track orbit offset are highly correlated due to the limited observation geometry. This yields the comparably large

uncertainties in these parameters.

Parameter	Estimate	Formal error
ZWD, Hb	3.4 cm	1.7 cm
ZWD, Ke	14.3 cm	2.1 cm
ZWD, Yg	7.3 cm	1.7 cm
Clock offset, Hb	14.0 m	2.3 m
Clock offset, Ke	-1.1 m	1.9 m
Orbit, radial	1.2 m	0.3 m
Orbit, along-track	-7.8 m	0.3 m
Orbit, cross-track	-1.9 m	1.3 m

Table 6.4: Estimates of Scans 168 and 169 in Experiment a332.

However, considering the non-ideal circumstances, such as relatively short scan times, constantly low observation elevations, low quality of the available orbit solution, tracking issues (more pronounced in Scan 169), and the non-ideal network geometry, which only allows for the observation of single-baseline scans, the estimation results of this test case are well within our area of expectations.

6.8 Discussion and Outlook

Although APOD is an exceptionally interesting mission, considering the geodetic payload, and allows for practical case studies towards frame interconnections, it was hardly observed by VLBI. One reason for the lack of VLBI observations was, that suitable observation and data processing strategies were not fully developed and prepared for this mission. Hence, the presented case study – representing an end-to-end realization of VLBI observations of APOD – was the only coordinated attempt to observe this satellite over multiple passes. By the example of Experiment a332 all applied processing steps were introduced and discussed, yielding results in terms of O-C residuals on the level of a few ns.

However, this study also revealed some limitations. A major issue was the rather bad quality of the available orbit solutions for APOD. The malfunction of the on-board GNSS receiver which was used for the POD led to a drop in the orbit accuracy from initially a few cm to the level of 10 to 20 m only – with wide-ranging consequences on different stages of this study. Additionally, orbit predictions used for satellite tracking showed offsets of up to about 1 km compared to the final orbit solutions, which were used to compute theoretical near-field delays for correlation and analysis. On the observation level, the inaccurate tracking data, in combination with potential deficiencies of the AZEL tracking mode of the ACUs, resulted in pointing errors of a few arc-minutes. This mis-pointing was large enough to cause amplitude variations and a time-variable and low SNR in the X-band (compared to the S-band), where the beam-width is about four times smaller than in the S-band. On the data processing level, the low quality of the final orbit solutions degraded the accuracy of the computed delays in turn. Consequently, the correlator input model

was not accurate enough to fully stop phase wrapping, and the residual rates only allowed for using short accumulation periods of 0.1 sec without introducing decorrelation. Concerning the data analysis, the severe inaccuracies in the orbit data made it mandatory to estimate orbit parameters. The APOD observations in Session a332 were exemplarily used to successfully validate newly implemented features in VieVS, enabling the estimation of orbit position offsets in terms of piece-wise linear offsets (which refers to a kinematic orbit modeling approach). However, the presented orbit estimation can only be considered as validation scenario. In order to estimate reliable and high quality orbit parameters a global tracking network would be required, rather than a regional one, such as the AuScope VLBI array. Globally distributed observations would enable to cover complete orbit arcs and to observe by far more satellite scans in total.

Considering the issues caused by the inaccurate orbit data it would be beneficial to use SLR observations (additionally to GNSS measurements) to improve the orbit determination. Due to the low orbit of APOD, and the low elevation at which most of the APOD tracking data are collected, SLR measurements could not only be used to calibrate orbit errors in radial direction, but also in along-track direction. According to Arnold *et al.* (2018), SLR is able to contribute along-track corrections on the mm-level and, thus, substantially improve the overall orbit accuracy. Our colleagues from BACC (group of Dr. Jianfeng Cao) tried to integrate the available SLR observations in the orbit determination process. Unfortunately, SLR measurements were sparsely available at the times VLBI observations were performed. Hence, this attempt was not successful due to the insufficient number of SLR observations. For future experiments it is highly recommended to better coordinate SLR tracking campaigns with VLBI observations.

Despite all difficulties, multi-band delays – based on zoom-bands used to extract the APOD signals from the recorded bands – could be obtained from all observed APOD tracks. For the sake of brevity, only one experiment is discussed in detail, choosing a332 as a representative example. The residual multi-band delays of all tracks show similar characteristics in terms of magnitude (time variable in the X-band), scatter (S-band is always smoother than X-band), and SNR (higher and more stable in the S-band). Investigations showed, that systematic signatures present in the (O-C) delay residuals were mainly caused by along-track errors in the orbit data that were used for modeling the computed delays. Additionally, mis-pointing of the antennas could have caused small systematic effects, as APOD was observed with slight off-axis angles. Considering all observed APOD tracks, the delays show a larger scatter with increasing elevation (especially in the X-band), indicating that improved tracking features utilizing more accurate orbit data would be highly beneficial.

The experience gained through the discussed experiments allow us to provide some suggestions for future experiments applying a similar observation approach. In general, the observation geometry determined by continental-wide baselines (between 2360 and 3432 km) and the very low orbit of APOD (about 450 km) strongly limited common visibility of the target, only enabling observations of single-baseline tracks during one to three overpasses per day. Furthermore, observations are restricted to elevation angles lower than 40° . While on the one side shorter baselines would enable observations of longer tracks with a larger variation in the elevation angle, globally

distributed tracking stations are a prerequisite for accurate orbit determination. Hence, further studies towards suitable observation networks for LEO satellites are recommended as preparation for future missions. The S- and X-band signals emitted by APOD are not ideal for the determination of group delay observables in a way common in geodetic VLBI. The redundantly spaced DOR tones yields a very narrow ambiguity spacing that has to be dealt with in the data analysis by adjusting the derived S- and X-band delays. A broad-band noise signal would be more suitable. However, DOR tones are suitable for other tracking techniques, such as Doppler ranging, and the power consumption is in general much lower compared to a broadband transmitter. Our experiments showed that adequate satellite tracking features are a key requirement for observations of LEO satellites. A step-wise tracking approach, as widely used for observations of GNSS satellites, is not applicable due to the high change rates in the topocentric pointing directions. While most of the legacy VLBI antennas do not provide dedicated satellite tracking functions, new VGOS-type antennas usually have such features, such as tracking modes using TLE data. Although suitable tracking capabilities are commonly neglected in simulation and feasibility studies, they are important to consider when designing the future global VLBI network in the view of co-location satellite missions. On the observation level, the integration of the ACU's AZEL tracking mode in the station-specific code of the Field System is still pending. This would be necessary to control satellite tracking via the Field System, and would be another step towards a rigorous automation of satellite observations based on VEX schedules

Concerning the data analysis features in VieVS we plan to take into account correlations between individual observations by using full covariance information rather than variances only. This is particularly important for observations being only sparsely separated in time and space, as it is the case in the presented study. Covariances could be modeled for example applying Kolmogorov's turbulence theory (Kolmogorov, 1991) as outlined by Pany *et al.* (2011). This study also showed that a sophisticated dynamic orbit model is highly beneficial for the analysis of future experiments. Considering a rather low number of observed tracks, and a non-ideal distribution of tracking stations around the globe – both circumstances will probably not improve drastically for experiments in the near future – a dynamic orbit modeling approach is more suitable than the purely kinematic approach currently implemented in VieVS. Therefore, it is planned to update VieVS with a suitable model.

Although the current set of observations is still not sufficient – mainly in terms of geographical distribution and total number of observations – to study actual frame ties, this work is valuable due to the gained experience in terms of observation, data processing, and analysis strategies for VLBI satellite observations. The applied observation and data processing schemes can be easily adopted for the specific requirements of future experiments, and hopefully help to be better prepared for upcoming co-location satellite missions.

Chapter 7

Discussion and Outlook

In the introduction (Chap. 1) the two main objectives of this work were outlined. The first task was to establish a complete end-to-end process chain that enables to carry out VLBI observations of Earth satellites in a semi-automatic manner, and by using standard procedures common in geodetic VLBI as far as possible. This part of the work is introduced in Chap. 4. It provides comprehensive guidelines for this specific application of VLBI. The second goal was to apply the established process chain for real experiments in order to collect actual observation data – which were widely missing so far – and to study and interpret the results. This was accomplished in the frame of two major case studies. In 2015 and 2016 a series of experiments was performed mainly on the Australian baseline Hobart-Ceduna in order to study VLBI observations of GNSS satellites (see Chap. 5). End of 2016 the Chinese APOD-A nano satellite – a first realization of a co-location satellite with VLBI, combining VLBI, SLR, and GNSS on a LEO satellite – was extensively observed by the AuScope VLBI array (see Chap. 6). Both case studies provided plenty of opportunities to test, validate, and further improve the underlying processes for scheduling, observations, correlation, and analysis.

While experiment-specific characteristics, limitations, and possibilities are already discussed in the corresponding chapters, in Sec. 5.8 (observations of GNSS satellites) and Sec. 6.8 (observations of APOD), respectively, more general aspects shall be discussed hereinafter. Besides reviewing the findings of the conducted observation experiments in a broader and more general context, future perspectives, and potentials for improvement shall be outlined.

Scheduling and observations Basically, all processes are in place to easily carry out further VLBI experiments including observations of satellites, as described in Chap. 4. However, there is still some room for improvements. Especially on the observation level, some workarounds are still required in order to include satellites as observation targets into the stations' observing routines. There is still no standardized approach within the geodetic VLBI community for how to treat satellites in the observation process.

Although the satellite scheduling program in VieVS (see Sec. 4.3) provides extensive capabilities for the planning of VLBI satellite observations, including flexible options for the integration

into classical geodetic VLBI schedules with observation of natural radio sources, the currently used standard scheduling file formats – VEX and skd – do not support satellites (or near-field targets in general) as observation targets. Basically, one would need to extend e.g. the VEX format (which is the more modern format) for possibilities to flag sources as near-field targets and to include orbit data in a suitable way. Orbit data is required for several purposes during a VLBI experiment. For scheduling, for satellite tracking during the observations, and for the calculation of modeled near-field delays required for the correlation (correlator input model) and the parameter estimation (e.g. linearization of the observables for a least-squares adjustment). While only orbit predictions are available at the time of observation, and for the observation planning, respectively, more consistent and accurate orbit solutions should be used for the delay modeling. For satellite tracking, orbit data could be added either directly to the schedule file, e.g. in terms of TLE data (which is a suitable format for this purpose due to its compact size), or by referencing to external orbit data files. Although adding orbit data directly to the schedule file would make observations less error prone, because everything needed is contained in a single file (as it is the case for standard VLBI experiments), the orbit data would probably still have to be updated shortly before an experiment is started in order to enter to most recent predictions. Another useful option, which is needed if the stations (i.e. the Field System, or the antenna controllers) are not able to directly process orbital elements, would be to include station-dependent source coordinates, e.g. in terms of azimuth and elevation angles. This is needed to enable cross-eyed observation configurations (see Sec. 3.3.1), without having individual schedule files for each station. Currently, the common workaround for the inclusion of satellites in the schedules files is to define them like astronomical sources in terms of discrete positions given by topocentric right ascension and declination – enabling a stepwise tracking approach as described in Sec. 3.4.1. The shortcoming concerning the schedule file formats could be solved by using the VEX 2.0 format¹, which was already drafted in 2014, after proposing that VEX 1.5b1 needs to be updated to meet the evolving requirements of VLBI operations in 2009². VEX 2.0 would allow to define new source types suitable for satellites and to include orbit data in terms of TLE datasets, Kepler elements, or ephemeris data for NASA's SPICE toolkit³ (so-called SPICE Kernels⁴).

The next item in the VLBI process chain is the Field System (FS) utility `drudg` (see Sec. 4.4), which extracts the station-relevant information from the VEX files and writes local control files for the FS containing snap-formatted control commands. Also `drudg` would have to be updated – along with the format of the global schedule files – in order to write dedicated snap commands enabling satellite tracking, while maintaining the control of all VLBI stations features via the FS. Since version 9.11.2, the FS supports dedicated snap commands for satellite tracking and provides features to calculate stacks of azimuth and elevation angles based on TLE data, which can be used

¹The VEX 2.0 format is defined at <https://safe.nrao.edu/wiki/bin/view/VLBA/Vex2doc>.

²See <https://safe.nrao.edu/wiki/bin/view/VLBA/Vex2>.

³SPICE is an observation geometry system for space missions, developed and maintained by NASA's Navigation and Ancillary Information Facility (NAIF), see <https://naif.jpl.nasa.gov/naif/index.html>.

⁴See <https://naif.jpl.nasa.gov/naif/data.html>.

for satellite tracking (see Sec. 3.4.2.2 for more details). However, the current FS implementations are tuned to be used with TLE orbit data only. Within the VLBI community there are also plans to integrate (parts of) the SPICE toolkit into the FS in order to enable antenna motion control and satellite tracking based on SPICE kernels. Therefore, as well as for the use of other kinds of orbit data, new snap commands would have to be defined, and drudg would have to be adopted accordingly.

Although commonly neglected in simulation studies, the experiments introduced in Chap. 5 and Chap. 6 showed, that accurate satellite tracking is a key requirement needed to obtain high quality observation data. The APOD experiments showed that observations of such fast LEO satellites are not feasible without dedicated tracking capabilities on the station level. Although a dedicated tracking mode was used (AZEL tracking mode, see Sec. 6.2.1), tracking inaccuracies still caused variable SNR and signal amplitudes. Tests at the Onsala Space Observatory (Sweden) and with the AuScope VLBI network (Australia) showed that in case of LEO satellites the workaround of stepwise tracking is not applicable. Even when observing GNSS satellites, as discussed in Chap. 5, where the situation is much more relaxed due to the higher orbit and the low slew rate requirements, artifacts from the stepwise tracking were found in the data (see Sec. 3.4.1). While most legacy VLBI antennas do not provide suitable tracking modes for satellites, most new VGOS-type antennas are equipped with such features. Commonly, the antenna controllers are directly able to load and process TLE data in order to continuously track satellites by precisely adopting the antennas slew speeds and accelerations. One example for antennas providing such features are the new VGOS twin telescopes at the Geodetic Observatory Wettzell (GOW). However, any satellite tracking features – either those provided by the FS, or directly by the antenna controllers – have to be enabled in the FS by programming the interface between the FS computer and the antenna control unit. There is no default way on how to do that, as the antennas’ communication interfaces are not standardized and the satellite tracking modes differ between the hardware manufacturers.

Correlation and post-correlation processing Basically, the only difference between the correlation processes of near- and far-field targets is the a priori delay model (correlator input model) that is used to initially align the two data-streams for the cross-correlation. For our experiments we applied DiFX, a highly versatile VLBI correlation software, which is widely used in the geodetic VLBI. Starting with DiFX version 2.5.1 an implementation of CALC 11 is available in DiFX through a program called *difxcalc* (Gordon *et al.*, 2016). In future, CalcServer (enabling CALC 9) should be phased out in favor of *difxcalc*, which is able to calculate input models for near-field observations by using different delay models (see Sec. 4.5.2). Information on the positions of near-field targets can either be inputted via state vectors (three-dimensional positions and velocities in the GCRF), or by referring to SPICE kernel files in the DiFX control files¹. Hence, *difxcalc* enables

¹More information on handling near-field targets in DiFX is provided at <https://www.atnf.csiro.au/vlbi/dokuwiki/doku.php/difx/spacecraft>.

to seamlessly introduce near-field targets to the DiFX environment. However, when testing difxcalc (difxcalc-11.0, personally provided by D. Gordon in February 2016) for the correlation of observations of GNSS satellites and of the APOD satellite in 2016, we still experienced significant discrepancies between the near-field delays calculated by the different models included in difxcalc. Furthermore, it was still not possible to control all features of difxcalc by the default DiFX control file (the .v2d file). For example, it was not possible to set delay polynomial intervals different than 120 sec, although shorter intervals were required for APOD in order to describe the high change rates in the delay accurately. For those reasons, we calculated the near-field delays in VieVS and inserted them to the DiFX delay model files (.im files), as described in Sec. 4.5.2. Although VieVS worked well, it is still a kind of detour, requiring additional working steps. Of course, it would be preferable to have a straightforward solution for the calculation of input models for near-field observations, consistent with the way it is done for standard observations of astronomical sources. Basically, the centerpiece, i.e. the program difxcalc, is already in place, but some refinements are still necessary to enable all features in a standardized way.

The HOPS package was used for the post-correlation processing, including the fringe fitting program fourfit that is commonly used in geodetic VLBI for the estimation of (single- and multi-band) group delays. Initially, fourfit was designed for geodetic legacy VLBI systems and observations of circular polarized signals in the S- and X-band. Being designed for a specific purpose, fourfit is rather inflexible. For example, it is not possible to define integration times shorter than 1 sec, which limits the temporal resolution of the delays when observing strong satellite signals (allowing for sub-second integration times) over longer tracks. Hence, for the investigation of temporally highly variable signatures in the data AIPS was used instead. In preparation for the evolving VGOS broadband systems (all currently available broadband receiver systems used for VGOS record in two orthogonal linear polarizations, referred to as X and Y), fourfit was recently updated with features to form the Stokes pseudo-I mode combination of the polarization products XX, YY, XY, and YX¹. Theoretically, this would enable to derive a single delay for each observed frequency band, as required for the observations of GNSS satellites on the baseline Hobart-Ceduna described in Chap. 5. However, a prerequisite for the combination of the different linear polarization products is a stable gain in the receiver, which is still a pending problem. As demonstrated in Experiment g336 (see Sec. 5.5.1), a stable gain could be maintained by deactivating the automatic gain control in the DBBC while recording. However, this needs manual interactions, and, therefore, is only feasible for tests. For operational applications, options that are more suitable have to be investigated. Fourfit is also rather inflexible concerning signal calibrations. For example, fourfit does not provide any options to apply bandpass calibrations based on observations of a selected calibrator source, as it is common for astronomical applications of VLBI. Fourfit works purely scan-wise and is not able to transfer any information between scans. An alternative software for fringe fitting is PIMA (Petrov *et al.*, 2011), which provides more flexibility and calibration options. First tests for applying PIMA on satellite observation data are planned for the near future.

¹For more information see https://www.haystack.mit.edu/tech/vlbi/hops/fourfit_3.7_features.pdf.

Analysis of VLBI satellite observations Regarding satellite observations, one shortcoming in the analysis chain is, that current standard formats for observation data (NGS and vgosDB) do not provide possibilities to distinguish between scans of near- and far-field targets. Therefore, a suitable observation file format (the VSO format, see Sec. 4.2.1.1) was defined. Although this new file format fulfills all requirements in order to load and analyze satellite observation data in VieVS, a community-wide standardized observation data format would be preferable. As the production of NGS card files will be dropped by the IVS mid of 2018, it would be desirable to expand the vgosDB format for the possibility to explicitly include satellites additionally to astronomical sources. Besides a priori delays, total group delays (actual observables), and delay rates for near-field observations, etc., also satellite positions should be handled in the vgosDB format in a convenient way. This has to be discussed in the broader VLBI community in order to find a solution that is suitable for all desired applications.

Another critical aspect in the data analysis is the estimation of satellite orbit parameters. Currently, VieVS only provides basic features to estimate piece-wise linear offsets on top of a priori orbits – which refers to a kinematic orbit determination. However, considering a rather low number of observed satellite tracks and a non-ideal distribution of tracking stations, a dynamic orbit modeling approach would be highly desirable. Currently, there is effort in the VieVS developers group to implement features for the analysis of SLR observations. Along with the program extension toward full compatibility with the SLR technique, it is planned to add a sophisticated orbit modeling module. This will then also be usable for satellite observations with VLBI, and – eventually – should enable an orbit determination based on the combination of observations by VLBI and SLR.

Alternatively, other analysis software packages could be used, such as C5++ (Hobiger *et al.*, 2010). It provides features to estimate satellite orbits based on VLBI observations and was used, for example, for analyzing observations of GNSS satellites as described by Hobiger *et al.* (2018).

Observation targets Throughout the experiments discussed in this work, two different types of satellites were observed: GNSS (GPS and GLONASS), and the Chinese APOD-A nano satellite. Both target types had intrinsically different characteristics. While GNSS satellites are in a rather high orbit at about 20,000 km, APOD orbits the Earth in an altitude of only about 450 km. While GNSS satellites transmit in the L-band, the VLBI beacon of APOD emits in the S- and X-band. Observing such different targets meant, that the process chain had to be adopted to the specific requirements of the observed satellites. On the other hand, it enabled to gain a broad spectrum of observation experience, and to investigate different satellite mission characteristics for their suitability towards VLBI observations.

Concerning orbit characteristics, APOD put stringent demands on the tracking capabilities of the ground station network due to its low orbit. Even when applying the AZEL tracking mode of the AuScope antennas (see Sec. 6.2.1), accurate tracking was still problematic – especially at higher elevations. Besides the implementation of suitable tracking modes on the station level (which is a key requirement, as mentioned above), accurate orbit predictions are required for

calculating the tracking data. Inaccuracies of up to 1 km in APOD's orbit predictions caused a mis-pointing on the level of several arc-minutes, resulting in severe amplitude variations in the recorded X-band signals (see Sec. 6.5). Also the low accuracy of the final orbit solutions for APOD (calculated in the post-processing, see Sec. 6.1.1) was a limiting factor throughout the case study, as this limited in turn the accuracy of the modeled delays required for correlation and data analysis. Hence, for future experiments it is highly recommended to coordinate VLBI observations with observations by SLR, as far as possible. Having an alternative way to determine accurate orbit elements would have helped tremendously when dealing with the APOD observation data. Furthermore, simultaneous observations with SLR and/or GNSS are a requirement for actual frame tie studies, as soon as the VLBI observations have reached a sufficient accuracy level.

Our experiments showed that neither the GNSS L-band signals, nor the S- and X-band DOR tones transmitted by APOD were ideal for deriving group delay observables as common in geodetic VLBI. For observations of the GNSS L-band signals, suitable L-band receivers are required, whereas many VLBI antennas used for geodesy lack such capabilities. Even antennas with L-band capabilities are often not able to capture the GPS L2 signals at 1227.60 MHz, because they are already out of the nominal frequency range (e.g. at Medicina, Italy). Even broadband receivers following the VGOS design specifications (see Sec. 2.3) will not cover the GNSS L-band frequencies below 2 GHz. One potential workaround – which requires more detailed investigations – would be to observe harmonics of the L-band signals at higher frequencies (according to personal communication with James Anderson, GFZ, Germany). The situation is different with APOD's DOR tones (see Sec. 6.1), which can be recorded by standard S/X VLBI systems. However, the DOR tones are not ideal, as they yield a very narrow ambiguity spacing (due to the redundant spacing of the tones), and only provide a limited frequency span. Other issues were caused by the extremely high power level of the observed satellite signals, compared to the faint natural radio sources. Although, the high power levels enabled to apply very short accumulation times in the correlation (while still yielding extremely high SNR), the automatic gain control systems of the DBBCs had problems to maintain an optimum signal level, as discussed in Sec. 5.5.1. Strong signals could also lead to a saturation of the receivers low noise amplifiers, yielding gain non-linearities, and a compression effects. At some stations, additional attenuators in the signal chains might be required in order to prevent such effects. This has to be investigated at individual stations before satellite observations are performed. For the computation of group delays as common in the geodetic VLBI, a simple broadband noise beacon would be preferable – imitating the characteristics of natural radio sources. Although such beacons are rather simple in design (basically a noise diode as signal source plus amplifiers and an antenna), there are still some open issues regarding the power consumption (which might be much higher compared to the transmission of discrete tones), and the frequency allocation which has to be consistent with the according ITU regulations¹.

Lately, there is effort in the geodetic community to install dedicated VLBI signal beacons on the

¹See <https://www.itu.int/>.

next-generation Galileo satellites, as discussed in Sec. 3.2. The Galileo II satellites are currently in the definition phase and should be deployed in 2025. It was proposed (e.g. by Petrachenko, 2016) to equip them with small VLBI transmitters in addition to the L-band antenna arrays that emit a low power broadband noise signal in a frequency range of 3 to 14 GHz. Such signals would be compatible with modern VGOS broadband receiver systems and the broadband noise would facilitate the derivation of delay observables with standard procedures of the geodetic VLBI. A small point-like source with a well defined phase center would mitigate issue with the calibration of phase center offsets as present when observing the L-band ranging signals with VLBI. Without doubt, Galileo satellites with proper VLBI capabilities (in addition to GNSS and SLR) would open unprecedented opportunities regarding technique co-location in space.

Station networks All experiments discussed in this thesis were observed on intra-continental baselines on the Australian continent, with lengths between about 1,700 and 3,400 km. These intra-continental baselines provided excellent (common) visibility of GNSS satellites (also see Fig. 3.2). However, the baseline lengths given by the AuScope network strongly limited common visibility of the APOD satellite on its very low orbit and only enable to observe a relatively small number of single baseline scans per day. Hence, for LEO satellites shorter baselines would be recommended. To find suitable network constellations for VLBI observations of LEO satellites, dedicated simulation studies would be desirable. The geographical distribution of the tracking stations is also highly important once the VLBI observations should be used for orbit determination. A globally distributed VLBI station network would be required in order to estimate reliable and accurate orbit parameters, eventually enabling frame-tie studies.

Concluding this work, it was shown that basically all processes required to observed artificial satellite signals in a geodetic VLBI mode – from scheduling to the analysis of group delays – are in place. Although the established process chain was successfully tested by conducting two series of experiments, observing satellites of the GNSS and the APOD satellite, there is still room for improvement, especially with regard to automation and standardization of observations, and a smooth interconnection of processes. This work is a solid basis for further refinements and developments in the field of VLBI observations of satellites. It hopefully helps to bring this novel observation approach soon to the next level in order to reach an accuracy level relevant for geodetic applications – paving the way for establishing actual space ties with VLBI.

Appendix A

Scheduled VLBI Experiments With Satellite Observations

Between 2014 and end of 2016 the author scheduled 47 VLBI experiments with satellite observations (which were actually observed) with the VieVS satellite scheduling program (see Sec. 4.3). A complete list is shown in Tab. A.1.

Table A.1: VLBI experiments with satellite observations scheduled by the author with VieVS between 2014 and 2016. For listing the observation targets the following abbreviations are used: *GLO* (GLONASS satellites), *GAL* (Galileo satellites), *GPS* (GPS satellites), *BD* (Beidou satellites), and *Q* (quasars). The observed frequency bands are indicated in the last column (*comments*) in parentheses.

exp. code	date	dur.	stations	targets	PI	comments
G140116a	2014-01-16	1 h	O8, Wz	GLO	R. Haas & A. Neidhardt	Test new tracking and receiver features at Wz (L1)
G140116b	2014-01-16	1 h	O8, Wz	GLO	R. Haas & A. Neidhardt	Test new tracking and receiver features at Wz (L1)
G140121a	2014-01-21	1 h	O8, Wz	GLO	R. Haas & A. Neidhardt	Test new tracking and receiver features at Wz (L1)
G140121b	2014-01-21	1 h	O8, Wz	GLO	R. Haas & A. Neidhardt	Test new tracking and receiver features at Wz (L1)
615aHo	2015-06-15	1 h	Ho	GLO, GPS	J. McCallum	1 st tracking test
169cHo	2015-06-18	1 h	Ho	GLO, GPS	J. McCallum	2 nd tracking test
169cCd	2015-06-18	2 h	Cd	GLO, GPS	J. McCallum	1 st tracking test
179a	2015-06-28	2 h	Ho, Cd	GLO, GPS, Q	J. McCallum	1 st Ho-Cd session (L1, L2)
ex1	2015-08-19	28 min	Wz, Wn	GLO, GPS	J. Kodet	1 st on-site test
ex2	2015-08-20	25 min	Wz, Wn	GLO, GPS	J. Kodet	2 nd on-site test
ex3a	2015-08-20	11 min	Wz, Wn	GPS	J. Kodet	3 rd on-site test
236a	2015-08-24	4 h	Ho, Cd	GPS, Q	L. McCallum	2 nd Ho-Cd session (L1, L2)
238a	2015-08-26	4 h	Ho, Cd	GLO, GPS, Q	L. McCallum	3 rd Ho-Cd session (L1, L2)
ex4a	2015-11-12	30 min	Wz, Wn	GLO, GPS	J. Kodet	4 th on-site test (L1)
23a1	2015-11-23	33 min	Mc, Wz	GLO, GPS, GAL	V. Tornatore	Test tracking and signal chain at Mc (L1, L2)

Continued on next page

Table A.1 – *Continued from previous page*

exp. code	date	dur.	stations	targets	PI	comments
23b1	2015-11-23	2.25 h	Mc, Wz	GLO, GPS, GAL, Q	V. Tornatore	Quasar blocks (S, X) observed between satellites (L1, L2)
23c1	2015-11-23	2.5 h	Mc, Wz	GLO, GPS, GAL, Q	V. Tornatore	Quasar blocks (S, X) observed between satellites (L1, L2)
ex5a	2016-04-18	9 min	Wz, Wn	GLO	J. Kodet	5 th on-site test (L1)
126b	2016-05-05	6 h	Ho, Cd	GPS, Q	L. McCallum	4 th Ho-Cd session (L1, L2)
131a	2016-05-10	6 h	Ho, Cd	GPS, Q	L. McCallum	5 th Ho-Cd session (L1, L2)
132a	2016-05-11	6 h	Ho, Cd	GPS, Q	L. McCallum	6 th Ho-Cd session (L1, L2)
ex6a	2016-05-17	12 min	Wz, Wn	GLO	J. Kodet	6 th on-site test (L1)
ex7a	2016-05-23	12 min	Wz, Wn	GLO	J. Kodet	7 th on-site test (L1)
144b	2016-05-23	3 h	Mc, O8, Sr	GLO, GPS, GAL, BD, Q	V. Tornatore	Test different GNSS signals (L1, L2, L3)
144d	2016-05-23	3 h	Mc, O8, Sr	GLO, GPS, GAL, BD	V. Tornatore	Antenna pointing test (L1, L2, L3)
ex8a	2016-05-30	12 min	Wz, Wn	GLO	J. Kodet	8 th on-site test (L1)
ap01	2016-07-06	6 min	On	APOD	R. Haas	Tracking test (S, X)
196b	2016-07-14	7 min	On	APOD	R. Haas	Tracking test (S, X)
196c	2016-07-14	9 min	On	APOD	R. Haas	Tracking test (S, X)
197c	2016-07-14	9 min	On	APOD	R. Haas	Tracking test (S, X)
200a	2016-07-18	10 min	Ke, Yg	APOD	J. Lovell	Tracking test (S, X)
202	2016-07-20	9 min	Ke, Yg	APOD	J. Lovell	Tracking test (S, X)
207a	2016-07-14	6 min	On	APOD	R. Haas	Tracking test (S, X)
207b	2016-07-14	5 min	On, Wn, Wz	APOD	R. Haas	Tracking test (S, X)
263a	2016-09-19	6 min	On	APOD	R. Haas	Tracking test (S, X)
263b	2016-09-19	6 min	On, Wn, Wz	APOD	R. Haas	Tracking test (S, X)
263c	2016-09-19	5 min	On, Wn, Wz	APOD	R. Haas	Tracking test (S, X)
316a	2016-11-11	33 min	Ke, Yg	APOD, Q	A. Hellerschmied	Q before + after APOD (S, X)
317a	2016-11-12	41 min	Hb, Ke	APOD, Q	A. Hellerschmied	Q before + after APOD (S, X)
317b	2016-11-12	35 min	Hb, Ke, Yg	APOD, Q	A. Hellerschmied	Q before + after APOD (S, X)
318b	2016-11-13	26 min	Hb, Ke, Yg	APOD, Q	A. Hellerschmied	Q before + after APOD (S, X)
318c	2016-11-13	26 min	Hb, Ke	APOD, Q	A. Hellerschmied	Q before + after APOD (S, X)
318d	2016-11-13	23 min	Ke, Yg	APOD, Q	A. Hellerschmied	Q before + after APOD (S, X)
319a	2016-11-14	40 min	Hb, Ke, Yg	APOD, Q	A. Hellerschmied	Q before + after APOD (S, X)
328a	2016-11-23	1 h	Wa	GPS	T. Natusch	Test tracking + signal chain (L1, L2)
a332	2016-11-27	24 h	Hb, Ke, Yg	APOD, Q	A. Hellerschmied.	Geodetic 24 h session with APOD tracks (S, X)
g336	2016-12-01	3 h	Ho, Cd, Wa	GPS, Q	A. Hellerschmied	First 3 station GNSS experi- ment (L1, L2)

The Experiments were planned in cooperation with different station networks and observatories, following the objectives of various PIs.

In January 2014 the first experiments with observations of GNSS satellites were scheduled with the main goal to test new features for VLBI satellite observations at the Geodetic Obser-

vatory Wettzell (GOW). Kodet *et al.* (2013, 2014) worked on the co-location of space-geodetic techniques and adopted the S-band receiver chain of the 20 m antenna (Wz) to enable the reception of L1 GNSS signals. Hellerschmied *et al.* (2014) implemented features to enable continuous satellite tracking (see Sec. 3.4.2). All new implementations at GOW could be tested successfully. A series of short on-site VLBI test observations of GNSS satellites using the antennas at GOW followed in 2015 and 2016 (PI: J. Kodet).

Vincenza Tornatore organized several experiments in 2015 and 2016. In cooperation with the radio observatories in Medicina (Mc) and Sardinia (Sr), both in Italy, the Onsala Space Observatory (Sweden), and the GOW, satellites of the different GNSS constellations were observed. In the Sessions 23b1 and 23c1 GNSS satellites were observed in the L-band, and in between blocks of classical S/X band observations of quasars.

Unfortunately, only a small subset of the experiments mentioned so far were correlated, and for non of them actual delay observables could be obtained. The main reason for that was the absence of suitable observation, correlation, and post-correlation processing strategies for VLBI satellite observations. To counteract these deficiencies a joint initiative of the Technische Universität Wien (Austria) and the University of Tasmania (UTAS, Australia) was started in order to develop the missing processes and to test them in real experiments. The established process chain for VLBI satellite observations is described in Chap. 4. In the frame of this joint initiative a series of successful VLBI experiments with observations of GNSS satellites were conducted in 2015 and 2016 on the Australian baseline Hobart (Ho) - Ceduna (Cd). Details are discussed in Chap. 5.

In the second half of 2016 observation efforts concentrated on the Chinese APOD-A nano satellite, which represented a first realization of a co-location satellite on a LEO orbit enabling SLR, VLBI, and GNSS on a common platform (see Sec. 6.1). First, several tracking tests were scheduled and conducted involving antennas at the GOW and at the Onsala Space Observatory in which we experienced severe difficulties at tracking this low and fast satellites properly. In November 2016 a final series of APOD tracks was successfully observed with the antennas of the AuScope geodetic VLBI array in Australia. These sessions are introduced in detail in Chap. 6, including the analysis of the derived observables.

Appendix B

Schedule Summaries of Satellite Observation Experiments

The presented schedule summaries were created by the VieVS satellite scheduling program (Sec. 4.3) during the observation planning. The summaries list all scans in an experiment, providing information about the scan times (scan start and duration), the observed source (source name and type), and the observing antenna network.

B.1 GNSS observations

Listing B.1: Schedule summary of Experiment 179a.

```
#####
# Schedule summary for session: 179a
#####
Nominal start: 2015-06-28 18:00:00
Nominal end: 2015-06-28 20:02:03
```

Scan#	Source name	Type	Start [UT]	End [UT]	Dur [s]	Sations
1	1921-293	q	18:00:00	18:10:00	600	Cd Ho
2	GPS BIIR-13 (PRN 02)	s	18:15:57	18:20:57	300	Cd Ho
3	COSMOS 2433 (720)	s	18:22:17	18:27:17	300	Cd Ho
4	GPS BIIF-6 (PRN 06)	s	18:28:03	18:33:03	300	Cd Ho
5	GPS BIIRM-3 (PRN 12)	s	18:35:07	18:40:07	300	Cd Ho
6	COSMOS 2464 (736)	s	18:42:56	18:47:56	300	Cd Ho
7	COSMOS 2426 (717)	s	18:50:15	18:55:15	300	Cd Ho
8	COSMOS 2500 (755)	s	18:56:44	19:01:44	300	Cd Ho
9	GPS BIIRM-5 (PRN 29)	s	19:02:39	19:07:39	300	Cd Ho
10	1921-293	q	19:08:52	19:18:52	600	Cd Ho
11	GPS BIIRM-2 (PRN 31)	s	19:20:49	19:25:49	300	Cd Ho
12	COSMOS 2500 (755)	s	19:27:11	19:32:11	300	Cd Ho
13	GPS BIIRM-5 (PRN 29)	s	19:33:03	19:38:03	300	Cd Ho
14	GPS BIIF-1 (PRN 25)	s	19:39:24	19:44:54	330	Cd Ho
15	COSMOS 2426 (717)	s	19:46:35	19:49:35	180	Cd Ho
16	1921-293	q	19:52:03	20:02:03	600	Cd Ho

Listing B.2: Schedule summary of Experiment 236a.

```
#####
# Schedule summary for session: 236a
#####
Nominal start: 2015-08-24 12:00:00
Nominal end: 2015-08-24 15:59:34
```

Scan#	Source name	Type	Start [UT]	End [UT]	Dur [s]	Sations
1	1921-293	q	12:00:00	12:05:00	300	Cd Ho
2	GPS BIIR-13 (PRN 02)	s	12:08:07	12:13:07	300	Cd Ho
3	GPS BIIF-3 (PRN 24)	s	12:17:54	12:22:54	300	Cd Ho
4	GPS BIIRM-3 (PRN 12)	s	12:25:41	12:30:41	300	Cd Ho
5	GPS BIIF-1 (PRN 25)	s	12:35:12	12:40:12	300	Cd Ho
6	1921-293	q	12:44:18	12:49:18	300	Cd Ho
7	GPS BIIR-13 (PRN 02)	s	12:53:13	12:58:13	300	Cd Ho
8	GPS BIIF-3 (PRN 24)	s	13:01:59	13:06:59	300	Cd Ho
9	GPS BIIRM-3 (PRN 12)	s	13:10:51	13:15:51	300	Cd Ho
10	GPS BIIF-1 (PRN 25)	s	13:18:34	13:23:34	300	Cd Ho
11	GPS BIIR-13 (PRN 02)	s	13:30:03	13:35:03	300	Cd Ho
12	GPS BIIF-3 (PRN 24)	s	13:39:06	13:44:06	300	Cd Ho
13	1921-293	q	13:46:58	13:51:58	300	Cd Ho
14	GPS BIIF-1 (PRN 25)	s	13:55:06	14:00:06	300	Cd Ho
15	GPS BIIF-3 (PRN 24)	s	14:04:27	14:09:27	300	Cd Ho
16	GPS BIIRM-3 (PRN 12)	s	14:14:52	14:19:52	300	Cd Ho
17	GPS BIIR-13 (PRN 02)	s	14:22:10	14:27:10	300	Cd Ho
18	GPS BIIF-1 (PRN 25)	s	14:30:31	14:35:31	300	Cd Ho
19	GPS BIIF-3 (PRN 24)	s	14:42:21	14:44:51	150	Cd Ho
20	GPS BIIRM-3 (PRN 12)	s	14:48:44	14:53:44	300	Cd Ho
21	0208-512	q	14:56:32	15:01:32	300	Cd Ho
22	GPS BIIR-13 (PRN 02)	s	15:03:29	15:08:29	300	Cd Ho
23	GPS BIIF-1 (PRN 25)	s	15:11:38	15:16:38	300	Cd Ho
24	GPS BIIRM-3 (PRN 12)	s	15:21:38	15:26:38	300	Cd Ho
25	GPS BIIR-13 (PRN 02)	s	15:30:11	15:35:11	300	Cd Ho
26	GPS BIIF-1 (PRN 25)	s	15:38:28	15:43:28	300	Cd Ho
27	0208-512	q	15:46:59	15:51:59	300	Cd Ho
28	GPS BIIRM-3 (PRN 12)	s	15:55:34	15:59:34	240	Cd Ho

Listing B.3: Schedule summary of Experiment 238a.

```
#####
# Schedule summary for session: 238a
#####
Nominal start: 2015-08-26 12:00:00
Nominal end: 2015-08-26 15:57:24
```

Scan#	Source name	Type	Start [UT]	End [UT]	Dur [s]	Sations
1	1921-293	q	12:00:00	12:05:00	300	Cd Ho
2	GPS BIIR-13 (PRN 02)	s	12:08:01	12:13:01	300	Cd Ho
3	COSMOS 2460 (732)	s	12:16:04	12:21:04	300	Cd Ho
4	COSMOS 2459 (731)	s	12:25:14	12:29:14	240	Cd Ho
5	GPS BIIR-3 (PRN 12)	s	12:31:56	12:36:56	300	Cd Ho
6	GPS BIIR-13 (PRN 02)	s	12:42:41	12:47:41	300	Cd Ho
7	COSMOS 2465 (737)	s	12:52:23	12:57:23	300	Cd Ho
8	1921-293	q	13:01:25	13:06:25	300	Cd Ho
9	GPS BIIR-13 (PRN 02)	s	13:13:04	13:18:04	300	Cd Ho
10	COSMOS 2460 (732)	s	13:23:15	13:28:15	300	Cd Ho
11	COSMOS 2465 (737)	s	13:32:21	13:37:21	300	Cd Ho
12	COSMOS 2459 (731)	s	13:42:06	13:47:06	300	Cd Ho
13	GPS BIIR-3 (PRN 12)	s	13:49:35	13:54:35	300	Cd Ho
14	1921-293	q	13:58:30	14:03:30	300	Cd Ho
15	COSMOS 2460 (732)	s	14:05:52	14:10:52	300	Cd Ho
16	GPS BIIR-13 (PRN 02)	s	14:14:28	14:19:28	300	Cd Ho
17	COSMOS 2459 (731)	s	14:22:11	14:27:11	300	Cd Ho
18	GPS BIIR-3 (PRN 12)	s	14:30:20	14:35:20	300	Cd Ho
19	COSMOS 2465 (737)	s	14:39:03	14:44:03	300	Cd Ho
20	COSMOS 2460 (732)	s	14:49:52	14:54:52	300	Cd Ho
21	COSMOS 2459 (731)	s	14:58:14	15:03:14	300	Cd Ho
22	0438-436	q	15:05:16	15:10:16	300	Cd Ho
23	GPS BIIR-13 (PRN 02)	s	15:12:30	15:17:30	300	Cd Ho
24	GPS BIIR-3 (PRN 12)	s	15:21:03	15:26:03	300	Cd Ho
25	COSMOS 2460 (732)	s	15:30:01	15:35:01	300	Cd Ho
26	GPS BIIR-13 (PRN 02)	s	15:37:37	15:42:37	300	Cd Ho
27	0208-512	q	15:45:07	15:50:07	300	Cd Ho
28	COSMOS 2460 (732)	s	15:52:24	15:57:24	300	Cd Ho

Listing B.4: Schedule summary of Experiment 126b.

```
#####
# Schedule summary for session: 126b
#####
Nominal start: 2016-05-05 17:00:00
Nominal end:   2016-05-05 22:58:13
```

Scan#	Source name	Type	Start [UT]	End [UT]	Dur [s]	Sations
1	1610-771	q	17:00:00	17:01:00	60	Cd Ho
2	1921-293	q	17:03:28	17:04:28	60	Cd Ho
3	2134+004	q	17:06:16	17:07:16	60	Cd Ho
4	1749+096	q	17:09:36	17:10:36	60	Cd Ho
5	GPS BIIR-11 (PRN 19)	s	17:12:46	17:17:46	300	Cd Ho
6	GPS BIIF-3 (PRN 24)	s	17:22:50	17:27:50	300	Cd Ho
7	GPS BIIR-11 (PRN 19)	s	17:31:40	17:36:40	300	Cd Ho
8	GPS BIIRM-3 (PRN 12)	s	17:41:02	17:46:02	300	Cd Ho
9	GPS BIIF-3 (PRN 24)	s	17:48:15	17:53:15	300	Cd Ho
10	GPS BIIR-11 (PRN 19)	s	17:56:08	18:01:08	300	Cd Ho
11	2134+004	q	18:03:41	18:04:41	60	Cd Ho
12	1749+096	q	18:07:01	18:08:01	60	Cd Ho
13	1730-130	q	18:09:31	18:10:31	60	Cd Ho
14	1921-293	q	18:13:29	18:14:29	60	Cd Ho
15	GPS BIIR-13 (PRN 02)	s	18:17:24	18:22:24	300	Cd Ho
16	GPS BIIRM-3 (PRN 12)	s	18:26:37	18:31:37	300	Cd Ho
17	GPS BIIF-3 (PRN 24)	s	18:33:47	18:38:47	300	Cd Ho
18	GPS BIIR-11 (PRN 19)	s	18:46:16	18:51:16	300	Cd Ho
19	GPS BIIR-13 (PRN 02)	s	18:55:08	19:00:08	300	Cd Ho
20	GPS BIIRM-3 (PRN 12)	s	19:04:55	19:09:55	300	Cd Ho
21	1730-130	q	19:12:54	19:13:54	60	Cd Ho
22	1749+096	q	19:15:30	19:16:30	60	Cd Ho
23	1921-293	q	19:18:46	19:19:46	60	Cd Ho
24	GPS BIIR-11 (PRN 19)	s	19:22:45	19:27:45	300	Cd Ho
25	GPS BIIRM-3 (PRN 12)	s	19:30:33	19:35:33	300	Cd Ho
26	GPS BIIR-13 (PRN 02)	s	19:40:23	19:45:23	300	Cd Ho
27	GPS BIIF-3 (PRN 24)	s	19:48:12	19:53:12	300	Cd Ho
28	GPS BIIR-11 (PRN 19)	s	19:58:00	20:03:00	300	Cd Ho
29	GPS BIIR-13 (PRN 02)	s	20:05:44	20:10:44	300	Cd Ho
30	2134+004	q	20:12:45	20:13:45	60	Cd Ho
31	1749+096	q	20:16:05	20:17:05	60	Cd Ho
32	1610-771	q	20:23:18	20:24:18	60	Cd Ho
33	GPS BIIRM-8 (PRN 05)	s	20:28:52	20:33:52	300	Cd Ho
34	GPS BIIR-13 (PRN 02)	s	20:37:00	20:42:00	300	Cd Ho
35	GPS BIIR-11 (PRN 19)	s	20:44:42	20:49:42	300	Cd Ho
36	GPS BIIF-3 (PRN 24)	s	20:53:45	20:58:45	300	Cd Ho
37	GPS BIIRM-8 (PRN 05)	s	21:01:29	21:06:29	300	Cd Ho
38	GPS BIIRM-3 (PRN 12)	s	21:09:07	21:14:07	300	Cd Ho
39	2134+004	q	21:17:05	21:18:05	60	Cd Ho
40	1749+096	q	21:20:22	21:21:22	60	Cd Ho
41	1610-771	q	21:27:58	21:28:58	60	Cd Ho
42	GPS BIIR-13 (PRN 02)	s	21:31:16	21:36:16	300	Cd Ho
43	GPS BIIRM-8 (PRN 05)	s	21:39:12	21:44:12	300	Cd Ho
44	GPS BIIRM-3 (PRN 12)	s	21:46:13	21:51:13	300	Cd Ho
45	GPS BIIR-13 (PRN 02)	s	21:54:04	21:59:04	300	Cd Ho
46	GPS BIIRM-8 (PRN 05)	s	22:01:52	22:06:52	300	Cd Ho
47	GPS BIIRM-3 (PRN 12)	s	22:08:52	22:13:52	300	Cd Ho
48	GPS BIIR-13 (PRN 02)	s	22:17:13	22:22:13	300	Cd Ho
49	1610-771	q	22:24:57	22:25:57	60	Cd Ho
50	2134+004	q	22:31:37	22:32:37	60	Cd Ho
51	GPS BIIRM-8 (PRN 05)	s	22:36:32	22:41:32	300	Cd Ho
52	GPS BIIR-13 (PRN 02)	s	22:44:06	22:49:06	300	Cd Ho
53	GPS BIIRM-3 (PRN 12)	s	22:53:13	22:58:13	300	Cd Ho

Listing B.5: Schedule summary of Experiment 131a.

```
#####
# Schedule summary for session: 131a
#####
Nominal start:    2016-05-10 17:00:00
Nominal end:      2016-05-10 22:56:59
```

Scan#	Source name	Type	Start [UT]	End [UT]	Dur [s]	Sations
1	1610-771	q	17:00:00	17:01:00	60	Cd Ho
2	1921-293	q	17:03:33	17:04:33	60	Cd Ho
3	2134+004	q	17:06:20	17:07:20	60	Cd Ho
4	1749+096	q	17:09:40	17:10:40	60	Cd Ho
5	GPS BIIR-11 (PRN 19)	s	17:13:53	17:18:53	300	Cd Ho
6	GPS BIIF-3 (PRN 24)	s	17:22:12	17:27:12	300	Cd Ho
7	GPS BIIRM-3 (PRN 12)	s	17:29:23	17:34:23	300	Cd Ho
8	GPS BIIR-11 (PRN 19)	s	17:37:58	17:42:58	300	Cd Ho
9	GPS BIIF-3 (PRN 24)	s	17:45:48	17:50:48	300	Cd Ho
10	GPS BIIRM-3 (PRN 12)	s	17:52:47	17:57:47	300	Cd Ho
11	GPS BIIR-11 (PRN 19)	s	18:01:00	18:06:00	300	Cd Ho
12	1610-771	q	18:08:06	18:09:06	60	Cd Ho
13	1921-293	q	18:12:01	18:13:01	60	Cd Ho
14	2134+004	q	18:14:44	18:15:44	60	Cd Ho
15	GPS BIIR-13 (PRN 02)	s	18:18:05	18:23:05	300	Cd Ho
16	GPS BIIR-11 (PRN 19)	s	18:27:02	18:32:02	300	Cd Ho
17	GPS BIIRM-3 (PRN 12)	s	18:34:53	18:39:53	300	Cd Ho
18	GPS BIIF-3 (PRN 24)	s	18:42:22	18:47:22	300	Cd Ho
19	GPS BIIR-11 (PRN 19)	s	18:51:25	18:56:25	300	Cd Ho
20	GPS BIIRM-3 (PRN 12)	s	18:59:13	19:04:13	300	Cd Ho
21	GPS BIIR-13 (PRN 02)	s	19:09:25	19:14:25	300	Cd Ho
22	2134+004	q	19:16:17	19:17:17	60	Cd Ho
23	1921-293	q	19:19:21	19:20:21	60	Cd Ho
24	1730-130	q	19:21:58	19:22:58	60	Cd Ho
25	1749+096	q	19:24:37	19:25:37	60	Cd Ho
26	GPS BIIF-3 (PRN 24)	s	19:27:31	19:32:31	300	Cd Ho
27	GPS BIIR-13 (PRN 02)	s	19:35:32	19:40:32	300	Cd Ho
28	GPS BIIR-11 (PRN 19)	s	19:43:21	19:48:21	300	Cd Ho
29	GPS BIIRM-3 (PRN 12)	s	19:51:13	19:56:13	300	Cd Ho
30	GPS BIIR-13 (PRN 02)	s	19:59:04	20:04:04	300	Cd Ho
31	GPS BIIR-11 (PRN 19)	s	20:06:40	20:11:40	300	Cd Ho
32	GPS BIIRM-3 (PRN 12)	s	20:14:37	20:19:37	300	Cd Ho
33	1610-771	q	20:22:02	20:23:02	60	Cd Ho
34	1921-293	q	20:25:20	20:26:20	60	Cd Ho
35	1730-130	q	20:27:59	20:28:59	60	Cd Ho
36	2134+004	q	20:35:46	20:36:46	60	Cd Ho
37	GPS BIIF-3 (PRN 24)	s	20:38:52	20:43:52	300	Cd Ho
38	GPS BIIRM-8 (PRN 05)	s	20:46:35	20:51:35	300	Cd Ho
39	GPS BIIRM-3 (PRN 12)	s	20:54:05	20:59:05	300	Cd Ho
40	GPS BIIR-13 (PRN 02)	s	21:01:12	21:06:12	300	Cd Ho
41	GPS BIIRM-8 (PRN 05)	s	21:09:11	21:14:11	300	Cd Ho
42	GPS BIIRM-3 (PRN 12)	s	21:16:13	21:21:13	300	Cd Ho
43	GPS BIIR-13 (PRN 02)	s	21:23:51	21:28:51	300	Cd Ho
44	1610-771	q	21:31:18	21:32:18	60	Cd Ho
45	1921-293	q	21:34:29	21:35:29	60	Cd Ho
46	1730-130	q	21:37:09	21:38:09	60	Cd Ho
47	2134+004	q	21:45:27	21:46:27	60	Cd Ho
48	GPS BIIRM-3 (PRN 12)	s	21:48:42	21:53:42	300	Cd Ho
49	GPS BIIRM-8 (PRN 05)	s	21:55:42	22:00:42	300	Cd Ho
50	GPS BIIR-13 (PRN 02)	s	22:03:26	22:08:26	300	Cd Ho
51	GPS BIIRM-3 (PRN 12)	s	22:12:07	22:17:07	300	Cd Ho
52	GPS BIIRM-8 (PRN 05)	s	22:19:46	22:24:46	300	Cd Ho
53	GPS BIIR-13 (PRN 02)	s	22:27:19	22:32:19	300	Cd Ho
54	GPS BIIRM-3 (PRN 12)	s	22:36:30	22:41:30	300	Cd Ho
55	2134+004	q	22:44:00	22:45:00	60	Cd Ho
56	1921-293	q	22:47:19	22:48:19	60	Cd Ho
57	1610-771	q	22:55:59	22:56:59	60	Cd Ho

Listing B.6: Schedule summary of Experiment 132a.

```
#####
# Schedule summary for session: 132a
#####
Nominal start: 2016-05-11 17:00:00
Nominal end:   2016-05-11 22:57:51
```

Scan#	Source name	Type	Start [UT]	End [UT]	Dur [s]	Sations
1	1610-771	q	17:00:00	17:01:00	60	Cd Ho
2	1921-293	q	17:03:35	17:04:35	60	Cd Ho
3	2134+004	q	17:06:21	17:07:21	60	Cd Ho
4	1749+096	q	17:09:41	17:10:41	60	Cd Ho
5	GPS BIIR-11 (PRN 19)	s	17:14:12	17:19:12	300	Cd Ho
6	GPS BIIF-3 (PRN 24)	s	17:22:21	17:27:21	300	Cd Ho
7	GPS BIIRM-3 (PRN 12)	s	17:29:30	17:34:30	300	Cd Ho
8	GPS BIIR-11 (PRN 19)	s	17:38:00	17:43:00	300	Cd Ho
9	GPS BIIF-3 (PRN 24)	s	17:45:49	17:50:49	300	Cd Ho
10	GPS BIIRM-3 (PRN 12)	s	17:52:47	17:57:47	300	Cd Ho
11	GPS BIIR-11 (PRN 19)	s	18:00:57	18:05:57	300	Cd Ho
12	1610-771	q	18:08:01	18:09:01	60	Cd Ho
13	1921-293	q	18:11:58	18:12:58	60	Cd Ho
14	2134+004	q	18:14:41	18:15:41	60	Cd Ho
15	GPS BIIR-13 (PRN 02)	s	18:18:01	18:23:01	300	Cd Ho
16	GPS BIIR-11 (PRN 19)	s	18:26:56	18:31:56	300	Cd Ho
17	GPS BIIRM-3 (PRN 12)	s	18:34:45	18:39:45	300	Cd Ho
18	GPS BIIF-3 (PRN 24)	s	18:42:16	18:47:16	300	Cd Ho
19	GPS BIIR-11 (PRN 19)	s	18:51:31	18:56:31	300	Cd Ho
20	GPS BIIRM-3 (PRN 12)	s	18:59:19	19:04:19	300	Cd Ho
21	GPS BIIR-13 (PRN 02)	s	19:09:24	19:14:24	300	Cd Ho
22	2134+004	q	19:16:14	19:17:14	60	Cd Ho
23	1749+096	q	19:19:35	19:20:35	60	Cd Ho
24	1730-130	q	19:22:15	19:23:15	60	Cd Ho
25	1921-293	q	19:24:51	19:25:51	60	Cd Ho
26	GPS BIIF-3 (PRN 24)	s	19:27:52	19:32:52	300	Cd Ho
27	GPS BIIR-13 (PRN 02)	s	19:35:58	19:40:58	300	Cd Ho
28	GPS BIIR-11 (PRN 19)	s	19:43:44	19:48:44	300	Cd Ho
29	GPS BIIRM-3 (PRN 12)	s	19:51:37	19:56:37	300	Cd Ho
30	GPS BIIR-13 (PRN 02)	s	19:59:13	20:04:13	300	Cd Ho
31	GPS BIIR-11 (PRN 19)	s	20:06:51	20:11:51	300	Cd Ho
32	GPS BIIRM-3 (PRN 12)	s	20:14:49	20:19:49	300	Cd Ho
33	1610-771	q	20:22:17	20:23:17	60	Cd Ho
34	1921-293	q	20:25:34	20:26:34	60	Cd Ho
35	1730-130	q	20:28:13	20:29:13	60	Cd Ho
36	2134+004	q	20:36:02	20:37:02	60	Cd Ho
37	GPS BIIF-3 (PRN 24)	s	20:39:11	20:44:11	300	Cd Ho
38	GPS BIIRM-8 (PRN 05)	s	20:46:53	20:51:53	300	Cd Ho
39	GPS BIIRM-3 (PRN 12)	s	20:54:16	20:59:16	300	Cd Ho
40	GPS BIIR-13 (PRN 02)	s	21:01:29	21:06:29	300	Cd Ho
41	GPS BIIRM-8 (PRN 05)	s	21:09:27	21:14:27	300	Cd Ho
42	GPS BIIRM-3 (PRN 12)	s	21:16:29	21:21:29	300	Cd Ho
43	GPS BIIR-13 (PRN 02)	s	21:24:12	21:29:12	300	Cd Ho
44	1610-771	q	21:31:41	21:32:41	60	Cd Ho
45	1921-293	q	21:34:51	21:35:51	60	Cd Ho
46	1730-130	q	21:37:31	21:38:31	60	Cd Ho
47	2134+004	q	21:45:52	21:46:52	60	Cd Ho
48	GPS BIIRM-3 (PRN 12)	s	21:49:07	21:54:07	300	Cd Ho
49	GPS BIIRM-8 (PRN 05)	s	21:56:13	22:01:13	300	Cd Ho
50	GPS BIIR-13 (PRN 02)	s	22:03:55	22:08:55	300	Cd Ho
51	GPS BIIRM-3 (PRN 12)	s	22:12:42	22:17:42	300	Cd Ho
52	GPS BIIRM-8 (PRN 05)	s	22:20:29	22:25:29	300	Cd Ho
53	GPS BIIR-13 (PRN 02)	s	22:28:00	22:33:00	300	Cd Ho
54	GPS BIIRM-3 (PRN 12)	s	22:37:17	22:42:17	300	Cd Ho
55	2134+004	q	22:44:49	22:45:49	60	Cd Ho
56	1921-293	q	22:48:10	22:49:10	60	Cd Ho
57	1610-771	q	22:56:51	22:57:51	60	Cd Ho

Listing B.7: Schedule summary of Experiment g336.

```
#####
# Schedule summary for session: g336 #
#####
Nominal start: 2016-12-01 03:30:00
Nominal end: 2016-12-01 06:40:22
```

Scan#	Source name	Type	Start [UT]	End [UT]	Dur [s]	Sations
1	1921-293	q	03:30:00	03:40:00	600	Cd Ho Wa
2	GPS BIIF-6 (PRN 06)	s	03:42:34	03:47:31	297	Cd Ho Wa
3	GPS BIIR-11 (PRN 19)	s	03:53:54	03:58:51	297	Cd Ho Wa
4	GPS BIIF-3 (PRN 24)	s	04:02:00	04:06:57	297	Cd Ho Wa
5	GPS BIIR-13 (PRN 02)	s	04:13:16	04:18:13	297	Cd Ho Wa
6	GPS BIIF-6 (PRN 06)	s	04:21:09	04:26:06	297	Cd Ho Wa
7	GPS BIIR-11 (PRN 19)	s	04:36:16	04:40:10	234	Cd Ho Wa
8	1921-293	q	04:46:09	04:56:09	600	Cd Ho Wa
9	GPS BIIR-13 (PRN 02)	s	04:58:39	05:03:36	297	Cd Ho Wa
10	GPS BIIF-3 (PRN 24)	s	05:07:07	05:12:04	297	Cd Ho Wa
11	GPS BIIF-6 (PRN 06)	s	05:17:32	05:22:29	297	Cd Ho Wa
12	GPS BIIR-11 (PRN 19)	s	05:25:01	05:29:58	297	Cd Ho Wa
13	1921-293	q	05:38:00	05:48:00	600	Cd Ho Wa
14	GPS BIIF-3 (PRN 24)	s	05:50:37	05:55:34	297	Cd Ho Wa
15	GPS BIIR-13 (PRN 02)	s	05:59:43	06:04:40	297	Cd Ho Wa
16	GPS BIIF-6 (PRN 06)	s	06:11:09	06:16:06	297	Cd Ho Wa
17	GPS BIIR-13 (PRN 02)	s	06:21:28	06:25:22	234	Cd Ho Wa
18	1921-293	q	06:30:22	06:40:22	600	Cd Ho Wa

B.2 APOD observations

Listing B.8: Schedule summary of Experiment 316a.

```
#####
# Schedule summary for session: 316a                                     #
#####
Nominal start:    2016-11-11 22:10:00
Nominal end:      2016-11-11 22:43:11
```

Scan#	Source name	Type	Start [UT]	End [UT]	Dur [s]	Sations
1	0454-234	q	22:10:00	22:10:30	30	Ke Yg
2	0642+449	q	22:10:59	22:11:29	30	Ke Yg
3	1334-127	q	22:12:06	22:12:36	30	Ke Yg
4	1057-797	q	22:13:06	22:13:40	34	Ke Yg
5	0851+202	q	22:14:34	22:15:04	30	Ke Yg
6	PN1A [BAC]	s	22:20:25	22:24:25	240	Ke
7	PN1A [BAC]	s	22:24:40	22:28:11	211	Ke Yg
8	PN1A [BAC]	s	22:28:26	22:32:50	264	Yg
9	1144-379	q	22:37:56	22:38:32	36	Ke Yg
10	0727-115	q	22:39:23	22:39:53	30	Ke Yg
11	0537-441	q	22:40:21	22:40:51	30	Ke Yg
12	1424-418	q	22:41:27	22:41:57	30	Ke Yg
13	1104-445	q	22:42:35	22:43:11	36	Ke Yg

Listing B.9: Schedule summary of Experiment 317a.

```
#####
# Schedule summary for session: 317a #
#####
Nominal start: 2016-11-12 09:34:00
Nominal end:   2016-11-12 10:15:33
```

Scan#	Source name	Type	Start [UT]	End [UT]	Dur [s]	Sations
1	0332-403	q	09:34:00	09:34:30	30	Hb Ho Ke
2	2255-282	q	09:36:23	09:37:03	40	Hb Ho Ke
3	1921-293	q	09:38:46	09:39:16	30	Hb Ho Ke
4	0332-403	q	09:42:19	09:42:49	30	Hb Ho Ke
5	PN1A [BAC]	s	09:48:40	09:51:52	192	Hb Ho
6	PN1A [BAC]	s	09:51:53	09:55:53	240	Hb
7	PN1A [BAC]	s	09:55:54	09:56:21	27	Hb Ke
8	PN1A [BAC]	s	09:56:21	10:03:55	454	Ke
9	1741-038	q	10:10:38	10:11:08	30	Hb Ke
10	1921-293	q	10:11:55	10:12:25	30	Hb Ke
11	0332-403	q	10:13:17	10:13:47	30	Hb Ke
12	2255-282	q	10:14:53	10:15:33	40	Hb Ke

Listing B.10: Schedule summary of Experiment 317b.

```
#####
# Schedule summary for session: 317b #
#####
Nominal start: 2016-11-12 21:35:00
Nominal end:   2016-11-12 22:09:49
```

Scan#	Source name	Type	Start [UT]	End [UT]	Dur [s]	Sations
1	0454-234	q	21:35:00	21:35:30	30	Hb Ke Yg
2	0851+202	q	21:36:16	21:36:46	30	Hb Ke Yg
3	1334-127	q	21:37:31	21:38:01	30	Hb Ke Yg
4	1057-797	q	21:38:46	21:39:24	38	Hb Ke Yg
5	0537-441	q	21:40:01	21:40:31	30	Hb Ke Yg
6	PN1A [BAC]	s	21:46:06	21:52:04	358	Ke
7	PN1A [BAC]	s	21:52:05	21:54:46	161	Ke Yg
8	PN1A [BAC]	s	21:54:47	21:55:41	54	Yg
9	PN1A [BAC]	s	21:55:42	21:57:59	137	Hb Yg
10	0454-234	q	22:03:45	22:04:15	30	Hb Ke Yg
11	1424-418	q	22:05:11	22:05:41	30	Hb Ke Yg
12	1057-797	q	22:06:18	22:06:56	38	Hb Ke Yg
13	0851+202	q	22:08:02	22:08:32	30	Hb Ke Yg
14	0537-441	q	22:09:19	22:09:49	30	Hb Ke Yg

Listing B.11: Schedule summary of Experiment 318b.

```
#####
# Schedule summary for session: 318b #
#####
Nominal start: 2016-11-13 10:48:30
Nominal end:   2016-11-13 11:14:27
```

Scan#	Source name	Type	Start [UT]	End [UT]	Dur [s]	Sations
1	PN1A [BAC]	s	10:48:30	10:51:57	207	Hb
2	PN1A [BAC]	s	10:51:58	10:52:39	41	Hb Yg
3	PN1A [BAC]	s	10:52:40	10:55:50	190	Yg
4	PN1A [BAC]	s	10:55:51	10:59:52	241	Ke Yg
5	PN1A [BAC]	s	10:59:53	11:01:42	109	Ke
6	0229+131	q	11:07:46	11:08:29	43	Hb Ke Yg
7	0537-441	q	11:09:09	11:09:49	40	Hb Ke Yg
8	1921-293	q	11:10:44	11:11:24	40	Hb Ke Yg
9	2052-474	q	11:12:03	11:12:43	40	Hb Ke Yg
10	0336-019	q	11:13:47	11:14:27	40	Hb Ke Yg

Listing B.12: Schedule summary of Experiment 318c.

```
#####
# Schedule summary for session: 318c                                     #
#####
Nominal start:    2016-11-13 21:01:00
Nominal end:      2016-11-13 21:26:59
-----
Scan#  Source name      Type  Start [UT]  End [UT]  Dur [s]  Sations
1      0332-403            q      21:01:00   21:01:40   40      Hb Ho Ke
2      0537-441            q      21:03:13   21:03:53   40      Hb Ho Ke
3      0454-234            q      21:05:11   21:05:51   40      Hb Ho Ke
4      0727-115            q      21:08:04   21:08:44   40      Hb Ho Ke
5      PN1A [BAC]          s      21:13:05   21:19:34  389      Ke
6      PN1A [BAC]          s      21:19:35   21:20:00   25      Hb Ke
7      PN1A [BAC]          s      21:20:01   21:20:20   19      Hb Ho Ke
8      PN1A [BAC]          s      21:20:21   21:22:39  138      Hb Ho
9      PN1A [BAC]          s      21:22:40   21:26:59  259      Hb
-----
```

Listing B.13: Schedule summary of Experiment 318d.

```
#####
# Schedule summary for session: 318d                                     #
#####
Nominal start:    2016-11-13 22:35:00
Nominal end:      2016-11-13 22:57:55
-----
Scan#  Source name      Type  Start [UT]  End [UT]  Dur [s]  Sations
1      0454-234            q      22:35:00   22:35:40   40      Ke Yg
2      0727-115            q      22:36:27   22:37:07   40      Ke Yg
3      0537-441            q      22:37:45   22:38:25   40      Ke Yg
4      0851+202            q      22:39:10   22:39:50   40      Ke Yg
5      1334-127            q      22:40:38   22:41:18   40      Ke Yg
6      PN1A [BAC]          s      22:46:39   22:49:21  162      Ke
7      PN1A [BAC]          s      22:49:22   22:51:55  153      Ke Yg
8      PN1A [BAC]          s      22:51:56   22:53:25   89      Yg
9      PN1A [BAC]          s      22:54:01   22:57:55  234      Yg
-----
```

Listing B.14: Schedule summary of Experiment 319a.

```
#####
# Schedule summary for session: 319a                                     #
#####
Nominal start:    2016-11-14 10:00:00
Nominal end:      2016-11-14 10:40:05
-----
Scan#  Source name      Type  Start [UT]  End [UT]  Dur [s]  Sations
1      0332-403            q      10:00:00   10:00:40   40      Hb Ho Ke Yg
2      2052-474            q      10:03:08   10:03:48   40      Hb Ho Ke Yg
3      0332-403            q      10:06:15   10:06:55   40      Hb Ho Ke Yg
4      PN1A [BAC]          s      10:13:26   10:18:50  324      Hb
5      PN1A [BAC]          s      10:18:51   10:19:29   38      Hb Ho
6      PN1A [BAC]          s      10:19:30   10:20:44   74      Hb Ho Yg
7      PN1A [BAC]          s      10:20:55   10:24:16  201      Ke Yg
8      PN1A [BAC]          s      10:24:17   10:28:55  278      Ke
9      0332-403            q      10:34:56   10:35:36   40      Hb Ke Yg
10     1921-293            q      10:36:28   10:37:08   40      Hb Ke Yg
11     2052-474            q      10:37:47   10:38:27   40      Hb Ke Yg
12     0332-403            q      10:39:25   10:40:05   40      Hb Ke Yg
-----
```

B. Schedule Summaries of Satellite Observation Experiments

Listing B.15: Schedule summary of Experiment a332. This Experiment was scheduled as a 24 h geodetic VLBI experiment with observations of strong natural sources, intersected by four APOD (PN1A [BAC]) tracks (see Sec. 6.3). At the begin and at the end of the session 1921-293 was observed for 10 min for calibration purposes. This Listing only depicts a shortend scan list, showing all four APOD scans.

```
#####
# Schedule summary for session: a332
#####
Nominal start: 2016-11-27 05:00:00
Nominal end: 2016-11-28 04:59:20
```

Scan#	Source name	Type	Start [UT]	End [UT]	Dur [s]	Sations
1	1921-293	q	05:00:00	05:10:00	600	Hb Ke Yg
2	1424-418	q	05:10:58	05:11:28	30	Hb Ke Yg
3	1334-127	q	05:13:01	05:13:31	30	Hb Ke Yg
4	2255-282	q	05:14:34	05:15:30	56	Hb Ke Yg
.
.
164	0454-234	q	10:27:35	10:28:05	30	Hb Ke Yg
165	2052-474	q	10:29:16	10:29:48	32	Hb Ke Yg
166	0332-403	q	10:30:46	10:31:24	38	Hb Ke Yg
167	1954-388	q	10:32:19	10:33:17	58	Hb Ke Yg
168	PN1A [BAC]	s	10:41:04	10:42:30	86	Hb Yg
169	PN1A [BAC]	s	10:44:02	10:48:18	256	Ke Yg
170	0336-019	q	10:54:00	10:54:30	30	Hb Ke Yg
171	2209+236	q	10:55:22	10:57:17	115	Hb Ke Yg
172	1921-293	q	10:58:03	10:58:33	30	Hb Ke Yg
173	0332-403	q	10:59:32	11:00:10	38	Hb Ke Yg
.
.
516	0454-234	q	20:57:47	20:58:17	30	Hb Ke Yg
517	0537-441	q	20:58:57	20:59:27	30	Hb Ke Yg
518	1057-797	q	21:00:09	21:00:54	45	Hb Ke Yg
519	0727-115	q	21:02:16	21:02:46	30	Hb Ke Yg
520	PN1A [BAC]	s	21:08:02	21:08:31	29	Hb Ke
521	1128+385	q	21:14:11	21:15:26	75	Hb Ke Yg
522	1156+295	q	21:15:56	21:17:16	80	Hb Ke Yg
523	1519-273	q	21:18:05	21:19:07	62	Hb Ke Yg
524	0454-234	q	21:20:17	21:20:47	30	Hb Ke Yg
.
.
560	0727-115	q	22:25:47	22:26:17	30	Hb Ke Yg
561	1622-253	q	22:27:19	22:28:29	70	Hb Ke Yg
562	0537-441	q	22:29:43	22:30:13	30	Hb Ke Yg
563	0700-197	q	22:30:49	22:32:36	107	Hb Ke Yg
564	PN1A [BAC]	s	22:38:17	22:41:26	189	Ke Yg
565	1057-797	q	22:46:56	22:47:40	44	Hb Ke Yg
566	1104-445	q	22:48:35	22:49:29	54	Hb Ke Yg
567	1424-418	q	22:50:36	22:51:06	30	Hb Ke Yg
568	1124-186	q	22:52:01	22:53:09	68	Hb Ke Yg
.
.
762	1255-316	q	04:44:08	04:45:04	56	Hb Ke Yg
763	1334-127	q	04:46:39	04:47:09	30	Hb Ke Yg
764	1424-418	q	04:47:54	04:48:24	30	Hb Ke Yg
765	1921-293	q	04:49:20	04:59:20	600	Hb Ke Yg

Appendix C

AZEL tracking files for AuScope VLBI antennas

AZEL tracking files can be directly loaded by the Antenna Control Units (ACUs) of the AuScope antennas after invoking the AZEL tracking mode (see Sec. 6.2.1).

The first line just contains a single integer value that indicates the total number of tracking points in the file. All remaining lines contain the tracking points (one per line) in the format described in Tab. C.1 (TAB delimited, integers only). An example is given in Listing C.1. The first column defines the *unambiguous azimuth*, i.e. the actual cable wrap position between the upper and lower limits.

Column	Parameter	Description
1	Azimuth	Degrees x 10,000, range: between cable wrap limits
2	Elevation	Degrees x 10,000, range: 0-90°
3	Position_Angle	Not used, set to 0
4	Modified Julian Date	Modified Julian Day number
5	Time	Milliseconds since the start of the MJD

Table C.1: Format of the data point definition in the AuScope AZEL tracking files. The columns are TAB delimited and only integer values are allowed.

Listing C.1: Example of an AZEL tracking file compatible with the AZEL tracking mode of the AuScope antennas.

```
10
-160689 050510 0      57703  80302000
-160689 050510 0      57703  80422000
-161700 051256 0      57703  80423000
-162718 052004 0      57703  80424000
-163742 052755 0      57703  80425000
-164774 053508 0      57703  80426000
-165812 054264 0      57703  80427000
-166858 055022 0      57703  80428000
-167911 055782 0      57703  80429000
-168971 056545 0      57703  80430000
```


Acronyms

Δ-DOR	Delta Differential One-way Ranging
ACU	Antenna Control Unit
AGC	Automatic Gain Control
AGN	Active Galactic Nuclei
AIPS	Astronomical Image Processing System
ANTEX	Antenna Exchange Format
APOD	Atmospheric density detection and Precise Orbit Determination
Az	Azimuth
BACC	Beijing Aerospace Control Center
BCRS	Barycentric Celestial Reference System
CCSDS	Consultative Committee for Space Data Systems
CNSA	Chinese National Space Administration
COM	Center Of Mass
CPF	Consolidated Prediction Format
CPU	Central Processing Unit
CRS	Celestial Reference System
DBBC	Digital Baseband Converter
De	Declination
DORIS	Doppler Orbitography and Radiopositioning Integrated by Satellites
DOR	Differential One-way Ranging
DSN	NASA Deep Space Network
ECI	Earth Centered Inertial
EIRP	Effective Isotropic Radiated Power
EI	Elevation
EOP	Earth Orientation Parameter
ERP	Earth Rotation Parameter
ESA	European Space Agency
FS	VLBI Field System
GCRS	Geocentric Celestial Reference System
GGOS	Global Geodetic Observing System
GNSS	Global Navigation Satellite Systems

GOW	Geodetic Observatory Wettzell
GPS	Global Positioning System
GPT3	Global Pressure and Temperature 3
GRASP	Geodetic Reference Antenna in Space
GSFC	Goddard Space Flight Center
HD	Hard Disc
HOPS	Haystack Observatory Postprocessing System
HPBW	Half Power Beam-Width
IAG	International Association of Geodesy
IAU	International Astronomical Union
ICRF	International Celestial Reference Frame
ICRS	International Celestial Reference System
IF	Intermediate Frequency
IGS	International GNSS Service
ILRS	International Laser Ranging Service
IM	Correlator Input Model
IONEX	Ionosphere Map Exchange Format
ITRF	International Terrestrial Reference Frame
ITRS	International Terrestrial Reference System
IUGG	International Union of Geodesy and Geophysics
IVS	International VLBI Service for Geodesy and Astrometry
Jy	Jansky
LBA	Long Baseline Array
LEO	Low Earth Orbit
LNA	Low-Noise Amplifier
MER-B	Mars Explorer Rover B
MIT	Massachusetts Institute of Technology
MJD	Modified Julian Date
MPIfR	Max-Planck-Institut für Radioastronomie
MPI	Message Passing Interface
NAIF	Navigation and Ancillary Information Facility
NAPEOS	Navigation Package for Earth Observation Satellites
NASA	National Aeronautics and Space Administration
NICT	National Institute of Information and Communications Technology
NORAD	North American Aerospace Defense Command
NRAO	National Radio Astronomy Observatory
OCEL	Observing of the Chang-E-3 Lander
PCO	Phase Center Offset
PLC	Programmable Logic Control unit
POD	Precise Orbit Determination

PRIDE	Planetary Radio Interferometry and Doppler Experiment
PWLO	Piece-Wise Linear Offsets
QRFH	Quad-ridged Flared Horn
Ra	Right Ascension
RFI	Radio Frequency Interference
RPC	Remote Procedure Call
SED	Spectral Energy Distribution
SEFD	Source Equivalent Flux Density
SELENE	Selenological and Engineering Explorer
SGP	Simplified General Perturbation
SLR	Satellite Laser Ranging
SNAP	Standard Notation for Astronomical Procedures
SNR	Signal-to-Noise Ratio
SP3	Standard Product 3
SSN	Space Surveillance Network
TCG	Geocentric Coordinate Time
TEC	Total Electron Content
TEME	True Equator and Mean Equinox
TLE	Two-Line Element
TOF	Time Of Flight
TRF	Terrestrial Reference Frame
TRS	Terrestrial Reference System
TT	Terrestrial Time
USA	United States of America
US	Unites States
UT1	Universal Time
UTAS	University of Tasmania
UTC	Coordinated Universal Time
VEX	VLBI Experiment
VGOS	VLBI Global Observing System
VieVS	Vienna VLBI and Satellite Software
VLBA	Very Long Baseline Array
VLBI	Very Long Baseline Interferometry
VMF1	Vienna Mapping Function 1
VSC3	Vienna Scientific Cluster 3
WRMS	Weighted Root-Mean-Squared
ZHD	Zenith Hydrostatic Delay
ZWD	Zenith Wet Delay

List of Figures

1.1	Concept of co-location in space.	3
2.1	Geometric principle of VLBI.	12
2.2	VLBI scheduling and observation workflow.	15
3.1	Observation geometry for satellites.	29
3.2	Common satellite visibility.	31
3.3	Antenna slew rates for GPS satellites.	33
3.4	Antenna slew rates for the APOD-A LEO satellite.	33
3.5	Cable wrap of the antenna WETTZ13S.	34
3.6	Stepwise satellite tracking approach.	36
3.7	Signal power of GPS satellites monitored at WARK30M.	38
4.1	Simplified process workflow for VLBI satellite observations.	45
4.2	Modules structure of VieVS 3.0.	46
4.3	Delay model geometry.	51
4.4	Workflow of the VieVS satellite scheduling program.	59
4.5	Elevation plot example.	61
4.6	Sky plot example.	62
4.7	Observation scheme for satellites.	66
4.8	Correlation of satellite observations with DiFX.	68
4.9	Polynomial fit of correlator input model.	71
4.10	Post-correlation processing workflow.	73
5.1	Station network for GNSS observations.	77
5.2	Sky plots for Experiment 236a.	80
5.3	Sky plots for Experiment 126b.	81
5.4	Sky plots for Experiment g336.	83
5.5	GPS L1 signal spectra observed in 179a.	87
5.6	GPS L1 and L2 (auto-correlation) spectra.	88
5.7	GPS signal history.	88
5.8	Correlator input model residuals for g336.	89

5.9	Typical GPS L1 cross-correlation spectrum.	91
5.10	Typical GPS L2 cross-correlation spectrum.	91
5.11	Gain variations of GPS L1 in 126b.	93
5.12	Auto-correlation of GPS L2 in g336, WARK30M.	94
5.13	Auto-correlation of GPS L2 in g336, HOBART26.	95
5.14	High time resolution fringe delays, GPS L1, 126b.	95
5.15	Fringe delays and SNR of g336.	98
5.16	Polarization product differences in g336.	99
5.17	Polarization product differences in 131a.	100
5.18	Fringe delays in 131a (L1).	100
5.19	Delay residuals of 126b.	103
5.20	Delay residuals of 131a.	104
5.21	Delay residuals of g336.	105
6.1	Simplified process workflow for VLBI observations of APOD.	110
6.2	Difference between final and predicted APOD orbit.	113
6.3	AuScope VLBI array.	113
6.4	APOD observation geometry.	116
6.5	Observation mode for APOD sessions.	117
6.6	Pointing errors vs. elevation for APOD.	119
6.7	S-band auto-spectra magnitudes in a332.	120
6.8	X-band auto-spectra magnitudes in a332.	121
6.9	S-band cross-spectra in a332.	121
6.10	X-band cross-spectra in a332.	122
6.11	Cross-spectra of the S- and X-band carriers in a332.	122
6.12	Fringe fitting results of Scan 168 in a332.	124
6.13	Fringe fitting results of Scan 169 in a332.	124
6.14	ZWD estimates from quasars in a332.	126
6.15	Delay residuals (O-C) of Scans 168 and 169 in Session a332.	126
6.16	Post-fit residual delays of Scans 168 and 169 in Session a332.	128

List of Tables

4.1	Parameters in VSO files.	50
5.1	List of VLBI experiments with observations of GNSS satellites.	76
5.2	Station specifications for GNSS observations.	84
5.3	Observation mode for GNSS observations.	86
6.1	APOD experiments by AuScope in November 2016.	110
6.2	VLBI signal structure of APOD.	111
6.3	Zoom-band channels for APOD observations.	119
6.4	Estimates of Scans 168 and 169 in Experiment a332.	129
A.1	VLBI satellite observations scheduled with VieVS from 2014 to 2016.	141
C.1	AZEL tracking file format.	157

List of Listings

B.1	Schedule summary of Experiment 179a.	146
B.2	Schedule summary of Experiment 236a.	146
B.3	Schedule summary of Experiment 238a.	147
B.4	Schedule summary of Experiment 126b.	148
B.5	Schedule summary of Experiment 131a.	149
B.6	Schedule summary of Experiment 132a.	150
B.7	Schedule summary of Experiment g336.	151
B.8	Schedule summary of Experiment 316a.	152
B.9	Schedule summary of Experiment 317a.	153
B.10	Schedule summary of Experiment 317b.	153
B.11	Schedule summary of Experiment 318b.	153
B.12	Schedule summary of Experiment 318c.	154
B.13	Schedule summary of Experiment 318d.	154
B.14	Schedule summary of Experiment 319a.	154
B.15	Schedule summary of Experiment a332.	155
C.1	AZEL tracking file example.	158

Bibliography

- AKGIRAY, A., WEINREB, S. AND IMBRIALE, W.A. (2013). The quadruple-ridged flared horn: A flexible, multi-octave reflector feed spanning $f/0,3$ to $f/2.5$. In *7th European Conference on Antennas and Propagation (EuCAP)*, 768–769.
- ALIZADEH, M.M., WIJAYA, D.D., HOBIGER, T., WEBER, R. AND SCHUH, H. (2013). Ionospheric Effects on Microwave Signals. In J. Böhm and H. Schuh, eds., *Atmospheric Effects in Space Geodesy*, 35–71, Springer Berlin Heidelberg, Berlin, Heidelberg.
- ALTAMIMI, Z., COLLILIEUX, X. AND MÉTIVIER, L. (2011). ITRF2008: an improved solution of the international terrestrial reference frame. *Journal of Geodesy*, 85, 457–473.
- ALTAMIMI, Z., REBISCHUNG, P., MÉTIVIER, L. AND COLLILIEUX, X. (2016). ITRF2014: A new release of the International Terrestrial Reference Frame modeling nonlinear station motions. *Journal of Geophysical Research: Solid Earth*, 121, 6109–6131.
- ANDERSON, M.J., BEYERLE, G., GLASER, S., LIU, L., MÄNNEL, B., NILSSON, T., HEINKELMANN, R. AND SCHUH, H. (2018). Simulations of VLBI observations of a geodetic satellite providing co-location in space. *Journal of Geodesy*, 92, 1023–1046.
- ARNOLD, D., MONTENBRUCK, O., HACKEL, S. AND SOŚNICA, K. (2018). Satellite laser ranging to low Earth orbiters: orbit and network validation. *Journal of Geodesy*.
- ASKNE, J. AND NORDIUS, H. (1987). Estimation of tropospheric delay for microwaves from surface weather data. *Radio Science*, 22, 379–386.
- BAE, T.S. (2006). *Near Real-Time Precise Orbit Determination of Low Earth Orbit Satellites Using an Optimal GPS Tripple-Differencing Technique*. No. 481 in Report of Geodetic Science and Surveying, The Ohio State University, Columbus, Ohio 43210.
- BAR-SEVER, Y., HAINES, B., BERTIGER, W., DESAI, S. AND WU, S. (2009). Geodetic Reference Antenna in Space (GRASP) - A Mission to Enhance Space-Based Geodesy. In *COSPAR Colloquium: Scientific and Fundamental Aspects of the Galileo Program, Padua, Italy, 2009*.
- BIANCALE, A., POLLET, A., COULOT, D. AND MANDEA, M. (2017). E-GRASP/Eratosthenes: a mission proposal for millimetric TRF realization. In *Conference Abstracts of the 19th EGU General Assembly*, 8752.

- BLEWITT, G., ALTAMIMI, Z., DAVIS, J., GROSS, R., KUO, C.Y., LEMOINE, E.G., MOORE, A.W., NEILAN, R.E., PLAG, H.P., ROTHACHER, M., SHUM, C.K., SIDERIS, M.G., SCHÖNE, T., TREGONING, P. AND ZERBINI, S. (2010). *Geodetic Observations and Global Reference Frame Contributions to Understanding Sea-Level Rise and Variability*, chap. 9, 256–284. Wiley-Blackwell.
- BÖHM, J., WERL, B. AND SCHUH, H. (2006). Troposphere mapping functions for GPS and very long baseline interferometry from European Centre for Medium-Range Weather Forecasts operational analysis data. *Journal of Geophysical Research: Solid Earth*, 111.
- BÖHM, J., KOUBA, J. AND SCHUH, H. (2009). Forecast Vienna Mapping Functions 1 for real-time analysis of space geodetic observations. *Journal of Geodesy*, 83, 397–401.
- BÖHM, J., BÖHM, S., NILSSON, T., PANY, A., PLANK, L., SPICAKOVA, H., TEKE, K. AND SCHUH, H. (2012). The New Vienna VLBI Software VieVS. In S. Kenyon, M.C. Pacino and U. Marti, eds., *Geodesy for Planet Earth*, Vol. 136 of *International Association of Geodesy Symposia*, 1007–1011, Springer Berlin Heidelberg.
- BÖHM, J., BÖHM, S., BOISITS, J., GIRDIUK, A., GRUBER, J., HELLERSCHMIED, A., KRÁSNÁ, H., LANDSKRON, D., MADZAK, M., MAYER, D., MCCALLUM, J., MCCALLUM, L., SCHARTNER, M. AND TEKE, K. (2018). Vienna VLBI and Satellite Software (VieVS) for Geodesy and Astrometry. *Publications of the Astronomical Society of the Pacific*, 130.
- BOLOTIN, S., BAVER, K., GIPSON, J., GORDON, D. AND MACMILLAN, D. (2014). The VLBI Data Analysis Software *v*Solve: Development Progress and Plans for the Future. In D. Behrend, K. Baver and K. Armstrong, eds., *IVS 2014 General Meeting Proceedings - "VGOS: The New VLBI Network"*, 253–257, Science Press.
- BOLOTIN, S., BAVER, K., GIPSON, J. AND MCMILLAN, D. (2017). Implementation of the vgosDB Format at the GSFC VLBI Analysis Center. In R. Haas and G. Elgered, eds., *Proceedings of the 23rd European VLBI Group for Geodesy and Astrometry Working Meeting, May 14-19, Gothenburg, Sweden*, 235–237.
- BORDER, J.S. (2009). Innovations in Delta Differential One-Way Range: From Viking to Mars Science Laboratory. In *21st International Symposium on Space Flight Dynamics, Toulouse, France, 28 Sep - 02 Oct 2009*.
- BRUNI, S., REBISCHUNG, P., ZERBINI, S., ALTAMIMI, Z., ERRICO, M. AND SANTI, E. (2018). Assessment of the possible contribution of space ties on-board GNSS satellites to the terrestrial reference frame. *Journal of Geodesy*, 92, 383–399.
- BRUNN, D.L., PRESTON, R.A., WU, S.C., SIEGEL, H.L., BROWN, D.S., CHRISTENSEN, C.S. AND HILT, D.E. (1978). Δ VLBI Spacecraft Tracking System Demonstration: Part I. Design and Planning. *DSN Progress Report*, 42-45, 111–132, Jet Propulsion Laboratory, Pasadena, California.

- CAMPBELL, J. (2000). From Quasars to Benchmarks: VLBI Links Heaven and Earth. In N.R. Vandenberg and K.D. Baver, eds., *IVS 2000 General Meeting Proceedings*, 19–34, NASA/CP-2000-209893.
- CAO, J., HUANG, Y., HU, X., MA, M. AND ZHENG, W. (2010). Mars Express tracking and orbit determination trials with Chinese VLBI network. *Chinese Science Bulletin*, 55, 3654–3660.
- CAPALLO, R. (2017). *Fourfit user's manual - Version 1.0*. MIT Haystack Observatory.
- CCSDS (2009). *Recommendations for Space Data System Standards: Radio Frequency and Modulation Systems, Part 1, Earth Stations and Spacecraft, Recommended Standard 401.0-B*. Consultative Committee for Space Data Systems, CCSDS Secretariat, NASA Headquarters, Washington, DC, USA.
- CHIPMAN, J.S. (2011). Gauss-Markov Theorem. In M. Lovric, ed., *International Encyclopedia of Statistical Science*, 577–582, Springer Berlin Heidelberg, Berlin, Heidelberg.
- CHRISTENSEN, C.S., MOULTRIE, B., CALLAHAN, P.S., DONIVAN, F.F. AND WU, S.C. (1980). Δ VLBI Spacecraft Tracking System Demonstration: Part II. Data Acquisition and Processing. *TDA Progress Report*, 42-60, 42–67, Jet Propulsion Laboratory, Pasadena, California.
- COREY, B. (2001). IVS/IGS/ILRS Working Group on GPS Phase Center Mapping . In N. Vandenberg and K. Baver, eds., *International VLBI Service for Geodesy and Astrometry 2000 Annual Report*, 13–16, NASA/TP-2001-209979.
- DEHANT, V., LAGUERRE, R., REKIER, J., RIVOLDINI, A., TRIANA, S.A., TRINH, A., VAN HOOLST, T. AND ZHU, P. (2017). Understanding the effects of the core on the nutation of the Earth. *Geodesy and Geodynamics*, 8, 389–395.
- DELLER, A., TINGAY, S., BAILES, M. AND WEST, C. (2007). DiFX: A Software Correlator for Very Long Baseline Interferometry Using Multiprocessor Computing Environments. *The Publications of the Astronomical Society of the Pacific*, 119, 318–336.
- DELLER, A.T., BRISKEN, W.F., PHILLIPS, C.J., MORGAN, J., ALEF, W., CAPPALLO, R., MIDDELBERG, E., ROMNEY, J., ROTTMANN, H., TINGAY, S.J. AND WAYTH, R. (2011). DiFX-2: A More Flexible, Efficient, Robust, and Powerful Software Correlator. *Publications of the Astronomical Society of the Pacific*, 123, 275.
- DICKEY, J.M. (2010). How and Why do VLBI on GPS. In D. Behrend and K. Baver, eds., *IVS 2010 General Meeting Proceedings, Hobart, Australia*, 65–69, NASA/CP 2010-215864.
- DICKEY, J.O., MARCUS, S.L. AND DE VIRON, O. (2011). Air Temperature and Anthropogenic Forcing: Insights from the Solid Earth. *Journal of Climate*, 24, 569–574.

- DIRKX, D., GURVITS, L., LAINEY, V., LARI, G., MILANI, A., CIMO, G., BOCANEGRA-BAHAMON, T. AND VISSER, P. (2017). On the contribution of PRIDE-JUICE to Jovian system ephemerides. *Planetary and Space Science*, 147, 14–27.
- DOW, J.M., NEILAN, R.E. AND RIZOS, C. (2009). The International GNSS Service in a changing landscape of Global Navigation Satellite Systems. *Journal of Geodesy*, 83, 191–198.
- DUEV, D.A., MOLERA CALVÉS, G., POGREBENKO, S.V., GURVITS, L.I., CIMÓ, G. AND BOCANEGRA BAHAMON, T. (2012). Spacecraft VLBI and Doppler tracking: algorithms and implementation. *Astronomy & Astrophysics*, 541.
- DUEV, D.A., POGREBENKO, S. V., CIMO, G., MOLERA CALVÉS, G., BOCANEGRA BAHAMON, T. M., GURVITS, L. I., KETTENIS, M. M., KANIA, J., TUDOSE, V., ROSENBLATT, P., MARTY, J.-C., LAINEY, V., DE VICENTE, P., QUICK, J., NICKOLA, M., NEIDHARDT, A., KRONSCHNABL, G., PLÖTZ, C., HAAS, R., LINDQVIST, M., ORLATI, A., IPATOV, A. V., KHARINOV, M. A., MIKHAILOV, A. G., LOVELL, J. E. J., MCCALLUM, J. N., STEVENS, J., GULYAEV, S. A., NATUSH, T., WESTON, S., WANG, W. H., XIA, B., YANG, W. J., HAO, L.-F., KALLUNKI, J. AND WITASSE, O. (2016). Planetary Radio Interferometry and Doppler Experiment (PRIDE) technique: A test case of the Mars Express Phobos fly-by. *Astronomy & Astrophysics*, 593.
- EUBANKS, T.M. (1991). A consensus model for relativistic effects in geodetic VLBI. In *Proceedings of the USNO Workshop on Relativistic Models for Use in Space Geodesy*, 60–82, U.S. Naval Observatory Washington D.C. 20392-5100, U.S.A.
- GIPSON, J. (2010). An Introduction to SKED. In *IVS 2010 General Meeting Proceedings, 2010, Feb. 7–13, Hobart, Australia*, 77–84.
- GIPSON, J. (2012). *Sked - VLBI Scheduling Software*.
- GOOSSENS, S., MATSUMOTO, K., LIU, Q., KIKUCHI, F., SATO, K., HANADA, H., ISHIHARA, Y., NODA, H., KAWANO, N., NAMIKI, N., IWATA, T., LEMOINE, F.G., ROWLANDS, D.D., HARADA, Y. AND CHEN, M. (2011a). Lunar gravity field determination using SELENE same-beam differential VLBI tracking data. *Journal of Geodesy*, 85, 205–228.
- GOOSSENS, S., MATSUMOTO, K., ROWLANDS, D.D., LEMOINE, F.G., NODA, H. AND ARAKI, H. (2011b). Orbit determination of the SELENE satellites using multi-satellite data types and evaluation of SELENE gravity field models. *Journal of Geodesy*, 85, 487–504.
- GORDON, D., BRISKEN, W. AND MAX-MOERBECK, W. (2016). Difxcalc - Calc11 for the DiFX Correlator. In D. Behrend, K.D. Baver and K.L. Armstrong, eds., *International VLBI Service for Geodesy and Astrometry 2016 General Meeting Proceedings - "New Horizons with VGOS"*, Johannesburg, South Africa, March 13-19, 2016, 187–189.
- GURTNER, W., NOOMEN, R. AND PEARLMAN, M. (2005). The International Laser Ranging Service: current status and future developments. *Advances in Space Research*, 36, 327–332.

- HAAS, R., NEIDHARDT, A., KODET, J., PLÖTZ, C., SCHREIBER, U., KRONSCHNABL, G., POGREBENKO, S., DUEV, D., CASEY, S., MARTI-VIDAL, I., YANG, J. AND PLANK, L. (2014). The Wettzell-Onsala G130128 experiment – VLBI-observations of a GLONASS satellite. In D. Behrend, K. Baver and K. Armstrong, eds., *IVS 2014 General Meeting Proceedings - "VGOS: The New VLBI Network"*, 451–455, Science Press.
- HAAS, R., HOBIGER, T., HELLERSCHMIED, A., NEIDHARDT, A. AND KODET, J. (2015). GLONASS–VLBI: Onsala–Wettzell test observations. In R. Haas and F. Colomer, eds., *Proceedings of the 22nd European VLBI Group for Geodesy and Astrometry Working Meeting, 18-21 May, 2015, Ponta Delgada, Azores*, 107–111.
- HAAS, R., HALSIG, S., IDINK, A., JARON, F., LA PORTA, L., LOVELL, J., NEIDHARDT, A., NOTHNAGEL, A., PLÖTZ, C., TANG, G. AND ZHANG, Z. (2016). Observing the Chang'E-3 Lander with VLBI (OCEL) – Technical Setups and First Results. In A. Nothnagel and F. Jaron, eds., *Proceedings of the First International Workshop on VLBI Observations of Near-field Targets, October 5 - 6, 2016*, Vol. 54 of *Schriftenreihe des Inst. f. Geodäsie u. Geoinformation*, 41–63, Bonn, Germany.
- HAAS, R., HOBIGER, T., KLOPOTEK, G., KAREINEN, N., YANG, J., COMBRINCK, L., DE WITT, A. AND NICKOLA, M. (2017). VLBI with GNSS–signals on an Intercontinental Baseline – A progress report. In R. Haas and G. Elgered, eds., *Proceedings of the 23rd European VLBI Group for Geodesy and Astrometry Working Meeting, May, 2017, Gothenburg, Sweden*, 117–121.
- HANADA, H., IWATA, T., NAMIKI, N., KAWANO, N., ASARI, K., ISHIKAWA, T., KIKUCHI, F., LIU, Q., MATSUMOTO, K., NODA, H., TSURUTA, S., GOOSSENS, S., IWADATE, K., KAMEYA, O., TAMURA, Y., HONG, X., PING, J., AILI, Y., ELLINGSEN, S. AND SCHLÄIJTER, W. (2008). VLBI for better gravimetry in SELENE. *Advances in Space Research*, 42, 341 – 346.
- HANADA, H., IWATA, T., LIU, Q., KIKUCHI, F., MATSUMOTO, K., GOOSSENS, S., HARADA, Y., ASARI, K., ISHIKAWA, T., ISHIHARA, Y., NODA, H., TSURUTA, S., PETROVA, N., KAWANO, N., SASAKI, S., SATO, K., NAMIKI, N., KONO, Y., IWADATE, K., KAMEYA, O., SHIBATA, K.M., TAMURA, Y., KAMATA, S., YAHAGI, Y., MASUI, W., TANAKA, K., MAEJIMA, H., HONG, X., PING, J., SHI, X., HUANG, Q., AILI, Y., ELLINGSEN, S. AND SCHLÜTER, W. (2010). Overview of Differential VLBI Observations of Lunar Orbiters in SELENE (Kaguya) for Precise Orbit Determination and Lunar Gravity Field Study. *Space Science Reviews*, 154, 123–144.
- HASE, H. (1999). Phase Centre Determinations at GPS-Satellites with VLBI. In *13th Working Meeting on European VLBI Group for Geodesy and Astrometry (EVGA), February 12-13, 1999, Wettzell, Germany*, 273–277.
- HEGARTY, C.J. (2017). *The Global Positioning System (GPS)*, chap. 7, 197–218. Springer Handbooks, Springer International Publishing, 1st edn.
- HELLERSCHMIED, A., PLANK, L., NEIDHARDT, A., HAAS, R., BÖHM, J., PLÖTZ AND KODET, J. (2014). Observing satellites with VLBI radio telescopes - practical realization at Wettzell. In D. Behrend,

- K. Baver and K. Armstrong, eds., *IVS 2014 General Meeting Proceedings - "VGOS: The New VLBI Network"*, 441–445, Science Press.
- HELLERSCHMIED, A., BÖHM, J., KWAK, Y., MCCALLUM, J. AND PLANK, L. (2016). VLBI observations of GNSS signals on the baseline Hobart-Ceduna. In D. Behrend, K.D. Baver and K.L. Armstrong, eds., *International VLBI Service for Geodesy and Astrometry 2016 General Meeting Proceedings - "New Horizons with VGOS"*, Johannesburg, South Africa, March 13-19, 2016, 373–377.
- HELLERSCHMIED, A., BÖHM, J., MCCALLUM, L., MCCALLUM, J. AND NATUSCH, T. (2017a). VLBI observations to satellites of the GNSS - A first time series. In *6th International Colloquium on Scientific and Fundamental Aspects of GNSS / Galileo, 25-27 October 2017, Valencia*.
- HELLERSCHMIED, A., BÖHM, J., NEIDHARDT, A., KODET, J., HAAS, R. AND PLANK, L. (2017b). Scheduling VLBI Observations to Satellites with VieVS. In T. van Dam, ed., *REFAG 2014: Proceedings of the IAG Commission 1 Symposium Kirchberg, Luxembourg, 13–17 October, 2014*, 59–64, Springer International Publishing.
- HELLERSCHMIED, A., MCCALLUM, L., MCCALLUM, J., SUN, J., BÖHM, J. AND CAO, J. (2018). Observing APOD with the AuScope VLBI Array. *Sensors*, 18.
- HERRING, T.A. (1992). Submillimeter horizontal position determination using very long baseline interferometry. *Journal of Geophysical Research: Solid Earth*, 97, 1981–1990.
- HIMWICH, E. AND GIPSON, J. (2012). GSFC Technology Development Center Report. *IVS Annual Report*, 280–282.
- HIMWICH, E. AND VANDENBERG, N. (2001). *SNAP Commands - Operations Manual, Version 9.5*. NASA/Goddard Space Flight Center, Space Geodesy Program, VLBI Software Documentation, Field System.
- HIMWICH, E., VANDENBERG, N., GONZALEZ, R. AND HOLMSTRÖM, C. (2003). New Development in the NASA Field System. In M. Y.C., ed., *New technologies in VLBI, Proceedings of a symposium of the International VLBI Service for Geodesy and Astrometry held in Gyeong-ju, Korea, 5-8 November 2002.*, Vol. 306 of *ASP Conference Series*, San Francisco, CA: Astronomical Society of the Pacific, 193–198.
- HINTEREGGER, H.F., SHAPIRO, I.I., ROBERTSON, D.S., KNIGHT, C.A., ERGAS, R.A., WHITNEY, A.R., ROGERS, A.E.E., MORAN, J.M., CLARK, T.A. AND BURKE, B.F. (1972). Precision Geodesy via Radio Interferometry. *Science*, 178, 396–398.
- HOBIGER, T., OTSUBO, T., SEKIDO, M., GOTOH, T., KUBOOKA, T. AND TAKIGUCHI, H. (2010). Fully automated VLBI analysis with c5++ for ultra-rapid determination of UT1. *Earth, Planets and Space*, 62, 933–937.

- HOBIGER, T., KLOPOTEK, G., TOSHIMICHI, O. AND HAAS, R. (2018). VLBI goes satellite - benefits and restrictions. In *Abstracts of the EGU General Assembly 2018*, Vol. 20 of *Geophysical Research Abstracts*, EGU2018-4954.
- HOFMEISTER, A. AND BÖHM, J. (2017). Application of ray-traced tropospheric slant delays to geodetic VLBI analysis. *Journal of Geodesy*, 91, 945–964.
- HOOTS, F. AND ROEHRICH, R. (1980). Spacetrack Report number 3: Models for Propagation of NORAD Element Sets. Tech. rep., US Airforce Aerospace Defense Command, Colorado Springs, CO.
- HUANG, Y., HU, X.G., HUANG, C., JIANG, D.R., ZHENG, W.M. AND ZHANG, X.Z. (2006). Orbit determination of satellite "Tance 1" with VLBI data. *Chinese Astronomy and Astrophysics*, 30, 318–329.
- HUANG, Y., HU, X., ZHANG, X., JIANG, D., GUO, R., WANG, H. AND SHI, S. (2011). Improvement of orbit determination for geostationary satellites with VLBI tracking. *Chinese Science Bulletin*, 56, 2765.
- IPCC (2013). *Summary for Policymakers*, book section SPM, 1–30. Cambridge University Press, Cambridge, United Kingdom and New York, NY, USA.
- JONES, D.L., FOMALONT, E., DHAWAN, V., ROMNEY, J., FOLKNER, W.M., LANYI, G., BORDER, J. AND JACOBSON, R.A. (2011). Very Long Baseline Array Astrometric Observations of the Cassini Spacecraft at Saturn. *The Astronomical Journal*, 141, 29.
- KATO, M., SASAKI, S., TANAKA, K., IJIMA, Y. AND TAKIZAWA, Y. (2008). The Japanese lunar mission SELENE: Science goals and present status. *Advances in Space Research*, 42, 294–300.
- KAWASE, S. AND TANAKA, T. (1979). Orbit determination of a geosynchronous satellite by the VLBI technique. *Journal of the Radio Research Laboratories*, 26, 65–71.
- KELLERMANN, K.I. AND MORAN, J.M. (2001). The Development of High-Resolution Imaging in Radio Astronomy. *Annual Review of Astronomy and Astrophysics*, 39, 457–509.
- KLIONER, S. (1991). General Relativistic Model of VLBI Observables. In W. Alef, S. Bernhart and A. Nothnagel, eds., *Proceedings of the AGU Chapman Conference on Geodetic VLBI: Monitoring Global Change, Washington D.C., April 22-26, 1991*, NOAA Technical Report NOS 137 NGS 49, 188–202.
- KLOPOTEK, G., HOBIGER, T. AND HAAS, R. (2018). Geodetic VLBI with an artificial radio source on the Moon: a simulation study. *Journal of Geodesy*, 92, 457–469.
- KODET, J., PLÖTZ, C., SCHREIBER, U., NEIDHARDT, A., POGREBENKO, S., HAAS, R., MOLERA CALVÉS, G. AND PROCHAZKA, I. (2013). Co-location of space geodetics techniques in Space and on the ground. In N. Zubko and M. Poutanen, eds., *Proceedings of the 21st Working Meeting of the European VLBI Group for Geodesy and Astrometry*, 223–226, Finnish Geodetic Institute.

- KODET, J., SCHREIBER, K., PLÖTZ, C., NEIDHARDT, A., KRONSCHNABL, G., HAAS, R., MOLERA CALVÉS, G., POGREBENKO, M., ROTHACHER, B., MAENNEL, B., PLANK, L. AND HELLERSCHMIED, A. (2014). Colocations of Space Geodetic Techniques on Ground and in Space. In *Proceedings of the 8th IVS General Meeting, Shanghai*, 446–450.
- KOLMOGOROV, A.N. (1991). The local structure of turbulence in incompressible viscous fluid for very large Reynolds numbers. *Proceedings of the Royal Society of London A: Mathematical, Physical and Engineering Sciences*, 434, 9–13.
- KRÁSNÁ, H., BÖHM, J., PLANK, L., NILSSON, T. AND SCHUH, H. (2014). Atmospheric Effects on VLBI-Derived Terrestrial and Celestial Reference Frames. In C. Rizos and P. Willis, eds., *Earth on the Edge: Science for a Sustainable Planet, Proc. IAG General Assembly, 2011*, International Association of Geodesy Symposia, 203–208, Springer Berlin Heidelberg.
- KRÜGEL, M. AND ANGERMANN, D. (2005). Analysis of Local Ties from Multi-year Solutions of Different Techniques. In B. Richter, W. Schwegmann and W.R. Dick, eds., *Proceedings of the IERS Workshop on site co-location. Matera, Italy, 23 - 24 October 2003*, no. 33 in IERS Technical Note, 32–37, Verlag des Bundesamts für Kartographie und Geodäsie, Frankfurt am Main.
- LANDSKRON, D. AND BÖHM, J. (2018). VMF3/GPT3: refined discrete and empirical troposphere mapping functions. *Journal of Geodesy*, 92, 349–360.
- LANYI, G., BORDER, J., BENSON, J., DHAWAN, V., FOMALONT, E., MARTIN-MUR, T., MCEL RATH, T., ROMNEY, J. AND WALKER, C. (2005). Determination of Angular Separation Between Spacecraft and Quasars with the Very Long Baseline Array. *IPN Progress Report*, 42–162, August 15.
- LANYI, G., BAGRI, D.S. AND BORDER, J.S. (2007). Angular Position Determination of Spacecraft by Radio Interferometry. *Proceedings of the IEEE*, 95, 2193–2201.
- LEBRETON, J.P., WITASSE, O., SOLLAZZO, C., BLANCQUAERT, T., COUZIN, P., SCHIPPER, A.M., JONES, J.B., MATSON, D.L., GURVITS, L.I., ATKINSON, D.H., KAZEMINEJAD, B. AND PEREZ-AYUCAR, M. (2005). An overview of the descent and landing of the Huygens probe on Titan. *Nature*, 438, 758–764.
- LOVELL, J.E.J., MCCALLUM, J.N., REID, P.B., MCCULLOCH, P.M., BAYNES, B.E., DICKEY, J.M., SHABALA, S.S., WATSON, C.S., TITOV, O., RUDDICK, R., TWILLEY, R., REYNOLDS, C., TINGAY, S.J., SHIELD, P., ADADA, R., ELLINGSEN, S.P., MORGAN, J.S. AND BIGNALL, H.E. (2013). The AuScope geodetic VLBI array. *Journal of Geodesy*, 87, 527–538.
- LOWE, S.T. (1992). Theory of post-block 2 VLBI observable extraction. Tech. rep., Jet Propulsion Lab., California Inst. of Tech, Pasadena, CA, United States, JPL-PUBL-92-7.
- MA, C., ARIAS, E.F., BIANCO, G., BOBOLTZ, D.A., BOLOTIN, S.L., CHARLOT, P., ENGELHARDT, G., FEY, A.L., GAUME, R.A., GONTIER, A.M., HEINKELMANN, R., JACOBS, C.S., KURDUBOV, S., LAMBERT,

- S.B., MALKIN, Z.M., NOTHNAGEL, A., PETROV, L., SKURIKHINA, E., SOKOLOVA, J.R., SOUCHAY, J., SOVERS, O.J., TESMER, V., TITOV, O.A., WANG, G., ZHAROV, V.E., BARACHE, C., BOECKMANN, S., COLLILOUD, A., GIPSON, J.M., GORDON, D., LYTVYN, S.O., MACMILLAN, D.S. AND OJHA, R. (2009). *The Second Realization of the International Celestial Reference Frame by Very Long Baseline Interferometry*. No. 35 in IERS Technical Note, Verlag des Bundesamtes für Kartographie und Geodäsie, Frankfurt am Main, Presented on behalf of the IERS / IVS Working Group.
- MÄNNEL, B. AND ROTHACHER, M. (2016). Ionospheric corrections for single-frequency tracking of GNSS satellites by VLBI based on co-located GNSS. *Journal of Geodesy*, 90, 189–203.
- MAYER, D., BÖHM, J., KRÁSNÁ, H. AND LANDSKRON, D. (2017). Tropospheric delay modelling and the celestial reference frame at radio wavelengths. *Astronomy & Astrophysics*, 606, A143.
- MCCALLUM, L., MAYER, D., LE BAIL, K., SCHATNER, M., MCCALLUM, J., LOVELL, J., TITOV, O., SHU, F. AND GULYAEV, S. (2017). Star Scheduling Mode – A New Observing Strategy for Monitoring Weak Southern Radio Sources with the AuScope VLBI Array. *Publications of the Astronomical Society of Australia*, 34, e063.
- MCCULLOCH, P., ELLINGSEN, S., JAUNCEY, D., CARTER, S., CIMÒ, G., LOVELL, J. AND DODSON, R. (2005). COSMIC:Microarcsecond resolution with a 30 meter radio telescope. *Astron. J.*, 129, 2034–2040.
- MOLERA CALVÉS, G., POGREBENKO, S.V., WAGNER, J., CIMÒ, G., GURVITS, L. AND DUEV, D. (2010). Tracking of Mars Express and Venus Express spacecraft with VLBI radio telescopes. *AGU Fall Meeting Abstracts*, P51D–1479.
- MONTENBRUCK, O., SCHMID, R., MERCIER, F., STEIGENBERGER, P., NOLL, C., FATKULIN, R., KOGURE, S. AND GANESHAN, A. (2015). GNSS satellite geometry and attitude models. *Advances in Space Research*, 56, 1015–1029.
- MOYA ESPINOSA, M. AND HAAS, R. (2007). SATTRACK A Satellite Tracking Module for the VLBI Field System. In J. Böhm, A. Pany and H. Schuh, eds., *Proceedings of the 18th European VLBI for Geodesy and Astrometry Working Meeting, 12-13 April 2007, Vienna*, Vol. 79, 53–58, Schriftenreihe der Studienrichtung Vermessung und Geoinformation, Technische Universität Wien, ISSN 1811-8380.
- MOYER, T.D. (2003). *Formulation for Observed and Computed Values of Deep Space Network Data Types for Navigation*. JPL Deep Space Communications and Navigation Series, John Wiley & Sons Inc.
- NEREM, R.S. AND DRAPER, R.W. (2011). Geodetic Reference Antenna in Space. *GRASP proposal submitted in response to NNH11ZDA0120*, prepared for National Aeronautics and Space Administration Science Mission Directorate September 29, 2011.

- NIELL, A., CAPPALLO, R., COREY, B., ECKERT, C., ELOSEGUI, P., MCWHIRTER, R., RAJAGOPALAN, G., RUSZCZYK, C. AND TITUS, M. (2016). VGOS Observations with Westford, GGAO, and the New Station at Kokee, Hawaii. In D. Behrend, K.D. Baver and K.L. Armstrong, eds., *International VLBI Service for Geodesy and Astrometry 2016 General Meeting Proceedings - "New Horizons with VGOS"*, Johannesburg, South Africa, March 13-19, 2016, 44–48.
- NIELL, A.E., WHITNEY, A., PETRACHENKO, B., SCHLÜTER, VANDENBERG, N., HASE, H., KOYAMA, Y., MA, C., SCHUH, H. AND TUCCARI, G. (2006). VLBI2010: Current and Future Requirements for Geodetic VLBI Systems. Tech. rep., IVS Memorandum 2006-008v01.
- NILSSON, T., BÖHM, J., WIJAYA, D.D., TRESCH, A., NAFISI, V. AND SCHUH, H. (2013). Path Delays in the Neutral Atmosphere. In J. Böhm and H. Schuh, eds., *Atmospheric Effects in Space Geodesy*, 73–136, Springer Berlin Heidelberg, Berlin, Heidelberg.
- NOTHNAGEL, A. (2009). Conventions on thermal expansion modelling of radio telescopes for geodetic and astrometric VLBI. *Journal of Geodesy*, 83, 787–792.
- PANY, A., BÖHM, J., MACMILLAN, D., SCHUH, H., NILSSON, T. AND WRESNIK, J. (2011). Monte Carlo simulations of the impact of troposphere, clock and measurement errors on the repeatability of VLBI positions. *Journal of Geodesy*, 85, 39–50.
- PARK, R.S., FOLKNER, W.M., JONES, D.L., BORDER, J.S., KONOPLIV, A.S., MARTIN-MUR, T.J., DHAWAN, V., FOMALONT, E. AND ROMNEY, J.D. (2015). Very Long Baseline Array Astrometric Observations of Mars Orbiters. *The Astronomical Journal*, 150, 121.
- PETIT, G. AND LUZUM, B., eds. (2010). *IERS Conventions 2010*. No. 36 in IERS Technical Note, Verlag des Bundesamtes für Kartographie und Geodäsie, Frankfurt am Main.
- PETRACHENKO, B. (2016). VLBI Tracking of Galileo II. Tech. rep., Natural resources Canada (NR-Can), International VLBI Service for Geodesy and Astrometry (IVS), vTC report.
- PETRACHENKO, B., NIELL, A., BEHREND, D., COREY, B., BÖHM, J., CHARLOT, P., COLLIOD, A., GIPSON, J., HAAS, R., HOBIGER, T., KOYAMA, Y., MACMILLAN, D., MALKIN, Z., NILSSON, T., PANY, A., TUCCARI, G., WHITNEY, A. AND WRESNIK, J. (2009). Progress Report of the IVS VLBI2010 Committee: Design Aspects of the VLBI2010 System. Tech. rep., NASA Goddard Space Flight Center, USA, Greenbelt, Maryland 20771, NASA/TM-2009-214180.
- PETROV, L., GORDON, D., GIPSON, J., MACMILLAN, D., MA, C., FOMALONT, E. AND WALKER, C., R. CRAIGAND CARABAJAL (2009). Precise geodesy with the Very Long Baseline Array. *Journal of Geodesy*, 83, 859–876.
- PETROV, L., KOVALEV, Y.Y., FOMALONT, E.B. AND GORDON, D. (2011). The Very Long Baseline Array Galactic Plane Survey – VGaPS. *The Astronomical Journal*, 142, 35.

- PETROV, L., NATUSCH, T., WESTON, S., MCCALLUM, J., ELLINGSEN, S. AND GULYAEV, S. (2015). First Scientific VLBI Observations Using New Zealand 30 Meter Radio Telescope WARK30M. *Publications of the Astronomical Society of the Pacific*, 127, 516–522.
- PLAG, H.P. AND PEARLMAN, M., eds. (2009). *Global Geodetic Observing System: Meeting the Requirements of a Global Society on a Changing Planet in 2020*. Springer-Verlag Berlin Heidelberg.
- PLANK, L. (2014). *VLBI satellite tracking for the realization of frame ties*. No. 95 in *Geowissenschaftliche Mitteilungen, Schriftenreihe der Studienrichtung Vermessung und Geoinformation*, Technische Universität Wien, Vienna, Austria.
- PLANK, L., BÖHM, J. AND SCHUH, H. (2014). Precise station positions from VLBI observations to satellites: a simulation study. *Journal of Geodesy*, 88, 659–673.
- PLANK, L., BÖHM, J. AND SCHUH, H. (2016). Simulated VLBI Satellite Tracking of the GNSS Constellation: Observing Strategies. In C. Rizos and P. Willis, eds., *IAG 150 Years: Proceedings of the IAG Scientific Assembly in Postdam, Germany, 2013*, 85–90, Springer International Publishing.
- PLANK, L., HELLERSCHMIED, A., MCCALLUM, J., BÖHM, J. AND LOVELL, J. (2017a). VLBI observations of GNSS-satellites: from scheduling to analysis. *Journal of Geodesy*, 91, 867–880.
- PLANK, L., LOVELL, J.E.J., MCCALLUM, J.N., MAYER, D., REYNOLDS, C., QUICK, J., WESTON, S., TITOV, O., SHABALA, S.S., BÖHM, J., NATUSCH, T., NICKOLA, M. AND GULYAEV, S. (2017b). The AUSTRAL VLBI observing program. *Journal of Geodesy*, 91, 803–817.
- PRESTON, R.A., ERGAS, R., HINTEREGGER, H.F., KNIGHT, C.A., ROBERTSON, D.S., SHAPIRO, I.I., WHITNEY, A.R., ROGERS, A.E.E. AND CLARK, T.A. (1972). Interferometric Observations of an Artificial Satellite. *Science*, 178-4059, 407–409.
- RAMASASTRY, J. AND ROSENBAUM, B. (1972). ATS C-2 satellite VLBI experiment. Tech. rep., NASA Goddard Space Flight Center, Greenbelt, MD, United States, NASA-TM-X-66001.
- RAMASASTRY, J., ROSENBAUM, B., MICHELINI, R.D., FROST, D., ROSS, S. AND BOORNAZIAN, A. (1972). Tracking of the ATS-3 synchronous satellite by the Very Long Baseline Interferometer (VLBI) technique. Tech. rep., NASA Goddard Space Flight Center, Greenbelt, MD, United States, NASA-TM-X-66018.
- RICKLEFS, R. (2006). *Consolidated Laser Ranging Prediction Format Version 1.01*. International Laser Ranging Service, Prediction Format Study Group of the Data Format and Procedures Working Group.
- ROGERS, A.E.E. (1970). Very Long Baseline Interferometry with Large Effective Bandwidth for Phase-Delay Measurements. *Radio Science*, 5, 1239–1247.
- ROGERS, A.E.E. (1975). A Receiver Phase and Group Delay Calibrator for Use in Very Long Baseline Interferometry. Tech. rep., Haystack Observatory, Westford, MA., United States.

- ROMNEY, J.D. (1999). *Cross Correlators*, Vol. 180 of *ASP Conference Series*, 57–78.
- ROSENBAUM, B. (1972). The VLBI Time Delay Function for Synchronous Orbits. Tech. rep., NASA Goddard Space Flight Center, Greenbelt, MD, United States, NASA-TM-X-66122.
- ROTHACHER, M., BEUTLER, G., BEHREND, D., DONNELLAN, A., HINDERER, J., MA, C., NOLL, C., OBERST, J., PEARLMAN, M., PLAG, H.P, RICHTER, B., SCHÖNE, T., TAVERNIER, G. AND WOODWORTH, P.L. (2009). The future Global Geodetic Observing System. In H.P. Plag and M. Pearlman, eds., *Global Geodetic Observing System: Meeting the Requirements of a Global Society on a Changing Planet in 2020*, 237–272, Springer Berlin Heidelberg.
- SAASTAMOINEN, J. (1972). *Atmospheric Correction for the Troposphere and Stratosphere in Radio Ranging Satellites*, 247–251. American Geophysical Union.
- SALZBERG, I. (1967). Mathematical relationships of the MFOD ANTENNA axes. Tech. Rep. 67N39334, NASA Goddard Space Flight Center, Greenbelt, MD, United States, report/Patent Number: NASA-TM-X-55956, X-553-67-213.
- SCHARTNER, M., BÖHM, J., MAYER, D., MCCALLUM, L. AND HELLERSCHMIED, A. (2017). Recent Development in Scheduling with VieVS. In R. Haas and G. Elgered, eds., *Proceedings of the 23rd European VLBI Group for Geodesy and Astrometry Working Meeting, May 14-19, Gothenburg, Sweden*, 113–116, ISBN 978-91-88041-09-8.
- SCHMID, R. AND ROTHACHER, M. (2003). Estimation of elevation-dependent satellite antenna phase center variations of GPS satellites. *Journal of Geodesy*, 77, 440–446.
- SCHMID, R., DACH, R., COLLILIEUX, X., JÄGGI, A., SCHMITZ, M. AND DILSSNER, F. (2016). Absolute IGS antenna phase center model igs08.atx: status and potential improvements. *Journal of Geodesy*, 90, 343–364.
- SCHUH, H. AND BÖHM, J. (2013). *Very Long Baseline Interferometry for Geodesy and Astrometry*, 339–376. Springer Berlin Heidelberg, Berlin, Heidelberg.
- SEITZ, M., ANGERMANN, D., BLOSSFELD, M., DREWES, H. AND GERSTL, M. (2012). The 2008 DGFI realization of the ITRS: DTRF2008. *Journal of Geodesy*, 86, 1097–1123.
- SEITZ, M., STEIGENBERGER, P. AND ARTZ, T. (2014). Consistent Adjustment of Combined Terrestrial and Celestial Reference Frames. In C. Rizos and P. Willis, eds., *Earth on the Edge: Science for a Sustainable Planet, Proc. IAG General Assembly, 2011*, International Association of Geodesy Symposia, 215–221, Springer Berlin Heidelberg.
- SEKIDO, M. AND FUKUSHIMA, T. (2006). A VLBI Delay Model for Radio Sources at a Finite Distance. *Journal of Geodesy*, 80, 137–149.
- SOŚNICA, K., THALLER, D., DACH, R., STEIGENBERGER, P., BEUTLER, G., ARNOLD, D. AND JÄGGI, A. (2015). Satellite laser ranging to gps and glonass. *Journal of Geodesy*, 89, 725–743.

- SOVERS, O.J., FANSELOW, J.L. AND JACOBS, C.S. (1998). Astrometry and geodesy with radio interferometry: experiments, models, results. *Rev. Mod. Phys.*, 70, 1393–1454.
- SPRINGER, T.A. (2009). NAPEOS mathematical models and algorithms. Tech. rep., ESA. DOPS-SYS-TN-0100-OPS-GN.
- SUN, J. (2013). *VLBI scheduling strategies with respect to VLBI2010*. No. 92 in Geowissenschaftliche Mitteilungen, Schriftenreihe der Studienrichtung Vermessung und Geoinformation, Technische Universität Wien, Vienna, Austria.
- SUN, J., BÖHM, J., NILSSON, T., KRÁSNÁ, H., BÖHM, S. AND SCHUH, H. (2014). New VLBI2010 scheduling strategies and implications on the terrestrial reference frames. *Journal of Geodesy*, 88, 449–461.
- SUN, J., TANG, G., SHU, F., LI, X., LIU, S., CAO, J., HELLERSCHMIED, A., BÖHM, J., MCCALLUM, L., MCCALLUM, J., LOVELL, J., HAAS, R., NEIDHARDT, A., LU, W., HAN, S., REN, T., CHEN, L., WANG, M. AND PING, J. (2018). VLBI observations to the APOD satellite. *Advances in Space Research*, 61, 823–829.
- ŠVEHLA, D. AND ROTHACHER, M. (2005). Kinematic Precise Orbit Determination for Gravity Field Determination. In F. Sansò, ed., *A Window on the Future of Geodesy, Proceedings of the International Association of Geodesy IAG General Assembly Sapporo, Japan, June 30 - July 11, 2003*, Vol. 128 of *International Association of Geodesy Symposia*, 181–188, Springer Berlin Heidelberg, Berlin, Heidelberg.
- SWATSCHINA, P. (2012). *Dynamic and reduced-Dynamic Precise Orbit Determination of Satellites in Low Earth Orbits*. No. 89 in Geowissenschaftliche Mitteilungen, Schriftenreihe der Studienrichtung Vermessung und Geoinformation, Technische Universität Wien.
- TANG, G., NOTHNAGEL, A., HAAS, R., SCHÜLER, T., ZHANG, Q., CAO, J., HAN, S., REN, T., CHEN, L., SUN, J., WANG, M., LU, W., ZHANG, Z. AND LA PORTA, L. (2016). Research and Analysis of Lunar Radio Measurements of the Chang'E-3 Lander. In A. Nothnagel and F. Jaron, eds., *Proceedings of the First International Workshop on VLBI Observations of Near-field Targets, October 5 - 6, 2016*, Vol. 54 of *Schriftenreihe des Inst. f. Geodäsie u. Geoinformation*, 35–39, Bonn, Germany.
- TEKE, K. (2011). *Sub-daily Parameter Estimation in VLBI Data Analysis*. No. 87 in Geowissenschaftliche Mitteilungen, Schriftenreihe der Studienrichtung Vermessung und Geoinformation, Technische Universität Wien, Vienna, Austria.
- THALLER, D., DACH, R., SEITZ, M., BEUTLER, G., MAREYEN, M. AND RICHTER, B. (2011). Combination of GNSS and SLR observations using satellite co-locations. *Journal of Geodesy*, 85, 257–272.
- THOMAS, J.B. (1987). Interferometry theory for the block 2 processor. Tech. rep., Jet Propulsion Lab., California Inst. of Tech, Pasadena, CA, United States, JPL-PUBL-87-29.

- THOMAS, L.M. AND MERKOVITZ, S.M. (2014). Update on the GPS III Laser Retroreflector Array. In *Proceedings of the 19th international workshop on laser ranging, Annapolis, US, October 27-31*.
- THOMPSON, A.R., MORAN, J.M. AND SWENSON JR., G.W. (2017). *Interferometry and Synthesis in Radio Astronomy*. Astronomy and Astrophysics Library, Springer, 3rd edn.
- THORNTON, C.L. AND BORDER, J.S. (2003). *Radiometric Tracking Techniques for Deep Space Navigation*. JPL Deep Space Communications and Navigation Series, John Wiley & Sons Inc.
- TIERNO ROS, C., BÖHM, J. AND SCHUH, H. (2011). Use of GNSS-derived TEC maps for VLBI observations. In W. Alef, S. Bernhart and A. Nothnagel, eds., *Proceedings of the 20th Meeting of the European VLBI Group for Geodesy and Astrometry*, Vol. 22, 114–117, Institut für Geodäsie und Geoinformation der Universität Bonn.
- TORNATORE, V., HAAS, R., MACCAFERRI, G., CASEY, S., POGREBENKO, S., MOLERA, G. AND DUEV, D. (2010a). Tracking of GLONASS satellites by VLBI radio telescopes. In *Proc. of the 5th ESA International Workshop on Tracking, Telemetry and Command Systems for Space Applications, TTC 2010, ESA-ESTEC, Noordwijk*.
- TORNATORE, V., HAAS, R., MOLERA, G. AND POGREBENKO, S. (2010b). Planning of an Experiment for VLBI Tracking of GNSS satellites. In D. Behrend and K. Baver, eds., *International VLBI Service for Geodesy and Astrometry 2010 General Meeting Proceedings, Hobart, Tasmania, Australia, February 7–13*, 70–74, Goddard Space Flight Center Greenbelt, MD 20771-0001.
- TORNATORE, V., HAAS, R., CASEY, S., POGREBENKO, S. AND MOLERA CALVÉS, G. (2014). Direct VLBI Observations of Global Navigation Satellite System Signals. In C. Rizos and P. Willis, eds., *Earth on the Edge: Science for a Sustainable Planet, Proc. IAG General Assembly, 2011*, Vol. 6 of *International Association of Geodesy Symposia*, 247–252, Springer Berlin Heidelberg.
- VALLADO, D. (2013). *Fundamentals of Astrodynamics and Applications*. Microcosm Press, 4th edn.
- VALLADO, D., CRAWFORD, P., HUJSAK, R. AND KELSO, T. (2006). Revisiting Spacetrack Report number 3. In *AIAA/AAS Astrodynamics Specialist Conference, Keystone, CO, 2006 August 21–24*.
- VANDENBERG, N. (1997). *sked's Catalogs - Program Reference Manual*. NASA/Goddard Space Flight Center, Space Geodesy Program, VLBI Software Documentation, Scheduling Program.
- WALKER, R.C. (2014). *The SCHED User Manual - Version 11.4 of March 14, 2015*.
- WHITNEY, A., LONSDALE, C., HIMWICH, E., VANDENBERG, N., VAN LANGEVELDE, H., MUJUNEN, A. AND WALKER, C. (2002). *VEX File Definition/Example, Rev. 1.5b1*.
- WHITNEY, A.R., CAPPALLO, R., ALDRICH, W., ANDERSON, B., BOS, A., CASSE, J., GOODMAN, J., PARSLEY, S., POGREBENKO, S., SCHILIZZI, R. AND SMYTHE, D. (2004). Mark 4 VLBI correlator: Architecture and algorithms. *Radio Science*, 39, RS1007.

- WOODBURN, L., NATUSCH, T., WESTON, S., THOMASSON, P., GODWIN, M., GRANET, C. AND GULYAEV, S. (2015). Conversion of a New Zealand 30-Metre Telecommunications Antenna into a Radio Telescope. *Publications of the Astronomical Society of Australia*, 32, e017.
- YAN, J., PING, J., LI, F., CAO, J., HUANG, Q. AND FUNG, L. (2010). Chang'e-1 precision orbit determination and lunar gravity field solution. *Advances in Space Research*, 46, 50 – 57.
- ZOULIDA, M., POLLET, A., COULOT, D., PEROSANZ, F., LOYER, S., BIANCALE, R. AND REBISCHUNG, P. (2016). Multi-technique combination of space geodesy observations: Impact of the Jason-2 satellite on the GPS satellite orbits estimation. *Advances in Space Research*, 58, 1376–1389.

Curriculum Vitae

Name: **Dipl.-Ing. Andreas Hellerschmied**
Date of birth: October 22, 1986
Place of birth: Krems an der Donau
Nationality: Austria
Address: Hasnerstraße 27/39
1160 Wien
Austria
E-mail: andreas.hellerschmied@geo.tuwien.ac.at

Academic Education

02/2015 – 11/2018 Doctoral programme in Engineering Sciences – Surveying and Geoinformation, Technische Universität Wien
03/2012 – 12/2014 Master's programme – Geodesy and Geophysics, Technische Universität Wien
10/2008 – 03/2012 Bachelor's programme – Geodesy and Geomatics Engineering, Technische Universität Wien

Employment Record

01/2015 – 11/2018 University assistant, Department of Geodesy and Geoinformation, Technische Universität Wien, 1040 Vienna
01/2014 – 12/2014 Student assistant, Department of Geodesy and Geoinformation, Technische Universität Wien, 1040 Vienna
01/2013 – 10/2015 Surveying technician, Vermessung Jürgen Müller (JMGeo), 2371 Hinterbrühl

Research Stays

11/2016 – 12/2016 University of Tasmania, Hobart, Australia
01/2014 Geodetic Observatory Wettzell, Germany
09/2013 – 10/2013 Geodetic Observatory Wettzell, Germany

